

Influence of particles in multiphase turbulent flows

John Edward Vickers

Submitted in accordance with the requirements for the degree of Doctor of Philosophy

University of Leeds

School of Chemical and Process Engineering

September 2017

Intellectual Property and Publication Statements

The candidate confirms that the work submitted is his own and that appropriate credit has been given where reference has been made to the work of others.

This copy has been supplied on the understanding that it is copyright material and that no quotation from the thesis may be published without proper acknowledgement.

The right of John Edward Vickers to be identified as the author of this work has been asserted by him in accordance with the Copyright, Designs and Patents Act 1988.

Abstract

Particle behaviour and the influence of particles in multiphase turbulent flows has been examined. The effects of particle size, density and volume fraction on both the particle and fluid phases of pipe flows and impinging jets have been measured. These systems were measured using a combination of ultrasonic Doppler velocimetry and particle image velocimetry with comparisons between the two techniques made.

UDV was used to measure axial particle velocity and velocity fluctuations within a pipe at particle volume fractions between 1×10^{-4} and 64×10^{-4} using a 2MHz ultrasonic transducer. Particle density effects were examined by comparing 225 μm glass Honite 12 particles with ($\rho = 2450$) with 225 μm polystyrene Flashbead particles ($\rho = 1050$). Size effects were examined using 500 μm glass Honite 8 particles.

PIV was then used to examine the fluid response to increased particle loading within a pipe. Fluorescent tracer particles combined with an optical filter allowed for the solid phase to be excluded from the measurement. Particle volume fractions between 1×10^{-4} and 8×10^{-4} were examined using the same particles as before in addition to smaller 40 μm glass Honite 22 particles. The influence of particles on fluid turbulence is examined in addition to velocities.

The technique was then expanded to examine the more complicated flow regime of an impinging jet. In this case particle volume fractions were tested up to 4×10^{-4} , the same range of particles was tested excluding the Honite 8 particles due to their size relative to the jet. The work is concluded with measurement of the solid phase using PIV and comparison of the effectiveness of various models for predicting enhancement or suppression of turbulent flow.

Table of Contents

1	Background and Introduction.....	1
2	Literature Review.....	4
2.1	Basics of fluid flows	4
2.1.1	Fluid Properties.....	4
2.1.2	Turbulence	6
2.1.3	Particle – Turbulence Interaction	9
2.2	Pipe Flows.....	10
2.2.1	Coordinate System for Pipe Flow	10
2.2.2	Pipe Flow Structure	11
2.2.3	Single Phase Pipe Flow Studies.....	18
2.2.4	Multiphase Measurements of Pipe Flows	23
2.3	Impinging Jet Flows	27
2.3.1	Coordinate system for impinging jet flow	28
2.3.2	Impinging Jet Structure.....	28
2.3.3	Single Phase Impinging Jet Studies.....	30
2.3.4	Multiphase measurements of impinging jets.....	39
2.4	Conclusions.....	44
2.5	References	46
3	Experimental Method.....	50

3.1	Measurement Techniques.....	50
3.1.1	Overview of rejected measurement techniques.....	50
3.1.2	Hot wire Anemometry (HWA)	51
3.1.3	Laser Doppler Anemometry (LDA/LDV).....	52
3.2	Description of Selected Measurement Techniques.....	53
3.2.1	Ultrasonic Doppler Velocimetry (UDV).....	53
3.2.2	Particle Image Velocimetry (PIV)	55
3.3	UDV Measurement	61
3.3.1	UDV Pipe Loop Specifications	61
3.3.2	UDV Equipment Specifications	63
3.3.3	UDV Method	65
3.4	PIV Measurement Facility.....	67
3.4.1	Pipe Loop Design Considerations	67
3.4.2	PIV Pipe Loop Specifications.....	70
3.4.3	Impinging Jet Rig Specifications.....	73
3.4.4	PIV Equipment Specifications	77
3.4.5	PIV Method	81
3.5	Particle Selection and Preparation	95
3.5.1	Particle Selection	95
3.5.2	Particle Preparation.....	98

3.6	Error Analysis	99
3.6.1	Analysis of possible errors for the UDV system.....	99
3.6.2	Analysis of possible errors for the PIV Systems.....	102
3.6.3	Summary of Errors.....	107
3.7	References	108
4	Acoustic Measurements of Multiphase Pipe Flows.....	109
4.1	Single Phase Pipe Flow Measurements	109
4.1.1	Axial Velocities.....	110
4.1.2	Turbulence Statistics.....	113
4.2	Changes in Particle Behaviour with Concentration	116
4.2.1	Change in Axial Velocity with Particle Concentration	117
4.2.2	Change in Axial Turbulence with Concentration	120
4.2.3	Discussion of Changes in Particle Behaviour with Concentration	121
4.3	Changes in Particle Behaviour with Density	124
4.3.1	Comparison of Changes in Axial Velocity	125
4.3.2	Comparison of Changes in Axial Turbulence	127
4.3.3	Discussion of Changes in Particle Behaviour with Density	128
4.4	Effect of Particle Size on Fluid Flow.....	132
4.4.1	Comparison of Changes in Axial Velocity	133
4.4.2	Comparison of Changes in Axial Turbulence	135

4.4.3	Discussion	136
4.5	Conclusions	139
4.6	References	143
5	Optical Measurements of Pipe Flows	144
5.1	Single Phase Measurements Using PIV	144
5.1.1	Images and Flow Visualisations	145
5.1.2	Velocity Profiles	148
5.1.3	Turbulence Statistics.....	150
5.1.4	Discussion	151
5.2	Effect of Concentration on Fluid-Phase Measurements	153
5.2.1	Discussion	156
5.3	Effect of Particle Density on Fluid Flow	158
5.3.1	Velocity Profiles	159
5.3.2	Turbulence Profiles	160
5.3.3	Discussion	163
5.4	Effect of Particle Size	165
5.4.1	Velocity Profiles	166
5.4.2	Turbulence Profiles.....	168
5.4.3	Discussion	172
5.5	Conclusions	180

5.6	References	182
6	Optical Measurements of Impinging Jets	183
6.1	Single Phase Measurements of Impinging Jets	183
6.1.1	Flow Visualisations	184
6.1.2	Horizontal Velocity Flow Profiles.....	186
6.1.3	Horizontal Turbulence Flow Profiles.....	187
6.1.4	Vertical Velocity Flow Profiles	188
6.1.5	Vertical Turbulence Flow Profiles.....	189
6.2	Validation of Results.....	191
6.2.1	Discussion	194
6.3	Effect of Particle Concentration and Density on Impinging Jet Flow	195
6.3.1	Horizontal Velocity Flow Profiles.....	197
6.3.2	Horizontal Turbulence Flow Profiles.....	202
6.3.3	Vertical Velocity Flow Profiles	207
6.3.4	Vertical Turbulence Flow Profiles.....	209
6.3.5	Discussion	212
6.4	Effect of Particle Size on Impinging Jet Flow	215
6.4.1	Horizontal Velocity Flow Profiles.....	216
6.4.2	Horizontal Turbulence Flow Profiles.....	220
6.4.3	Vertical Velocity Profiles.....	225

6.4.4	Vertical Turbulence Profiles.....	228
6.4.5	Discussion	231
6.4.6	Comparison with Turbulence Models	234
6.5	Comparison of Particle and Fluid Measurements	238
6.5.1	Velocity Measurements.....	238
6.5.2	Turbulence Measurements	241
6.5.3	Discussion	244
6.6	Impinging Jet Summary and Conclusions	248
6.7	References	250
7	Conclusions and Recommendations for Future Work.....	252
7.1	Effect of Introducing Dense Solid Particles.....	252
7.2	Effect of Particle Concentration	253
7.3	Effect of Particle Size	254
7.4	Effect of Particle Density	255
7.5	Summary.....	256
7.6	Future Work.....	257

List of Figures

<i>Figure 2.1 - Fluid Parcel (Schlichting and Gersten, 2000)</i>	5
<i>Figure 2.2 – Representation of high and low turbulence within a system.</i>	6
<i>Figure 2.3 – Pipe Flow coordinate diagram.</i>	10
<i>Figure 2.4 – Showing transition as the flow develops (Cengel and Cimbala, 2006)</i>	11
<i>Figure 2.5 – Laminar and Turbulent Flow Profiles (Cengel and Cimbala, 2006)</i>	14
<i>Figure 2.6 - Flattening of velocity profile with increased velocity (Laufer, 1954)</i>	16
<i>Figure 2.7 – Axial and radial turbulence measurements with increased solids loading (Zisselmar and Molerus, 1979)</i>	24
<i>Figure 2.8 – Diagram of the flow structure of an impinging jet</i>	27
<i>Figure 3.1– PIV measurement technique from Dantec Dynamics, (2017)</i>	56
<i>Figure 3.2 – Diagram of the measurement section</i>	61
<i>Figure 3.3 – UDV Pipe loop flow diagram.</i>	63
<i>Figure 3.4 – Change in axial velocity with change in number of pulses.</i>	64
<i>Figure 3.5 – Change in axial turbulence with change in number of pulses.</i>	64
<i>Figure 3.6 – Drawing of the box section which encloses the pipe.</i>	67
<i>Figure 3.7 – Calibration plate without box section showing optical distortion.</i>	68
<i>Figure 3.8 – Calibration plate with box section showing reduction in distortion.</i>	68
<i>Figure 3.9 – PIV pipe loop drawing with areas of interest labelled.</i>	70
<i>Figure 3.10 – PIV pipe loop measurement section diagram.</i>	70
<i>Figure 3.11 – Flow diagram of PIV pipe loop.</i>	70
<i>Figure 3.12 – Drawing of impinging jet test facility.</i>	73
<i>Figure 3.13 – Cross section of the impinging jet test tank showing the region of interrogation.</i>	74
<i>Figure 3.14 – Impinging jet flow diagram.</i>	77
<i>Figure 3.15 – Number of pixels required for PIV images as a function of scale factor.</i>	80
<i>Figure 3.16 – Redesigned cross brace for impinging jet tank.</i>	83
<i>Figure 3.17 - Calibration within Dantec Dynamics PIV software.</i>	86
<i>Figure 3.18 – Picture of tape measure used for calibration along the right-hand side of the pipe.</i>	86
<i>Figure 3.19 - Cropped Image of region of interest showing fluorescent particles.</i>	88
<i>Figure 3.20 – Percentage change in velocity and turbulence values as number of image pairs is increased.</i>	90

<i>Figure 3.21 – Change in maximum velocity with number of image pairs.</i>	90
<i>Figure 3.22 – Vectors displayed after cross correlation</i>	92
<i>Figure 3.23 – Uncertainty with regards to gradient, where σ is the systematic uncertainty value and σ_{lower} and σ_{upper} are the lower and upper bounds in which 95% of the data is contained. Timmins et al (2012).</i>	104
<i>Figure 3.24 – Uncertainty with regards to particle image diameter, where σ is the systematic uncertainty value and σ_{lower} and σ_{upper} are the lower and upper bounds in which 95% of the data is contained. Timmins et al (2012).</i>	105
<i>Figure 4.1 – Diagram showing the location of the ultrasonic probe in relation to the pipe, in addition to the coordinate system used.</i>	109
<i>Figure 4.2 – Comparison between acoustic results and the DNS predictions of Wu and Moin, (2008)</i>	110
<i>Figure 4.3 – Axial velocity in wall units with log law equation overlay.</i>	113
<i>Figure 4.4 – Comparison of UDV axial turbulence measurements with those of Laufer, (1954)</i>	114
<i>Figure 4.5 – Change in axial velocity with increase in particle volume fraction of Honite 12 particles.</i>	117
<i>Figure 4.6 – Change in axial velocity with increase in particle volume fraction of Honite 12 particles plotted in wall units.</i>	118
<i>Figure 4.7 – Axial velocity percentage change with increased Honite 12 particle loading in the near wall region.</i>	119
<i>Figure 4.8 – Axial velocity percentage change with increased Honite 12 particle loading in the bulk flow region.</i>	119
<i>Figure 4.9 – Change in axial velocity fluctuations with increase in particle volume fraction of Honite 12.</i>	120
<i>Figure 4.10 – Axial turbulence percentage change with increased Honite 12 particle loading in the near wall region.</i>	121
<i>Figure 4.11 – Axial turbulence percentage change with increased Honite 12 particle loading in the bulk flow region.</i>	121
<i>Figure 4.12 – Change in axial velocity with increasing concentration of Flashbead and Honite 12 particles.</i>	125
<i>Figure 4.13 – Change in axial velocity with increasing concentration of Honite 12 and Flashbead particles plotted in wall units.</i>	126

<i>Figure 4.14 – Percentage change in axial velocity with change in Honite 12 and Flashbead particle loading in the near wall region.</i>	126
<i>Figure 4.15 – Percentage change in axial velocity with change in Honite 12 and Flashbead particle loading in the bulk flow region.</i>	126
<i>Figure 4.16 – Change in axial velocity fluctuations with increasing concentration of Honite 12 and Flashbead particles.</i>	127
<i>Figure 4.17 – Percentage change in axial velocity fluctuations with change in Honite 12 and Flashbead particle loading in the near wall region.</i>	128
<i>Figure 4.18 – Percentage change in axial velocity fluctuations with change in Honite 12 and Flashbead particle loading in the bulk flow region.</i>	128
<i>Figure 4.19 – Mechanism of particle resuspension. Rashidi et al., (1990)</i>	129
<i>Figure 4.20 – Ratio of particle to fluid velocity immediately before and after the particle. Kaftori et al., (1995)</i>	130
<i>Figure 4.21 – Change in axial velocity with increasing concentration of Honite 8 and Honite 12 particles.</i>	133
<i>Figure 4.22 – Change in axial velocity with increasing concentration of Honite 8 and Honite 12 particles plotted in wall units.</i>	134
<i>Figure 4.23 – Percentage change in axial velocity with change in Honite 12 and Honite 8 particle loading in the near wall region.</i>	134
<i>Figure 4.24 – Percentage change in axial velocity with change in Honite 12 and Honite 8 particle loading in the bulk flow region.</i>	134
<i>Figure 4.25 – Change in axial velocity fluctuations with increasing concentration of Honite 8 and Honite 12 particles.</i>	135
<i>Figure 4.26 – Percentage change in axial velocity fluctuations with change in Honite 12 and Honite 8 particle loading in the near wall region.</i>	136
<i>Figure 4.27 – Percentage change in axial velocity fluctuations with change in Honite 12 and Honite 8 particle loading in the bulk flow region</i>	136
<i>Figure 4.28 – Near wall change in axial velocity with increased particle concentration</i>	140
<i>Figure 4.29 – Centreline change in axial velocity with increased particle concentration.</i>	140
<i>Figure 4.30 – Near wall change in axial velocity fluctuations with increased particle concentration.</i>	141

<i>Figure 4.31 – Centreline change in axial velocity fluctuations with increased particle concentration.</i>	141
<i>Figure 5.1 - Schematic of measurement area and coordinate system.</i>	145
<i>Figure 5.2 – Axial and radial velocity contour plots where the pipe wall is located at $y/R = 1$.and the centreline at $y/R=0$.</i>	146
<i>Figure 5.3 – Axial and radial turbulence contour plots where the pipe wall is located at $y/R = 1$.and the centreline at $y/R=0$.</i>	147
<i>Figure 5.4 – Comparison of PIV axial velocity measurements, with UDV measurements and DNS predictions.</i>	148
<i>Figure 5.5 – Comparison of PIV and UDV measurements plotted in wall units.</i>	149
<i>Figure 5.6 – PIV radial velocity measurements.</i>	149
<i>Figure 5.7 Comparison of axial PIV and UDV measurements against those of Laufer, (1954).</i>	150
<i>Figure 5.8 – Comparison of radial PIV measurements against those of Laufer, (1954).</i>	150
<i>Figure 5.9 – Change in axial velocity with distance and concentration.</i>	153
<i>Figure 5.10 – Change in axial velocity with distance and concentration plotted in wall units.</i>	153
<i>Figure 5.11 – Change in axial turbulence measurements with distance and concentration.</i>	154
<i>Figure 5.12 – Combined images of the same region as particle volume fraction is increased.</i>	155
<i>Figure 5.13 – Velocity profiles in the presence of increasing concentrations of Honite and Flashbead particles</i>	159
<i>Figure 5.14 – Velocity profiles in the presence of increasing concentrations of Honite and Flashbead particles plotted in wall units</i>	159
<i>Figure 5.15 – Percentage change in axial velocity with change in Honite 12 and Flashbead particle loading in the near wall region.</i>	160
<i>Figure 5.16 – Percentage change in axial velocity with change in Honite 12 and Flashbead particle loading in the bulk flow region.</i>	160
<i>Figure 5.17 – Axial turbulence profiles in the presence of increasing concentrations of Honite and Flashbead particles.</i>	160
<i>Figure 5.18 – Radial turbulence profiles in the presence of increasing concentrations of Honite and Flashbead particles</i>	160

<i>Figure 5.19 – Percentage change in axial turbulence with change in Honite 12 and Flashbead particle loading in the near wall region.</i>	161
<i>Figure 5.20 – Percentage change in axial turbulence with change in Honite 12 and Flashbead particle loading in the bulk flow region.</i>	161
<i>Figure 5.21 – Percentage change in radial turbulence with change in Honite 12 and Flashbead particle loading in the near wall region.</i>	162
<i>Figure 5.22 – Percentage change in radial turbulence with change in Honite 12 and Flashbead particle loading in the bulk flow region.</i>	162
<i>Figure 5.23 – Comparison of the effect of Honite 12 and Honite 22 particles on the axial velocity profile.</i>	166
<i>Figure 5.24 – Comparison of the effect of Honite 12 and Honite 8 particles on the axial velocity profile.</i>	166
<i>Figure 5.25 – Comparison of the effect of Honite 12 and Honite 22 particles on the axial velocity profile plotted in wall units.</i>	166
<i>Figure 5.26 – Comparison of the effect of Honite 12 and Honite 8 particles on the axial velocity profile plotted in wall units.</i>	166
<i>Figure 5.27 – Percentage change in axial velocity with change in Honite 12 and Honite 22 particle loading in the near wall region.</i>	167
<i>Figure 5.28 – Percentage change in axial velocity with change in Honite 12 and Honite 22 particle loading in the bulk flow region.</i>	167
<i>Figure 5.29 – Percentage change in axial velocity with change in Honite 12 and Honite 8 particle loading in the near wall region.</i>	168
<i>Figure 5.30 – Percentage change in axial velocity with change in Honite 12 and Honite 8 particle loading in the bulk flow region.</i>	168
<i>Figure 5.31 – Comparison of the effect of Honite 12 and Honite 22 particles on the axial turbulence profile.</i>	169
<i>Figure 5.32 – Comparison of the effect of Honite 12 and Honite 8 particles on the axial turbulence profile.</i>	169
<i>Figure 5.33 – Comparison of the effect of Honite 12 and Honite 22 particles on the radial turbulence profile.</i>	169
<i>Figure 5.34 – Comparison of the effect of Honite 12 and Honite 8 particles on the radial turbulence profile.</i>	169
<i>Figure 5.35 – Percentage change in axial turbulence with change in Honite 12 and Honite 22 particle loading in the near wall region.</i>	170

<i>Figure 5.36 – Percentage change in axial turbulence with change in Honite 12 and Honite 22 particle loading in the bulk flow region.</i>	170
<i>Figure 5.37 – Percentage change in axial turbulence with change in Honite 12 and Honite 8 particle loading in the near wall region.</i>	170
<i>Figure 5.38 – Percentage change in axial turbulence with change in Honite 12 and Honite 8 particle loading in the bulk flow region.</i>	170
<i>Figure 5.39 – Percentage change in radial turbulence with change in Honite 12 and Honite 22 particle loading in the near wall region.</i>	171
<i>Figure 5.40 – Percentage change in radial turbulence with change in Honite 12 and Honite 22 particle loading in the bulk flow region.</i>	171
<i>Figure 5.41 – Percentage change in radial turbulence with change in Honite 12 and Honite 8 particle loading in the near wall region.</i>	172
<i>Figure 5.42 – Percentage change in radial turbulence with change in Honite 12 and Honite 8 particle loading in the bulk flow region.</i>	172
<i>Figure 5.43 – Change in shape of velocity profiles as particle concentration is increased, Tsuji and Morikawa (1982).</i>	173
<i>Figure 5.44 – Change in turbulent intensity as a function of the ratio of particle diameter to characteristic eddy size Gore and Crowe (1989).</i>	176
<i>Figure 5.45 - Change in turbulent intensity as a function of the ratio of particle diameter to characteristic eddy size for PIV measurements.</i>	176
<i>Figure 5.47 – Flashbead particle Reynolds number across the pipe</i>	177
<i>Figure 5.47 – Honite 8 particle Reynolds number across the pipe</i>	177
<i>Figure 5.48 – Honite 12 particle Reynolds number across the pipe</i>	177
<i>Figure 5.49 Percentage change in fluid turbulence with particle Reynolds number</i>	178
<i>Figure 5.50 - Map of regimes of interaction between particles and turbulence Elghobashi. (1994).</i>	179
<i>Figure 5.51 – Map showing locations of PIV results on a scaled version of Figure 5.50.</i>	179
<i>Figure 6.1 – Axial velocity contour plot from PIV measurements of the impinging jet.</i>	184
<i>Figure 6.2 – Radial velocity contour plot from PIV measurements of the impinging jet.</i>	184
<i>Figure 6.3 – Axial turbulence contour plot from PIV measurements of the impinging jet.</i>	185

<i>Figure 6.4 – Radial turbulence contour plot from PIV measurements of the impinging jet.</i>	185
<i>Figure 6.5 – Change in jet axial velocity as impingement plate is approached.</i>	186
<i>Figure 6.7 - Change in axial turbulence as impingement plate is approached.</i>	187
<i>Figure 6.8 - Change in radial turbulence as impingement plate is approached.</i>	187
<i>Figure 6.9 – Change in axial velocity as distance from the jet centreline is increased.</i>	188
<i>Figure 6.10 – Change in radial velocity as distance from the jet centreline is increased.</i>	189
<i>Figure 6.11 – Change in axial turbulence as distance from the jet centreline is increased</i>	189
<i>Figure 6.12 – Change in radial turbulence as distance from the jet centreline is increased.</i>	190
<i>Figure 6.13 – Comparison of axial velocity horizontal flow profile with the PIV results of Hammad and Milanovic (2011).</i>	191
<i>Figure 6.14 – Comparison of current PIV axial velocity decay with the PIV results of Hammad and Milanovic (2011).</i>	191
<i>Figure 6.15 – Comparison of current axial turbulence with the PIV results of Hammad and Milanovic (2011).</i>	192
<i>Figure 6.16 – Comparison of current radial turbulence with the PIV results of Hammad and Milanovic (2011).</i>	192
<i>Figure 6.17 – Comparison of current PIV axial velocity with the results of Poreh et al., (1967)</i>	192
<i>Figure 6.18 – Comparison of current PIV axial turbulence with the results of Poreh et al., (1967).</i>	193
<i>Figure 6.19 – Comparison of current PIV radial turbulence with the results of Poreh et al., (1967).</i>	193
<i>Figure 6.20 – Diagram of impinging jet measurement locations, yellow shows the location of the horizontal profiles whereas blue shows the location of the vertical profiles.</i>	196
<i>Figure 6.21 – Change in axial velocity with increased Honite 12 and Flashbead particle concentration 5D from impingement.</i>	197
<i>Figure 6.22 – Change in axial velocity with increased Honite 12 and Flashbead particle concentration 1D from impingement.</i>	197

<i>Figure 6.23 – Change in axial velocity with increased Honite 12 and Flashbead particle concentration 0.5D from impingement.</i>	198
<i>Figure 6.24 – Change in axial velocity with increased Honite 12 and Flashbead particle concentration 0.2D from impingement.</i>	198
<i>Figure 6.25 – Change in radial velocity with increased Honite 12 and Flashbead particle concentration 5D from impingement.</i>	199
<i>Figure 6.26 – Change in radial velocity with increased Honite 12 and Flashbead particle concentration 1D from impingement.</i>	199
<i>Figure 6.27 – Change in radial velocity with increased Honite 12 and Flashbead particle concentration 0.5D from impingement.</i>	200
<i>Figure 6.28 – Change in radial velocity with increased Honite 12 and Flashbead particle concentration 0.2D from impingement.</i>	200
<i>Figure 6.29 – Percentage change in axial velocity with change in Honite 12 and Flashbead particle loading 1D from impingement.</i>	201
<i>Figure 6.30 – Percentage change in radial velocity with change in Honite 12 and Flashbead particle loading 1D from impingement.</i>	201
<i>Figure 6.31 – Percentage change in axial velocity with change in Honite 12 and Flashbead particle loading 0.2D from impingement.</i>	201
<i>Figure 6.32 – Percentage change in radial velocity with change in Honite 12 and Flashbead particle loading 0.2D from impingement.</i>	201
<i>Figure 6.33 – Change in axial turbulence with increased Honite 12 and Flashbead particle concentration 5D from impingement.</i>	202
<i>Figure 6.34 – Change in axial turbulence with increased Honite 12 and Flashbead particle concentration 1D from impingement.</i>	202
<i>Figure 6.35 – Change in axial turbulence with increased Honite 12 and Flashbead particle concentration 0.5D from impingement.</i>	203
<i>Figure 6.36 – Change in axial turbulence with increased Honite 12 and Flashbead particle concentration 0.2D from impingement.</i>	203
<i>Figure 6.37 – Change in radial turbulence with increased Honite 12 and Flashbead particle concentration 5D from impingement.</i>	204
<i>Figure 6.38 – Change in radial turbulence with increased Honite 12 and Flashbead particle concentration 1D from impingement.</i>	204
<i>Figure 6.39 – Change in radial turbulence with increased Honite 12 and Flashbead particle concentration 0.5D from impingement.</i>	204

<i>Figure 6.40 – Change in radial turbulence with increased Honite 12 and Flashbead particle concentration 0.2D from impingement.</i>	204
<i>Figure 6.41 – Percentage change in axial turbulence with change in Honite 12 and Flashbead particle loading 1D from impingement.</i>	206
<i>Figure 6.42 – Percentage change in radial turbulence with change in Honite 12 and Flashbead particle loading 1D from impingement.</i>	206
<i>Figure 6.43 – Percentage change in axial turbulence with change in Honite 12 and Flashbead particle loading 0.2D from impingement.</i>	206
<i>Figure 6.44 – Percentage change in radial turbulence with change in Honite 12 and Flashbead particle loading 0.2D from impingement.</i>	206
<i>Figure 6.45 – Change in axial velocity with change in Honite 12 and Flashbead particle loading along the jet centreline.</i>	207
<i>Figure 6.46 – Change in axial velocity with change in Honite 12 and Flashbead particle loading 0.5D from the jet centreline.</i>	207
<i>Figure 6.47 – Change in axial velocity with change in Honite 12 and Flashbead particle loading 1D from the jet centreline.</i>	208
<i>Figure 6.48 – Change in axial velocity with change in Honite 12 and Flashbead particle loading 5D from the jet centreline.</i>	208
<i>Figure 6.49 – Change in radial velocity with change in Honite 12 and Flashbead particle loading 0.5D from the jet centreline</i>	208
<i>Figure 6.50 – Change in radial velocity with change in Honite 12 and Flashbead particle loading 1D from the jet centreline.</i>	209
<i>Figure 6.51 – Change in radial velocity with change in Honite 12 and Flashbead particle loading 5D from the jet centreline.</i>	209
<i>Figure 6.52 – Change in axial turbulence with change in Honite 12 and Flashbead particle loading along the jet centreline.</i>	30
<i>Figure 6.53 – Change in axial turbulence with change in Honite 12 and Flashbead particle loading 0.5D from the jet centreline.</i>	210
<i>Figure 6.54 – Change in axial turbulence with change in Honite 12 and Flashbead particle loading 1D from the jet centreline.</i>	210
<i>Figure 6.55 – Change in axial turbulence with change in Honite 12 and Flashbead particle loading 5D from the jet centreline</i>	210
<i>Figure 6.56 – Change in radial turbulence with change in Honite 12 and Flashbead particle loading along the jet centreline.</i>	211

<i>Figure 6.57 – Change in radial turbulence with change in Honite 12 and Flashbead particle loading 0.5D from the jet centreline.</i>	211
<i>Figure 6.58 –Change in radial turbulence with change in Honite 12 and Flashbead particle loading 1D from the jet centreline.</i>	212
<i>Figure 6.59 – Change in radial turbulence with change in Honite 12 and Flashbead particle loading 5D from the jet centreline.</i>	212
<i>Figure 6.60 –Change in axial velocity with change in Honite 12 and Honite 22 particle loading 5D from impingement.</i>	216
<i>Figure 6.61 – Change in axial velocity with change in Honite 12 and Honite 22 particle loading 1D from impingement.</i>	216
<i>Figure 6.62 –Change in axial velocity with change in Honite 12 and Honite 22 particle loading 0.5D from impingement.</i>	217
<i>Figure 6.63 – Change in axial velocity with change in Honite 12 and Honite 22 particle loading 0.2D from impingement.</i>	217
<i>Figure 6.64 –Change in radial velocity with change in Honite 12 and Honite 22 particle loading 5D from impingement.</i>	218
<i>Figure 6.65 – Change in radial velocity with change in Honite 12 and Honite 22 particle loading 1D from impingement.</i>	218
<i>Figure 6.66 –Change in radial velocity with change in Honite 12 and Honite 22 particle loading 0.5D from impingement.</i>	219
<i>Figure 6.67 – Change in radial velocity with change in Honite 12 and Honite 22 particle loading 0.2D from impingement.</i>	219
<i>Figure 6.68 – Percentage change in axial velocity with change in Honite 12 and Honite 22 particle loading 1D from impingement.</i>	219
<i>Figure 6.69 – Percentage change in radial velocity with change in Honite 12 and Honite 22 particle loading 1D from impingement.</i>	219
<i>Figure 6.70 – Percentage change in axial velocity with change in Honite 12 and Honite 22 particle loading 0.2D from impingement.</i>	220
<i>Figure 6.71 – Percentage change in radial velocity with change in Honite 12 and Honite 22 particle loading 0.2D from impingement.</i>	220
<i>Figure 6.72 –Change in axial turbulence with change in Honite 12 and Honite 22 particle loading 5D from impingement.</i>	221
<i>Figure 6.73 – Change in axial turbulence with change in Honite 12 and Honite 22 particle loading 1D from impingement.</i>	221

<i>Figure 6.74 –Change in axial turbulence with change in Honite 12 and Honite 22 particle loading 0.5D from impingement.</i>	221
<i>Figure 6.75 – Change in axial turbulence with change in Honite 12 and Honite 22 particle loading 0.2D from impingement.</i>	221
<i>Figure 6.76 –Change in radial turbulence with change in Honite 12 and Honite 22 particle loading 5D from impingement.</i>	222
<i>Figure 6.77 – Change in radial turbulence with change in Honite 12 and Honite 22 particle loading 1D from impingement.</i>	222
<i>Figure 6.78 –Change in radial turbulence with change in Honite 12 and Honite 22 particle loading 0.5D from impingement.</i>	223
<i>Figure 6.79 – Change in radial turbulence with change in Honite 12 and Honite 22 particle loading 0.2D from impingement.</i>	223
<i>Figure 6.80 – Percentage change in axial turbulence with change in Honite 12 and Honite 22 particle loading 1D from impingement.</i>	224
<i>Figure 6.81 – Percentage change in radial turbulence with change in Honite 12 and Honite 22 particle loading 1D from impingement.</i>	224
<i>Figure 6.82 – Percentage change in axial turbulence with change in Honite 12 and Honite 22 particle loading 0.2D from impingement.</i>	225
<i>Figure 6.83 – Percentage change in radial turbulence with change in Honite 12 and Honite 22 particle loading 0.2D from impingement.</i>	225
<i>Figure 6.84 –Change in axial velocity with change in Honite 12 and Honite 22 particle loading along the jet centreline.</i>	226
<i>Figure 6.85 – Change in axial velocity with change in Honite 12 and Honite 22 particle loading 0.5 D from the jet centreline.</i>	226
<i>Figure 6.86 –Change in axial velocity with change in Honite 12 and Honite 22 particle loading 1D from the jet centreline.</i>	227
<i>Figure 6.87 – Change in axial velocity with change in Honite 12 and Honite 22 particle loading 5 D from the jet centreline.</i>	227
<i>Figure 6.88 – Change in radial velocity with change in Honite 12 and Honite 22 particle loading 0.5 D from the jet centreline.</i>	227
<i>Figure 6.89 –Change in radial velocity with change in Honite 12 and Honite 22 particle loading 1D from the jet centreline.</i>	228
<i>Figure 6.90 – Change in radial velocity with change in Honite 12 and Honite 22 particle loading 5 D from the jet centreline.</i>	228

<i>Figure 6.91 –Change in axial turbulence with change in Honite 12 and Honite 22 particle loading along the jet centreline.</i>	229
<i>Figure 6.92 – Change in axial turbulence with change in Honite 12 and Honite 22 particle loading 0.5D from the jet centreline.</i>	229
<i>Figure 6.93 –Change in axial turbulence with change in Honite 12 and Honite 22 particle loading 1D from the jet centreline.</i>	229
<i>Figure 6.94 – Change in axial turbulence with change in Honite 12 and Honite 22 particle loading 5D from the jet centreline</i>	229
<i>Figure 6.95 –Change in radial turbulence with change in Honite 12 and Honite 22 particle loading along the jet centreline.</i>	230
<i>Figure 6.96 – Change in radial turbulence with change in Honite 12 and Honite 22 particle loading 0.5D from the jet centreline.</i>	230
<i>Figure 6.97 –Change in radial turbulence with change in Honite 12 and Honite 22 particle loading 1D from the jet centreline.</i>	231
<i>Figure 6.98 – Change in radial turbulence with change in Honite 12 and Honite 22 particle loading 5D from the jet centreline.</i>	231
<i>Figure 6.99– Particle trajectories in the stagnation zone. (a) $St = 2.4$; (b) $St = 0.6$. (Anderson and Longmire 1995)</i>	233
<i>Figure 6.100 – Change in turbulent intensity as a function of the ratio of particle diameter to characteristic eddy size Gore and Crowe (1989).</i>	235
<i>Figure 6.101 - Change in turbulent intensity as a function of the ratio of particle diameter to characteristic eddy size for impinging jet PIV measurements (Honite black, Flashbead Blue).</i>	235
<i>Figure 6.102 - Map of regimes of interaction between particles and turbulence Elghobashi (1994).</i>	236
<i>Figure 6.103 – Map showing locations of impinging jet PIV results on a scaled version of Figure 6.102. Particles plotted at: Honite 22 ϕ, Honite 12 $\phi+0.2 \times 10^{-4}$ Flashbead $\phi-0.2 \times 10^{-4}$ to avoid overlap.</i>	236
<i>Figure 6.104 –Change in axial fluid and particle velocities with change in Honite 22 particle loading 5D from impingement.</i>	239
<i>Figure 6.105 – Change in axial fluid and particle velocities with change in Honite 22 particle loading 1D from impingement.</i>	239
<i>Figure 6.106 –Change in axial fluid and particle velocities with change in Honite 22 particle loading 0.5D from impingement.</i>	239

<i>Figure 6.107 – Change in axial fluid and particle velocities with change in Honite 22 particle loading 0.2D from impingement.</i>	239
<i>Figure 6.108 – Change in radial fluid and particle velocities with change in Honite 22 particle loading 5D from impingement.</i>	240
<i>Figure 6.109 – Change in radial fluid and particle velocities with change in Honite 22 particle loading 1D from impingement.</i>	240
<i>Figure 6.110 – Change in radial fluid and particle velocities with change in Honite 22 particle loading 0.5D from impingement.</i>	241
<i>Figure 6.111 – Change in radial fluid and particle velocities with change in Honite 22 particle loading 0.2D from impingement.</i>	241
<i>Figure 6.112 – Change in axial fluid and particle velocity fluctuations with change in Honite 22 particle loading 5D from impingement.</i>	242
<i>Figure 6.113 – Change in axial fluid and particle velocity fluctuations with change in Honite 22 particle loading 1D from impingement.</i>	242
<i>Figure 6.114 – Change in axial fluid and particle velocity fluctuations with change in Honite 22 particle loading 0.5D from impingement.</i>	242
<i>Figure 6.115 – Change in axial fluid and particle velocity fluctuations with change in Honite 22 particle loading 0.2D from impingement.</i>	242
<i>Figure 6.116 – Change in radial fluid and particle velocity fluctuations with change in Honite 22 particle loading 5D from impingement.</i>	243
<i>Figure 6.117 – Change in radial fluid and particle velocity fluctuations with change in Honite 22 particle loading 1D from impingement.</i>	243
<i>Figure 6.118 – Change in radial fluid and particle velocity fluctuations with change in Honite 22 particle loading 0.5D from impingement.</i>	244
<i>Figure 6.119 – Change in radial fluid and particle velocity fluctuations with change in Honite 22 particle loading 0.2D from impingement.</i>	244
<i>Figure 6.120 – Contour plot of the relative velocity between the particles and the fluid for the impinging jet laden with Honite 22 particles at $\varphi = 2 \times 10^{-4}$.</i>	245
<i>Figure 6.121 – Contour plot of the particle Reynolds number for the impinging jet laden with Honite 22 particles at $\varphi = 2 \times 10^{-4}$.</i>	245

List of Tables

<i>Table 2.1 – Nomenclature used for Pipe Flow measurements.</i>	11
<i>Table 2.2 – Suggested constants for Log-Law equations.</i>	21
<i>Table 2.3 – Effect of Stokes number on particle behaviour</i>	41
<i>Table 3.1 – UDV measurement parameters.</i>	63
<i>Table 3.2 – PIV measurement parameters.</i>	81
<i>Table 3.3 – Errors associated with misalignments in PIV.</i>	103
<i>Table 4.1 – Honite 12 particle properties.</i>	116
<i>Table 4.2 – Mass of Honite particles for a given volume fraction.</i>	116
<i>Table 4.3 – Flashbead particle properties.</i>	124
<i>Table 4.4 – Mass of Flashbead particles for a given particle volume fraction.</i>	124
<i>Table 4.5 – Honite 8 particle properties.</i>	132
<i>Table 4.6 – Mass of Honite particles for a given volume fraction.</i>	132
<i>Table 5.1 – Honite 12 particle properties.</i>	158
<i>Table 5.2 – Flashbead particle properties.</i>	158
<i>Table 5.3 – Mass of Honite particles for a given volume fraction.</i>	158
<i>Table 5.4 – Mass of Flashbead particles for a given volume fraction.</i>	158
<i>Table 5.5 – Particle properties for various sizes of Honite particles.</i>	165
<i>Table 5.6 – Mass of Honite particles for a given volume fraction.</i>	165
<i>Table 6.1 – Honite 12 particle properties.</i>	195
<i>Table 6.2 – Flashbead particle properties.</i>	195
<i>Table 6.3 – Mass of Honite particles for a given volume fraction.</i>	196
<i>Table 6.4 – Mass of Flashbead particles for a given volume fraction.</i>	197
<i>Table 6.5 – Particle properties for various sizes of Honite particles.</i>	215
<i>Table 6.6 – Mass of Honite particles for a given volume fraction.</i>	215

Nomenclature

C	Speed of Sound	T	Time
C^+	Log law Constant	t_k	Kolmogorov Time Scale
C_{k_w}	Kolmogorov Power Law Constant	t_p	Particle Response Time
D	Pipe/Jet Diameter	U	Axial Velocity
D_a	Aperture Diameter	U_0	Maximum Velocity
d_p	Particle Diameter	U_f	Fluid Velocity
d_{ps}	Particle Image Diameter	U_k	Kolmogorov Velocity
d_{pt}	Airy Patter	U_N	Mean Velocity over N Samples
E	Energy	U_p	Particle Velocity
e_r	Wall Roughness	U_y	Mean Velocity at y
F	Focal Length	U_τ	Friction Velocity
f	Friction Factor	U^+	Axial velocity in Wall Units
f_0	Probe Operating Frequency	u	Axial Fluctuating Velocity
f_D	Doppler Frequency	u_i	Axial Instantaneous Velocity
f_{prf}	Probe Repetition Frequency	u'	Axial RMS
g	Acceleration due to Gravity	V	Radial Velocity
k	Von Karman Constant	V_m	Maximal Radial Velocity
k_w	Wave Number	v	Radial Fluctuating Velocity
L	Length	v_i	Radial Instantaneous Velocity
l_e	Characteristic Eddy Size	v'	Radial RMS
l^+	Length in Wall Units	W	Azimuthal Velocity
M	Magnification	w	Azimuthal Fluctuating Velocity
N	Number of Samples	w_i	Azimuthal Instantaneous Velocity
N_0	Number of Channels	X, x	Axial Displacement
Q	Flow Rate	Y, y	Radial Displacement
R	Pipe Radius	y^+	Radial Displacement in Wall Units
Re	Reynolds Number	Z	Bandwidth
Re_p	Particle Reynolds Number	z_0	Image Distance
St	Stokes Number		

Greek Letters

ε	<i>Dissipation Rate</i>	ξ	<i>Diffusivity Constant</i>
ε_b	<i>Beam Divergence</i>	ρ	<i>Density</i>
ε_d	<i>Diffusivity</i>	ρ_f	<i>Fluid Density</i>
η	<i>Kolmogorov Length Scale</i>	ρ_p	<i>Particle Density</i>
θ	<i>Azimuthal Displacement</i>	τ	<i>Shear Stress</i>
λ	<i>Wavelength</i>	τ_w	<i>Wall Shear Stress</i>
μ	<i>Dynamic Viscosity</i>	φ	<i>Volume Fraction</i>
ν	<i>Kinematic Viscosity</i>	ω_b	<i>Beam Divergence Angle</i>

List of Abbreviations

<i>CFD</i>	<i>Computational Fluid Dynamics</i>
<i>DNS</i>	<i>Direct Numerical Simulation</i>
<i>HWA</i>	<i>Hot Wire Anemometry</i>
<i>LDA/LDV</i>	<i>Laser Doppler Anemometry/Velocimetry</i>
<i>LES</i>	<i>Large Eddy Simulation</i>
<i>PIV</i>	<i>Particle Image Velocimetry</i>
<i>PTV</i>	<i>Particle Tracking Velocimetry</i>
<i>RMS</i>	<i>Root Mean Square</i>
<i>UDV</i>	<i>Ultrasonic Doppler Velocimetry</i>

1 Background and Introduction

The ability to accurately and easily model the behaviour of fluids in complex situations is one of the ultimate goals of fluid dynamics as the ability to predict how a fluid will behave in a certain situation will provide immense benefit in a variety of engineering disciplines. From understanding how far an aerofoil can be deformed before the fluid will separate, minimising losses in pipes, to understanding the microfluidic properties of blood in veins and arteries, fluid mechanics has a role to play.

To develop the models needed to predict these behaviours fluids need to be studied in a variety of situations; this is to gain an understanding of the underlying physics required. As these models and equations become more advanced the work then shifts towards using simulations to explore the fluid behaviours and validating the work through an experimental regime, before finally reaching a stage where simulations are capable and trusted enough to be the sole resource for predicting fluid behaviour.

In developing these models and validating the simulations, experimental techniques must be improved to accurately reflect the true behaviour of a flow. The earliest techniques were designed to simply measure the velocity of the fluid, and as time progressed more variables could be determined, but often these techniques were invasive and so the measuring equipment itself influenced the flow. Because of this less invasive methods have been developed such as ultrasonic Doppler velocimetry and particle image velocimetry (PIV).

The purpose of this investigation is twofold the first being to validate and compare the UDV and PIV techniques against other methods of acquiring flow characteristic data, the second is to probe the turbulent structure of pipe flows and impinging jets. Impinging jets have been chosen due to their multitude of engineering applications, but with additional significance attached to their use in the nuclear industry.

During the process of nuclear fission, the process which occurs within a nuclear reactor, atoms are split from large fuel atoms such as uranium and plutonium, to their smaller daughter products, releasing energy. The daughter products are of varying half-lives and activity and so when fuel is reprocessed and these products are stripped they must be stored with no way to escape to the environment. The preferred way is to vitrify the waste from the power plants, encapsulating it within borosilicate glass, however before the liquors, which are highly active, can be vitrified they must be stored safely.

Impinging jets and airlifts are used to ensure that within the highly active storage tanks (HAST) these liquors are kept suspended preventing particles from settling out and forming hot spots within the tanks. These particles are of varying sizes, shapes and densities and so it is important to understand not only how the particles will behave within the fluid but also to understand how the fluid is affected by the particles.

Chapter 2 contains a combined literature review for both pipe and impinging jet flows. Section 2.1 gives a basic introduction to fluid flows. Section 2.2 examines available literature on pipe flows. Section 2.3 looks at impinging jet studies. Section 2.4 concludes the chapter. Section 2.5 contains the references used within the chapter.

Chapter 3 is a description of the experimental methods and the equipment and facilities used to obtain the results presented in the following chapters. Section 3.1 discusses rejected measurement techniques. Section 3.2 describes in more detail UDV and PIV. Section 3.3 provides information on the UDV measurement facility and operation. Section 3.4 describes the PIV measurement facilities and equipment used. Section 3.5 discusses particle preparation and Section 3.6 contains references for the chapter.

Chapter 4 is the first results chapter, covering the use of UDV to study particle behaviour in a horizontal liquid pipe. Section 4.1 covers single phase flow measurements and compares with published work. Section 4.2 is an examination of particle behaviour within a pipe.

Section 4.3 is an examination of the effects of particle density. Section 4.4 compares particles of different sizes and section 4.5 summarises and concludes the chapter. References are contained within Section 4.6.

Chapter 5 is the second results chapter and progresses from using UDV to study pipe flow to making optical measurements using PIV. Unlike the UDV chapter this section attempts to characterise the influence of the particles on the fluid phase. Section 5.1 contains single phase measurements using PIV and compares them with UDV. Section 5.2 examines how particle volume fraction effects the accuracy of PIV measurements. Section 5.3 compares particle density effects followed by particle size effects in Section 5.4. The chapter is concluded in Section 5.5 with references in Section 5.6.

Chapter 6 is the final results chapter and covers the progression from a relatively simple pipe flow to the much more complicated impinging jet flow. Section 6.1 contains single phase measurements to ensure validity of the data (Section 6.2) before the effect of particles on the flow is examined. Section 6.3 examines particle concentration and density effects followed by particle size effects in Section 6.4. Section 6.5 contains solid phase measurements before the chapter is concluded in Section 6.6 followed by the references in Section 6.7.

Chapter 7 presents a summary of the findings and outcomes of the thesis in addition to suggestions for related future work.

2 Literature Review

The following chapter is broken up into multiple sections. Section 2.1 will introduce the basics of fluid flows and the current understanding of the influence of particles on a fluid flow. This is followed by a description of fluid flows in a pipe and an overview of the studies performed in pipes both single and multi-phase in Section 2.2. Section 2.3 follows with a description of impinging jets which continues into current studies on relevant single and multi-phase flows. Section 2.4 contains a brief conclusion on the limitations of the literature and an identification of how the work presented in this study is relevant to the field. Finally, Section 2.5 contains the references used within this chapter.

2.1 Basics of fluid flows

This section will give a brief overview of fluid properties and some of the relationships which govern their behaviour. Velocity, shear and turbulence are briefly covered in this section as well as the use of Reynolds decomposition which allows for higher order statistics to be measured from the fluid velocity.

2.1.1 Fluid Properties

The behaviour of a fluid system is dependent on several properties, in engineering systems the most important of these are: velocity, density, viscosity, pressure, temperature and specific heat capacity.

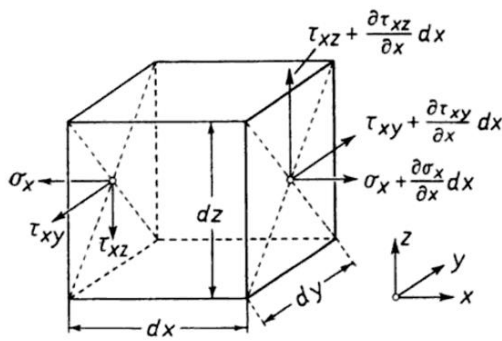


Figure 2.1 - Fluid Parcel (Schlichting and Gersten, 2000)

Velocity (U) – The fluids velocity is a measure of how quickly it is moving, when dealing with fluids it can be helpful to reduce the bulk of the fluid into individual fluid parcels or elements, which are effectively particles of fluid as seen in

Figure 2.1. The fluid velocity can refer to the entire mass of the fluid, the velocity of an individual fluid element or anything in-between depending on what is being considered. For example, a flow in a pipe has a mean fluid velocity across the entire pipe, if the pipe is divided into smaller sections however the flow near the walls will have a smaller mean velocity than at the centreline, and if the instantaneous velocity of a single fluid element is considered it can have a wildly different velocity to that of the mean.

Viscosity (μ) – This is a measure of resistance to shear deformation due to interaction between fluid molecules. Higher viscosity fluids deform more slowly under the same shear stress. Unlike a solid where the deformation (shear strain) is fixed for a constant shear stress, a fluid will continue to deform if the stress is applied, this is what causes a fluid to flow. If there is no shear stress in the system, then the fluid is stationary. A Newtonian fluid will obey Newton’s law of viscosity given in Equation 2.1 which states that the shear stress is proportional to the shear strain and are linked by a constant of proportionality (μ) this constant is known as the dynamic viscosity. The constant has the units of $\text{N}\cdot\text{s}\cdot\text{m}^{-2}$ and is the shear force per area to drag one layer of fluid past another.

$$\tau = \mu \frac{du}{dy}$$

Equation 2.1 – Newton’s law of viscosity where τ = shear stress, μ = dynamic viscosity and $\frac{du}{dy}$ = the local shear velocity.

Another term known as the kinematic viscosity (ν) is also sometimes used, this is the ratio of the dynamic viscosity to the fluid density.

2.1.2 Turbulence

Turbulent flow is highly irregular and chaotic and as such provides great difficulty when trying to predict its behaviour. In turbulent flow, there is deviation of the instantaneous pressure and velocity from the local mean values. This can be seen in Figure 2.2 which gives a simulated example of what a turbulent flow may look like. Each sample is taken at the same point in the flow, if the flow was laminar all points would lie on the same line as the mean, however as the flow is turbulent there is random scatter around the mean. The blue solid line represents a system with low turbulence where the fluctuations around the mean are small, the dashed orange line represents a higher turbulence system with greater fluctuations.

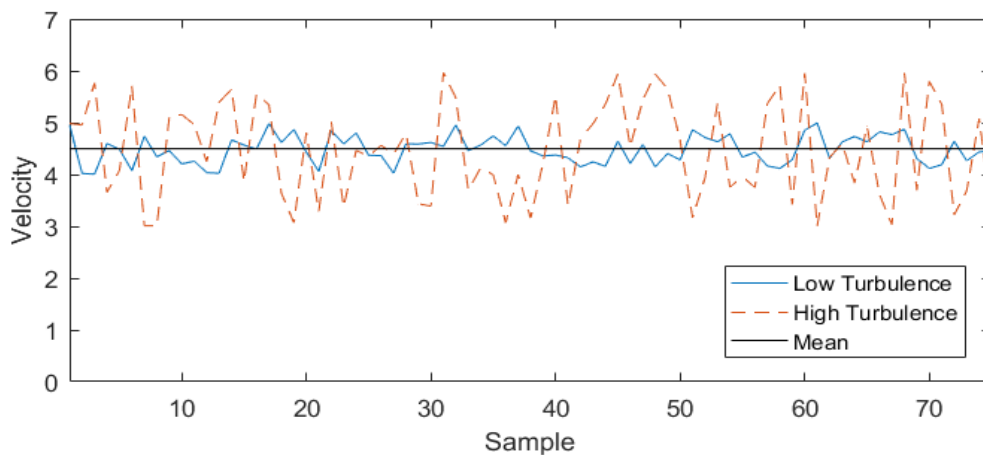


Figure 2.2 – Representation of high and low turbulence within a system.

2.1.2.1 Turbulent Length Scales

When the kinetic energy of a fluid overcomes the energy dissipation due to viscosity slight instabilities arise for individual fluid elements. This chaotic disturbance which gives rise to turbulence manifests in the form of rotating eddies. Most of this energy goes into the formation of large scale eddies, on the 'integral length scale'. The limit to the size of these

eddies is determined by the physical constraints of the fluid and flow. As the flow progresses, inertial forces cause this energy to be transferred to smaller and smaller eddies through turbulent decay also known as an energy cascade. Eventually eddies are reduced to their smallest possible size, known as the Kolmogorov length scale. At this point the fluids viscosity dominates and the turbulent kinetic energy dissipates into heat rather than cascading down and forming smaller eddies. The size of these eddies is determined by the mean rate of energy dissipation and the fluids kinematic viscosity as given in Equation 2.2

$$\eta = \left(\frac{\nu^3}{\varepsilon} \right)^{\frac{1}{4}}$$

Equation 2.2 – Kolmogorov length scale, where ν = kinematic viscosity and ε = is the average dissipation rate of turbulent kinetic energy.

The eddies of this size have a rotational velocity given by Equation 2.3

$$U_k = (\nu\varepsilon)^{\frac{1}{4}}$$

Equation 2.3 – Kolmogorov velocity scale, where ν = kinematic viscosity and ε = is the average dissipation rate of turbulent kinetic energy.

And the time taken for viscous effects to dissipate their energy is given by Equation 2.4

$$t_k = \left(\frac{\nu}{\varepsilon} \right)^{\frac{1}{2}}$$

Equation 2.4 - Kolmogorov time scale, where ν = kinematic viscosity and ε = is the average dissipation rate of turbulent kinetic energy.

To calculate these values, it is required that the energy dissipation rate is known, an approximation for this is given by Equation 2.5 where u' is the RMS of the turbulent velocity.

$$\varepsilon = \frac{(u')^3}{l_e}$$

Equation 2.5 – where ε = dissipation rate, u' = the RMS of the turbulent velocity, l_e = characteristic eddy size

Between the integral length scale and the Kolmogorov length scale are the Taylor microscales which are not dissipative but exist in the region where energy is transferred from larger eddies to smaller ones.

2.1.2.2 Calculating Turbulence

As turbulence is characterised as deviations from the mean flow it can easily be calculated if enough instantaneous velocity values are present. An instantaneous velocity value can be thought of to be composed of two parts, a mean velocity and a fluctuating velocity with turbulence represented by the fluctuating velocity. The process of separating these two components is known as a Reynolds decomposition and is shown in Equation 2.6.

$$u_i = U + u$$

Equation 2.6 – Reynolds decomposition of velocity where u_i = instantaneous velocity U = mean velocity and u = fluctuating velocity.

The mean value of the fluctuating velocity is then zero as the values fluctuate around the mean, therefore the root mean square (RMS) value is used to represent the turbulence within the system shown by Equation 2.7. As can be seen this is equal to that standard deviation of a sample and so for large sample sizes can be used interchangeably to calculate the turbulence within a system.

$$u' = \sqrt{\frac{1}{n} \sum_{1}^n (u_i - U)^2}$$

Equation 2.7 – calculation of velocity RMS (u'), where n = number of samples u_i = instantaneous velocity and U = mean velocity

2.1.3 Particle – Turbulence Interaction

Although it is known that particles have an influence on the turbulence of the continuous phase (Hetsroni, 1989), the specifics depending on the particle and the fluid are much harder to determine. Gore and Crowe, (1989) suggest that the suppression or enhancement of turbulence can be determined by the ratio of particle diameter to eddy length. With a ratio of 0.1 between the particle diameter and length of the most energetic eddies acting as the transition between enhancement and dissipation. This was done through an examination of multiphase pipe and jet systems. This would be in agreement with the assertion of Zisselmar and Molerus, (1979) that significant enhancement occurs near the wall due to particle and eddy size usually being similar in this region .

Around the same time Hetsroni, (1989) used these studies in addition to experimental observations of jet flows to try and determine a rule for when particles will enhance or suppress turbulence. He concludes that the relative velocity of the particle to the fluid can be used to predict suppression or enhancement. A value of $Re_p \approx 400$ was determined to be the transitioning condition. Above this value particles enhance turbulence due to the occurrence of vortex shedding as found by Achenbach. Vortex shedding was not found to occur below this value and so the dissipative effects of the drag force on the particles is not countered resulting in overall turbulence suppression. This is consistent with the proposed explanation of Gore and Crowe, in that smaller particles will follow the turbulent eddies for some of their lifetime over the course of which some of the turbulent energy will be converted into particle kinetic energy through the drag force as the eddies move the particle. Whereas the larger particles tend to create turbulence in its wake, this turbulence is near the scale of the most energetic eddy and so energy is transferred from the mean flow which is moving the particles to turbulent kinetic energy.

Following on from this study Elghobashi, (1994) produced a map of regimes considering the effect of particle concentration and the ratio of the particle response time to Kolmogorov time scale in order to attempt to predict the effect of particles on the carrier phase turbulence levels.

Further work on establishing guidelines for the influence of particles on flows is more limited and so being able to make predictions on how a specific multiphase system will behave is very challenging. Later in this chapter individual observations will be examined more thoroughly for jet and pipe systems.

2.2 Pipe Flows

Circular pipes are used in an almost innumerable number of fluid transport applications, from reservoirs supplying clean drinking water to households, oil and gas being pumped from source to refinery, to the supply of blood around the body. Despite the number of engineering processes heavily reliant on pipes for fluid transport, theoretical solutions only exist for a very small number of these flows. A huge factor in this is the unpredictability caused by turbulence and the factors which cause the turbulent properties to change.

2.2.1 Coordinate System for Pipe Flow

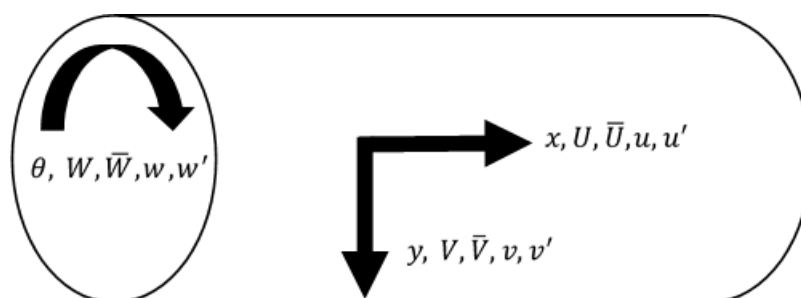


Figure 2.3 – Pipe Flow coordinate diagram.

With many authors using various annotations to represent the same property it is helpful to define some of the terms and symbols which will be used in this work. A cylindrical coordinate system is often used to describe pipe flow, where r is almost universally used to represent the radial coordinates and either x or z used for the axial a variety of symbols have been used to represent the azimuthal direction including but not limited to θ and ϕ .

When regarding the velocities in these directions it is common to use the symbols as a subscript as follows: U_x, U_r and U_θ . As this study, has focused on 1 and 2 dimensional measurements and comprises both pipe and impinging jet work it has been decided that the coordinates will be consistent between the systems and represented as shown in Table 2.1.

Table 2.1 – Nomenclature used for Pipe Flow measurements

	Symbol	Mean Velocity	Instantaneous Velocity	Fluctuating Velocity	'RMS'
Axial	X	U	u_i	u	u'
Radial	Y	V	v_i	v	v'
Azimuthal	θ	W	w_i	w	w'

2.2.2 Pipe Flow Structure

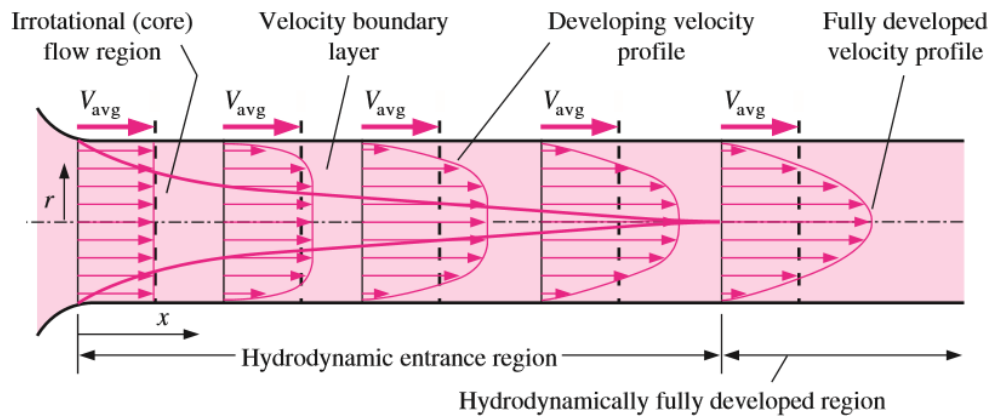


Figure 2.4 – Showing transition as the flow develops (Cengel and Cimbala, 2006)

Flow within a pipe can easily be divided into two main sections, the entrance region, where the flow enters the pipe, and the fully developed region, where the mean flow properties no longer change with increased axial distance.

2.2.2.1 Entrance Region

As can be inferred from the name, the entrance region is the immediate area where the pipe begins, at this point the flow is uniform across the pipe. As can be seen in Figure 2.4 the flow at the wall decelerates as the flow travels axially along the length of the pipe. This is due to the wall no-slip condition where a fluid in contact with a surface has zero velocity relative to that surface. Viscous effects propagate throughout the flow causing flow near the wall to travel more slowly, to maintain a constant flow rate through the pipe the flow closest to the centre of the pipe must therefore accelerate. Eventually an equilibrium is reached where the fluid layers closest to the wall are no longer being decelerated and the centreline velocity is constant. At this point the flow is considered to be fully developed.

The length of this entrance region is dependent on the properties of the fluid (viscosity, density, velocity, etc.) and the conditions of the pipe (diameter, surface roughness, orientation, etc.). The following study is examining the properties of fully developed flow so it is important to estimate when this transition occurs. The calculations change significantly depending on whether the flow is laminar or turbulent. Except at very low Reynolds numbers, laminar flow requires a much greater distance to become fully developed as the diffusion of momentum between fluid layers is a much slower process than momentum transfer due to turbulent fluctuations. For turbulent flow Zagarola and Smits, (1998) propose that the ratio of entry length to pipe diameter can be predicted through the use of the Darcy friction factor, as shown in Equation 2.8. Whereas Shames, (1982) proposes a simpler method which relies solely on the Reynolds number of the flow as given by Equation 2.9.

These equations should, however, be used with caution, as different experimental tests have produced varying results. Laufer, (1954) for example found the flow to be fully developed at a distance of 30 L/D whereas Barbin and Jones, (1963) found that over 40 diameters (the entry length suggested by Equation 2.9) fully developed flow was not achieved, although wall shear stress and the static pressure gradient reached their fully developed values within 15D.

$$\frac{L}{D} = \frac{0.5}{f} + \frac{5}{f^{\frac{1}{2}}}$$

Equation 2.8 - Required pipe length for fully developed flow where L is pipe length, D is pipe diameter and f is the pipe friction factor (Zagarola and Smits, 1998)

$$\frac{L}{D} = 4.4Re^{\frac{1}{6}}$$

Equation 2.9 - Required pipe length for fully developed flow where L is pipe length, D is pipe diameter and Re is the flow Reynolds number (Shames, 2003)

2.2.2.2 Fully Developed Region

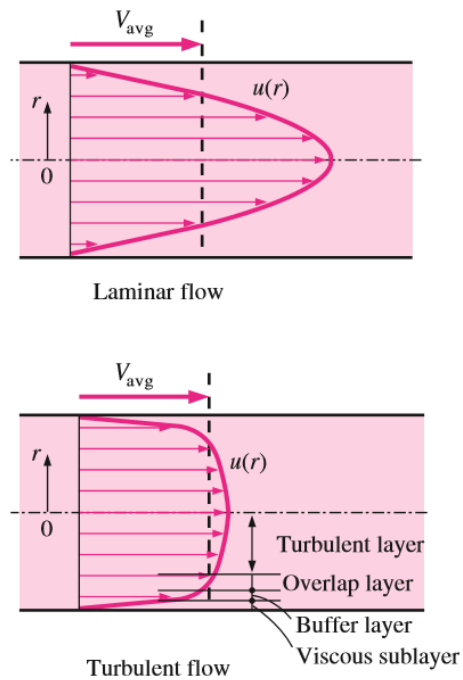


Figure 2.5 – Laminar and Turbulent Flow Profiles (Cengel and Cimbala, 2006)

behaviour of turbulent flow so difficult.

The turbulent profile is much flatter and can be further sub-divided into more regions. Depending on the author there is slight variation in the number and names of these regions. For this study, we will use four main regions (Viscous Sublayer, Buffer Layer, Inertial Sublayer and Turbulent Layer) and define further divisions when appropriate. As can be seen in Figure 2.5 the gradual decrease in velocity seen as the wall is approached in the laminar flow is replaced with a rapid drop off in the turbulent flow, within this area the viscous sublayer and buffer layer are observed.

The viscous sublayer is a very thin region immediately adjacent to the wall. Due to the dampening of turbulent eddies by the wall the flow in this region is approximately laminar, with a near constant velocity gradient given by Equation 2.10 and wall shear stress given by Equation 2.11.

In the fully developed region mean flow velocities remain constant and so the velocity profiles must also become fixed. For laminar flow the profile is almost parabolic in shape, fluid particles move at a constant velocity along streamlines with no acceleration and no radial velocity. In turbulent flow the mean velocities remain constant, although there is significant fluctuation, both axially and radially, in the velocity of fluid particles. It is these random fluctuations which make predicting the

$$\frac{du}{dy} = \frac{u}{y}$$

Equation 2.10- Velocity gradient, where y is displacement and u is velocity.

$$\tau_w = \mu \frac{u}{y} = \rho \nu \frac{u}{y}$$

Equation 2.11- Wall shear stress (τ_w) where μ = dynamic viscosity, $\frac{u}{y}$ = the velocity gradient, ρ = density and ν = kinematic viscosity.

Commonly, flow very close to the wall is non-dimensionalised using the shear or friction velocity (U_τ). This value can be calculated using Equation 2.12 (Laufer, 1954).

$$U_\tau^2 = -\nu \left(\frac{\delta U}{\delta y} \right)_{wall}$$

Equation 2.12 – Friction velocity where $\frac{\delta U}{\delta r}$ = the gradient of the mean axial velocity, U , with respect to the radial distance, y , from the pipe centreline and ν = kinematic viscosity.

However, for this to be used, velocity measurements with a high special resolution must be taken very close to the pipe wall. As this is often difficult the more general method described by Roberson and Crowe, (1975) is often used, where the wall shear stress is calculated using the Darcy friction factor (Equation 2.13) and the friction velocity is calculated from the wall shear stress (Equation 2.14).

$$\tau_w = \frac{f\rho U^2}{8}$$

Equation 2.13 – Wall shear stress (τ_w), from friction factor (f) density (ρ) and velocity (U^2)

$$U_\tau^2 = \frac{\tau_w}{\rho}$$

Equation 2.14 – Friction velocity from wall shear stress (τ_w), and density (ρ).

The wall shear stress can then be used to express variables such as distance or velocity in wall units, examples of which are given by Equations 2.15 and 2.16.

$$y^+ = \frac{y U_\tau}{\nu}$$

Equation 2.15 = Radial displacement in wall units, where y = radial displacement, U_τ = friction velocity and ν = kinematic viscosity.

$$U^+ = \frac{U}{U_\tau}$$

Equation 2.16 – Axial velocity in wall units, where U = mean axial velocity and U_τ = friction velocity

It is generally accepted that the viscous sub layer extends from the wall to a maximum value around 5 wall units ($5 y^+$), in this region y^+ is equal to U^+ . From this the thickness of the viscous sublayer (y) increases with the kinematic viscosity, and decreases with an increase in mean velocity. Therefore, increasing the Reynolds number of the flow will result in greater flattening of the velocity profile, which can be seen in Figure 2.6.

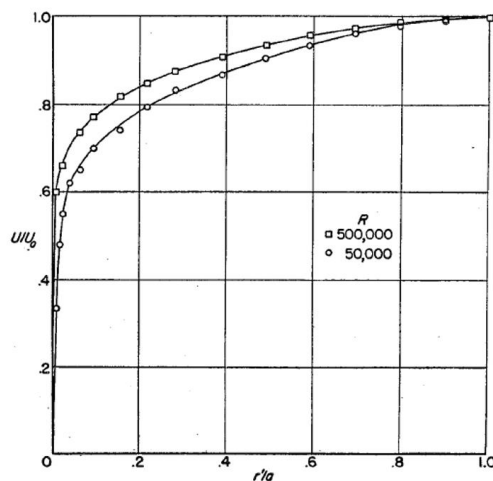


Figure 2.6 - Flattening of velocity profile with increased velocity (Laufer, 1954)

Between 5 and 30 wall units is the buffer layer in which the effect of turbulence is more pronounced, however viscous forces still dominate. In this region, the relationship of $y^+ = U^+$ no longer holds true, although the logarithmic law used to describe the overlap layer remains invalid.

From 30 wall units to around 20% of the height of the flow lies the inertial sublayer where turbulent effects are significant however still not dominant. This is also known as the Log-Law region due to the relationship between velocity and the distance from the wall, the relationship was first published by Theodore von Karman and states that within this region the average velocity is proportional to the logarithm of the distance to the wall. Equation 2.17 gives the formula which describes this region.

$$U^+ = \frac{1}{k} \ln y^+ + C^+$$

Equation 2.17 – Log law equation where U^+ = Axial velocity in wall units, k = von Karman constant, y^+ = radial displacement in wall units, and C^+ = additional constant

The values for the von Karman constant (k) and C^+ have been determined empirically and as such there is some variation in the accepted values. Marusic et al., (2013) examined several of these studies and found that values for k ranged from 0.384 to 0.438 and C^+ ranged from 2.61 to 6.27.

Beyond this is the turbulent layer, which comprises the rest of the flow. Here the turbulent effects become dominant over the flow with viscous effects becoming much less significant. Here the mean velocity profile is characterised by the velocity defect. The velocity defect is the difference between the local velocity and, in the case of pipe flow, the centreline velocity and give rise to the universal function for the velocity defect law shown in Equation 2.18 (Perry et al., 1986).

$$\frac{U_0 - U}{U_\tau} = g\left(\frac{y}{\delta}\right)$$

Equation 2.18 – Velocity defect equation where U_0 = maximum velocity, U = mean local velocity, U_τ = friction velocity

Another empirically derived model for the velocity profile of a smooth pipe is known as the power-law velocity profile given by Equation 2.19.

$$\frac{U}{U_0} = \left(\frac{y}{R}\right)^{\frac{1}{n}}$$

Equation 2.19 – Power law profile where U_0 = maximum velocity, U = mean local velocity, R = pipe radius and y = radial displacement.

The exponent n varies in accordance with Reynolds number, higher values of n correspond to higher Reynolds number flows. For many practical applications n is set to 7 and provides a good approximation. The problem with this approach is the inability to calculate wall shear stress as the velocity gradient approaches infinity near to the wall.

2.2.3 Single Phase Pipe Flow Studies

One of the earliest and most widely cited studies regarding the structure of flow within a pipe was produced by Laufer, (1954). In this study, hot wire anemometry was used to compare velocity and turbulence profiles at Reynolds numbers of 50,000 and 500,000 with special attention paid to the near wall regions. It was shown that when wall units are used the velocity profile is independent of Reynolds number up to $30 y^+$. Laufer was also one of the first authors to suggest the division of the fully developed flow into various regions depending on the turbulence structure and the roles of turbulence production, diffusion and viscous action as discussed previously. Barbin and Jones, (1963) followed this early work with a study concerning the entrance region and the time taken for the flow to become fully developed, finding that for a Reynolds number of 388,000 fully developed flow was not achieved within $40D$. This contrasts with Laufer who reported fully developed flow at $30D$ suggesting that their technique of roughening the entrance region to accelerate boundary layer growth was successful. Despite this, wall shear stress and static pressure gradient were found to attain their fully developed values within the first 15 diameters of the pipe. Further concerns regarding Laufer's findings were highlighted by Lawn, (1971) who acknowledges the inadequacy of hot wire anemometry for the direct measurement of dissipation rate in both Laufer's study and their own. However, Lawn continues to recommend the use of these measurements for Reynolds numbers $< 10^5$. Above this Reynolds number it is suggested that

the dissipating motions in the core region of the pipe flow are isotropic and can be approximated using Kolmogorov's 5/3rds power law with a constant of 0.53.

$$E(k_w) = C_{k_w} \varepsilon^{\frac{2}{3}} k_w^{-\frac{5}{3}}$$

Equation 2.20 – Kolmogorov's 5/3rds power law where $E(k_w)$ is the energy density per wave number k_w , ε = the rate of energy dissipation per unit volume and C_{k_w} = power law constant.

Perry et al., (1986) used pressure drop measurements to obtain the wall shear velocity, and hot wire anemometry to make velocity measurements at a range of Reynolds numbers from 75,000 to 200,000. The authors proposed that attached eddies are formed from the viscous sublayer which stretch and grow with fixed orientation to the wall. These eddies are responsible for mean vorticity, Reynolds shear stress and most of the energy containing motions, they do not however contribute to energy dissipation except in the smallest scales. They propose that these eddies alone cannot account for the Kolmogorov region and as such they are accompanied by detached isotropic small scale eddies, which are responsible for energy dissipation.

Kim et al., (1987) performed a Direct Numerical Simulation (DNS) of a turbulent channel flow. When compared with experimental results at a similar Reynolds number they found that the computed Reynolds stresses were consistently lower than measured values while computed vorticity fluctuations were higher. This was attributed to a discrepancy in the wall-shear velocity, where when this value is replaced with an experimentally recorded value the overall agreement between computed and experimental data is better. Alternatively, it is identified that the source of error could lie with the experimental procedure, as the aspect ratio for the channel used is below the recommended value to be representative of 2-dimensional flow. In 1994 these results were included in a study by Eggels et al., (1994) who performed a comparison between DNS and a number of different experimental procedures. Two DNS measurements were independently performed on a pipe flow and compared with existing

data to verify their validity, then hot wire anemometry, laser Doppler anemometry and particle image velocimetry measurements were performed on the same system. When comparing centreline velocities, they found that hot wire anemometry and laser Doppler anemometry consistently underreported the centreline velocity across 90% of the pipe radius, PIV measurements allowed for higher resolution results which matched the DNS measurements closely between the centreline and half the radius, however these results showed higher velocities when compared with the DNS past this point as the wall was approached. Although these deviations were observed all measurements fell within a 95% confidence interval with the authors concluding that all measurement techniques used were valid. Problems occurred with the acquisition of PIV data close to the wall where noise obscured small scale motions resulting in larger RMS velocities. Variations between the PIV measurements and LDA and HWA measurements were attributed to the difference in acquisition technique, where the LDA and HWA techniques capture data at a single point and the result is time averaged PIV also undergoes a degree of spatial averaging due to interrogation areas. This can result in smoothing of deviations, seen in the RMS measurements, which may lead to inaccuracies.

LDA measurements of a pipe were made at varying Reynolds numbers by Toonder and Nieuwstadt, (1997). They found clear evidence that below a Reynolds number of 25,000 the velocity profile is heavily dependent on Reynolds number. Within the inertial sublayer of the pipe they found the additive constant to the log-law equation (C^+) decreased as Reynolds number increased. They also found that there was little effect on axial turbulence measurements with variation in Reynolds number, however an increase in Re resulted in peak radial turbulence measurements shifting away from the wall. This work was expanded on by Zagarola and Smits, (1998) who used pitot probes to measure Reynolds numbers between 31,000 and 35,000,000 in a compressed air flow facility. They dispute the boundaries established for the log-law region and suggest that in the inertial sublayer there

are two distinct regions, a power law region between 60 and 500 y^+ and then a log law applies beyond this. They also propose using an alternate scaling method to normalise the velocity profiles, using the velocity deficit in contrast to the friction velocity. This scaling allows for better agreement across different Reynolds numbers. The difference between using inner and outer scaling can be seen in Equations 2.17 and 2.20 where 2.17 shows the previously seen log-law equation and 2.20 shows the same equation using outer variables.

$$U^+ = \frac{1}{k} \ln y^+ + C^+$$

Equation 2.17 (repeated) – Log law equation where U^+ = Axial velocity in wall units, k = von Karman constant, y^+ = radial displacement in wall units, and C^+ = additional constant

$$U_0^+ - U^+ = \frac{1}{k} \ln \left(\frac{y}{r} \right) + C^*$$

Equation 2.21 – Outer variable log law equation, where U_0^+ = centreline velocity in wall units, U^+ = Axial velocity in wall units, k = von Karman constant, y = radial displacement, r = pipe radius and C^ = additional constant*

Mckeen et al., (2004) repeated the work of Zagarola and Smits using a smaller pitot probe to reduce uncertainties due to velocity gradients. They too found the existence of a power law region near the wall, however they suggest that this region only extends to $y^+ = 300$ and that the log-law region extends to $0.12 R^+$ compared with Zagarola and Smits measured value of $0.07R^+$ when R^+ is defined as in Equation 2.22.

$$R^+ = \frac{R U_\tau}{\nu}$$

Equation 2.22 – Pipe radius in wall units, where R = pipe radius, U_τ = friction velocity and ν = kinematic viscosity.

They also suggest that the values for the constants in Equations 2.21 and 2.22 are in error and new values are suggested as presented in Table 2.2.

Table 2.2 – Suggested constants for Log-Law equations.

	k	C^+	C^*
<i>Zagarola and Smits, (1998)</i>	0.436±0.002	6.15±0.08	1.51±0.03
<i>Mckeen et al., (2004)</i>	0.421±0.002	5.60±0.08	1.20±0.10

The same experimental facility was then used by Morrison et al., (2004) who replaced the pitot probes with hot wire anemometers. They examined higher moments of the stream wise velocity component. They found that near wall peaks in turbulence are Reynolds number dependant, and this does not scale with the inner variables, leading to the conclusion that outer layer eddies are influencing turbulence close to the wall. This contrasts with previous work which has described the outer layer motion as inactive.

Wu and Moin, (2008) simulated pipe flow at a Reynolds number of 44,000 allowing comparison between their results and the work of Zagarola and Smits, however they felt unable to comment on the debate between power law vs log-law due to the relatively small inertial sublayer simulated in their study. The results of the DNS showed very good agreement with experimental results, and their method allowed for visualisation of the flow which revealed “high speed wavy structures” in the core section of the pipe.

In contrast to the findings of Morrison et al., (2004), Hultmark et al., (2010) argued that the location and magnitude of the near wall peak in turbulence intensity was invariant of the Reynolds number and the movement observed previously was due to spatial filtering and velocity gradients. This is supported by new experiments performed using hot wire anemometry up to Re 145,000 in addition to analysis of previous studies when the measurement volume $l^+ < 25$. They state that the inner peak is located at $y^+ \approx 15$ and has a magnitude of 7.34 ± 0.13

$$l^+ = \frac{lu_\tau}{\nu}$$

Equation 2.23 – length in wall units where l = length, U_τ = friction velocity and ν = kinematic viscosity.

2.2.4 Multiphase Measurements of Pipe Flows

Early measurements in multiphase pipe flows focused on the distribution of particles within the flow, such as the study by Karabelas, (1977), who then provided an expression for predicting the concentration profile in a pipe or channel flow. In addition work was performed to obtain a non-dimensional expression for particle diffusivity (ξ). As in horizontal pipe and channel flows the difference in density between the solids and carrier fluid can result in a non-uniform distribution across the pipe. A particle diffusivity constant ($\xi = 0.25$) was obtained which was several times larger than the fluid diffusivity in the absence of particles where the constant is defined as the ratio of diffusivity to the product of the pipe diameter and friction velocity. This constant was found to be independent of velocity, particle size and fluid viscosity.

$$\xi = \frac{\varepsilon_d}{RU_\tau}$$

Equation 2.24 – Dimensionless diffusivity in pipe flows (ξ) where ε_d = diffusivity, R = pipe radius and U_τ = friction velocity.

Zisselmar and Molerus, (1979) used LDA to examine the effect of particles with regards to turbulence modulation in a solid-liquid pipe horizontal pipe flow. In order to make measurements as close to the wall as possible the test section was machined from glass with plane parallel outer walls and a 50 mm cylindrical hole parallel to the walls. Glass particles with a mean particle size of 53 μm were used and the solids concentration varied between 0 to 5.6% by volume in turbulent flow conditions ($Re \approx 10^5$). The suspensions were created using methyl benzoate as this has similar mechanical properties to water however also has the advantage that it can be optically matched to the glass used for the particles and walls of the test section, allowing for fluid turbulence measurements. The presence of particles was found to decrease axial turbulence except for very close to the wall, where turbulence values exceed those of the single phase as particle concentration increases, reaching a

maximum at 3 volume percent. Once the concentration exceeds this value peak turbulence measurements fall and continue to fall with an increase in particle concentration. The authors suggest that this is due to the hindrance of fluid motion by interacting particles, as the mean distance between the particles is less than 3 particle diameters the interactions between particles dominate obscuring the phase interaction between the fluid and the particles which is responsible for the enhancement of turbulence in this region. At concentrations, less than 3 vol.% particle-fluid interactions dominate, and near the wall where the particles are a similar size to the turbulent eddies there is a turbulence increase. This is in contrast with radial turbulence measurements; the addition of particles causes a flattening of the profile, resulting in low particle concentrations reporting lower turbulence measurements in the core region compared with the single phase. As concentration increases there is an overall increase in radial turbulence across the entirety of the pipe. This is seen in Figure 2.7. Reynolds shear stress measurements across the pipe show a consistent reduction as solids loading is increased.

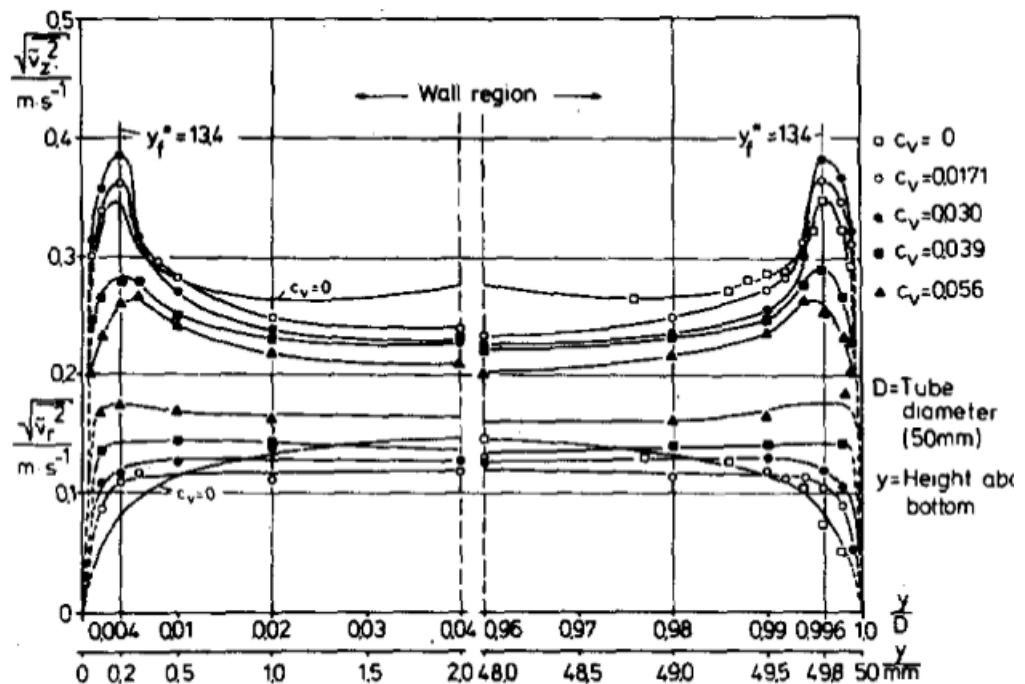


Figure 2.7 – Axial and radial turbulence measurements with increased solids loading, where C_v = solids volume fraction (Zisselmar and Molerus, 1979)

Tsuji and Morikawa, (1982) followed this studying the effect of concentration in a solid-gas system, with a pipe diameter of 30 mm and two particle species (0.2 mm and 3.4 mm). Through simultaneous measurement of the solid and gas phases they could compare particle and fluid velocities. The profiles have greater asymmetry with lower fluid velocities and greater particle loadings due to gravity causing a greater particle concentration in the lower half of the pipe. This causes an uneven retardation of the fluid flow. Particle size was found to greatly affect the turbulence levels with large particles causing enhancement and the smaller particles causing a reduction, again this was found to be very asymmetric for larger particles and lower velocity flows. The large particles were found to travel at 80% the velocity of the air, contributing to turbulence through the shedding of a wake.

The authors then expanded this work to cover a greater range of particle species in a vertical pipe (Tsuji et al., 1985). They found a change in the shape of the velocity profile as the peak axial velocity moved away from the centreline when 500 μm particles were seeded into the flow, the 200 μm particles showed a similar effect to a lesser extent. The extent of profile flattening was greater as the particle diameter is reduced. Medium sized particles were found to both enhance and dissipate turbulence in different regions of the flow. The near wall region experienced a reduction in turbulence whereas the turbulent layer experienced gain. The largest particles produced a near uniform increase in turbulence with increased mass loading, whereas the smallest suppressed turbulence throughout the pipe section.

Kulick et al., (1994) studied the interaction between solid particles and fluid turbulence in an air channel using LDV. 50 μm and 90 μm glass and 70 μm copper spheres were introduced at mass loadings up to 80%. Both the velocity of the fluid and the particles were measured. In contrast with Tsuji and Morikawa, (1982) they found the mean velocity profile of the fluid to be unaffected in the presence of particles. However, this was qualified with a statement regarding a difficulty in obtaining near wall measurements as mass loading was increased and particle mass decreased. Although the velocity profiles were unchanged they did find attenuation of the turbulence, with increasing attenuation with particle Stokes number, mass loading and distance from the wall. They also found when comparing particle velocity fluctuations to single phase fluid turbulence measurements, the particle fluctuations were greater axially, whereas the fluid turbulence was greater radially.

Ljus et al., (2002) studied the effect of both spherical particles and high aspect ratio fibres in a horizontal air pipe flow. For the particle flows they found the same effect as Tsuji et al., where there is enhancement close to the centre of the pipe and reduction at the walls, however they suggest an alternate explanation for the centreline increase. They propose that the asymmetry of the velocity profile leads to a larger gradient in the centre of the pipe, generating shear stress and causing additional turbulence production. They found that as the fluid velocity was increased these effects were lessened. Low concentrations of fibres had no effect on the fluid flow. As the concentration of fibres was increased flocculation occurred. Whereas the fibres were more evenly distributed in the flow than particles the flocs were theorised to be more prevalent in the lower half of the pipe. The individual fibres caused a reduction in turbulence across the entire pipe, however this effect was lessened in the lower part of the pipe due to the presence of turbulence generating flocs. Overall a lower concentration of fibres compared with particles were required to affect the turbulence due to a lower response time.

The use of PIV to study turbulence in a particle laden flow was examined by Poelma et al., (2006) using a vertical water channel. A relatively low Reynolds number of 3750 was selected to allow capture of all turbulent length scales. The test section was a circular glass pipe enclosed in a water filled square box to minimise distortion. The PIV measurements were validated against LDA measurements for a single-phase flow before particles were introduced. They found problems with data loss at particle volume loads as low as 0.5%. Despite this they could accurately record useful turbulence statistics.

2.3 Impinging Jet Flows

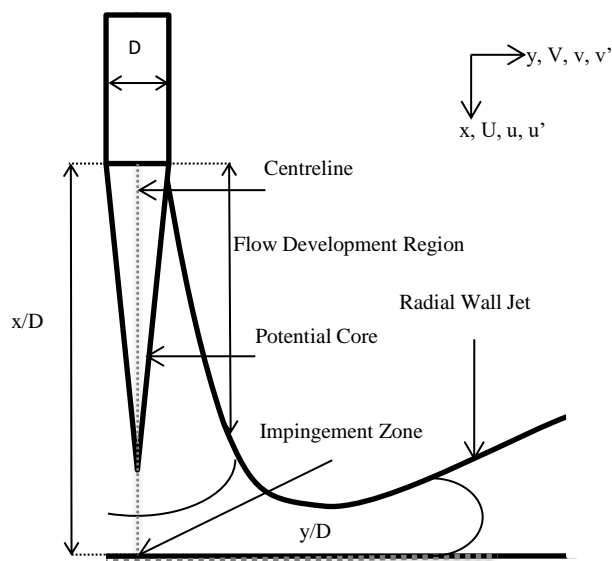


Figure 2.8 – Diagram of the flow structure of an impinging jet.

An impinging jet is a stream of fluid which impinges (impacts) upon a surface. This impingement creates a region with high convection currents. Due to the potential heat transfer applications these jets are of interest to a variety of different industries and as such heat transfer data can be found for a range of Reynolds

numbers and nozzle to plate separations in a review by Jambunathan et al., (1992).

Impinging jets are also utilised to mix viscous process streams which have characteristic mixing times of several minutes and need to achieve homogeneity in just a few seconds. Examples of this are given by Unger and Muzzio, (1998) and include reaction injection

moulding and pharmaceutical crystallisation, which use shear sensitive materials. This makes understanding the turbulent structures within the jet ever more important.

Mass transfer applications exist in both the application of coatings to the impingement surface, and ablation of the surface material. Erosion rates are dependent upon the shear stress with threshold stresses existing below which erosion is non-existent (Giralt and Trass, 1976). This erosion is integral to the work performed at Sellafield in Cumbria, where impinging jets and air lifts are used to suspend nuclear materials in highly active storage tanks (McArthur et al., 2005).

2.3.1 Coordinate system for impinging jet flow

The basic coordinate system for the impinging jet flow is shown in Figure 2.8 and will be used throughout the thesis. In general U represents axial velocities, with displacements in this direction represented by X . V represent radial velocities with displacements in this direction represented by y . Positive axial velocities act towards the impingement plate whereas positive radial velocities are acting towards the right-hand side of the jet, away from the centreline.

2.3.2 Impinging Jet Structure

Due to the changing behaviour of impinging jet flow it is prudent to divide the flow regime into several smaller regimes with similar flow properties, as the conditions at the jet outlet are very different to those at the jet-plate interface. The flow is commonly divided into three main regions. The free jet region, the impingement region and the wall jet region, occasionally the flow in the pipe supplying the jet is considered as a fourth region and other times the regions are further sub-divided to focus on different aspects of the flow.

2.3.2.1 Free Jet Region / Flow Development Region

The free jet region exists between the nozzle and a few jet diameters from the impingement surface. As the name suggests this region behaves similarly to a free jet and it has been shown that for large Reynolds numbers there is no difference in the free jet region between a free jet and an impinging jet with the same initial conditions.

The free jet region comprises of what is known as the potential core, where the fluid velocity is at least 95% of the outlet velocity, surrounded by a shear mixing layer where there is an increase in turbulence. The potential core is cone-like in shape tapering off downstream of the nozzle exit. The potential core usually extends to around $6D$ from the nozzle, however factors such as the nozzle geometry and confinement of the jet can change this. The dissipation of the potential core is caused by the momentum exchange between the shear mixing layer and the surrounding fluid. The jet boundary grows as the surrounding fluid is entrained, dampening momentum from the potential core.

2.3.2.2 Impingement Region / Stagnation Region

The impingement region is the area in which the jet impinges on the surface, generally a flat plate. This is where the flow is accelerated radially due to the static pressure generated by impingement. In this area upstream effects of the impingement are present, with velocity effects seen up to 25% of the jet length from the impingement surface whereas the turbulent properties change closer to the stagnation line, the first effects being noticed around 15% from the impingement. As the nozzle to plate spacing is increased the fluid velocity in the stagnation region is reduced as expected due to increased losses to the turbulent mixing layer, however the turbulent intensity has been found to increase.

The mean flow within the stagnation region causes the stretching of larger eddies and the dissipation of the smaller eddies. Vortices forming along the impingement wall are more

prominent at higher Reynolds numbers, compared with lower Reynolds number jets where these vortices were found in the jet shear mixing layer.

2.3.2.3 *Wall Jet Region / Radial Wall Jet*

The wall jet region occurs after the impingement and is created by the redirected fluid travelling along the base of the impingement surface. This flow region is dominated by the interactions between the fluid and the wall and the free shear layer between the now mostly radial jet and the surrounding fluid. As the radial distance from the jet centreline is increased the height of the wall jet grows linearly, although this growth is less than for a similar radial free jet, due to a decrease in the entrainment of surrounding fluid, and the velocity decay is also greater (Poreh et al., 1967). As the distance between the nozzle and impingement surface is increased the rate of jet growth also increases (Cooper et al., 1993).

Peak radial velocity occurs within $1.5D$ of the jet centreline, where the flow is accelerated away from the stagnation point, before then slowing as the jet expands across the base of the impingement surface (Cooper et al., 1993; Fairweather and Hargrave, 2002).

2.3.3 *Single Phase Impinging Jet Studies*

Some of the earliest measurements of the impinging jet were performed by (Bradshaw and Love, 1961). The flow velocities were measured using a diamond-section yawmeter and a circular pitot tube. Static pressure was measured with a disc static probe and the skin friction with a flat pitot tube. The impingement surface was located 18 nozzle diameters ($18D$) from the nozzle outlet. The authors found that most the transition from free jet to wall jet was within a $3D$ radius hemisphere, slightly larger than the radius of the free jet just before impingement. They also stated that the wall jet was fully developed at $8D$ from the impingement point.

After the work of Bradshaw and Love a number of studies were performed using hot wire anemometry. Poreh et al., (1967) presented measurements for the mean velocities,

turbulence intensities, Reynolds stresses and the wall friction for the radial wall jet formed by a circular impinging jet. This work highlighted an issue with previous work by Glauert, (1956), there is a discrepancy in the predictions of the wall jet development, the rate of spread is found to be smaller and the rate of velocity decay larger than what is suggested by the model. They also found that the properties of the wall jet were highly dependent on the separation distance between the jet outlet and the impingement surface, even at large distances from the impingement region.

The effects of Reynolds number on the resulting wall jet were then studied by Era and Saima, (1976) They found a transition Reynolds number of 2000 for the free jet, below this value the resulting wall jet was laminar, above the wall jet was turbulent. They also observed that the eddy viscosity and entrainment of surrounding fluid is larger for an impinging jet than that of a similar free jet.

Chevray and Tutu, (1978) used a special instrument constructed of two hot wire probes with one running in a low-overheat constant current mode and the other running in a constant temperature mode, this allowed for the simultaneous measurement of the temperature and velocity. However, they did notice an issue with contamination of the temperature readings by the velocity hot wire in regions of reverse flow. They observed that the large scale turbulent eddies were responsible for the bulk of momentum and heat transfer, however, the smaller scale eddies were more efficient at transporting heat. They also found that the maximum peak turbulent energy coincided with peak shear stress $6D$ from the jet outlet.

The initial region of a free jet was examined by Bogusławski and Popiel, (1979) who found that the potential core of the jet had decayed between 4 and $9D$ from the jet outlet as the shear mixing layer spread across the whole cross section of the jet, this coincided with a rapid increase in the turbulent intensity. This work used the jet outlet Reynolds number to compare different jets however, later work (Malmström et al., 1997) would show that there

was no simple relationship between the jet centreline decay coefficient (K-Coefficient) and Reynolds Number, instead the rate of decay was proportional to the outlet velocity.

Gutmark et al., (1978) performed a study focusing on the turbulent structure of the jet centreline as it impinged. Some important observations they made were that the velocity of the jet remained unaffected by the presence of the plate for 75% of the distance between the nozzle and the plate and the turbulent properties were unaffected until even closer to impingement with no deviation from the equilibrium levels for over 85% of this distance.

Landreth and Adrian, (1990) produced some of the first images of the instantaneous velocity field surrounding an impinging jet using particle image velocimetry. An impinging water jet was examined with PIV allowing the simultaneous acquisition of both axial and radial velocity vectors revealing flow structures on a millimetre scale. The results were compared with LDV measurements to verify the accuracy. They found boundary layer separation occurred around 1.8D from the jet centreline indicated by flow reversal (upwards) and a significant decrease in radial velocity.

One of the most highly cited papers' relating to the study of impinging jets is from Cooper et al., (1993) who measured the velocity field resulting from the impinging jet. Cooper et al. found an issue with using hot wire anemometry to measure very close to the impingement surface, in that the hot wire became sensitive to radial velocity fluctuations when trying to measure axial fluctuations. This is similar to the issues experienced by Chevray and Tutu, (1978) and would also be encountered by Knowles and Myszko, (1998). Cooper et al. considered two Reynolds numbers (23,000 and 70,000) for their study and varied the jet to plate spacing between 2D and 10D, particular attention was paid to the measurements at 2D and 6D as these points were identified as the most interesting in a previous study by Baughn and Shimizu, (1989). They focused on the heat transfer characteristics of an impinging jet and found that a jet-to-plate separation of 6D provided maximum stagnation point heat

transfer, and a separation of 2D created a second maximum in addition to a stagnation point approximately 1.8D away radially unlike the other measurements at 6D, 10D, and 14D where there was a steady decline in Nusselt number as radial distance from the stagnation point increased. The main objective of Cooper et al., (1993) was to create a data set suitable for assessing the suitability of different turbulence models, and thus provided adequate description of the inlet condition and ensured a fully developed flow before the nozzle.

Comparison was done in a corresponding paper (Craft et al., 1993) comparing 4 different turbulence models against the experimental data. One of the models was the k-epsilon model of Launder and Sharma, (1974), the other three models were second moment closures. They found the eddy viscosity model and the basic Reynolds stress model had poor agreement with experimental results attributed to a weakness in the stress – strain relation of the K-epsilon model and an issue with the wall reflection process in the Reynolds stress model. The Reynold stress model with a replacement wall reflection process performed much better.

In addition to creating data suitable for comparison with computational models it also allowed for a more direct comparison with other experimental data using the same normalising techniques. Knowles and Myszko, (1998) used a combination of data (Cooper et al., 1993; Padmanabham and Lakshmana Gowda, 1991) to validate their findings when examining the turbulence in radial wall jets. Where Bradshaw and Love, (1961) states that jet self-similarity is reached at 8D, Knowles and Myszko, (1998) found that mean velocity profiles became self-similar at a distance of 2.5D and turbulent profiles at a distance from the jet centreline at 4.5D. Knowles and Myszko, (1998) also found that peak levels of turbulence fluctuations and Reynolds stress occurred at about 2D and the magnitude decreased with an increase in nozzle-to-plate separation. The increase in nozzle-to-plate separation also produced an increase in wall jet thickness except for an anomaly when the

separation was $4D$, which was attributed to be a critical height for the experimental arrangement, coinciding with the end of the potential core.

Particle tracking velocimetry, a similar method to PIV, was employed by Nishino et al., (1996) in both 2D and 3D configurations. This allowed for resolution of the azimuthal component of the flow which showed close similarities with the radial component when examining velocity fluctuations. They also showed there was a negative production of turbulent kinetic energy in the near wall region as momentum was transferred to the mean flow.

Using LDA Ashforth-Frost and Jambunathan, (1996) examined the effect of confinement and nozzle geometry on the potential core and overall development of a free jet. The study found that a jet with a fully developed exit profile extended the potential core by 7% when compared with a jet exhibiting a flat profile. This is attributed to greater shear at the jet boundaries due to greater velocity gradients between the jet and ambient fluid when the exit profile is flat. This was despite the fact the initial turbulence was found to be higher in the fully developed profile. The effect of semi-confinement on the jet had the effect of extending the potential core by a further 20% due to the semi-confinement plate limiting the entrainment of the surrounding fluid and reducing the absolute levels of turbulence by around 15% for the fully developed jet and around 12% for the flat jet. It was also found that the peak turbulence level was greater for the flat jets and occurred closer to the nozzle, but also decayed more rapidly than for the fully developed case.

Fitzgerald and Garimella, (1998) studied the flow field of a confined and submerged impinging jet, however due to the experimental set up the effect of confinement on the potential core could not be quantified except to state that it was longer than $4D$. They did however show the presence of a toroidal recirculation zone in the radial wall jet created due to the confinement of the jet. The centre point of this toroid moved closer to the impingement surface with an increase in jet Reynolds number and moved further away from

the jet centre line radially with both an increase in Reynolds number and an increase in distance between the nozzle and impingement surface. A confined impinging jet was previously studied by Barata et al., (1993) who analysed the effect of a cross flow on said impinging jet. They found that the crossflow produced a pair of counter rotating vortices which developed downstream.

Behnia et al., (1999) used an elliptic relaxation model ($\nu^2 - f$) to simulate flow and heat transfer of confined and unconfined impinging jets, showing that confinement of the jet leads to a decrease in the average heat transfer rates. Comparisons of their model to the K-epsilon model showed better predictions of the Nusselt number. This was due to an error produced by the K-epsilon method where high levels of turbulence were produced in the stagnation region of the potential core. This issue was addressed by (Park and Sung, 2001) who developed an adaptation of the K-epsilon method to be applied to impinging jet heat transfer. They introduced an additional function to derive the eddy viscosity which prevented spurious generation of turbulent kinetic energy in the stagnation region. This allowed for a satisfactory capture of the dynamic and thermal characteristics of an impinging jet flow.

Large eddy simulation (LES) of a slot jet was performed with a dynamic sub grid scale model used for the small scales of turbulence (Cziesla et al., 2001). They used evidence of the self-similarity of the axial velocity to validate the accuracy of the results in addition to comparison with previous experimental data. Like Nishino et al., (1996) the authors observed the negative production of turbulent kinetic energy in the near wall region, close to the centreline.

Tsubokura et al., (2003) examined the eddy structure of slot and circular impinging jets using LES and direct numerical simulation (DNS) when the jet is excited at the inlet. In exploring the differences between slot and circular jets they found that an excited slot jet produces

organised structures in the stagnation region, in the form of twin counter rotating vortices. These structures were not present in the round jet. This is attributed to a difference in stretching directions, as a slot jet undergoes significant transverse stretching with minimal span wise, in comparison with the round jet where azimuthal stretching dominates. In the development region both slot and circular jets developed roll-up eddies as the jet progressed downstream.

PIV was used in addition to the Fluent CFD package to study flow patterns in an impinging jet contactor by Unger and Muzzio, (1998) The combination of PIV and numerical simulation allowed for a significantly more efficient mixing method to be discovered via very slight changes to the geometry of the impinging jets by having them impinge at a slight angle rather than head on. Experimental results were in good agreement with the simulations, quantified by comparison of velocity probability density functions.

Fairweather and Hargrave, (2002) also used PIV to obtain the mean and fluctuating velocities, in addition to the shear stresses of an air jet impinging onto a flat surface. Their results showed good agreement with previous LDA measurements, however discrepancies were found when comparing the data against hot wire anemometry measurements. A possible explanation for this is the inability of single hot wires to discriminate between axial and radial velocity components. They also observed the presence of a large low velocity recirculation zone, transporting material from the edge of the wall jet back to the origin.

Narayanan et al., (2004) studied the flow field and heat transfer characteristics of an impinging slot jet, at nozzle-to plate-spacing of 3.5 and 0.5 nozzle exit hydraulic diameters (hydraulic diameter is double the width of the slot), corresponding to transitional and potential core impingement. For the potential core impingement they observed the same heat transfer phenomena as Baughn and Shimizu, (1989), where there is a second peak in heat transfer. It is suggested this peak is due to the interaction between the motion in the

outer region of the wall jet and the near wall turbulence. The near wall streamline turbulence was at its peak in the same region as the secondary peak in heat transfer.

Birch et al., (2005) examined methane impingement on a flat surface with a nozzle-to-plate spacing of around 13D relating to transitional impingement. They found that the jet was unaffected by the plates presence for 84% of the jet-to-plate spacing, this is in good agreement with the 85% suggested by Gutmark et al., (1978) and the 86% suggested by Beltaos and Rajaratnam, (1974). Due to difficulties measuring close to the surface they were unable to measure the abrupt decrease in fluctuating velocity close to the wall observed by Cooper et al., (1991). It is theorised that this decrease occurs due to the wall exerting a dampening effect on the turbulence. In comparing their data with earlier work they found a slight but non-significant difference between their measurements and the work done by Poreh et al., (1967), suggesting that the peak velocity in the wall jet occurs closer to the wall. Their data is however in good agreement with Fairweather and Hargrave, (2002), who utilised Particle Image Velocimetry, the slight differences in some aspects are attributed to a higher spatial and temporal resolution being used in the LDA study. They observed a simple linear relationship in the growth of the radial wall jet and the outer shear layer of this jet is the same as a free shear layer. In examining the concentration profiles, they found that their Raman spectroscopy technique produced results in good agreement with data collected using Mie scattering by Fairweather and Hargrave, (2002), and call into question the accuracy of probe based measurement techniques when compared with the less intrusive laser measurement techniques.

Hwang et al., (2001) manipulated the flow and heat transfer characteristics of an impinging jet using a secondary shear flow and acoustic excitation. The secondary shear flow surrounded the impinging jet and was operated in two modes, one with the secondary flow co-flowing with the impinging jet, and one with the secondary flow counter-flowing. The co-

flowing flow inhibited the vortex pairing of the inner vortices and the entrainment of ambient air, this delayed the development of the main jet and as such caused the potential core to extend much further downstream. The opposite effect is seen for the counter-flowing case where relatively high shear between the primary and secondary flow cause the jet to have a shorter potential core and slightly higher turbulence intensity.

Geers et al., (2004) used PIV to examine impinging jet arrays, their findings support the work of Ashforth-Frost and Jambunathan (1996) in their suggestion that elongation of the potential core in confined jets is due to limited entrainment. Geers et al. (2004) found up-wash from neighbouring jets increased the entrainment of the central jets. This reduced the length of the potential cores in comparison to jets at the periphery of the array.

Guerra et al., (2005) examined the applicability of the “law of the wall” to an impinging jet. They measured the velocity and local temperature distributions of an impinging jet at a Reynolds number of 35000. They suggest that there is an increase in the logarithmic portion of the velocity in the log-law layer with an increase in maximum jet velocity.

A comparison between free and impinging jets was made at a distance of 1D from impingement, show that there is no significant effect on the velocity or turbulence structure by the impingement plate at this distance (Hofmann et al., 2007). For the two cases examined 1D from impingement relates to the jet being unaffected for 60% and 87.5% for nozzle separations of 2.5D and 8D, respectively. This aligns well with the findings of Birch et al., (2005) and the previously referenced authors in relation to that.

More recent studies using LDA include the work of Tummers et al., (2011) and Loureiro and Freire, (2012) both studies made measurements very close to the wall for the radial wall jet. Tummers et al., (2011) found at a radial distance of 0.5D from the centreline peak radial velocity occurred 0.012D from the impingement surface in good agreement with the LES of Hadžiabdić and Hanjalić., (2008). They also found that two peaks occurred for the RMS values

of the radial velocity component, one $0.011D$ from the plate and another even closer at $0.0018D$. This double peak was also observed by Loureiro and Freire., (2012), who build on the work of Guerra et al., (2005) confirming that the level of logarithmic profile within the wall jet increases with increasing maximum jet velocity.

Tummers et al., (2011) also show the presence of instantaneous flow reversals very close to the wall at a radial distance of $1.4D$ and the authors suggest this as a possible explanation for the local minima in Nusselt number found around $1.5D$ from the jet centreline. These reversals were confirmed using PIV, a small area around the $1.5D$ radial profile was examined and a histogram compiled from 10,000 velocity samples $0.02D$ from the impingement surface. The histogram shows that multiple velocity vectors have negative values and an accompanying flow visualisation demonstrates separation from the impingement plate under the formation of a secondary vortex.

2.3.4 Multiphase measurements of impinging jets

Data for multiphase impinging jets is much more limited especially concerning solid-liquid systems. Fortunately, studies have been performed on free jets, which the flow development region of an impinging jet can be directly compared.

Hetsroni and Sokolov, (1971) examined the effect of small droplets on an air jet using hot wire anemometry. The droplets resulted in a narrowing of the jet, and a reduction in the normalised velocity fluctuations. This turbulence suppression occurred in the dissipation range (small eddies) and was dependent upon the size and concentration of the droplets. The absolute value of the turbulence intensity was unchanged but the centreline velocity increased in the droplets presence resulting in a reduction when the velocity fluctuations were normalised against the centreline velocity.

Fleckhaus et al., (1987) found similar results using LDA. Fluid velocity in a two-phase jet decelerates slower than in a single-phase jet and the spreading rate of the jet is reduced (K-coefficient), this effect is magnified by smaller particles at the same mass loading. There is a decrease in shear stress and kinetic energy, caused by these particles. The particles decelerate slower than the fluid and the larger particles maintain their momentum to a higher degree. The larger particles are less affected by fluid velocity fluctuations and the shear stress of the particles is much smaller than the fluid. Yoshida et al., (1990) then developed an approach to study jet impingement. Like the results of Fleckhaus, the jet spreading in the upstream region was reduced when particles were added and this was attributed to the transfer of momentum from the particles to the gas and the modulation of gas turbulence by the particles. Due to the solid particles maintaining their momentum the particles were found to rebound from the plate surface with high energy, this produced a wake amplifying axial turbulence. Downstream of the stagnation point the turbulent intensity of the two-phase flow is around 50% larger than for single phase flow and this is attributed to the interaction between the solids moving towards the plate and the gas flowing along the plate. The peak flow for the multiphase system is reduced by around 20%. As the distance from the stagnation point increases the gas phase turbulent intensity decreased to match the levels of the single-phase jet.

Tsuji et al., (1988) examined: 4 particle diameters, their diffusion rate, their effect on the spreading rate of the jet, the fluid phase velocity, and turbulent intensity. They found the presence of particles reduced velocity fluctuations near the jet nozzle, however as the jet progressed the smaller particles caused an increase in turbulence whereas the largest particles continued to reduce turbulence. As particle concentration was increased the peak value of turbulence intensity was reduced, however data was only presented for one particle species so no comparison could be made across particle diameters.

Longmire and Eaton, (1992) explored the interaction of particles in an axially forced air jet. They found a clustering of particles in the saddle region of the created vortex rings, which were then propelled away from the jet axis. When large ring structures are present distinct regions of high and low particle concentrations are formed. This could be important in shear sensitive flows as turbulence modulation is affected by particle concentration. Large scale turbulence structures were found to be responsible for the dispersion and concentration of particles, and these structures persisted even at mass loading ratios up to 0.65. Hishida et al., (1992) also explored particle dispersion in a shear mixing layer and agree that particle motion is dependent on the ability of the particles to follow large scale turbulent structures.

The conclusions from studying a range of particle numbers are presented in Table 2.3.

Table 2.3 – Effect of Stokes number on particle behaviour

Stokes #	EFFECT
>4	Particles move independent of turbulence structures. Particle dispersion barely affected by vortex motion.
2.5 - 4	Particle eddy diffusivity rapidly increases with decreasing Stokes number.
0.5 – 2.5	Particles disperse further than the fluid phase.

PIV has also been used for gas solid jets by Anderson and Longmire, (1995) who used a combination of flow visualisation, image analysis and PIV to study the particle motion within the impingement zone. Using a jet Reynolds number of 21,000 and jet to plate spacing of 5D, the team seeded an air jet with glass particles. They found that particle velocities near the wall deviated strongly from the fluid velocity, with lower Stokes number particles accelerated more quickly, not only due to lower inertia but also because they encountered larger fluid velocities. Like Yoshida et al., (1990) the particles were found to rebound from the plate causing long residence times in the stagnation region, increasing the particle concentration above the plate. Only particles within the vicinity of the vortex core were influenced by the vortex induced velocity field, the particle motion in the stagnation region being mostly reliant on the mean flow.

Prevost et al., (1996) showed how particle Stokes number decreases dramatically as a jet develops and that this can be used to describe the influence of the fluid velocity field on a particle. There is a notable increase in the anisotropy between the axial and radial turbulence with an increase in particle relaxation time with the ratio of the square fluctuating components of the jet axis being 0.25 for the 30-35 μm particles compared with 0.6 for the 10-15 μm . They also validate the work of Longmire and Eaton concerning the preferential concentration of particles as particles were found to concentrate in regions of the flow with a high outward radial velocity.

A solid-liquid jet was examined using PIV and CFD (Virdung and Rasmuson, 2007). In this work 1500 μm particles were examined at several concentrations emanating from a square nozzle 17x17mm. They found the upper limit for the solids volume fraction was reached at 1.9% beyond this the accuracy of the measurements was reduced by the dispersed phase in a similar fashion to Poelma et al., (2006). The centreline RMS velocities were found to remain fairly constant regardless of axial position whereas the turbulence peaks either side of the potential core increased in magnitude with an increased particle loading. It was noted that the difference in turbulence levels between the single phase and lowest concentration multiphase flow was much greater than the difference between any of the multiphase flows, suggesting that the mere presence of the particles is much more important than their concentration. Unlike a number of other authors (Hetsroni and Sokolov, 1971; Fleckhaus et al., 1987) an expansion of the jet width occurred with an increase in particle concentration. Three versions of the K-epsilon model were used to numerically evaluate the flow, mixture, where mixture properties are used to evaluate K and epsilon, dispersed, where secondary phase turbulence is derived from the primary and per-phase, where K and epsilon transport equations are solved for each phase. They found the per-phase model to produce results most like the experimental results and although it was expected to be more computationally

expensive this was not always the case due to numerical instabilities arising in the simulations using the other models increasing total simulation time.

To improve the ability of PIV for use in multiphase applications the use of multi-camera and colour systems has been investigated by Towers et al., (1999) who outlined an approach for separating distinct phases using colour recording and fluorescent doped particles to differentiate the phases. A beam splitter was used coupled with two monochromatic CCD cameras fitted with filters; this allowed a single experiment to be performed tracking both the solid and fluid phases of the system. Although the team used impinging jets to test the system they were not focused on examining the properties of the jets. Lindken and Merzkirch, (2002) described a technique of differentiating between the two states of matter in bubbly flow using a combination of tracer particles, shadowgraphy and digital phase separation. This was done by shifting the background intensity to a higher uniform grey level. This allowed for the velocity distributions in the two flows to be measured using only one camera. Although this work was not done on impinging jets the technique was utilised by Alekseenko et al., (2008) to study such a jet. The team examined a variety of bubble diameters and gas content percentages. They found that the addition of the bubbles had almost no effect on the velocity components of the flow; however, the turbulent structure was altered. Liquid phase velocity fluctuations were suppressed by the bubbles. Larger bubbles appeared to have less of a suppression effect at greater distances from the nozzle. The bubbles strongly affect the turbulence characteristics near the wall, with the magnitude of the second and third order velocity fluctuations dramatically increasing with the increase in gas content.

One of the key functions of impinging jets and part of the impetus for this study is their use in particle resuspension. Smedley et al., (1999) translated an impinging air jet across a glass plane covered in polystyrene particles to examine the entrainment of the particles by the jet.

They found that at high pressure ratios the clearance of particles was independent of jet height, particle removal was now due to wall jet effects and not impingement. In this region jet momentum is a greater indicator of removal efficiency than proximity of the jet to the surface. At low pressure ratios particle removal is heavily dependent on jet height. The particle removal effects were used to estimate shear stress in the jet and found to fit well with the data of Beltaos and Rajaratnam, (1974). Young et al., (2013) performed similar measurements however measured the shear stress directly, finding the data sets were similar however differences were observed at larger jet height. Beyond the edge of the impingement region measured shear stress values were smaller than those predicted by Smedley et al., (1999) through particle removal.

Further work on the use of impinging jets to re-suspend particles has been performed by Hunter et al., (2013) who found that the scale of the experimental facility has an impact on particle resuspension due to the recirculation of fluid. Smaller vessels reached a steady state sooner with a higher rate of sediment erosion. Optimum jet height for particle resuspension was determined to be at 10D.

2.4 Conclusions

After reviewing the literature it is clear that there is very limited data available for multiphase flows. Although some studies have been performed in pipes and free jets the ability to accurately predict the effect of a particle on a fluid is lacking. Attempts have been made to categorise particles in different ways to determine if turbulence will be enhanced or dissipated through the presence of particles however the magnitude of these changes cannot be quantified. In order to have a realistic idea of how a real system will behave computational models are the most cost effective way to probe this. Effective computational models however need empirical data to be validated against and especially for multiphase impinging jets there just is not enough data to rigorously test these models.

Gas-solid systems have been explored more thoroughly than liquid-solid systems, which present different challenges. In a gas-solid system large mass loading ratios are easy to achieve due to the relative densities of the fluid and the particle so the effects of concentration will depend on the normalisation used as the same number of particles can have wildly different effects across the two systems.

Most of the data applicable to impinging jets has come from similar studies on free jets, this leads to problems when trying to quantify effects as it has been shown that the effect of particles can be related to the Stokes number and the rapidly changing flow configuration of an impinging jet will cause the Stokes number to vary greatly depending on the flow region.

In order to determine the applicability of various suggested models the models suggested (Hetsroni, 1989; Gore and Crowe, 1989; Elghobashi, 1994), further data is required for both pipe and impinging jet multiphase systems. The bulk of this thesis will attempt to extract fluid velocity and turbulence statistics for a range of particle species in both impinging jet and pipe systems, providing a greater range of data to validate these predictions and for future work to be compared against.

2.5 References

- Alekseenko, S. V., Dulin, V.M., Markovich, D.M. and Pervunin, K.S. 2008. Bubbles Effect on Turbulence in Free and Confined Jet Flows. *Ltces.Dem.Ist.Utl.Pt.* (2000),pp.7–10.
- Anderson, S.L. and Longmire, E.K. 1995. Particle motion in the stagnation zone of an impinging air jet. *Journal of Fluid Mechanics*. **299**,pp.333–366.
- Ashforth-Frost, S. and Jambunathan, K. 1996. Effect of nozzle geometry and semi-confinement on the potential core of a turbulent axisymmetric free jet. *International Communications in Heat and Mass Transfer*. **23**(2),pp.155–162.
- Barata, J.M.M., Durão, D.F.G., Heitor, M. V. and McGuirk, J.J. 1993. On the analysis of an impinging jet on ground effects. *Experiments in Fluids*. **15**(2),pp.117–129.
- Barbin, A.R. and Jones, J.B. 1963. Turbulent flow in the inlet region of a smooth pipe. *Journal of Basic Engineering*. **85**(1),pp.29–33.
- Baughn, J.W. and Shimizu, S. 1989. Heat Transfer Measurements From a Surface With Uniform Heat Flux and an Impinging Jet. *Transactions ASME*. **111**(November 1989),pp.1096–1098.
- Behnia, M., Parneix, S., Shabany, Y. and Durbin, P.A. 1999. Numerical study of turbulent heat transfer in confined and unconfined impinging jets. *Int. J. Heat Fluid Flow*. **20**,pp.1–9.
- Beltaos, S. and Rajaratnam, N. 1974. Impinging Circular Turbulent Jets. *Journal of the Hydraulics Division*. **100**(10),pp.1313–1328.
- Birch, A.D., Cleaver, R.P., Fairweather, M. and Hargrave, G.K. 2005. Velocity and concentration field measurements in a turbulent, impinging flammable jet. *Chemical Engineering Science*. **60**(1),pp.219–230.
- Bogustawski, L. and Popiel, C.O. 1979. Flow structure of the free round turbulent jet in the initial region. *Journal of Fluid Mechanics*. **90**(3),pp.531–539.
- Bradshaw, B.P. and Love, E.M. 1961. *The normal impingement of a circular air jet on a flat surface*.
- Cengel, Y. and Cimbala, J. 2006. *Fluid Mechanics: Fundamentals and Applications*.
- Chevray, R. and Tutu, N.K. 1978. Intermittency and preferential transport of heat in a round jet. *Journal of Fluid Mechanics*. **88**(1),pp.133–160.
- Cooper, D., Jackson, D.C., Launder, B.E. and Liao, G.X. 1993. Impinging jet studies for turbulence model assessment -- I. Flow-field experiments. *Int. J. Heat Mass Transfer*. **36**(10),pp.2675–2684.
- Craft, T.J., Graham, L.J.W. and Launder, B.E. 1993. Impinging jet studies for turbulence model An examination of the performance of four turbulence models. *Int. J. Heat Mass Transfer*. **36**(10),pp.2685–2697.
- Cziesla, T., Biswas, G., Chattopadhyay, H. and Mitra, N.K.K. 2001. Large-eddy simulation of flow and heat transfer in an impinging slot jet. *International Journal of Heat and Fluid Flow*. **22**(5),pp.500–508.
- Eggels, J.G., Unger, F., Wiess, M.H., Westerweel, J., Adrian, R.J., Friedrich, R. and Nieuwstadt, F.T.M. 1994. Fully Developed Turbulent Pipe Flow: A Comparison Between Direct Numerical Simulation and Experiment. *J. Fluid Mech.* **268**(1994),pp.175–209.
- Elghobashi, S. 1994. On predicting particulate-laden turbulent flows. *Applied Scientific Research*. **52**,pp.309–329.
- Era, Y. and Saima, A. 1976. An Investigation of Impinging Jet: Experiments by Air, Hot Air and Carbon dioxide. *Bulletin of JSME*.
- Fairweather, M. and Hargrave, G. 2002. Experimental investigation of an axisymmetric impinging turbulent jet. 1. Velocity Field. *Experiments in Fluids*. **33**,pp.464–471.
- Fitzgerald, J. a. and Garimella, S. V. 1998. A study of the flow field of a confined and submerged impinging jet. *International Journal of Heat and Mass Transfer*. **41**(8–9),pp.1025–1034.
- Fleckhaus, D., Hishida, K. and Maeda, M. 1987. Effect of laden solid particles on the turbulent flow structure of a round free jet. *Exp.* **5**(323–333).
- Geers, L.F.G., Tummers, M.J. and Hanjalić, K. 2004. Experimental investigation of impinging jet arrays.

- Experiments in Fluids*. **36**(6),pp.946–958.
- Giralt, F. and Trass, O. 1976. Mass transfer from crystalline surfaces in a turbulent impinging jet. part 2: Erosion and diffusional transfer. *The Canadian Journal of Chemical Engineering*. **54**(3),pp.148–155.
- Glauert, M.B. 1956. The wall jet. *Journal of Fluid Mechanics*. **1**(6),pp.625–643.
- Gore, R. and Crowe, C. 1989. Effect of particle size on modulating turbulent intensity. *International Journal of Multiphase Flow*. **15**(2),pp.279–285.
- Guerra, D.R.S. and Freire, A.P.S. 2004. The near wall behaviour of an orthogonally impinging jet. *International journal of heat and mass*,p.10.
- Gutmark, E., Wolfshtein, M. and Wygnanski, I. 1978. The plane turbulent impinging jet. *Journal of Fluid Mechanics*. **88**(4),pp.737–756.
- Hadžiabdić, M. and Hanjalić, K. 2008. Vortical structures and heat transfer in a round impinging jet. *Journal of Fluid Mechanics*. **596**,pp.221–260.
- Hetsroni, G. 1989. Particles-turbulence interaction. *International Journal of Multiphase Flow*. **15**(5),pp.735–746.
- Hetsroni, G. and Sokolov, M. 1971. Distribution of mass, velocity, and intensity of turbulence in a two-phase turbulent jet. *Trans. ASME J. Appl. Mech.* **38**(2),pp.315–327.
- Hishida, K., Ando, A. and Maeda, M. 1992. Experiments on Particle Dispersion in a Turbulent Mixing Layer. *International Journal of Multiphase Flow*. **18**(2),pp.181–194.
- Hofmann, H.M., Kind, M. and Martin, H. 2007. Measurements on steady state heat transfer and flow structure and new correlations for heat and mass transfer in submerged impinging jets. *International Journal of Heat and Mass Transfer*. **50**,pp.3957–3965.
- Hultmark, M., Bailey, S.C.C. and Smits, A.J. 2010. Scaling of near-wall turbulence in pipe flow. *Journal of Fluid Mechanics*. **649**,pp.103–113.
- Hunter, T.N., Peakall, J., Unsworth, T.J., Acun, M.H., Keevil, G., Rice, H. and Biggs, S. 2013. The influence of system scale on impinging jet sediment erosion: Observed using novel and standard measurement techniques. *Chemical Engineering Research and Design*. **91**(4),pp.722–734.
- Hwang, S., Lee, C. and Cho, H. 2001. 2001 Heat Transfer and Flow Structures in Axisymmetric Impinging Jet Controlled by Vortex Pairing - Hwang, Lee, Cho.pdf. *International Journal of Heat and Fluid Flow*.
- Jambunathan, K., Lai, E., Moss, M. and Flow, B.B. 1992. A review of heat transfer data for single circular jet impingement. *International Journal of Heat and Fluid Flow*. **22**(2),pp.106–115.
- Karabelas, A.J. 1977. Vertical distribution of dilute suspensions in turbulent pipe flow. *AIChE Journal*. **23**(4),pp.426–434.
- Kim, J., Moin, P. and Moser, R. 1987. Turbulence statistics in fully developed channel flow at low Reynolds number. *J. Fluid Mech.* **177**,pp.133–166.
- Knowles, K. and Myszkowski, M. 1998. Turbulence Measurements in radial wall jets. *Experimental Thermal and Fluid Science*. **17**(2),pp.71–78.
- Landreth, C.C. and Adrian, R.J. 1990. Impingement of a Reynolds number turbulent circular jet onto a flat plate at normal incidence. *Experiments in Fluids*. **9**,pp.74–84.
- Laufer, J. 1954. The structure of turbulence in fully developed pipe flow. *Naca Tr 1174*,pp.417–434.
- Launder B.E. and Shama 1974. Application of the energy dissipation model of turbulence to the calculation of flow near a spinning disc. *Letters in Heat and Mass Transfer*. **1**(2),p.1974.
- Lawn, C. 1971. The determination of the rate of dissipation in turbulent pipe flow. *Journal of Fluid Mechanics*. **48**(3),p.477.
- Lindken, R. and Merzkirch, W. 2002. A novel PIV technique for measurements in multiphase flows and its application to two-phase bubbly flows. *Experiments in Fluids*. **33**,pp.814–825.
- Ljus, C., Johansson, B. and Almstedt, A.E. 2002. Turbulence modification by particles in a horizontal pipe flow. *International Journal of Multiphase Flow*. **28**(7),pp.1075–1090.

- Longmire, E.K. and Eaton, J.K. 1992. Structure of a particle-laden round jet. *Journal of Fluid Mechanics*. **236**(217),pp.217–257.
- Loureiro, J.B.R. and Freire, A.P.S. 2012. Wall shear stress measurements and parametric analysis of impinging wall jets. *International Journal of Heat and Mass Transfer*. **55**(23–24),pp.6400–6409.
- Malmström, T.G., Kirkpatrick, A.T., Christensen, B. and Knappmiller, K.D. 1997. Centreline velocity decay measurements in low-velocity axisymmetric jets. *Journal of Fluid Mechanics*. **246**,pp.363–377.
- Marusic, I., Monty, J.P., Hultmark, M. and Smits, A.J. 2013. On the logarithmic region in wall turbulence. *Journal of Fluid Mechanics*. **716**.
- McArthur, G., Tinsley, T. and McKendrick, D. 2005. Development of a liquid jet sludge re-suspension model (used on pulse jets or jet ballasts). *AIChE Annual Meeting*.
- McKeon, B.J., Li, J., Jiang, W., Morrison, J.F. and Smits, A.J. 2004. Further observations on the mean velocity distribution in fully developed pipe flow. *Journal of Fluid Mechanics*. **501**,pp.135–147.
- Morrison, J.F., McKeon, B.J., Jiang, W. and Smits, A.J. 2004. Scaling of the streamwise velocity component in turbulent pipe flow. *Journal of Fluid Mechanics*. (508),pp.99–131.
- Narayanan, V., Seyed-Yagoobi, J. and Page, R.H. 2004. An experimental study of fluid mechanics and heat transfer in an impinging slot jet flow. *International Journal of Heat and Mass Transfer*. **47**(8–9),pp.1827–1845.
- Nishino, K., Samada, M., Kasuya, K. and Torii, K. 1996. Turbulence statistics in the stagnation region of an axisymmetric impinging jet flow. *International Journal of Heat and Fluid Flow*. **17**(3),pp.193–201.
- Padmanabham, G. and Lakshmana Gowda, B.H. 1991. Mean and Turbulence Characteristics of a Class of Three-Dimensional Wall Jets—Part 1: Mean Flow Characteristics. *Journal of Fluids Engineering*. **113**(4),pp.620–628.
- Park, T.S. and Sung, H.J. 2001. Development of a near-wall turbulence model and application to jet impingement heat transfer. *International Journal of Heat and Fluid Flow*. **22**(1),pp.10–18.
- Perry, A.E., Henbest, S. and Chong, M.S. 1986. A theoretical and experimental study of wall turbulence. *Journal of Fluid Mechanics*. **165**.
- Poelma, C., Westerweel, J. and Ooms, G. 2006. Turbulence statistics from optical whole-field measurements in particle-laden turbulence. *Experiments in Fluids*. **40**(3),pp.347–363.
- Poreh, M., Tsuei, Y.G. and Cermak, J.E. 1967. Investigation of a Turbulent Radial Wall Jet. *Journal of Applied Mechanics*. **34**(2),p.457.
- Prevost, F., Boree, J., Nuglisch, H.J. and Charnay, G. 1996. Measurements of fluid/particle correlated motion in the far field of an axisymmetric jet. *International Journal of Multiphase Flow*. **22**(4),pp.685–701.
- Roberson, J.A. and Crowe, C.T. 1996. *Engineering Fluid Mechanics*. New York, John Wiley & Sons.
- Schlichting, H. and Gersten, K. 2000. *Boundary-Layer Theory*. New Dheli, Springer.
- Shames, I.. 2003. *Mechanics of Fluids*. New York, McGraw-Hill.
- Smedley, G.T., Phares, D.J. and Flagan, R.C. 1999. Entrainment of fine particles from surfaces by impinging shock waves. *Experiments in Fluids*. **26**(1–2),pp.116–125.
- Squires, J. and Eaton, K. 1990. Particle Response and Turbulence Modification in Isotropic Turbulence. *Phys Fluid*. **2**(7),pp.1191–1203.
- Toonder, J. Den and Nieuwstadt, F. 1997. Reynolds number effects in a turbulent pipe flow for low to moderate Re. *Physics of Fluids*.
- Towers, D. ~P., Towers, C. ~E., Buckberry, C. ~H. and Reeves, M. 1999. A colour \rm{PIV} system employing fluorescent particles for two-phase flow measurements. *Measurement Science and Technology*. **10**,pp.824–830.
- Tsubokura, M., Kobayashi, T., Taniguchi, N. and Jones, W.P. 2003. A numerical study on the eddy structures of impinging jets excited at the inlet. *International Journal of Heat and Fluid Flow*. **24**(4),pp.500–511.
- Tsuji, Y. and Morikawa, Y. 1982. LDV measurements of an air-solid two-phase flow in a horizontal pipe. *Journal of*

- Fluid Mechanics*. **120**(1982),pp.385–409.
- Tsuji, Y., Morikawa, Y. and Shiomi, H. 1985. LDV measurements of air- solid two-phase flow in a vertical pipe. *Journal of Fluid Mechanics*. **139**,pp.417–434.
- Tsuji, Y., Morikawa, Y., Tanaka, T. and Karimine, K. 1988. Measurements of an axisymmetric jet laden with coarse particles. *Int. J. Multiphase Flow*. **14**,p.565.
- Tummers, M.J., Jacobse, J. and Voorbrood, S.G.J. 2011. Turbulent flow in the near field of a round impinging jet. *International Journal of Heat and Mass Transfer*. **54**(23),pp.4939–4948.
- Unger, D.R. 1998. Experimental and Numerical Characterization of Viscous Flow and Mixing in an Impinging Jet Contactor. *The Canadian Journal of*. **76**(1980).
- Virdung, T. and Rasmuson, A. 2007. Hydrodynamic properties of a turbulent confined solid-liquid jet evaluated using PIV and CFD. *Chemical Engineering Science*. **62**(21),pp.5963–5978.
- Wu, X. and Moin, P. 2008. A direct numerical simulation study on the mean velocity characteristics in turbulent pipe flow. *Journal of Fluid Mechanics*. **608**,pp.81–112.
- Yoshida, H., Suenaga, K. and Echigo, R. 1990. Turbulence structure and heat transfer of a two-dimensional impinging jet with gas-solid suspensions. *International Journal of Heat and Mass Transfer*. **33**(5),pp.859–867.
- Young, R.M., Hargather, M.J. and Settles, G.S. 2013. Shear stress and particle removal measurements of a round turbulent air jet impinging normally upon a planar wall. *Journal of Aerosol Science*. **62**,pp.15–25.
- Zagarola, M. V. and Smits, A.J. 1998. Mean-flow scaling of turbulent pipe flow. *Journal of Fluid Mechanics*. **373**,pp.33–79.
- Zisselmar, R. and Molerus, O. 1979. Investigation of solid-liquid pipe flow with regard to turbulence modification. *The Chemical Engineering Journal*. **18**(3),pp.233–239.

3 Experimental Method

The following chapter provides details on the experimental techniques used in the project in addition to the specifications of the experimental facilities. Section 3.1 gives an overview of possible measurement techniques and their reason for rejection. Section 3.2 provides a more detailed description of the measurement techniques used in the thesis. Section 3.3 Describes the UDV measurement facility, including the equipment used and operating procedure. Section 3.4 describes the PIV measurement facility, covering both the pipe loop and impinging jet systems tested in the thesis. Section 3.5 discusses the steps taken to prepare particles for the multiphase experiments and Section 3.6 contains an error analysis of the two techniques and Section 3.7 contains the references used within this chapter.

3.1 Measurement Techniques

Previous studies have used a variety of measurement techniques to study fluid flows, the most common techniques used to examine the turbulence properties will be described in more detail below.

3.1.1 Overview of rejected measurement techniques.

When deciding on which measurement technique to use, a variety of parameters must be examined and the strengths and weaknesses of each method closely examined to determine the suitability. Reviewing the literature some of the most widely used techniques for examining turbulent flows are hot wire anemometry and laser Doppler anemometry. A brief description of the two techniques and reasons for their rejection are detailed below.

3.1.2 Hot wire Anemometry (HWA)

Hot wire anemometry uses very fine heated wires to examine the flow. The thin metallic wires are heated by an electrical current through the joule effect, and then cooled by the incident flow, mainly through convection. Cooling of the wire leads to a change in electrical resistance which can then be measured. With the relationship between cooling rate and flow velocity known, and hence resistance change and flow velocity known, the flow can be very precisely measured. A major advantage of hot wire anemometry is its high signal to noise ratio, and excellent temporal and spatial resolution making it ideally suited to the study of low intensity turbulent flows and their spectra. Westerweel et al., (2013). Other advantages of the technique include low cost and low signal processing requirements.

This is an invasive technique as measurements rely on contact between the wires and the incident flow leading to possible flow disturbances. These disturbances can be reduced to a minimum through making the apparatus as small as possible, however flow intrusion still exists and can cause problems when trying to detect very small flow phenomena. These problems were observed by Cooper et al., (1993) when trying to resolve velocity measurements close to the wall. As HWA is a single point measurement technique it creates additional challenges when trying to capture whole field measurements of the flow as the apparatus needs to be movable within the measurement volume.

3.1.3 Laser Doppler Anemometry (LDA/LDV)

Laser Doppler anemometry (LDA) or laser Doppler velocimetry (LDV), used interchangeably is a laser based measurement technique operating on the principal of measuring the Doppler shift of a moving object. If an object is moving relative to a source of radiation the frequency of the radiation is shifted by an amount relative to the velocity of the object. By measurement of the frequency shift the relative velocity can be calculated. LDA systems have the advantage of being less intrusive than HWA systems as the measurement equipment can be situated outside the measurement area. Although seeding particles are generally required for LDA measurements, if properly selected the impact of these seeds on the flow will be minimal as discussed further in the section relating to PIV. LDA is well suited to measure high intensity fluctuations about the mean (Westerweel and Elsinga, 2013). It has the advantage of high spatial resolution and like HWA low signal processing requirements.

Again, LDA has the drawback of being a single point measurement technique in addition to having issues with frequency broadening with aperture, difficulty with regards to using optical systems and alignment problems, especially in hostile environments. Although these difficulties can be overcome by crossing multiple beams of the same colour and measuring the differences in frequency shift between the beams.

3.2 Description of Selected Measurement Techniques

PIV and UDV were ultimately selected for this study. The following section gives a detailed description of the operation of the two techniques, including some of the limiting parameters which effect the ability to obtain high quality results.

3.2.1 Ultrasonic Doppler Velocimetry (UDV)

UDV was selected as an easy to use, low cost and quick measurement alternative to PIV, which would also be able to measure entire profiles at once. This is in contrast with the single point measurements obtained by LDA and HWA. Analysis and comparison of the two systems will allow for comparisons to be made aiding in future measurement technique selection.

UDV measurements work slightly differently to LDV. A transmitter periodically sends short ultrasonic bursts while a receiver detects reflections from particles within the system.

First the height or depth of the particle within the system is measured, this is calculated from the speed at which the sound wave propagates through the liquid and the travel time of the wave. Shown in Equation 3.1 where C is the speed of sound for a given fluid, T_1 is the time at which emission occurs, and T_3 is the time at which the reflection is detected (T_2 being the time of incidence with the particle).

$$Depth = \frac{C}{2 * (T_3 - T_1)}$$

Equation 3.1 – Calculation to find depth of particle within the fluid where C = speed of sound in the measurement fluid, T_1 = time of pulse emission and T_3 = Time of detection.

If the particle is moving, successive measurements will change over time allowing the displacement to be calculated, at the same time the particle velocity is calculated from the shift in frequency using Equation 3.2.

$$u = \frac{C f_D}{2f_0}$$

Equation 3.2 – velocity calculation from Doppler frequency where u = instantaneous velocity C = speed of sound in the measurement fluid, f_D = the Doppler frequency and f_0 = the probe operating frequency.

Some of the limitations of the UDV system involve the fact that the UDV probes can only operate up to a certain measurement distance determined by the pulse repetition frequency.

$$y_{max} = \frac{C}{2f_{prf}}$$

Equation 3.3 – maximum measurement distance of a probe (y_{max}) where C = speed of sound in the measurement fluid and f_{prf} = pulse repetition frequency.

The maximum detectable velocity determined by the Nyquist sampling theorem, which states that a perfect reconstruction of a signal is possible if the sample rate is greater or equal to twice the maximum frequency of the signal, Equation 3.3.

$$u_{max} < \frac{c f_{prf}}{4f_0}$$

Equation 3.4 – maximum velocity measurement distance of a probe (u_{max}) where C = speed of sound in the measurement fluid, f_{prf} = pulse repetition frequency and f_0 = the probe operating frequency.

Therefore, a balance must be found between the maximum measurable distance and the maximum velocity which can be measured (Equation 3.4), limiting the use of UDV in some applications. The resolution of the measurement, also known as the channel width is determined by the frequency of the ultrasonic transmitter given by Equation 3.5.

$$Width = \frac{N_c C}{2f_0}$$

Equation 3.5 – width of each measurement channel where C = speed of sound in the measurement fluid, N_c = number of channels and f_0 = the probe operating frequency.

3.2.2 Particle Image Velocimetry (PIV)

A non-intrusive method of flow visualisation, Particle Image Velocimetry (PIV) works via the tracking of the bulk movement of seeding particles suspended within a flow. The tracking of these particles between two instances of time allow for the velocity field to be inferred from the displacements.

PIV does not track particles individually, that is a separate field known as Particle Tracking Velocimetry (PTV), and instead the bulk movements of particles within individual interrogation areas are tracked.

The main components of a PIV system include: i) the test subject, ii) seeding particles, iii) the illumination system, iv) camera and v) imaging system. A schematic of a typical PIV setup is shown in Figure 3.1.

PIV relies on the use of particles to seed the flow which can then be tracked. In the current study, the flow comprises of both tracer particles (neutrally buoyant) to represent the flow and larger, denser particles to act as a secondary phase.

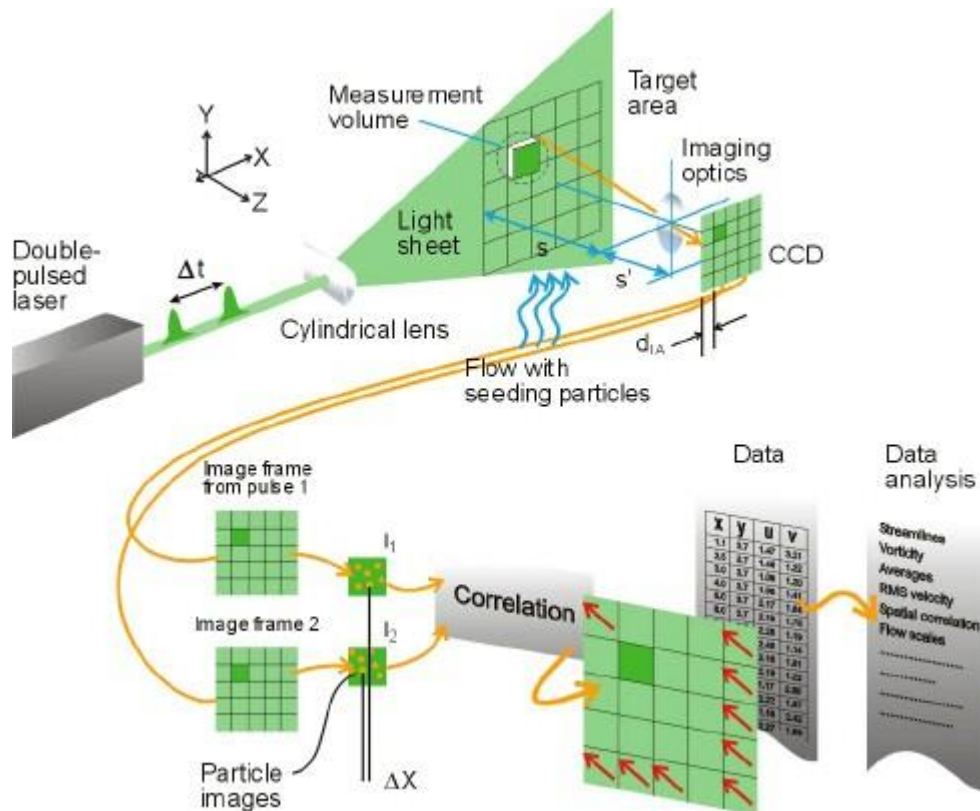


Figure 3.1– PIV measurement technique from Dantec Dynamics, (2017)

3.2.2.1 Tracer Particles

To accurately measure the flow suitable tracer particles must be used to seed the flow. A tracer particle is considered to be ‘ideal’ when it: exactly follows the fluid motion, with no effect on the flow or fluid properties, and does not interact with other particles (Westerweel, 1993). In reality a particle cannot be ideal as the relative motion of a particle is due to slip caused by fluid acceleration. In order to accurately measure the turbulent fluctuations of the flow the Stokes number of the particles must be calculated. The Stokes number which takes into account the bulk exit velocity of the fluid in the jet, the diameter of the jet and the particle response time gives us a value which can then be used to compare the suitability of different particles. Samimy

and Lele, (1991) state that particles with low Stokes numbers will undergo perfect advection where they follow the streamlines exactly and as Stokes number increases the inertia of the particle increases. It is therefore essential to use particles with low Stokes numbers for measuring the fluid properties to reduce error, with particles of Stokes number less than 0.2, tracing accuracy errors are generally below 2%.

$$S_t = \frac{\tau_p U_0}{D}$$

Equation 3.6 - Stokes Number: where τ_p is the particle response time U_0 is the exit velocity of the jet and D is the jet orifice diameter.

$$\tau_p = \frac{\rho_p d_p^2}{18\mu_f}$$

Equation 3.7 – The Particle Response Time: where ρ_p is the particle density, d_p is particle diameter and μ_f is the fluid viscosity.

$$Re_p = \frac{\rho_f U_p d_p}{\mu_f}$$

Equation 3.8 – Particle Reynolds Number: where ρ_f is the fluid density, d_p is particle diameter and μ_f is the fluid viscosity.

Ideally, spherical particles are used as this reduces differences between images due to rotation, and reduces errors due to some calculations requiring the particles to be assumed spherical, such as those used to calculate the particle response time. As particle shape can significantly affect the flow resistance it is important that an aerodynamically equivalent diameter is used for irregular shaped particles. (Melling, 1997)

For PIV in water, tracer particles are chosen to have almost neutral density (density ratio of 1) to adequately track the fluid responses. Experiments conducted with ceramic seeding particles of density ratio 3-4 require the use of very small particles and therefore high powered lasers to obtain results. Other experiments using very low density hydrogen bubbles as the tracers lead to issues with possible buoyancy effects. (Melling, 1997)

The seeding of tracer particles should be performed to ensure that any flow structures only become apparent when the velocity field is evaluated; this is done by ensuring the seeding is homogeneous, as opposed to flow visualisation methods which rely on the use of specific seeding points and inhomogeneous seeding. (Westerweel, 1997) Homogeneous seeding is achieved by seeding both the jet and the ambient fluid.

As PIV relies on tracking the shift in intensity peak, it is important that the particle seeding density is adequate. Too few particles and the random noise inherent in the system may cause a false peak to occur skewing the results. It is generally recommended that a minimum of 8 particles are visible in each interrogation area. (Keane and Adrian, 1992)

3.2.2.2 Illumination

For the seeding particles to be tracked they must be detected by the imaging equipment. This means that for most PIV applications flow is illuminated using a laser. The power of the laser required is a function of the scattering characteristics of the particles being used, the opacity of the fluid being investigated, and the size of the measurement area. Whereas the dimensions of the light sheet required are dependent upon the experimental conditions.

Small particles such as those used to seed gas flows generally scatter much less light and so high powered double pulsed lasers such as the frequency doubled Nd:YAG, ruby, or copper vapour lasers must be used. Whereas the larger particles used for measuring water flows can be

measured using lower powered continuous lasers such as the gated argon ion laser. (Melling, 1997)

Higher energy lasers will provide better illumination of the interrogation area; however, care must be taken not to increase the intensity too much, and this is due to the risk of damage being caused to the optical equipment if the camera sensors are overloaded. Overloaded sensors can result in dead spots in the images where no information can be recorded.

The light from the laser travels through a series of optical lenses, which convert the beam from the laser into a light sheet, allowing for only a thin test section to be illuminated and therefore interrogated.

3.2.2.3 Image Capture

When PIV was first developed digital cameras were still in their infancy and so analogue film cameras had to be used to capture the images. With analogue cameras, the images are recorded onto film with the images then scanned into the computer for cross correlation to be performed.

Today, technology has progressed to the point where digital cameras can reliably provide high resolution images with the benefit of the images directly processed using the PIV software. The software allows the camera to be synchronised with the pulses from a laser creating sets of image pairs. These are the image pairs which are then used for cross correlation and tracking of the bulk movement of particles. Monochromatic cameras are generally used since colour data is not important, however newer systems are being developed to take advantage of being able to distinguish between different wavelengths and so colour cameras become more important.

Good cameras and lenses have a high pixel density and spatial resolution allowing for detailed high-quality images to be recorded. High quality lenses produce clearer magnified images of the interrogation area allowing the environment to be probed with more detail than normally possible. They also can change the size of the aperture, having a larger aperture means that the sensor is exposed to more light but has a reduced depth of field.

3.2.2.4 Image Processing

Once the images have been captured they can be processed, pre-processing techniques such as background subtraction and the selection of regions of interest allow for specific parts of an image to be analysed and for the clarity of the image to be increased.

The image is separated into interrogation areas and the interrogation areas from each image pair are cross correlated pixel by pixel. This produces a signal peak which identifies the common particle displacement for each interrogation area. This then allows for an accurate measure of the displacement through subpixel interpolation.

3.3 UDV Measurement

This section details the experimental equipment used, including a description of the flow loop and the UDV equipment. The pipe flow system for the UDV measurements was commissioned prior to the start of this study and so was used with no major alterations.

3.3.1 UDV Pipe Loop Specifications

3.3.1.1 Measurement Section

The measurement section of the flow loop comprised of a straight 4 m section of clear UPVC pipe O.D. 50mm, I.D. 46mm with collars attached at various distances along the pipe. The collars served as mounting points for the measurement probes with holes drilled through the pipe wall so that the probe could be fully inserted as shown in Figure 3.2. The collars which were not in use were plugged to ensure there were no leaks in the system.

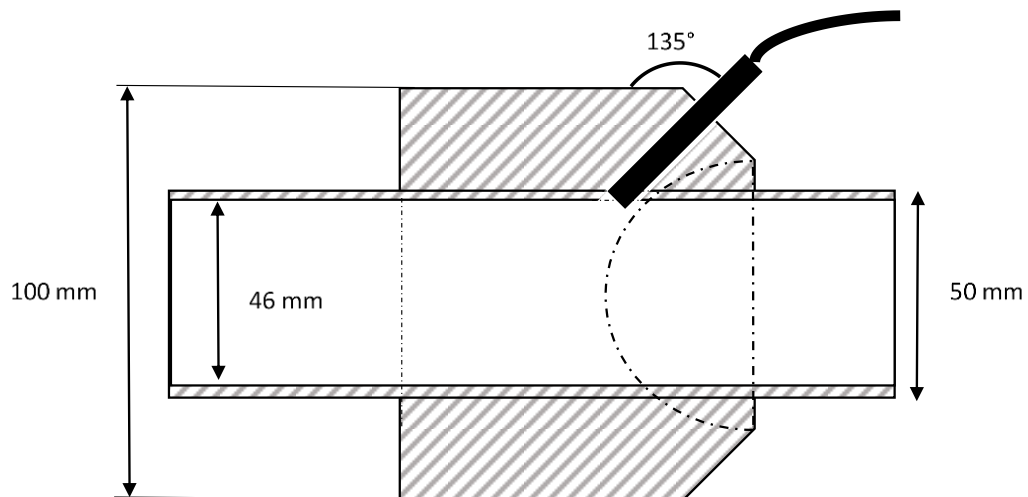


Figure 3.2 – Diagram of the measurement section.

3.3.1.2 Mixing/ Feed Tank

The mixing tank was constructed from stainless steel with internal baffles and a down pipe to prevent entrainment of air as the flow discharges from the main flow loop. The mixing tank was fixed in place bolted through 3 steel legs to ensure no movement could occur, while giving enough clearance for piping to be attached underneath. The base of the tank is convex aiding in draining the tank as fluid is drawn from the bottom. The return flow from the pipe impinged downwards onto the base of the tank. The maximum volume of the tank is 80 L, however in general operation the maximum volume of the flow loop does not exceed 60 L.

In addition to resuspension by the impingement of the returning fluid, a variable speed mixer was included coupled with a three-vane propeller. In normal operation, this would be set to 300 rpm to ensure the flow (particle distribution) remained homogeneous.

3.3.1.3 Control System

Flow rate is controlled through the control box attached to the Ebara DWO 200 centrifugal pump allowing the flow loop to operate up to a Reynolds number of 42,000. The flow rate was measured using an ultrasonic flow meter upstream of the measurement area with a digital display allowing for precise control over the system.

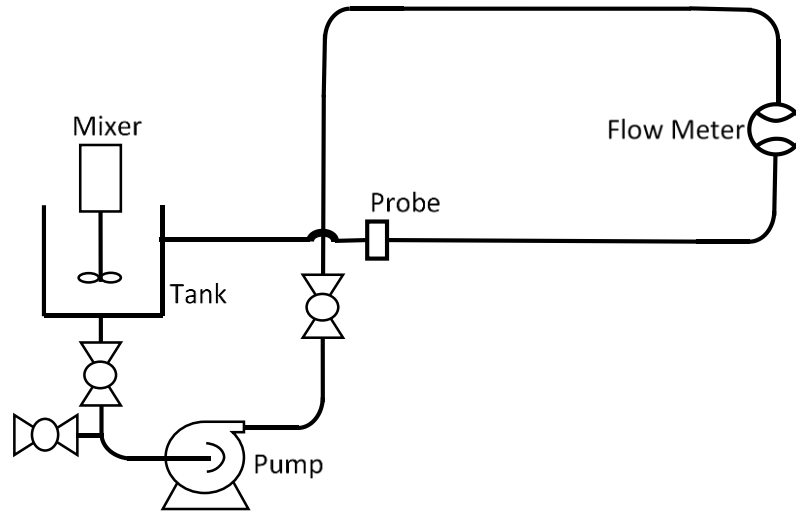


Figure 3.3 – UDV Pipe loop flow diagram

3.3.2 UDV Equipment Specifications

An Imasonic 2MHz, piezoelectric, 5 mm active diameter transducer was used for the UDV measurements. The probe was mounted at an angle of 135° pointing towards the flow, as a compromise between wanting a shallow angle to accurately track the axial velocity and not wanting to insert the probe too far into the flow. A non-intrusive arrangement for the probe was initially attempted, however even with ultrasonic gel reliable contact with the pipe wall was difficult to achieve.

The transducer was controlled and the signal processed by a UVP-DUO Doppler velocimeter (Met-Flow, Switzerland). The measurement parameters used are given in Table 3.1.

Table 3.1 – UDV measurement parameters.

Frequency	2 MHz	Channel Width (mm)	0.74 or 0.37
# of Cycles	1 or 2	# of Channels	100 or 200
# of Repetitions	64	Overlap	None or 50%
Noise Filter	0	Voltage	150 V

By increasing the number of cycles (1 to 2) the signal quality is increased, however the longitudinal resolution is decreased and the effective resolution is halved. This can be overcome to some degree by having a region of overlap which allows for the signals to be resampled to create measurement points in between channels effectively increasing the resolution.

The effect of changing these parameters is shown in Figures 3.4 and 3.5 which show the velocity and turbulence profiles taken with a single pulse, a double pulse with no overlap and a double pulse with 50% overlap. As can be seen there is very little change in the reported values (axial velocity and axial turbulence) as the parameters are changed. For the rest of the study the analysis was performed using a single pulse as there was no appreciable increase in signal quality as the number of cycles was increased and the single pulse method offered the highest spatial resolution.

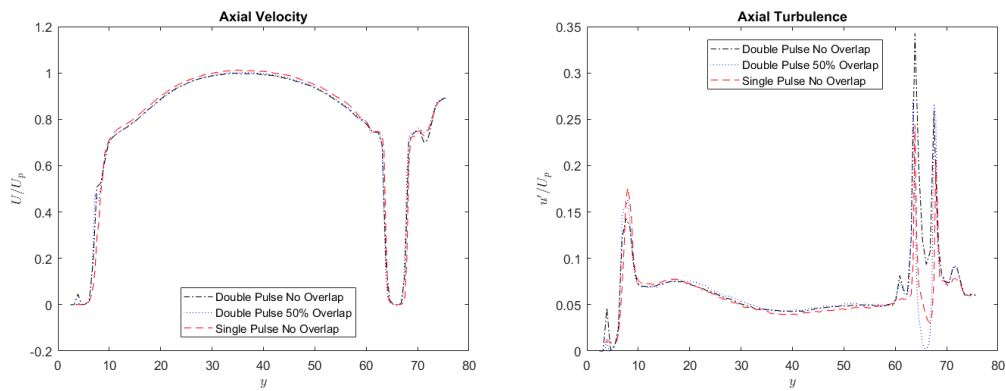


Figure 3.4 (left) – Change in axial velocity with change in number of pulses. Figure 3.5(right) – Change in axial turbulence with change in number of pulses.

3.3.3 UDV Method

This section details the method used for the acquisition and processing of the UDV data.

3.3.3.1 Preparation

To ensure repeatability between results it is essential that the same preparation procedure is followed before each run. The first step is to perform a visual check of the flow loop to ensure no damage has occurred, should any damage be detected the component should be repaired or replaced before the test can continue. Once the equipment has been deemed suitable for use the probe is inserted into the holding mechanism and checked to ensure that a water tight seal has been formed.

The flow loop is then flushed through several times with clean water to ensure no particles remain from previous tests. The fluid is visually checked for particle content before disposal so that it can be ensured no particles from previous tests remain in the system. Once this condition has been satisfied the system is fully drained and the valve below the feed tank closed.

3.3.3.2 Operation

60 L of fresh water are added to the test tank ensuring the same fluid volume each time. This is then cycled through the system several times as a final check for leaks and unwanted particles. When testing with particles the mixer would at this point be activated and the pump set to the required flow rate. The system is then left to run for several minutes to ensure an even dispersion of the test particles. For single-phase measurements, the mixer is not required however the system is still cycled for several minutes before testing to ensure a steady flow has developed. Flow rate is then checked on the flowmeter and any required adjustments are made by adjusting the pump speed. For the reported results the pump was operated at its safe maximum operating speed which corresponded to a pipe Reynolds number of 40,000.

The UDV-DUO system was then enabled and the software checked to ensure correct operation. The measurement period was over 27 ms during which 64 measurements were taken for each channel and averaged to give an array of velocity values for that time step. This process was repeated to create 6200 data points for each channel, ensuring sufficient data points were available to accurately obtain the turbulence statistics in addition to the mean velocity. Once all measurements had been taken a known mass of particles was added to the feed tank with the mixer enabled and allowed to cycle for several minutes to ensure homogeneity of the flow before measurements were repeated for the increased particle concentration.

3.3.3.3 Data Processing

Once measurements at all particle concentrations had been performed the raw velocity values and spatial locations were exported in text files to be processed in MATLAB. Spatial locations were scaled to represent the fact that the measurements were taken at an angle to the flow, whereas this was accounted for in the velocity values by the UDV-DUO system in the frequency conversion. The mean flow value was obtained by taking the average of the velocities of each channel across all time steps. The turbulence values were then obtained by calculating the standard deviation from the mean using Equation 3.9 as discussed in Chapter 2. Plotting and presentation of the figures was performed in MATLAB.

$$u' = \sqrt{\frac{1}{n} \sum_{1}^n (u_i - U)^2}$$

Equation 3.9 – calculation of velocity RMS (u'), where n = number of samples u_i = instantaneous velocity and U = mean velocity

3.4 PIV Measurement Facility

This section details the specification of the PIV system used on both the newly constructed flow loop and the impinging jet test tank.

3.4.1 Pipe Loop Design Considerations

Several factors had to be considered when designing the pipe loop, the most important ensuring the flow was fully developed and having the ability to resolve measurements as close to the pipe wall as possible. The ability to do this is restricted by the fact that the pipe is curved. Pipe curvature causes optical distortion of the flow and reflections of the laser off the pipe wall can obscure the flow. The material for the pipe wall was selected to be as thin as possible while still allowing maximum transmission of the laser light. Clear plastic acrylic tube O.D. of 50 mm and I.D. of 48 mm was selected as it fits both criteria.

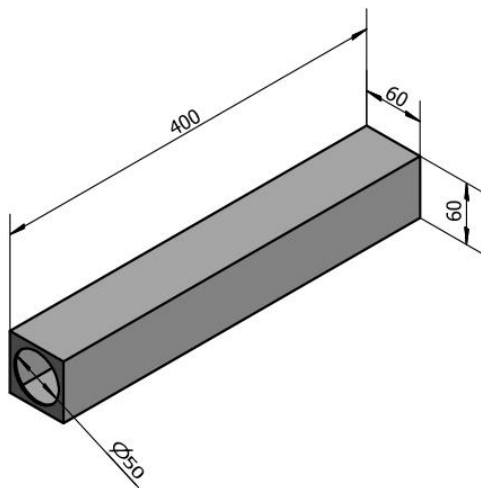


Figure 3.6 – Drawing of the box section which encloses the pipe.

The curvature of the pipe could be accounted for in part through the use of a fluid filled box section with removable lid which enclosed the measurement area, as utilised by Poelma et al., (2006). A drawing of the box is shown in Figure 3.6. It was constructed from clear acrylic like the pipe and was positioned around the pipe before the ends were sealed to create a watertight fit.

The effects of including this box section are shown in Figures 3.7 and 3.8 which displays a calibration plate within the pipe in the presence of the water filled box and without it. As the distance between holes in the calibration plate are

constant the optical distortion without the box section is readily visible especially at the pipe wall towards the bottom of the images where the uniformly spaced holes in the plate appear to move closer together in Figure 3.7 but remain a fixed distance apart in Figure 3.8.

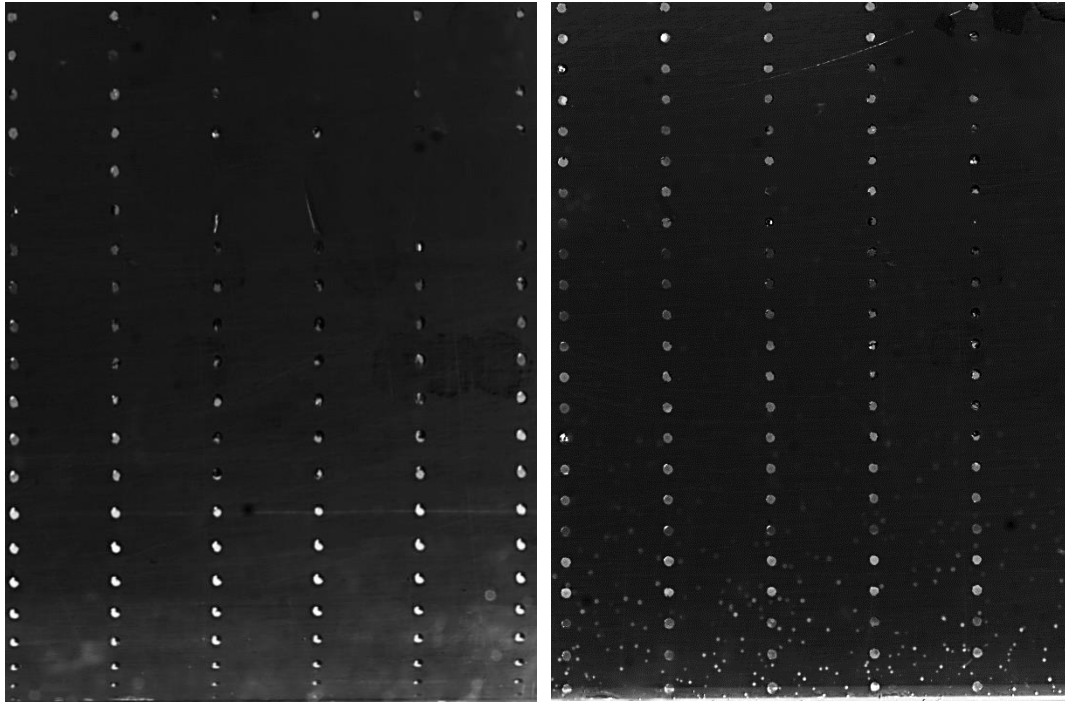


Figure 3.7 (left) – Calibration plate without box section showing optical distortion. Figure 3.8 (right) – Calibration plate with box section showing reduction in distortion.

There is however distortion very close to the wall, initially the calibration plate was designed so that the distortion could be accounted for within the PIV software. However, the additional cost of machining a plate to tolerances such that the very fine distortion near to the wall could be measured proved prohibitive. An alternate method would be to increase the pipe diameter to scale up the flow, however the challenge associated with this is then ensuring that the flow is fully developed. As pipe diameter increases so does the length required to ensure fully developed flow.

Using Equation 3.10 (Shames, 1982) a minimum run up length for a 50 mm diameter pipe at a Reynolds number of 100,000 is only 1.5 m, whereas using Equation 3.11 from Zagarola and Smits, (1998) the minimum entry length is 3.25 m. The constraints of the measurement area required that the total length of the test section be less than 6 m. Factoring in the requirement that measurements should not be taken at the very end of the pipe so that no upstream influence of the corners influences the measurements, it was decided that the pipe diameter should not exceed 50 mm, ensuring the flow was fully developed.

$$\frac{L}{D} = 4.4Re^{\frac{1}{6}}$$

Equation 3.10- Required pipe length for fully developed flow where L is pipe length, D is pipe diameter and Re is the flow Reynolds number Shames, (2003)

$$\frac{L}{D} = \frac{0.5}{f} + \frac{5}{f^{\frac{1}{2}}}$$

Equation 3.11-Required pipe length for fully developed flow where L is pipe length, D is pipe diameter and f is the pipe friction factor Zagarola and Smits, (1998)

The flow loop was also designed for easy drainage with a T-section placed immediately after the pump allowing the fluid to be pumped out of the mixing tank and into storage containers for disposal.

3.4.2 PIV Pipe Loop Specifications

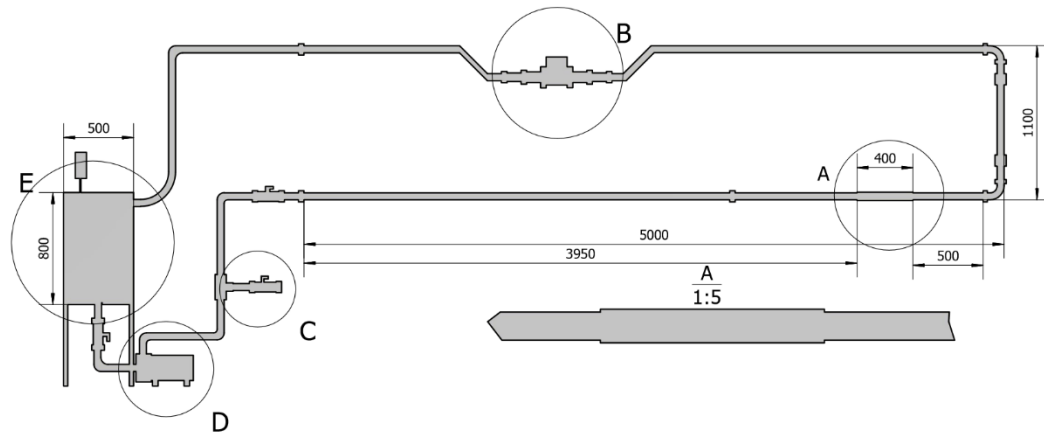


Figure 3.9 – PIV pipe loop drawing with areas of interest labelled.

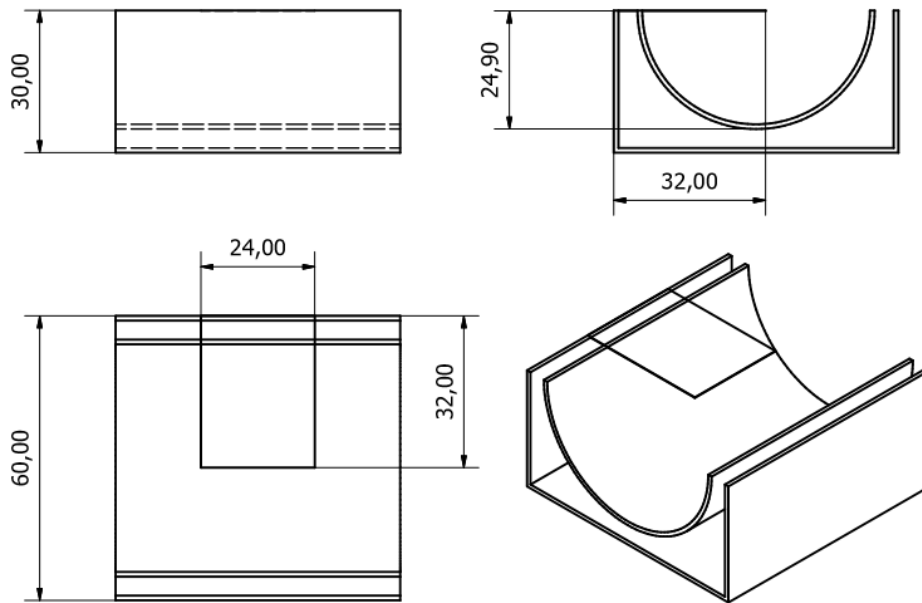


Figure 3.10 – PIV pipe loop measurement section diagram.

3.4.2.1 Measurement Section

As previously discussed, the measurement section (A in Figure 3.9) comprises of 50 mm O.D. and 48 mm I.D. optically clear acrylic pipe enclosed in a 1 mm thick rectangular box section which can be filled and drained with water to reduce optical interference due to pipe curvature. The box is 500 mm in length with a height and depth of 60 mm allowing enough space for the pipe to travel through. The light sheet travels horizontally through the centre of the measurement section with the camera underneath pointing upwards, the interrogation area is shown in Figure 3.10.

3.4.2.2 Mixing/ Feed Tank

The mixing tank (E in Figure 3.9) was of the same design as the one used for the acoustic system, however the tank was scaled up to operate with a larger fluid volume. The tank was made from stainless steel with internal baffles and a down pipe to prevent entrainment of air as the returning flow discharges. Due to its larger size an additional leg was included and used to fix the tank to the floor. The maximum volume of the tank was 150 L, however in general operation the maximum volume of the flow loop did not exceed 100 L. Again, a variable speed mixer was included coupled with a three-vane propeller, in normal operation this would be set to 300 rpm to ensure the flow remained homogeneous.

3.4.2.3 Control System

Flow rate is controlled through the control box attached to the Ebara DWO 200 centrifugal pump (D in Figure 3.9) providing flow rates up to Reynolds number of 60,000. The flow rate was measured using an Omega FMG-2003 electromagnetic flow meter with digital display (B in Figure 3.9) allowing for precise control over the system.

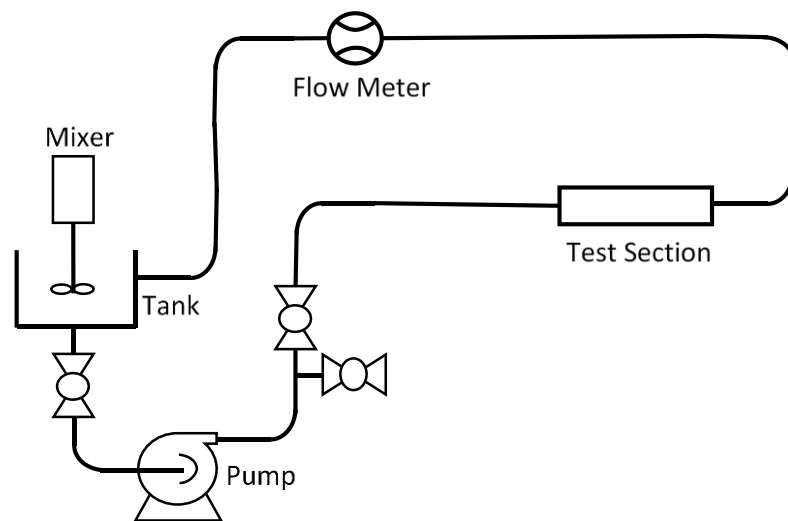


Figure 3.11 – Flow diagram of PIV pipe loop

3.4.3 Impinging Jet Rig Specifications

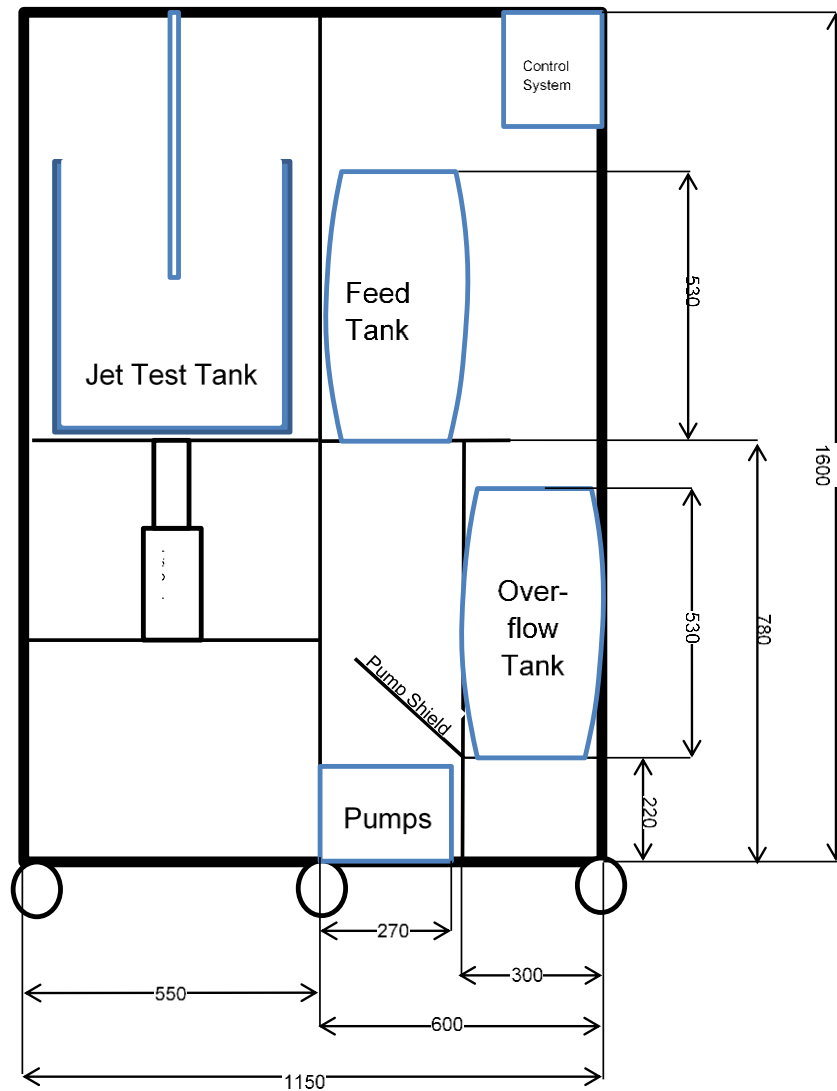


Figure 3.12 – Drawing of impinging jet test facility

3.4.3.1 Test Tank

The test tank is where the jet impingement occurs, the tank itself is constructed from 10 mm thick panes of low iron extra clear float glass, this material was chosen due to its ability to transmit light with minimal reflectance and absorbance, an important property in PIV to ensure as much of the light scattered by the particles is detected by the camera.

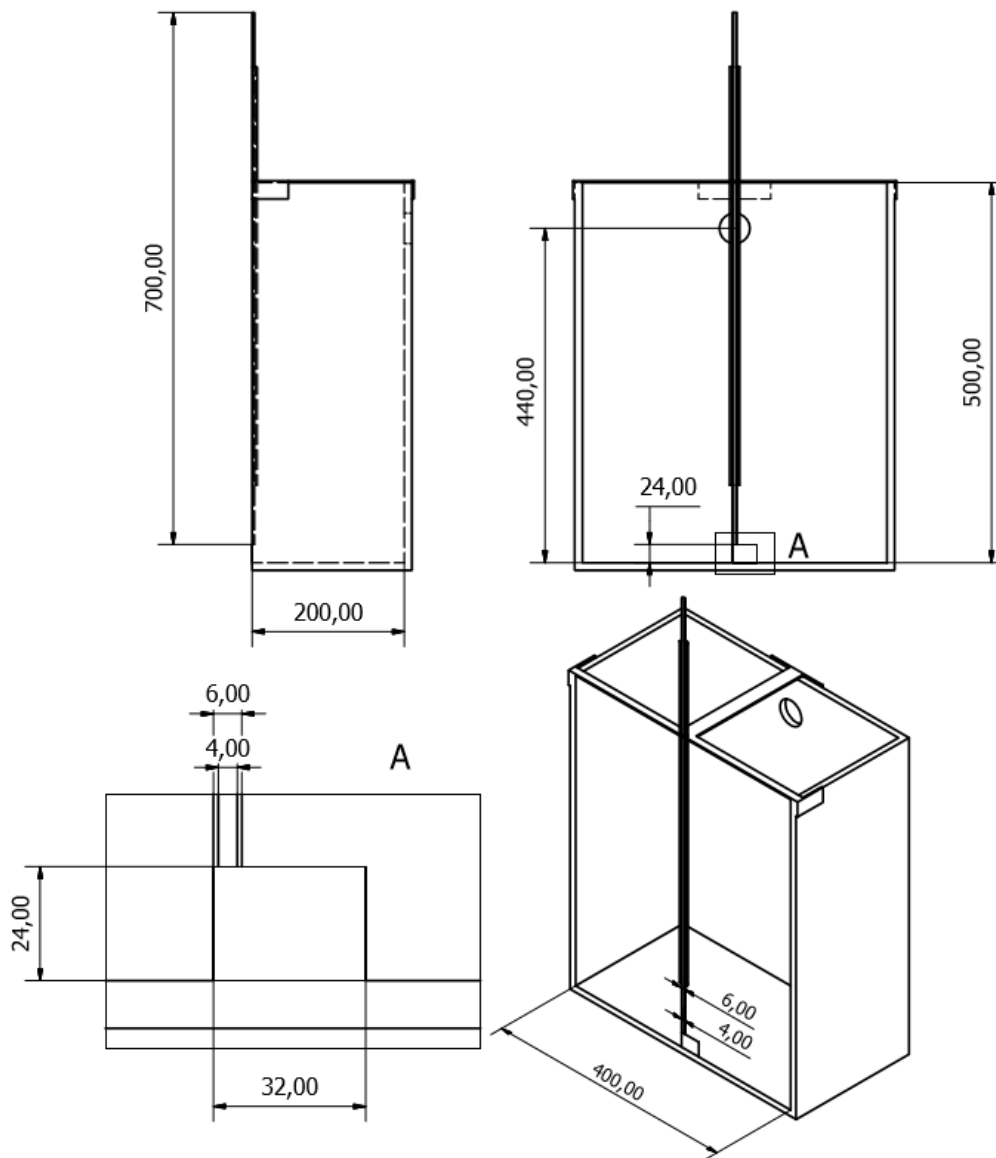


Figure 3.13 – Cross section of the impinging jet test tank showing the region of interrogation.

The tank has a square base of 400 mm (l x w) and height 500 mm(h), with an outlet pipe to the overflow tank 440 mm from the base a cross section of which can be seen in Figure 3.13. During normal operation as the jet line is in use the outlet pipe will maintain a constant volume within the tank. The top of the tank includes a cross brace to support the jet line. The jet line is 700 mm in length of stainless steel, with a 4 mm I.D. and 6 mm O.D., the jet line is fixed in place by the

cross brace and adjustable screws allowing the jet height from the tank base to be adjusted. The tank is supported by a movable platform allowing the jet line to be suspended even further from the base of the tank should the experimental regime require. However, the distance to impingement in this study was fixed at 6 D (24 mm).

The dimensions of the jet and the tank were selected to allow for the formation of a fully developed flow in the jet line, and the tank was large enough to minimise influence from the tank side walls. The upper limit of the tank volume was determined by the requirement to manoeuvre the tank between labs and into position, which then dictated the maximum internal diameter of the jet line. Although a smaller diameter jet line could have been used to increase the relative distance of the jet centreline to the tank walls, it was considered that anything smaller than 4 mm internal diameter would create problems and limitations with regards to particle use and flow velocities. A larger diameter jet line has the benefit of being more visible to the camera and so would provide clearer and more robust images. However, an increase in the jet-line diameter in the current tank would start to introduce more pronounced effects from the side walls.

The length of the jet line was determined by the experimental flow velocity and pipe diameter. For the designed maximum flow rate of the impinging jet, the required entry length of the jet for fully developed hydrodynamic flow was calculated using the two methods previously described to calculate the required length for the pipe systems. The first method determined the L/D ratio required to be 21.85 (Equation 3.10) whereas the second calculated the required ratio of L/D to be 49.02 (Equation 3.11), both values are well below the actual L/D ratio of 175 so ensures confidence that the flow is fully developed.

3.4.3.2 Feed and Overflow Tank

The feed and overflow tanks are cylindrical plastic drums. The overflow tank sits on the base of the rig and is connected to the overflow port of the test tank via flexible tubing. Tubing from the bottom of the overflow tank connects to a pump which sprays the water at the base of the feed tank; this has the benefit of scrubbing and lifting particles from the base of the feed tank and maintaining them in a suspension when used frequently.

The feed tank contains the fluid and in the case of multiphase trials, the solid suspension, ready to be pumped into the test tank. The tank is connected via a pump and needle valve system allowing the flow rate to be controlled. Within the feed tank an overhead stirrer is connected to an impeller, this coupled with the scrubbing action of the overflow tank input allows larger solid particles to be kept suspended and homogenous in the fluid. The Ebara 3D pumps used were selected for their ability to maintain a constant velocity for long periods of time without pulsing and can handle low solids concentrations. The volume of the system while in operation is set to 120 L to ensure consistency between runs. The entire system is fitted with non-return valves to prevent the siphoning of water from the test tank when the rig is not in use.

3.4.3.3 Frame and Shielding

The frame of the tank was designed to be mobile, allowing for the rig to be moved to a secure storage area when not in use, and to allow for the rig to be repositioned as needed. The fact that the rig is mobile creates additional challenges during alignment; however, the mobility requirement outweighs these concerns. Due to the nature of PIV, integrated shielding is used to prevent laser emissions from creating an unnecessary hazard to the operator. Shielding is in place on 5 of the 6 sides of the test tank, with a small slot cut out of one of the panels to allow the laser sheet into the tank. The final side of the tank must remain open for the camera. Splash

plates are used on the feed and overflow tanks of the rig to protect the pumps from encountering liquids should an error occur.

3.4.3.4 Control System

The two pumps on the rig can be operated independently via the two switches on the control panel. Pump 2 operates at a constant flow rate when activated pumping water from the overflow tank into the feed tank. The flow rate from pump 1 is controlled using the needle valve, allowing a range of flow rates between 0-4 L/min. In addition to manual pump control the rig is outfitted with an automatic system, which can be used to activate the pumps maintaining a minimum level in the feed tank.

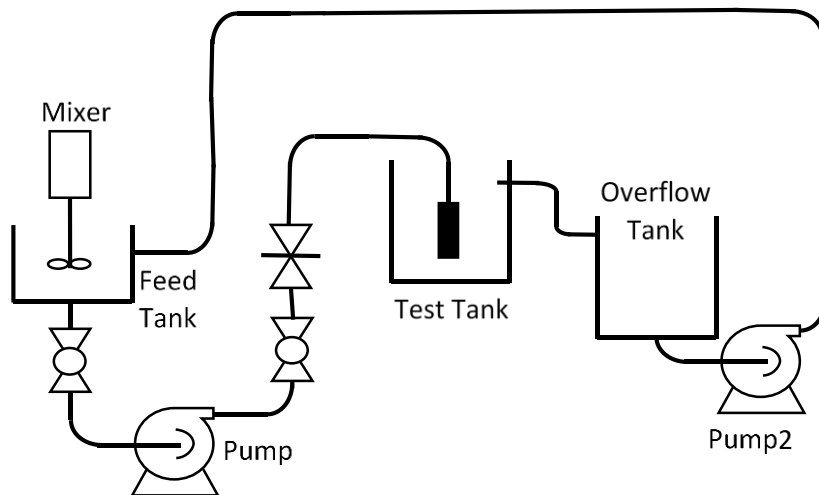


Figure 3.14 – Impinging jet flow diagram.

3.4.4 PIV Equipment Specifications

The main components of the PIV system (Laser and Camera) were provided by Dantec Dynamics and controlled using Dynamic Studio software loaded onto a standard desktop PC. The flow field was illuminated using an adjustable power output Class 4 Nd:YAG laser supplied by Litron Lasers. The wavelength of the emissions from the laser were isolated to 532 nm as the green light is

visible by the naked eye and so the chance of accidental exposure is reduced. To provide the 2D light sheet required for PIV the laser passes through several optics, including spherical and cylindrical lenses with a variable focus module, to produce a thin sheet. The thickness of this sheet is determined by the focal point of the optics and the wavelength of the laser. For both pipe and jet measurements the light sheet was made as thin as possible and so did not exceed 1 mm in thickness.

For the measurements in the pipe, the light sheet was orientated horizontally illuminating a cross section through the centreline and along the pipe, using the previously mentioned box section. Impinging jet measurements were performed by orientating the light sheet vertically, again along the axis of the dominant flow, and positioned across the jet centreline to capture the flow cross section.

A FlowSense EO 2M digital camera was used to capture the images of the flow field. The camera had a maximum operating speed of 44 fps with a sensor resolution of 1600 x 1200 pixels and an individual pixel size of 7.4 μm . This was combined with a Sigma Macro Lens to obtain high quality images of the area of interest and to ensure that possible errors were minimised by ensuring the minimum pixel density (pixels per mm) was obtained to accurately represent the images (Figure 3.15). The number of samples required for an exact optical reproduction is, like the UDV measurements, determined by the Nyquist sampling theorem. The bandwidth of a PIV image can be calculated using Equation 3.12.

$$Z = \frac{D_a}{\lambda F (M + 1)}$$

Equation 3.12 – Where Z = bandwidth, F = focal length, M = magnification, D_a = aperture diameter and λ = wavelength of light Willert and Gharib, (1991)

However, an exact reproduction of the image is not required, only sufficient information to ensure that the shift in the intensity peak can be obtained. Therefore, assuming that the particle images can be reproduced as Gaussian curves the required bandwidth of the image can be calculated using Equation 3.13.

$$Z = \frac{1.22}{d_{pt}\sqrt{2}}$$

Equation 3.13 – required bandwidth where Z =bandwidth and d_{pt} =image diameter Willert and Gharib, (1991)

where d_{pt} is the Gaussian approximation for the image diameter of a small circular object and is given by Equation 3.14.

$$d_{pt} = M^2 d_p^2 + d_{ps}^2$$

Equation 3.14 - Gaussian approximation for image diameter where M = magnification , d_p = particle diameter and d_{ps} = Airy pattern diameter Willert and Gharib, (1991)

d_{ps} is the diameter of the Airy pattern and is calculated using Equation 3.15.

$$d_{ps} = 2.44 \frac{\lambda z_0}{D_a}$$

Equation 3.15 – Calculation of Airy pattern (d_{ps}) where D_a = aperture diameter, λ = wavelength of light and z_0 = image distance Willert and Gharib, (1991)

$$d_{ps} = 2.44 \frac{\lambda z_0}{D_a}$$

Equation 3.15 – Calculation of Airy pattern (d_{ps}) where D_a = aperture diameter, λ = wavelength of light and z_0 = image distance Willert and Gharib, (1991)

Using an aperture ratio of 16 and 532 nm light, Figure 3.15 shows the required number of pixels per mm to ensure valid PIV images as the scale factor (inverse of magnification) increases. The tracer particles have a diameter of 20 μm and the solids of 225 μm . As the sensor size of the CCD camera was fixed the lens had to be selected to minimise the scale factor ($1/M$) to ensure the flow could be traced accurately.

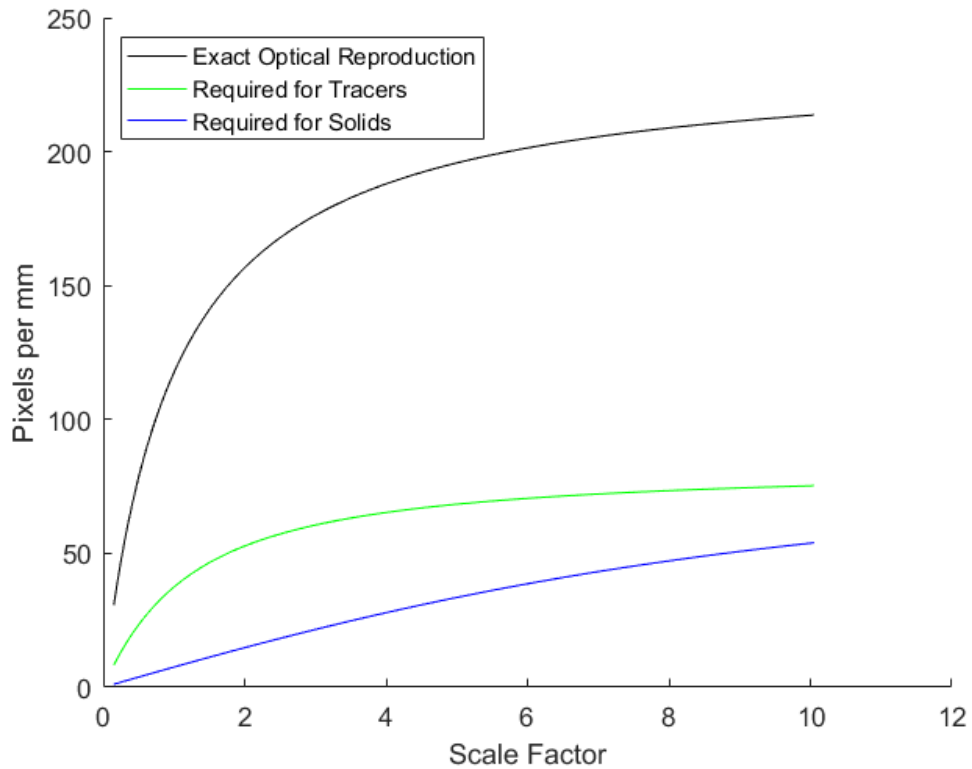


Figure 3.15 – Number of pixels required for PIV images as a function of scale factor.

To isolate the seeding particles from the test particles a Red-Orange long-pass optical filter (supplied by MidOpt) was used in combination with fluorescent seeding particles. The fluorescent particles are doped with rhodamine-b which absorbs and re-emits the incident light from the laser, increasing the wavelength. The long-pass filter has a working range of 585-1100 nm and so will block reflections of the light sheet while allowing transmission of the light created through laser induced fluorescence.

3.4.4.1 PIV Settings Used

Table 3.2 – PIV measurement parameters.

Time delay	50 us	Measurement Frequency	15 Hz
Images pairs per run	63	Run Time	4.2 s
Laser Wavelength	532 nm	Light sheet thickness	<1mm
Camera Resolution	1600x1200	f-number	16
Imaged area	32 mm x 24 mm	Magnification	0.25

3.4.5 PIV Method

This section details the method used to obtain and process the PIV data. The technique to process the data was the same for both the pipe and impinging jet systems, and so a combined method will be presented.

3.4.5.1 Preparation and Alignment

As with the acoustic measurements, repeatable results require that the preparation of the system be performed following the same method. The preparation procedure using PIV is more involved than UDV and so the steps have been broken down into several stages to aid the reader.

3.4.5.1.1 Tank /Pipe Preparation

The first step in the experimental procedure is to prepare the pipe loop or test tank, if either have been used previously there may be particles from previous runs still within the system, therefore the system is cleaned and flushed with fresh water to remove unwanted particles. Any marks in the interrogation area are cleaned and the feed tanks filled with water ready for the experiment. At this point the pump system is tested again to ensure smooth running and ensure

all particles have been flushed from the system, if particles remain, the system is drained and flushed again. Once the system is clean fresh water is added. In the case of the pipe loop the feed tank is filled with 100 L of water with the valve at the bottom of the feed tank closed to ensure accuracy when calculating the volume fractions. For the impinging jet system water is added to fill the feed and test tank leaving the overflow tank empty, this ensures that an overflow situation cannot happen if the pump from the overflow tank to the feed tank is left running.

3.4.5.1.2 Equipment Alignment

The test section of the pipe is checked to ensure it is level and any corrections required are made by adjusting the height of one end of the pipe through the clips used to attach the pipework to the wall. Alignment for the impinging jet is more involved. The jet is aligned using an engineer square placed on the base of the tank. The positioning of the jet line can drift over time due to vibrations from the flow so it essential that the alignment is checked before every run. The alignment is checked in the x-y and x-z planes to ensure the jet is perpendicular to the base of the tank. To align the jet the positioning can be altered via the tightening and loosening of two screws on the cross brace used to support the jet line. Additional adjustment can be performed by altering the position of the cross brace within the tank. To minimise vibrations and movement of the jet the cross-brace system was redesigned to provide additional support along the length of the jet. This provided additional securing points for the jet closer to impingement ensuring the jet remained aligned between experiments and vibration was reduced to a minimum. A schematic of the redesigned cross brace is shown in Figure 3.16.

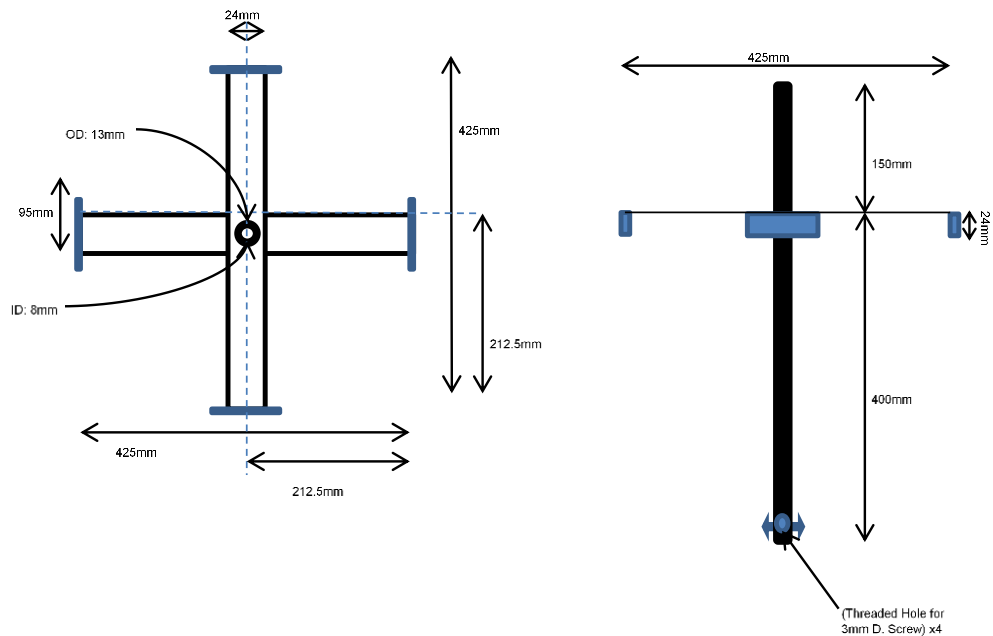


Figure 3.16 – Redesigned cross brace for impinging jet tank.

The height of the jet from the base of the tank can also be changed at this stage allowing for the influence of jet height to be explored, which can change the expected results significantly if the impingement zone is inside or outside the jets potential core.

3.4.5.1.3 Optical Alignment

With successful alignment of the jet the experimental rig can be positioned in-front of the laser system. The laser is a double pulsed Nd:YAG which outputs green light of wavelength 532 nm. The position of the light sheet can be changed using a mirror to direct the light sheet into the tank. The mirror can be used to change the vertical and horizontal position of the light sheet, whereas the laser optic can be manipulated to rotate and change the thickness of the laser sheet. The alignment is checked to ensure the laser sheet is perpendicular to the base of the tank and passes through the centre of the jet line, to ensure the correct sections of the flow are

illuminated. The pipe system is fixed and so alignment of the laser is checked to ensure that the light sheet passes horizontally through the pipe centreline, perpendicular to the floor. This allows for measurements across the flow while neglecting the effects of gravity.

The camera is then aligned and focused to the laser sheet. By changing the focal ratio of the camera to the largest diameter, it becomes easier to focus the camera onto the light sheet as the depth of field is massively reduced, so unless the camera is perfectly focused the particles will not be visible or will be incredibly blurred. Once the camera is focused the focal ratio is increased to reduce the brightness of the images and produce more contrast to differentiate the particles. At this point the optical filter is added if required for the experiment.

3.4.5.1.4 Particle Preparation / Seeding

The solid phase particle preparation is the same as used for the UDV measurements, with the particles sieved before use to ensure the correct particle diameters. For seeding the flow fluorescent PMMA tracer particles are used which are pre-treated and can be used straight from the bottle.

Seed particles are then added to the feed tank and the test tank to obtain an even dispersion. Particles are added with the flow loop or jet in operation and the laser and camera systems running so that the optimum concentration for flow tracking can be obtained.

3.4.5.1.5 Laser Delay

Once the correct seeding has been achieved the settings for the laser are programmed. The laser delay is the time between the first and second pulses of the double pulsed laser.

Depending on the region of flow being studied the delay needs to be altered to account for the differing flow velocities. If the delay is too long particles will have moved outside of the interrogation areas before the second image is captured and so the movement cannot be tracked or the software may detect alternate particles and create erroneous vectors. If the laser delay is too short the particles will not have travelled far enough for the vectors to be calculated with accuracy, this introduces error into the system where the true velocity of the particles become unknown.

In the current experimental program the delay is set to 50 μs , as a compromise between capturing both high and low velocity regions. Window shifting was enabled which allows the interrogation area to shift reducing errors for large particle displacements. Westerweel, (1997)

3.4.5.2 *Operation*

Most the time taken to obtain results from PIV is spent in the preparation and processing stages. Once the experiment has been prepared and everything aligned the experimental rig is ready and images can be collected. The PIV software is now set to acquisition mode.

3.4.5.2.1 *Calibration*

The initial images recorded are used to calibrate the system; this is done to ensure that the length scales are correct and the origin of the flow has been selected properly. Although placing the origin marker is not essential for the calculation of the velocity field, it is useful as it makes determining the positions of flow features and the positioning of flow profile plots easier. The placing of the length scale markers is essential to ensure the displacements of the particles between images are calculated correctly and so the true velocities are recorded. Failure to calibrate the system properly can lead to unusable results depending on the filtering methods used.

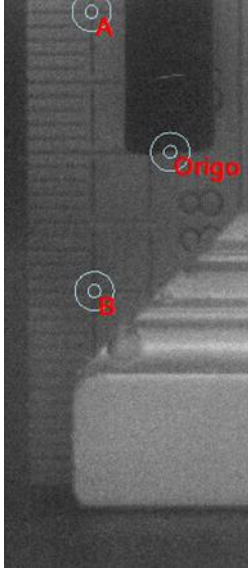


Figure 3.17 - Calibration within Dantec Dynamics PIV software.

Calibration of the jet is performed with the jet inactive and a ruler or set square placed in the tank adjacent to the jet line for reference as seen in Figure 3.17. The origin marker is placed at the jet outlet and the length scale is calculated by placing points A and B on the ruler graduations and the absolute distance between the points entered into the program. All distances will then be calculated relative to the absolute distance between the two points so it is important to be as accurate as possible, hence the need for the graduated ruler.

Calibration of the pipe is performed using a tape measure inserted into the distortion reducing box alongside the measurement section as can

be seen in Figure 3.18.



Figure 3.18 – Picture of tape measure used for calibration along the right-hand side of the pipe.

3.4.5.2.2 Image Capture

With the system calibrated the images can be captured. The pump for the pipe loop can be controlled directly, whereas the pumps controlling the jet are activated and the flow adjusted using a needle valve to ensure the desired flow rate for the experiment is achieved.

The camera is synchronised with the pulses from the laser, this is done automatically by the PIV software, although it can be changed by hand should the operator require. This causes the images for the PIV analysis to be obtained in the required pairs for cross correlation. Due to limitations on the amount of buffer space in the camera memory it is only possible to obtain sets of 63 image pairs before the camera is full, and the images must be downloaded to the computer and saved to the project database. To achieve time averaged results, it is therefore required that the image acquisition is repeated multiple times with each image set saved to the database.

Once enough image pairs have been recorded the sets of images can be collated and processed as a single image set. The number of image sets required can vary depending on the level of detail required and the features of the flow being investigated. Mean velocity fields are accurately obtained with fewer images than turbulence structures which require thousands of images to yield usable results.

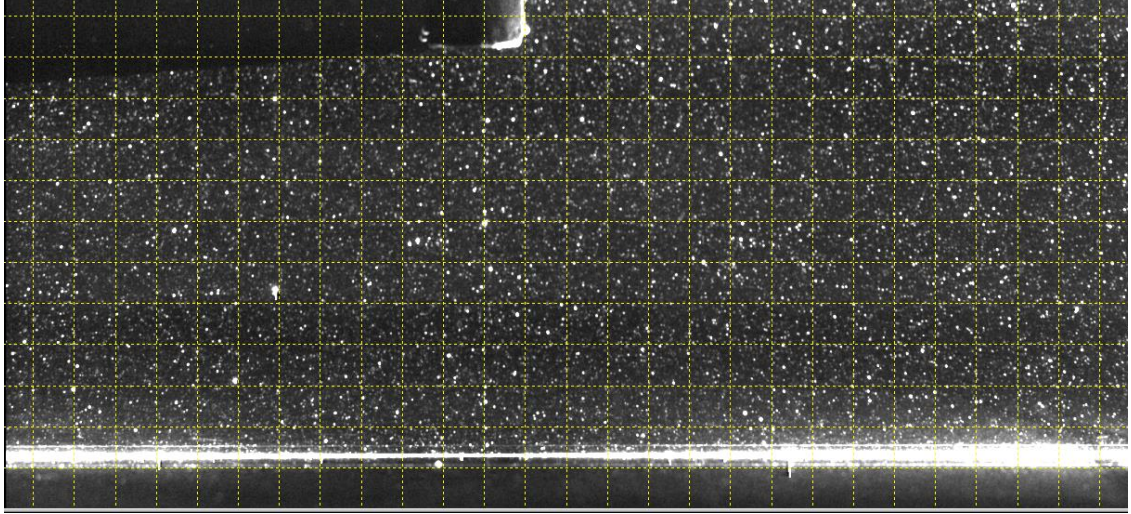


Figure 3.19 - Cropped Image of region of interest showing fluorescent particles.

3.4.5.2.3 Sensitivity Testing

To accurately calculate how many image pairs would be required to ensure confidence in the results, sensitivity testing was performed by repeating the measurements several hundred times to obtain thousands of image pairs. The effect of increasing the number of image pairs for analysis was then studied and an appropriate value selected.

The mean axial velocity and axial turbulence were calculated across the entire jet section for an increasing number of time steps. The percentage change in velocity and turbulence from the previous iteration was calculated to give the percentage change with increased number of image pairs. The mean percentage change across the entire profile was then calculated, allowing the total change for the profile to be easily seen. Equation 3.16 shows how this was calculated for the mean velocity.

$$U_{PC,y} = 100 \sqrt{\left(\frac{(U_{N,y} - U_{N-1,y})}{U_{N-1,y}}\right)^2}$$

Equation 3.16 – Percentage change at a given location ($U_{PC,y}$) where $U_{N,y}$ = the mean velocity at location y over N samples.

$$U_{N,y} = \sum_1^N \frac{u_{i,y}}{N}$$

Equation 3.17 - Mean velocity at location y over N samples ($U_{N,y}$) where $u_{i,y}$ is the instantaneous velocity at location y

The change in mean axial velocity for the entire profile was then calculated by taking the sum of the percentage changes at each y location across the profile as shown by Equation 3.18.

$$\text{Percentage Change} = \sum U_{PC,y}$$

Equation 3.18 – Percentage change in mean axial velocity across jet where ($U_{PC,y}$) Percentage change at a given location at location y

The change in axial velocity fluctuations followed the same method as above except the fluctuating velocity was used instead of the mean. These changes are shown in Figure 3.20. As expected, as the number of image pairs increase the change in velocity decreases, turbulence values require a greater number of image pairs to converge. 6200 image pairs was decided as a good compromise between the time taken to process the results and the diminishing returns obtained by increasing the number of samples taken. At this point each additional image pair has an average change of 0.005% on the mean flow and 0.01% on the turbulence statistics. 6200 image pairs required 100 runs due to the camera buffer limit.

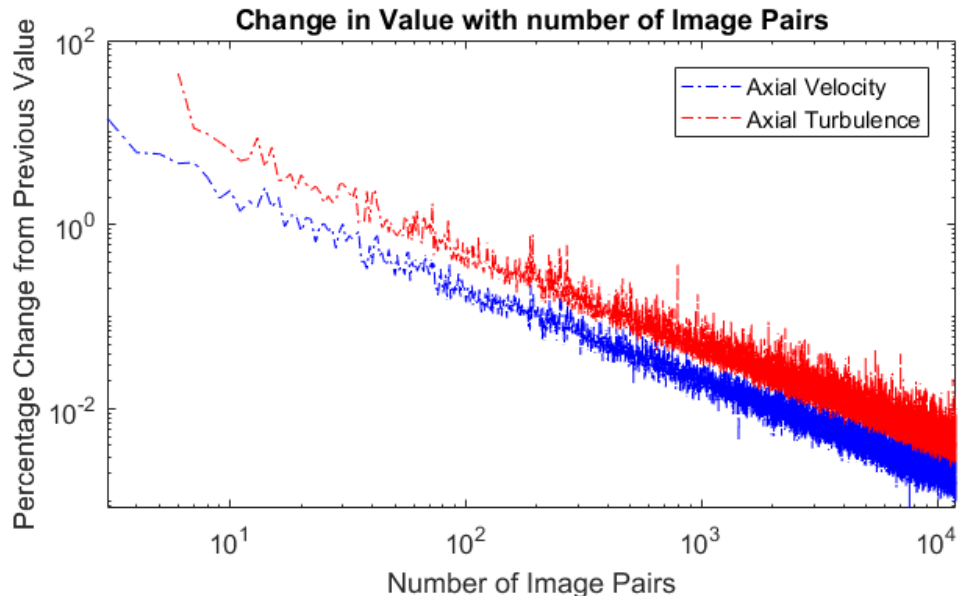


Figure 3.20 – Percentage change in velocity and turbulence values as number of image pairs is increased.

An example of how the velocity changes at a single measurement location is given in Figure 3.21.

Here we show that by increasing the number of image pairs the mean velocity change is less than 0.005 m.s⁻¹ if an additional 6200 image pairs were collected and processed.

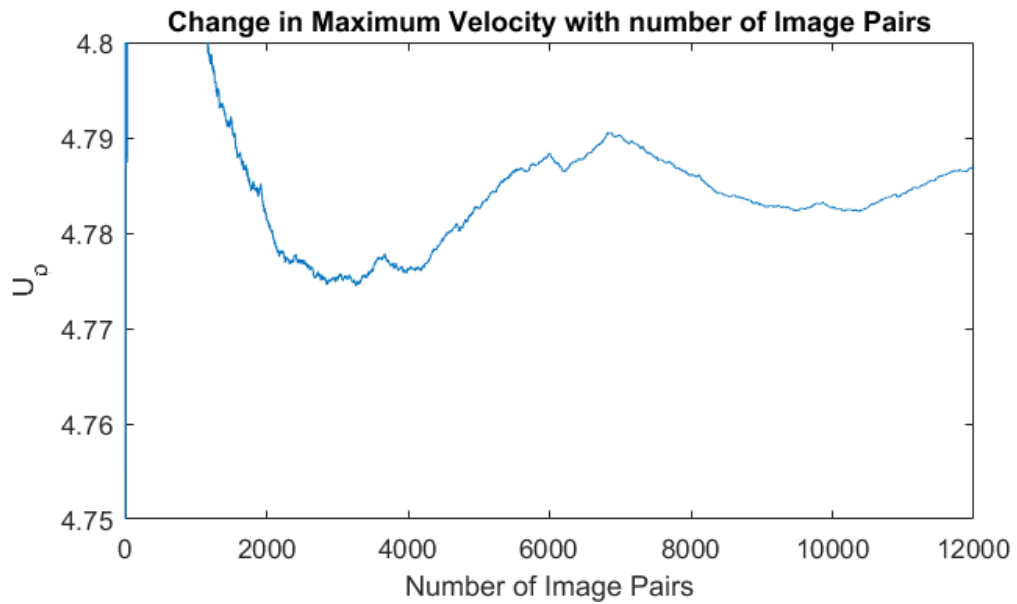


Figure 3.21 - Change in maximum velocity with number of image pairs.

3.4.5.3 Processing

Once the experiment has been completed and all images captured and stored the data processing can begin to calculate the displacements and velocity vectors required to map the velocity field.

3.4.5.3.1 Region of Interest

To reduce computational time, a region of interest is selected for the computer to analyse, this prevents the entire image being used and so can reduce the time taken in subsequent steps if only a small section of the image is relevant. In the current set of experiments the area above the jet line and images of the tank base are discarded as these are not vectors of interest to the current experimental regime. Unfortunately, due to the shape of the area of interest it is not possible to only capture this area with the camera to eliminate this step. It is possible to achieve the same result by using image masks, which are applied to ensure vectors are only calculated in specific areas. The image in Figure 3.19 shows the interrogation area after the region of interest has been selected.

3.4.5.3.2 Background Subtraction

Once the region to be investigated has been selected the dataset is analysed and the mean image is calculated, this image is then subtracted from the original images. This has the effect of eliminating any optical artefacts from the images as well as reducing background noise and increasing clarity of the particles, this allows them to be tracked more easily and reduces the probability of errors occurring and misidentification of particles.

3.4.5.3.3 Cross Correlation

Cross correlation is used to track the movement of the particles in the flow. The region of interest is divided into individual interrogation areas by overlaying a grid. The bulk movement of particles within each interrogation area is then tracked. The interrogation areas for each image frame are compared with each pixel analysed for a signal peak, which identifies a common particle displacement. An accurate measure of the displacement can then be calculated using sub-pixel interpolation. The cross correlation is then repeated for each interrogation area to obtain a vector map for the entire region of interest.

The software used to calculate the displacements has a function known as Adaptive PIV; this function iteratively adapts the size and shape of the interrogation areas. This adaptation is performed to optimise results by sizing interrogation areas to have the ideal number of particles to track within it.

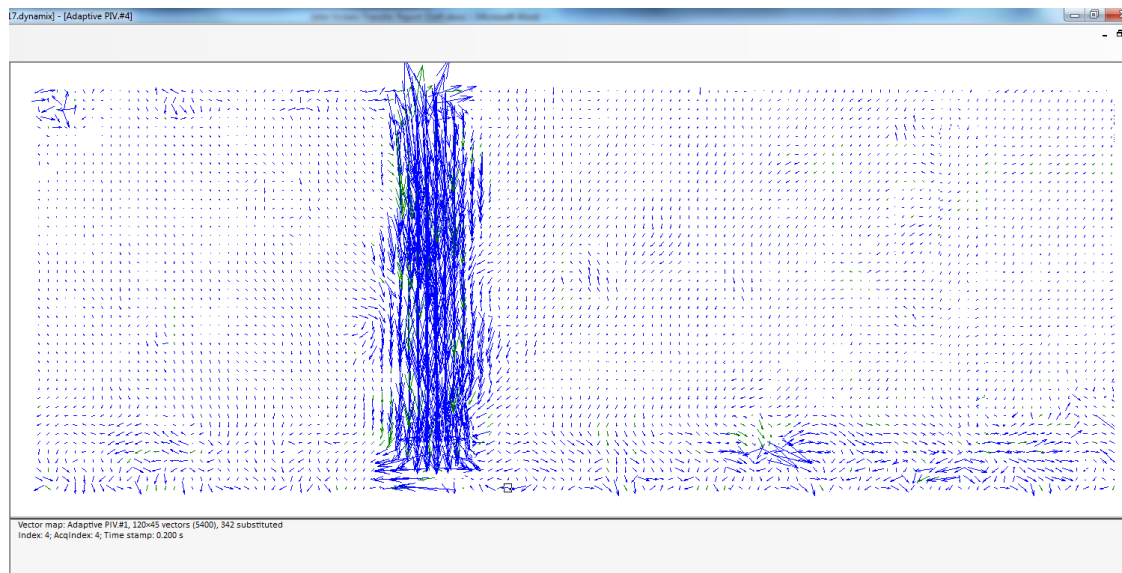


Figure 3.22 - Vectors displayed after cross correlation

3.4.5.4 Validation

Validation of the vectors is performed using methods included in the Dynamic Studio software to increase the reliability of the results.

3.4.5.4.1 Range Validation

The first step towards validating the results is to validate the reported velocities, this is done by setting a maximum and minimum velocity that we expect all real vectors to fall between. Erroneous vectors are created by the tracking errors of particles where particles enter or leave the interrogation area so this method helps to reduce those errors.

3.4.5.4.2 Peak Validation

The second validation step is to validate the intensity of the signal; this is done to ensure that particles are correctly identified. If the signal intensity is not high enough the vector is discarded as it cannot be definitively proven to be a valid particle and maybe an optical artefact.

3.4.5.4.3 Moving Average Validation

The final step of validating the vectors using the PIV software is the Moving Average Validation, this method looks at the surrounding neighbours of each vector and compares it with the vector in question. If the vector is significantly different from its neighbours it is either eliminated or substituted with an average of its neighbours.

3.4.5.5 Exportation

Once the data has been validated it is exported as text files. Points of interest are explored using 'profiles'. Horizontal profiles are taken at various heights from the base of the tank. These profiles are used to determine the composition of the jet from the outlet and before impingement. Vertical profiles are taken along the jet centreline and outwards along the base of the tank, these profiles are used to characterise the expanding wall jet, which is formed after impingement.

3.4.5.6 Data Analysis

The text files are then imported into MATLAB for final analysis and presentation of the results. The mean value for each data point is calculated from the image sets. Once the mean is calculated it is used to find the standard deviation of each data point and any of the instantaneous velocities which fall outside two standard deviations are discarded. This is done to eliminate anomalous results.

Once the anomalous results are filtered out the new mean is found and the root mean square of the instantaneous velocities are calculated to give the intensity of the turbulent fluctuations in the U and V directions.

3.5 Particle Selection and Preparation

This section contains details on why the particles used in this study were chosen and the steps taken to prepare the particles for the experiments.

3.5.1 Particle Selection

Several criteria had to be fulfilled when selecting the solid phase particles used for the current study. To ensure the suitability of the particles it was essential to know the experimental regime to be examined and the variables being tested.

3.5.1.1 Particle Diameter

A significant objective of this research is based on the observation by Gore and Crowe, (1989), whose research showed the ratio of particle diameter to the length of the most energetic eddy can provide an estimate on whether a particle will increase or decrease the turbulent intensity of a fluid. If the ratio is above 0.1 it is predicted that the particles will enhance the turbulence, whereas a ratio below will dissipate turbulence. For this reason, solid particles were chosen with diameters which are predicted to either enhance or dissipate fluid turbulence.

$$\frac{d_p}{l_e} > 0.1 = \textit{Enhancement}$$

Equation 3.19 - Where d_p is the particle diameter and l_e is the characteristic length of the most energetic eddy Gore and Crowe, (1989).

$$\frac{d_p}{l_e} < 0.1 = \textit{Dissipation}$$

Equation 3.20 - Where d_p is the particle diameter and l_e is the characteristic length of the most energetic eddy Gore and Crowe, (1989).

The length of the most energetic eddies was calculated using the same procedure as Gore and Crowe, who used the work of Hutchinson et al., (1971) to show that a good approximation for the characteristic fluid length scale in a pipe was 0.2 R (pipe radius).

$$\frac{l_e}{R} \cong 0.2$$

Equation 3.21 - Where R is the pipe radius and l_e is the characteristic length of the most energetic eddy Hutchinson et al., (1971).

For jet flows Wygnanski and Fiedler, (1969) demonstrated that the turbulent length scale was dependant on the distance from the jet exit.

$$\frac{l_e}{x} \cong 0.039$$

Equation 3.22– Where x is the axial distance from the jet outlet and l_e is the characteristic length of the most energetic eddy Wygnanski and Fiedler, (1969).

A narrow size distribution of particles is preferred as it allows for greater confidence when stating that an effect is due to the size of the particle. However, the procurement of particles which have a very low degree of variance in diameter is prohibitively expensive. For this reason, a balance had to be obtained between the particle size distribution and cost.

An upper limit of the particle size was found due to the design of the impinging jet rig. A needle valve flow meter was used to measure and adjust the flow rate of the impinging jet which could block when using larger diameter particles. Due to this, the maximum particle size tested in this system was 225 μm .

3.5.1.2 Particle Shape

In keeping with the fact that it was important to have a limited range of particle sizes it was also important to ensure the particle shape was consistent. The easiest way to do this was to ensure the particles were spherical. Cubic and rod like particles were initially considered to test the

effect of shape on the flow, however available time prohibited this testing. Shape dependence would be an interesting follow on study and will be discussed further in the Future Work section.

3.5.1.3 Particle Density

Later work by Elghobashi, (1994) suggests that a more accurate way to predict whether a particle enhances or dissipates turbulence is the ratio of the particle response time to the Kolmogorov time scale. If this ratio is above 100 the particles enhance turbulence and conversely below this value the particles dissipate turbulence.

$$\frac{t_p}{t_K} > 100 = \textit{Enhancement}$$

Equation 3.23 – Enhancement of turbulence where t_p = particle response time and t_K = Kolmogorov time scale Elghobashi, (1994).

$$\frac{t_p}{t_K} < 100 = \textit{Dissipation}$$

Equation 3.24 – Dissipation of turbulence where t_p = particle response time and t_K = Kolmogorov time scale Elghobashi, (1994).

As shown in the following equation the particle response time is dependent on the ratio of particle density to fluid density as well as the particle diameter.

$$t_p = \frac{\rho_p d_p^2}{18\rho_f \nu}$$

Equation 3.25 – Particle response time (t_p), ρ_p is particle density, d_p is particle diameter, ρ_f is the fluid density and ν is the kinematic viscosity of the fluid.

To compare the two methods particles were required to have the same diameter and shape as the previously tested particles, but of different density. Particles were chosen to have a density almost equal to that of the fluid to contrast with the denser glass particles. Problems were encountered testing significantly denser particles due to the settling velocity and the ability to

source particles with similar diameters but varying densities to isolate density as the only changing variable.

3.5.2 Particle Preparation

For the current study particles were purchased from Guyson, who supply glass particles as a blast medium. As the tolerances on particle size distribution were not suitable the particles were sieved down to obtain a narrower range of particle diameters.

The sieves used were BS standard; with each mesh size, approximately 1.14 times the size of the previous one. Therefore, to sieve the Honite 12 and Flashbead particles, sieves with a mesh size of 212 μm and 250 μm were used; and to sieve the Honite 8 particles sieves of 500 μm and 600 μm mesh size were used. The Honite 22 particles were too fine for any of the available meshes and it was decided not to sieve these particles as the range of particle diameters in the raw product was deemed to be acceptable.

Particles were sieved a minimum of three times before being weighed and transferred into individual containers marking the mass and volume of particles. The particles were then washed with distilled water to remove any dust and impurities introduced during sieving. After cleaning the particles were mixed with Milli-Q water and stored until used in the measurement facility.

3.6 Error Analysis

As with all experiments there is some degree of error which cannot be eliminated altogether but can be minimized by carefully controlling factors that are considered a source of error. The measurement resolution of the equipment can have significant effects on the precision of the data, whereas slight misalignments and variations in the experimental set up can significantly impact the accuracy. The most likely sources of error and their potential to influence the accuracy of the data are given below. Error values less than 0.01% are considered negligible.

3.6.1 Analysis of possible errors for the UDV system.

3.6.1.1 *Alignment Error:*

For the UDV system, error may be introduced through misalignment of the UDV probe which would lead to a miscalculation of the axial velocity and distance from the probe. As the slot (holder) for the probe was previously machined into a support collar this position cannot change between runs. It is estimated that the collar was machined and measured within a tolerance of 1° , any deviation from this could have been corrected within the UDV software.

For a probe angle of 135° this means that the true angle would have been between 134.5° and 135.5° . Such variance gives a maximum velocity error for misalignment of the probe to be 0.87%, as the contribution from misalignment would cause a component of the velocity to be misattributed.

3.6.1.2 Beam Divergence:

As the UDV probe emits a pulse it unavoidably diverges with increasing distance from the probe leading to increased measurement error. This causes a radial band of fluid to be measured instead of a singular point. The thickness of this band depends on the divergence angle of the beam, for simplification the chord length is approximated to be equal to the arc length and so the uncertainty due to beam divergence can be calculated from Equation 3.26.

$$\varepsilon_b = y\omega_b * \sin \omega_b$$

Equation 3.26 – Calculation of uncertainty due to beam divergence ε_b , where y = distance from probe and ω_b = beam divergence angle.

For a given beam divergence angle of 4.33°, the error varies linearly across the pipe from 0 at the probe surface to 0.57% at the pipe wall opposite the probe.

3.6.1.3 Variation in flow velocity:

Variations in flow velocity are dependent on the ability of the pump to maintain a constant output with a constant input. The input frequency could be varied within 0.1 Hz over 50 Hz giving an input accuracy of 0.2%. This was verified against a flow meter with a resolution of 0.01 m.s⁻¹. The bulk flow velocity was maintained within ± 0.015 m.s⁻¹ of the mean fluid velocity of 0.95 m.s⁻¹ giving a maximum error of 1.58%.

3.6.1.4 Temperature Variation:

It is vital to ensure the temperature of the fluid does not drift excessively over the course of the experiment as this leads to variations in the fluid speed of sound. UDV calculates both the distance to the measurement point and the particle velocity using the sound velocity of the fluid

and so variation in this value can lead to significant errors. Lubbers and Graaff., (1998) propose a simple formula (Equation 3.27) for calculating the speed of sound within a fluid within the range of 15-35 °C, which perfectly encapsulates the range of temperatures experienced in this study.

$$c = 1404.3 + 4.7T - 0.04T^2$$

Equation 3.27 – Speed of sound c , in $m.s^{-1}$ with regards to temperature T in °C

The temperature of the fluid is dependent on the outlet temperature of the fluid from the laboratory tap, the temperature of the surrounding atmosphere and heat transfer from the pump and mixer. The experimental results were obtained in a matter of minutes and so fluid heating from the pump and mixer were minimal. After filling the tank, the fluid was cycled through the loop several times to ensure that no unwanted particles (dirt and air bubbles) remained in the system. During this process, the fluid would gradually reach atmospheric temperature, therefore the temperature within the laboratory should be considered. Again, as the measurement time was short the variation in temperature between different measurements (particle concentration) would be minimal. All measurements presented in the thesis were taken within a limited time period, making variations in atmospheric temperature minimal. Successive measurements of the laboratory air temperature showed less than 2°C variation at the same time each day.

At 20°C this gives a speed of sound of $1482.3 \pm 3.14 \text{ m s}^{-1}$ or an error of 0.21%.

3.6.2 Analysis of possible errors for the PIV Systems.

Like the UDV measurements there exists unavoidable sources of error when collecting PIV data. Some of these sources of error remain the same between the two systems (pipe loop and impinging jet), as similar equipment was used and particles investigated were from the same batch. The differences are mainly due to the implementation of the measurement technique.

3.6.2.1 Alignment Error:

For both the pipe loop and impinging jet systems proper alignment of the camera and laser systems was vital to ensure accurate measurement. In addition, it was vital that the test section of the pipe was perfectly horizontal and the impinging jet was perpendicular to the tank base. Errors due to alignment will result in miscalculation of velocity vectors as the velocity components will be at an angle proportional to the misalignment.

Alignment was performed using the PIV camera and different reference points (Engineer Square, edge of test section), with deviations from the desired direction measured in pixels and corrected. This ensures the camera is aligned to the test section with an accuracy of 1 pixel per 1600 pixels giving a maximum angular disparity of 0.11° .

The impinging jet required additional alignment to ensure the jet was both perpendicular to the tank base and was vertical in the captured images. This was not aligned using the entire frame and so was aligned to within 1 pixel over 700 pixels giving a maximum angular disparity of 0.26° .

Alignment of the laser along the pipe centreline was performed using centreline markings on either end of the test section and so alignment accuracy was within 0.25 mm over 400 mm giving a maximum angular disparity of 0.11°.

Alignment of the laser along the jet centreline was achieved by projecting the laser onto an angled plane, multiplying any difference in position between the top and bottom of the jet. This allowed for more precise positioning. The measured difference between the top and bottom of the light sheet was 24 pixels over 660 pixels, with this distance magnified by 23x due to the angle of the plane. This results in an in-plane displacement of 0.96 pixels over 660 pixels giving a maximum angular disparity of 0.26°.

The combined effect of these errors on the axial and radial components of the flow are calculated using standard trigonometric functions and are summarized in Table 3.3.

Table 3.3 – Errors associated with misalignments in PIV.

Maximum Error	Pipe Flow		Impinging Jet Flow	
	Axial	Radial	Axial	Radial
Camera	Negligible	0.06%	Negligible	0.06%
Test Section	Negligible	0.06%	Negligible	0.14%
Laser	Negligible	0.06%	Negligible	0.15%
Total Error	Negligible	0.18%	Negligible	0.35%

Misalignment of the equipment has a much greater effect on the radial component of the flow, and due to the larger relative distances from which the camera and flow systems were aligned the error has been reduced to the condition where the effects are negligible in comparison to other factors.

3.6.2.2 Processing and Resolution Error

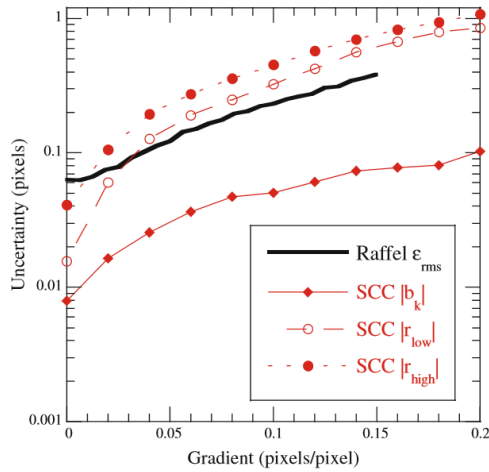


Figure 3.23– Uncertainty with regards to gradient, where b_k is the systematic uncertainty value and r_{low} and r_{high} are the lower and upper bounds in which 95% of the data is contained. Timmins et al (2012).

Due to the limitations of the equipment the number of interrogation areas in the region of interest was limited. This results in a limited number of vectors leading to unavoidable spatial averaging as seen by the spatial averaging in the UDV measurements. This effect is most pronounced in regions of high shear and high velocity gradients. The problem is somewhat mitigated in the pipe flow as the region with the highest velocity gradients is at

the wall and measurements in this region could not be made due to optical distortion. However, the impinging jet flow has multiple locations with large velocity gradients.

For the pipe flow the region of highest velocity gradient is close to the pipe wall and was calculated to be 0.01 pixels per pixel. Using the work of Timmins et al., (2012), as shown in Figure 3.23, which shows how the measurement uncertainty increases as the velocity gradient increases we estimate the uncertainty in the measurement to be around 0.025 pixels, which corresponds to a fluid velocity of $0.012 \text{ m}\cdot\text{s}^{-1}$. Across the wall region this corresponds to a measurement uncertainty of between 9.23% at the pipe wall and 1.82% at the transition to the bulk flow region.

The same calculation was performed for the impinging jet using the transition from the edge of the jet 1D from the outlet, to the surrounding fluid. Here we have a velocity change of $3.6 \text{ m}\cdot\text{s}^{-1}$

over 4 interrogation areas which gives a pixel velocity gradient of 0.09 pixels per pixel. Again, using Figure 3.23 we can see this corresponds to an uncertainty of 0.25 pixels and a velocity uncertainty of 0.15 m.s⁻¹. This gives a maximum possible error of 16.67% for the axial velocity of the jet and a possible 3.33% error for the fluid at the edge of the potential core.

Additional measurement uncertainty comes from the particle image diameter. This is calculated from Equations 3.12 to 3.15 which combine to form Equation 3.28.

$$d_{pt} = \sqrt{(M^2)d_p^2 + (2.44F^\#(M + 1)\lambda)^2}$$

Equation 3.28 – Calculation of Image Diameter d_{pt} where M = magnification, d_p = particle diameter, λ = wavelength of light and $F^\#$ = F Number

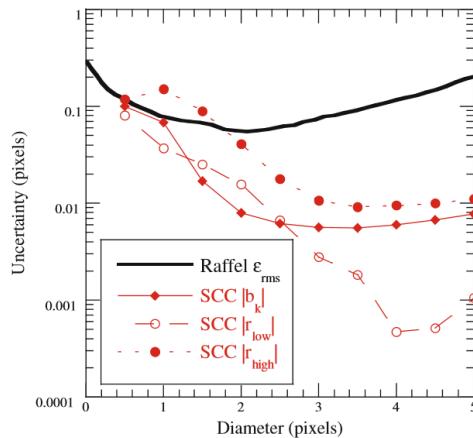


Figure 3.24 – Uncertainty with regards to particle image diameter, where b_k is the systematic uncertainty value and r_{low} and r_{high} are the lower and upper bounds in which 95% of the data is contained. Timmins et al (2012).

For a magnification of 0.25, a particle diameter of 20 μ m, F number of 16 and light wavelength of 532 nm, the image diameter is 26 μ m, which corresponds to 3.3 pixels. This is the same for both the pipe flow and impinging jet. Using the results of Timmins et al. (2012) in Figure 3.24 we determine a measurement uncertainty of 0.005 pixels, thus an error uncertainty between 0.25% and 3% for the pipe flow measurements and between 0.06% and 3% for

the impinging jet, with the uncertainty lowest in high velocity regions.

3.6.2.3 *Variation in flow velocity*

The variation in flow velocity for the PIV pipe loop was the same as for the UDV system, with the fluid velocity controlled to within $0.015 \text{ m}\cdot\text{s}^{-1}$ with a mean fluid velocity of $1.05 \text{ m}\cdot\text{s}^{-1}$. This gives a maximum flow velocity uncertainty of 1.43%.

For the impinging jet the flow rate was controlled with a series of valves used to restrict the flow, and measured using a rotameter. As the accuracy of the rotameter was limited (0.1 Litres per minute) it was decided that the pump would remain running and new single phase measurement would be made at the start of each experiment to form the baseline case, thus reducing the error to that caused by the variation in pump speed. Multiple single phase data sets were collected and the centreline velocity examined without changing the valve or pump settings. This gave a steady state pump velocity variation of 0.28%.

3.6.3 Summary of Errors.

Both UDV and PIV systems require precise alignment of measurement equipment as error due to misalignment can be significant but avoidable, through following proper procedures. This is especially apparent in the PIV measurements where uncertainty in the axial measurements due to misalignment has been negligible. A common unavoidable error between the systems is down to the ability of the pump to maintain a constant flow velocity and the inline flow measurement equipment which was used to ensure that the flow rate was the same between runs. The only way to further significantly reduce this error involves large capital expenditure on higher quality pumps and flow meters.

UDV also has errors associated with temperature and beam divergence which are not present in the PIV system, which instead is influenced more by optical errors such as particle image diameters.

All reasonable steps were taken to minimise errors within the measurement systems and as such did not have a significant influence on the results. This allows for the results to be presented with confidence that the results accurately reflect the systems studied and the observed differences between the systems are a real effect of the particle loading.

3.7 References

- Cooper, D., Jackson, D.C., Launder, B.E. and Liao, G.X. (1993). Impinging jet studies for turbulence model assessment -- I. Flow-field experiments. *Int. J. Heat Mass Transfer*. **36**(10),pp.2675–2684.
- Dantec Dynamics (2017). Particle Image Velocimetry measurement principles. [Accessed 21 September 2017]. Available from: <https://www.dantecdynamics.com/measurement-principles-of-piv>.
- Elghobashi, S. (1994). On predicting particle-laden turbulent flows. *Applied Scientific Research*. **52**,pp.309–329.
- Gore, R. and Crowe, C. (1989). Effect of particle size on modulating turbulent intensity. *International Journal of Multiphase Flow*. **15**(2),pp.279–285.
- Hutchinson, P., Hewitt, G. and Dukler, A.E. (1971). Deposition of liquid or solid suspension from turbulent gas streams: a stochastic model. *Chemical Engineering Science*. **26**,pp.419–439.
- Keane, R.D. and Adrian, R.J. (1992). Theory of cross-correlation analysis of PIV images RICHARD D. KEANE & RONALD J. ADRIAN. *Applied Scientific Research*. **49**,pp.191–215.
- Lubbers, J. and Graaff, R. (1998). A simple and accurate formula for the sound velocity in water. *Ultrasound in medicine & biology*. **24**(7),pp.1065–8.
- Melling, A. (1997). Tracer particles and seeding for particle image velocimetry. *Measurement Science and Technology*. **8**(12),pp.1406–1416.
- Poelma, C., Westerweel, J. and Ooms, G. (2006). Turbulence statistics from optical whole-field measurements in particle-laden turbulence. *Experiments in Fluids*. **40**(3),pp.347–363.
- Samimy, M. and Lele, S.K. (1991). Motion of particles with inertia in a compressible free shear layer. *Physics of Fluids A*. **3**(8),pp.1915–1923.
- Shames, I.. (2003). *Mechanics of Fluids*. New York, McGraw-Hill.
- Timmins, B.H., Wilson, B.W., Smith, B.L. and Vlachos, P.P. (2012). A method for automatic estimation of instantaneous local uncertainty in particle image velocimetry measurements. *Experiments in Fluids*. **53**(4),pp.1133–1147.
- Westerweel, J. (1993). Digital particle image velocimetry: theory and application.
- Westerweel, J. (1997). Fundamentals of digital particle image velocimetry. *Measurement Science and Technology*. **8**(12),pp.1379–1392.
- Westerweel, J., Elsinga, G.E. and Adrian, R.J. (2013). Particle Image Velocimetry for Complex and Turbulent Flows. *Annual Review of Fluid Mechanics*. **45**(1),pp.409–436.
- Wynanski, I. and Fiedler, H. (1969). Some measurements in the self preserving jet. *Journal of Fluid Mechanics*. **38**(3),pp.577–612.
- Zagarola, M. V. and Smits, A.J. (1998). Mean-flow scaling of turbulent pipe flow. *Journal of Fluid Mechanics*. **373**,pp.33–79.

4 Acoustic Measurements of Multiphase Pipe Flows

This chapter will examine the use of Ultrasonic Doppler Velocimetry to measure fluid and particle behaviour in a pipe flow system. Section 4.1 contains single phase measurements of the pipe compared with results published by other authors. Section 4.2 then introduces particles into the system and explores measuring both mean and fluctuating particle velocities, comparing them against the single phase measurements. Section 4.3 explores how particles of differing densities behave within the flow and respond to increases in concentration. Section 4.4 looks at how particle size effects behaviour within the system and Section 4.5 contains the chapter summary and conclusions. Finally sources referenced in the chapter are contained in Section 4.6.

4.1 Single Phase Pipe Flow Measurements

In order to ensure the reliability of results it is important to obtain an accurate baseline for measurements, this section contains single phase measurements of the flow and compares them with results found in the literature to ensure confidence in further results. The basic coordinate system used throughout this chapter is shown in Figure 4.1.

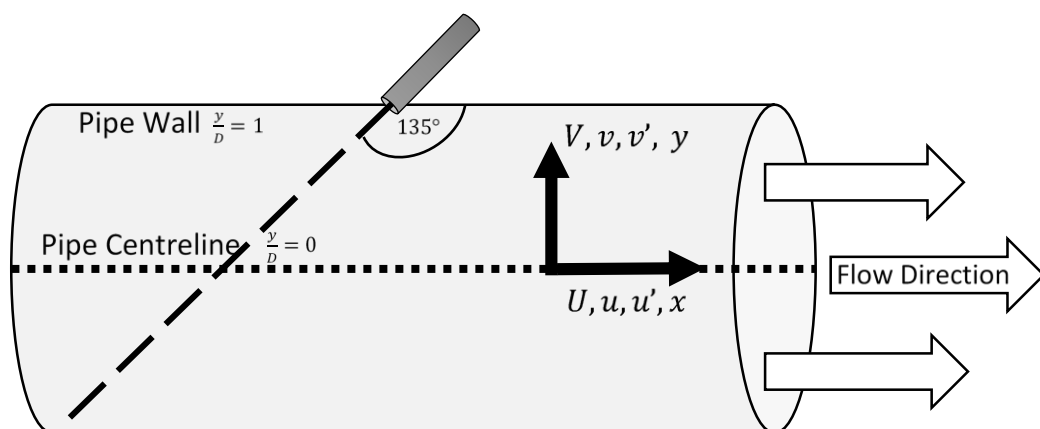


Figure 4.1 – Diagram showing the location of the ultrasonic probe in relation to the pipe, in addition to the coordinate system used.

Single phase measurements were taken of the pipe at a Reynolds number of 40,000, with measurements taken horizontally across the pipe to eliminate the effects of gravity on the measurement volume. The pipe had an internal diameter of 42.6 mm and external diameter of 50 mm. The mean fluid velocity across the pipe was $0.95 \text{ m}\cdot\text{s}^{-1}$ which corresponds to a volumetric flow rate of $1.35 \text{ L}\cdot\text{s}^{-1}$ causing the entire feed tank to be completely recycled every minute ensuring the flow remained homogenous. Measurements were taken using a 2 MHz Imasonic ultrasonic probe and processed using a Met-Flow UVP-DUO Doppler velocimeter. The experimental facility and method were previously discussed in the experimental methods chapter, thus the readers are referred to Chapter 3 for a more detailed explanation of the technique and equipment used.

4.1.1 Axial Velocities

To ensure confidence in the results the measurements from the acoustic probe were compared with DNS predictions of Wu and Moin, (2008) and are displayed in Figure 4.2.

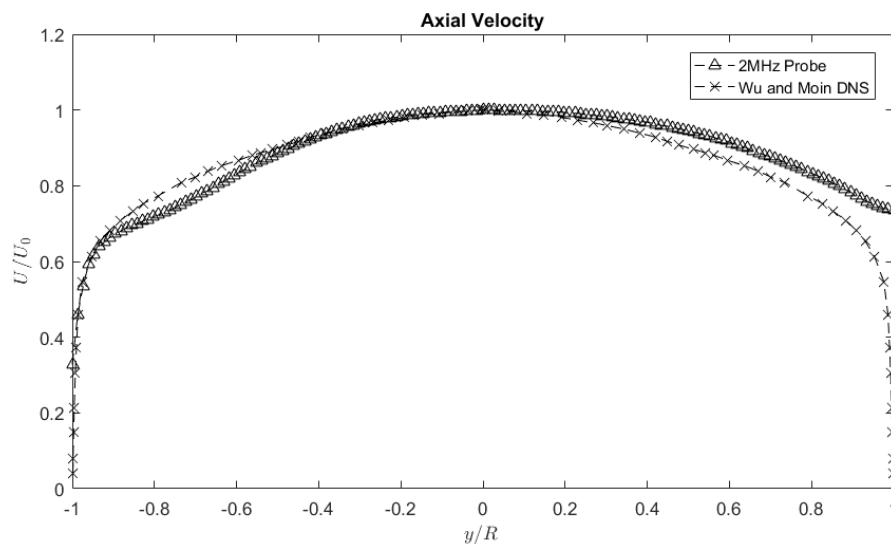


Figure 4.2 – Comparison between acoustic results and the DNS predictions of Wu and Moin, (2008)

As can be seen the acoustic results show a reasonable agreement with the DNS measurements, especially in the central region of the flow ($y/R = 0$). There is a slight deviation in the region of $y/R = -0.8$, this is believed to be the result of a flow disturbance caused by the presence of the acoustic probe. As the probe location was intrusive a small flow disturbance was unavoidable, the effect could be minimised by further inserting the probe however this would result in problems in obtaining results near to the wall as the minimum measurement distance discussed in Chapter 3 would not be met.

Beyond the centreline of the pipe the acoustic results begin to diverge from the DNS results ($y/R = 0.2$), this is due to a slight asymmetry in the results obtained, however this asymmetry was present in all the acoustic measurements and so comparison of the results remains valid when discussing differences within a data set. As the far wall ($y/R = 1$) is approached the velocity profile begins to curve upwards instead of rapidly decreasing to 0. This is due to reflections from the pipe wall and the fact that measurements at this distance from the probe are unreliable as it exceeds the maximum measuring distance as calculated using the Nyquist sampling theorem discussed in Chapter 3.

We were unable to resolve measurements within the viscous sublayer as the resolution of the acoustic probes was not great enough. The absolute width of the viscous sublayer was calculated to be $101.2 \mu\text{m}$ (i.e. $y^+ = 5$), whereas the maximum resolution of the probe was $370 \mu\text{m}$ between measurement locations. As a result, it is not possible to directly measure the velocity gradient in order to obtain the value for friction velocity using the following expression given by Laufer, (1954).

$$U_{\tau}^2 = -v \left(\frac{\partial U}{\partial y} \right)_{wall}$$

Equation 4.1 – Friction velocity where $\frac{\delta \bar{U}}{\delta r}$ = the gradient of the mean axial velocity, U , with respect to the radial distance, y , from the pipe centreline and v = kinematic viscosity.

Instead the method outlined by Roberson and Crowe, (1996) is used to estimate the friction velocity. With a pipe diameter of 42.6 mm, roughness of 0.0025 mm at a Reynolds number of 40,000. Equation 4.2 can be used to calculate the friction factor f giving a value of 0.0219.

$$f = \frac{0.308642}{\left[\log \left(\left(\frac{e_r}{3.7D} \right)^{1.11} + \frac{6.9}{Re} \right) \right]^2}$$

Equation 4.2 - Calculation of the friction factor where e_r = wall roughness, D = pipe diameter and Re = Reynolds number.

Using Equations 4.3 and 4.4 as stated in Chapter 2 the values for wall shear stress and friction velocity were calculated to be $2.4415 \text{ kg}\cdot\text{m}^{-1}\cdot\text{s}^{-2}$ and $0.0494 \text{ m}\cdot\text{s}^{-1}$ respectively. These values were used to convert the acoustic measurements into wall units.

$$\tau_w = \frac{f\rho U^2}{8}$$

Equation 4.3 – Wall shear stress (τ_w), from friction factor (f) density (ρ) and velocity (U^2)

$$U_\tau^2 = \frac{\tau_w}{\rho}$$

Equation 4.4 – Friction velocity from wall shear stress (τ_w), and density (ρ).

The results of using this scaling technique can be seen in Figure 4.3 where the axial velocity and distance from the wall have been converted into wall units. As previously stated no measurements exist within the viscous sublayer due to the limitations of the measurement equipment. The log-law region shows a reasonable agreement with the von Karman model when coefficients of 0.435 and 4.32 are used for k and C , respectively. Both of these values are valid within the range of results examined by Marusic et al., (2013). However, the effects of the probe can be seen in the underestimation of the axial velocity.

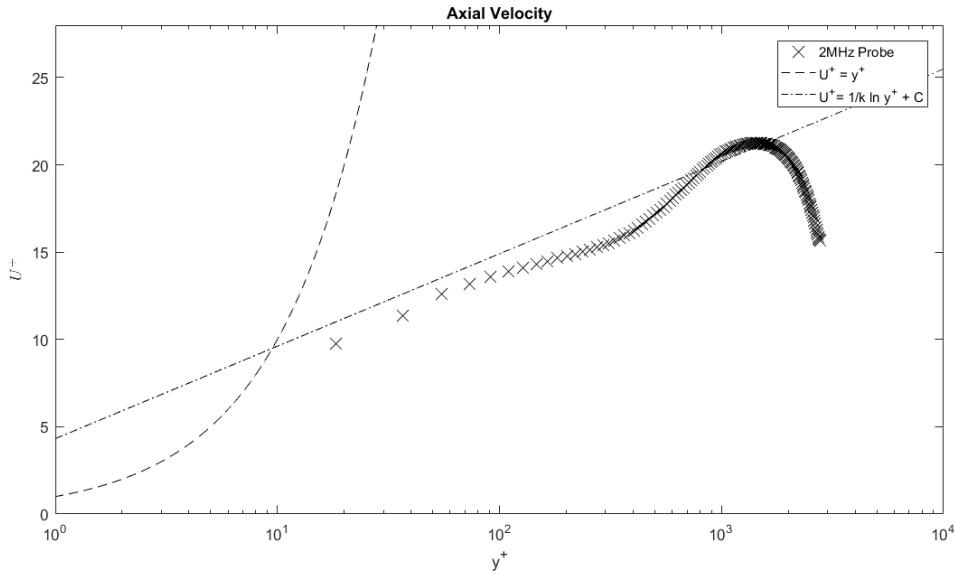


Figure 4.3 – Axial velocity in wall units with log law equation overlay.

4.1.2 Turbulence Statistics

One acoustic probe was used in the experimental set up, thus it was only possible to obtain turbulence statistics in the axial direction. As explained in Chapter 3 a Reynolds decomposition was performed to obtain the fluctuating velocities, which represent the turbulence in the system. Figure 4.4 displays the measurements obtained from the acoustic probe compared with hot wire anemometry results of Laufer, (1954) at a Reynolds number of 50,000. Both sets of results have been normalised by dividing the RMS values by the friction velocity. As previously mentioned, due to the maximum measurement distance of the probe and the effect of wall reflections it was not possible to obtain measurements at the far wall of the pipe and as such the turbulence statistics here are irrelevant. At the near wall, peak turbulence levels are in good agreement with Laufer, (1954) with regards to distance from the wall, however the magnitude is around 30% greater. Between $-0.6 y/R$ and $0 y/R$ the difference between the values of Laufer, (1954) and the acoustic measurements is around 30% , possibly due to a difference in the friction velocity used. Between $-0.9y/R$ and

$-0.6y/R$ the acoustic results underestimate the turbulence when compared with hot wire anemometry, however this is the same region where the velocity results are underestimated when compared with DNS, and so this underestimation is probably due to the flow disturbance caused by the presence of the acoustic probes. Beyond the pipe centreline the results begin to diverge in a similar manner to the velocity results suggesting an unreliability in measurement with an increase in distance. This can be attributed to beam divergence as discussed in Chapter 3.

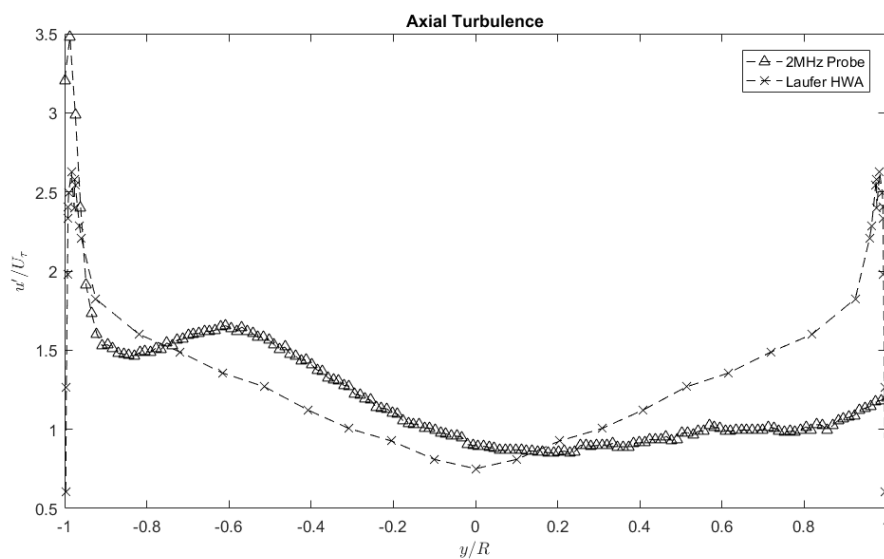


Figure 4.4 – Comparison of UDV axial turbulence measurements with those of Laufer, (1954)

From the single phase measurements it can be seen that it is possible to obtain both velocity and turbulence statistics using ultrasonic Doppler velocimetry, although caution must be taken with regards to the measurement volume due to maximum measurement distances, beam divergence and wall reflections. It should be noted that particles must be present within the system for a signal (signal to noise) to be obtained.

However, no particles were added to the system, the only particles present were naturally occurring as part of the tap water used to fill the loop and so it is possible that some discrepancies were due to a lack of particles.

Higher quality single phase results could potentially be obtained through the use of tracer particles known to accurately follow the flow. It was decided not to introduce such particles into the system due to the difficulty in trying to differentiate them from the solid phase added to the system for the multiphase experiments.

There is of course the possibility of errors arising in the following experiments due to these natural tracers which can be mistaken for the solids we wish to track, however it is believed the relative concentrations of the naturally occurring particles and the test particles to be great enough to minimise this risk. However this should be considered when drawing conclusions from the results. Alternatively, filtered and purified water could be used which would yield greater accuracy, however this would be prohibitively expensive for such a system.

4.2 Changes in Particle Behaviour with Concentration

The effect of solid particles on both the mean velocity and axial turbulence were explored by adding Honite 12 glass particles (Table 4.1) to the flow loop while in operation. Once the particles had been added, the system was left to circulate ensuring that the system was well mixed and homogeneous before any measurements were taken. In this time the readings of

Table 4.1 – Honite 12 particle properties.

Honite 12	
Particle Diameter (μm)	225
Particle Density (kg m^{-3})	2450
Particle Material	Silica Glass
Particle Settling Velocity (m s^{-1})	39.92×10^{-3}
Particle Response Time (ms)	6.9

the flow meter were checked to ensure the loop was operating at the correct flow rate. In order to explore a wide range of particle volume fractions in a limited time the mass of particles was doubled with each subsequent run giving a range of volume fractions from 1×10^{-4} to 64×10^{-4} . This range was chosen as it crossed the boundary between dilute

and dense suspensions, (Elghobashi, 1994) where particle-particle interactions begin to become relevant as opposed to just particle–fluid interactions seen in dilute suspensions.

The mass of particles at each volume fraction is given in Table 4.2 when using the flow loop system with a total volume of 40 L.

Table 4.2 – Mass of Honite particles for a given volume fraction.

Run #	Volume Fraction	Particle Mass (g)	Run #	Volume Fraction	Particle Mass (g)
1	0	0	5	8×10^{-4}	117.6
2	1×10^{-4}	14.7	6	16×10^{-4}	235.2
3	2×10^{-4}	29.4	7	32×10^{-4}	470.4
4	4×10^{-4}	58.8	8	64×10^{-4}	940.8

4.2.1 Change in Axial Velocity with Particle Concentration

Figure 4.5 shows the combined velocity profiles for all experimental runs. Since the magnitude of the change is very small across the majority of the pipe it is difficult to observe any meaningful differences. However, it does display consistency in the measurement technique as the shape of the profiles remains almost constant giving confidence that any changes are real effects and not artefacts of the measurement technique.

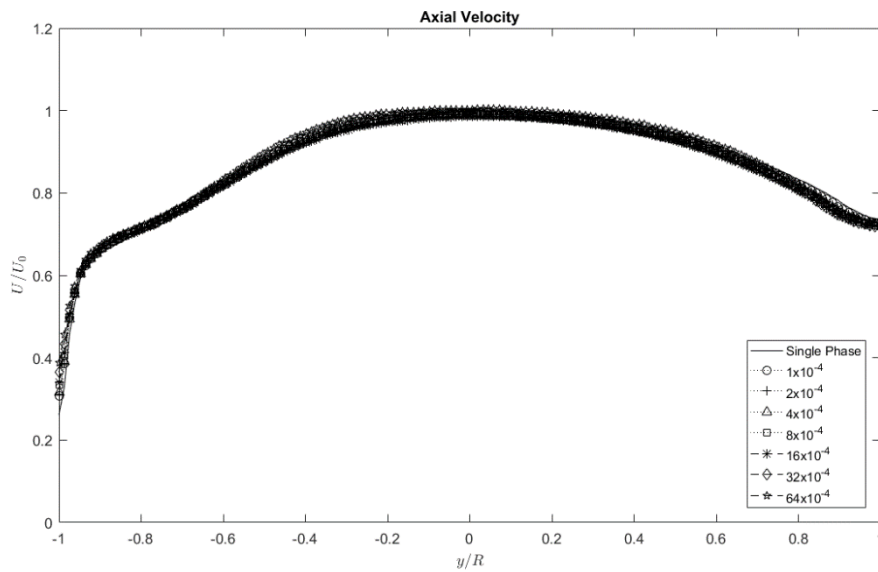


Figure 4.5 – Change in axial velocity with increase in particle volume fraction of Honite 12 particles.

Figure 4.6 shows the same data as Figure 4.5 replotted in wall units. From Figure 4.6 we can see that the introduction of particles has led to an increase in the axial velocity close to the wall, with the velocity increase corresponding to the particle concentration. The increase in particle concentration also causes the profile to more closely approximate the log-law region found in literature (Toonder and Nieuwstadt, (1997); Marusic et al., (2013)), although there is still a slight underestimation, see previous discussions.

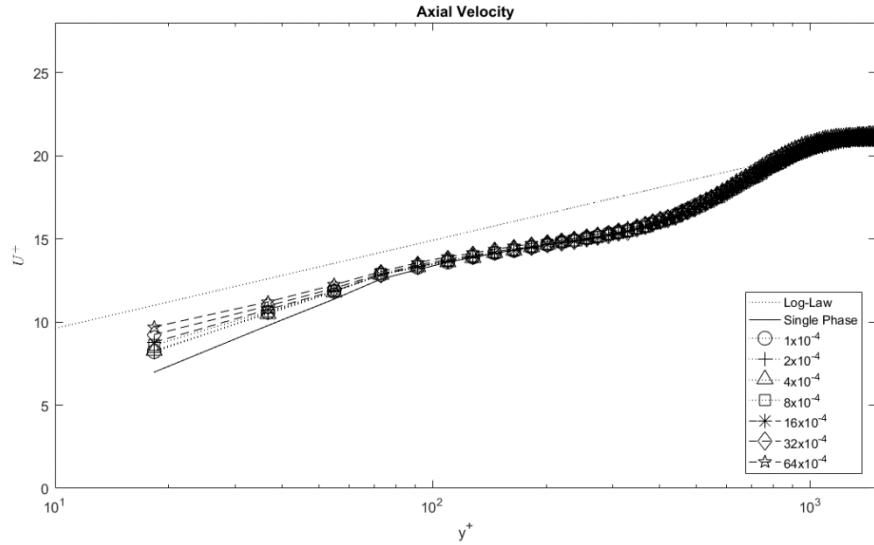


Figure 4.6 – Change in axial velocity with increase in particle volume fraction of Honite 12 particles plotted in wall units.

In order to quantify the magnitude of the change in velocity the percentage difference between the single phase measurements and the multi-phase measurements have been calculated using Equation 4.5 and plotted in Figures 4.7 and 4.8.

$$\% \text{ Change} = 100 * \frac{\overline{\phi U} - \overline{\phi_0 U}}{\overline{\phi_0 U}}$$

Equation 4.5 – Percentage change in velocity where $\overline{\phi U}$ = axial velocity at particle volume fraction ϕ , and $\overline{\phi_0 U}$ = axial velocity for the single phase flow.

Wall units have been used to scale the pipe diameter. Although the wall region only comprises a small portion of the pipe it is where significant changes in the flow occur and so this region has been extracted for separate analysis. The near wall region $y^+ < 300$ extends from the pipe wall to the approximate edge of the log-law region, and the turbulent core $300 < y^+ < 1400$ extends from the edge of the near wall region to the pipe centreline. From this we can see that even at the lowest particle concentration ($\phi = 1 \times 10^{-4}$) a significant effect in the near wall region is observed increasing the particle velocity up to 17.5%. Increasing the particle volume fraction results in an increase in the velocity enhancement with the highest

particle concentration tested ($\varphi = 64 \times 10^{-4}$) increasing the measured particle velocity up to 48%. As the centre of the pipe is approached the effect of the particles on the velocity becomes almost negligible with a significant increase in particle concentration having a minimal effect as the velocity changes become less than 2% compared with up to 50% at the wall.

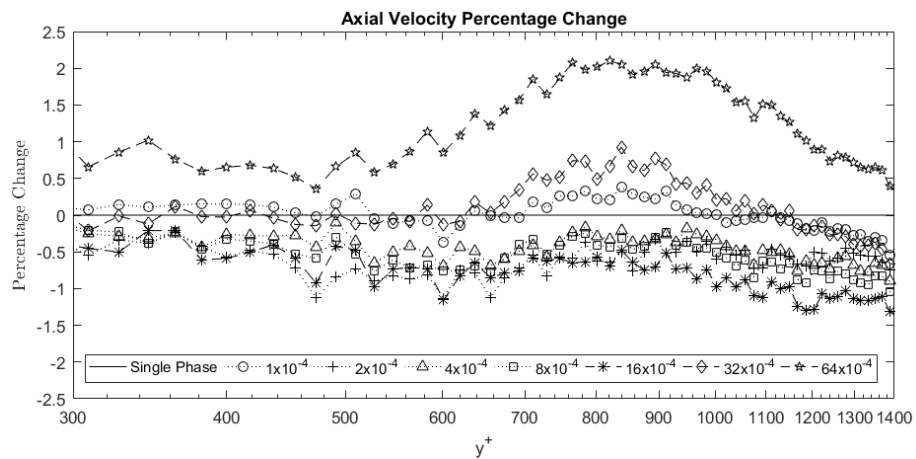
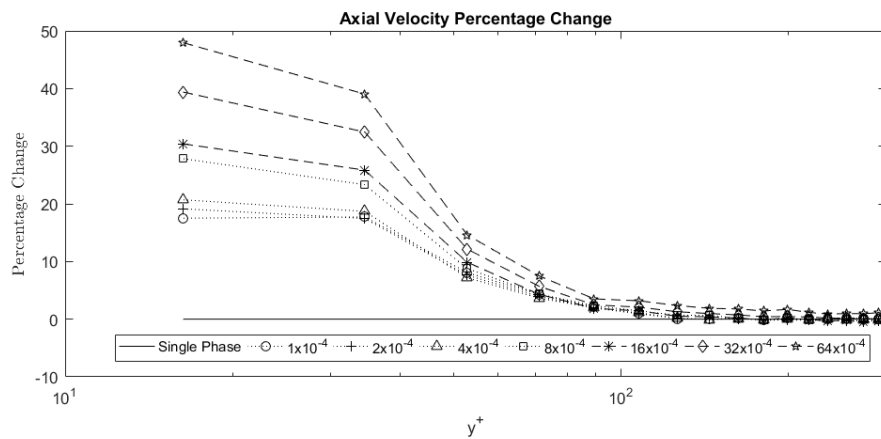


Figure 4.7 (top) – Axial velocity percentage change with increased Honite 12 particle loading in the near wall region.

Figure 4.8 (bottom) – Axial velocity percentage change with increased Honite 12 particle loading in the bulk flow region.

4.2.2 Change in Axial Turbulence with Concentration

Figure 4.9 shows the axial particle RMS measurements across the range of particle concentrations tested. Like the single phase results these measurements have been scaled with respect to the friction velocity. As with the velocity profile, the turbulence profile remains fairly constant as the particle concentration is increased. At the near wall it can be seen that there is a reduction in turbulence as particle concentration is increased, this can be seen more clearly in Figures 4.10 and 4.11 where the pipe has been split into the two regions and the percentage difference from the single phase measurements calculated in the same way as for the velocity changes.

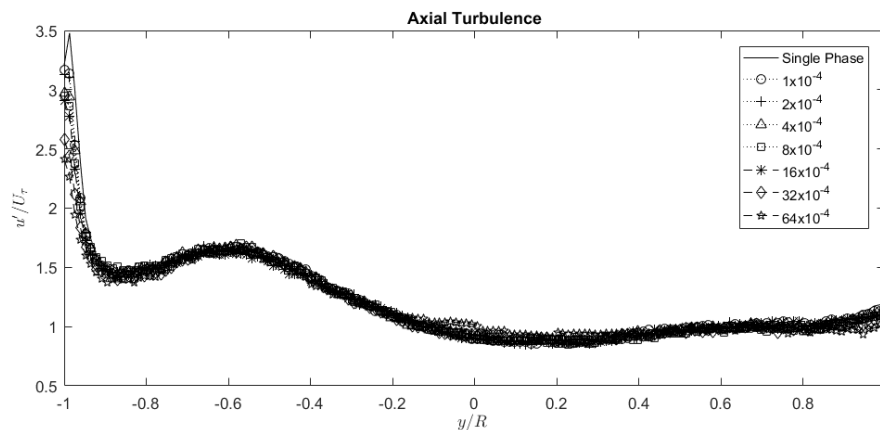


Figure 4.9 – Change in axial velocity fluctuations with increase in particle volume fraction of Honite 12.

We can see that in the near wall region an increase in particle concentration results in a significant decrease in axial turbulence. Increasing the particle volume fraction (ϕ) to 64×10^{-4} resulted in a maximum turbulence reduction of 35% and an average reduction in the wall region of 13.5%. No clear trends were observed in the turbulent core, although the deviations from the single phase values were greater than the deviations in the velocity measurements. Significant fluctuations in the percentage change for the velocity fluctuations ($\pm 5\%$) can be seen in Figure 4.11. These fluctuations about the mean result in

the mean value for turbulence modulation across the entire region to be between 1.5% and -1.5% for all particle volume fractions.

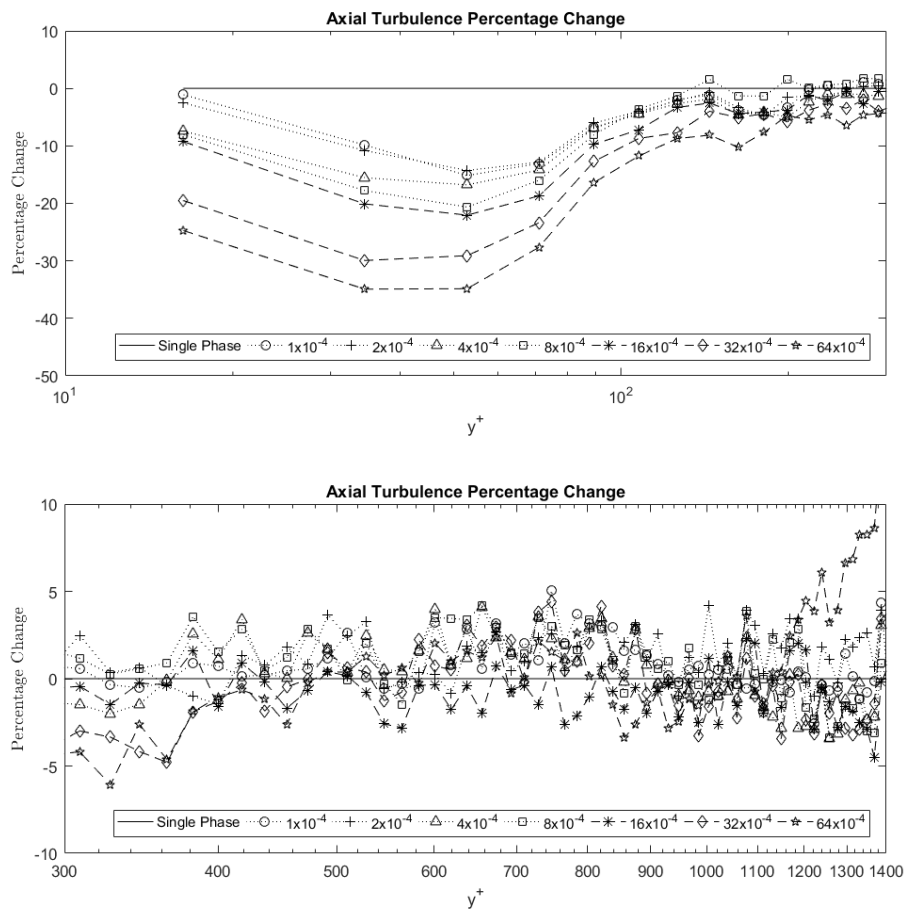


Figure 4.10 (top) – Axial turbulence percentage change with increased Honite 12 particle loading in the near wall region.

Figure 4.11 (bottom) – Axial turbulence percentage change with increased Honite 12 particle loading in the bulk flow region.

4.2.3 Discussion of Changes in Particle Behaviour with Concentration

Varying the particle concentration of Honite 12 within the pipe loop has a significant effect on both the velocity and the fluctuating velocity of the particles within the system. This effect is most pronounced in the near wall region where an increase in velocity coincides with a reduction in fluctuations.

Alajbegović et al., (1994) observed a similar increase in particle velocity near the wall and reduction at the pipe centreline. The decrease at the pipe centreline was attributed to

negative buoyancy of ceramic particles in the upward flow, whereas at the pipe wall the effect was caused by the particles being large enough to be influenced by the higher velocity fluid further from the wall, having the result of particles moving faster than the flow. A contrasting theory is proposed by Kulick et al., (1994) who observed flatter velocity profiles for the particles compared with the single phase measurements. This was coupled with increased particle velocity at the wall as shown in the current study. The authors suggest that this behaviour is due to motion of particles perpendicular to the flow allowing particles to cross streamlines and rebound from the channel walls, this would result in the measured particle velocity being larger than the local fluid velocity. Unlike Alajbegović et al., (1994) and the current study, Kulick et al., (1994) examined a gas-solid system, so movement of particles perpendicular to the flow would experience less hindrance due to drag.

The authors also observed that increasing particle concentration resulted in a reduction in particle velocities away from the wall, however these measurements considered much higher particle concentrations than tested in the current study and the variations were small for the glass particles. With regards to turbulence the glass particle velocity fluctuations were almost the same as the fluid turbulence intensity and increasing the particle concentration had almost no effect on the fluid turbulence, whereas the fluctuations of denser copper particles were greater than the fluid turbulence and increased with mass loading in the outer wall region but decreased in the inner wall region.

Varaksin et al., (2000) used a pipe system to examine three volume fractions closer to those used in the current study, however as a gas-solid system was used the mass loading is much greater and so direct comparisons are difficult especially when considering particle drag and inertia. However, it is useful for comparing effects such as particle-particle interactions due to similar particle numbers. The authors observed the particles moving more rapidly than the carrier phase across the entire pipe, although in their system the flow was travelling

downwards and so gravitational effects would influence the particle behaviour. The velocity increase in the near wall region at the highest particle concentration was less due to momentum loss through particle-particle, particle-wall interactions, and increased momentum exchange between the phases. This is not observed in the current study and most likely results from the relative difference in momentum being much greater in the gas-solid system as the density ratio between the glass particles and fluid is several orders of magnitude smaller.

The mechanisms for particle fluctuating velocities can be considered as four distinct processes:

- Particle velocity fluctuations due to the fluctuating motion by turbulent eddies of the fluid phase.
- Appearance of fluctuations caused by the use of polydisperse particles, which have slightly different velocities, this creates the appearance of velocity fluctuations.
- Variation of particle velocity due to particle-particle and particle-wall interactions.
- Migration of particles across regions of shear when time averaged.

They identify particle entrainment by turbulent air eddies and errors caused by polydispersity as the main mechanisms effecting the particle velocity fluctuations in their flow. They found the particles were able to take up energy from large scale turbulent motions and so reduce turbulence in the carrier phase. As particle concentration was increased more energy could be sapped from the carrier phase and this dampening of fluid turbulence causes a decrease in the particle velocity fluctuations caused by their interaction with the turbulent eddies. At higher concentrations they also note particle-particle collisions have the effect of normalising velocities as momentum is transferred between particles.

4.3 Changes in Particle Behaviour with Density

Table 4.3 - Flashbead particle properties.

Flashbead	
Particle Diameter (μm)	225
Particle Density (kg m^{-3})	1050
Particle Material	Styrene Divinylbenzene Copolymer
Particle Settling Velocity (m s^{-1})	1.37×10^{-3}
Particle Response Time (ms)	2.9

In Section 4.2 we explored how a change in particle concentration can change the velocity and turbulence profiles within a flow. In this section the same range of concentrations will be tested however the particle density has been reduced to

approximately match that of the fluid. Flashbead particles (Table 4.3) were introduced to the flow in the same manner as the Honite particles. In order to ensure internal consistency within the results, single phase measurements were repeated immediately prior to the introduction of particles to ensure a relevant baseline measurement to be compared against. Due to the lower particle density the mass added was reduced to ensure the volume fraction remained the same as can be seen in Table 4.4.

Table 4.4 - Mass of Flashbead particles for a given particle volume fraction.

Run #	Volume Fraction	Particle Mass (g)	Run #	Volume Fraction	Particle Mass (g)
1	0	0	5	8×10^{-4}	50.4
2	1×10^{-4}	6.3	6	16×10^{-4}	100.8
3	2×10^{-4}	12.6	7	32×10^{-4}	201.6
4	4×10^{-4}	25.2	8	64×10^{-4}	403.2

In order to clearly display the differences between the two particle densities both sets of results have been plotted on the same figure. The neutrally buoyant Flashbead particles have been plotted on the left hand y-axis. The denser Honite particles have been plotted on a

vertically shifted y-axis displayed on the right to avoid overlapping the data and obscuring results. In addition only the flow region closest to the acoustic sensor has been plotted as this region provides the most reliable data. It also creates greater consistency between chapters as data is only available for half of the pipe width in the following chapter.

4.3.1 Comparison of Changes in Axial Velocity

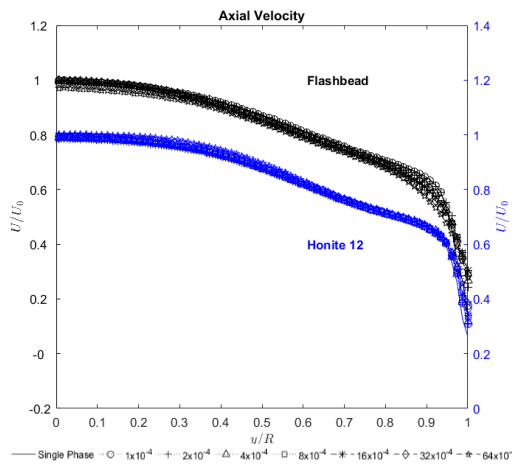


Figure 4.12 – Change in axial velocity with increasing concentration of Flashbead and Honite 12 particles.

Figure 4.12 shows there is a difference in the shape of the velocity profiles as the particle concentration increased. Unlike the previous test using Honite, where the increase in particle concentration had very little effect on the shape of the velocity profile the

neutrally buoyant Flashbead particles cause the velocity profile to become more parabolic as the particle concentration is increased.

Figure 4.13 shows that this change also results in the velocity profile better approximating the straight line dependence in the log-law region, however the U^+ values are still lower than those found by Zagarola and Smits, (1998) when they examined how Reynolds number effects the flow within a pipe.

Figures 4.14 and 4.15 clearly show that increasing the particle concentration of Flashbead does not have the same effect as increasing the particle concentration of Honite 12. Below $y^+ = 50$ increasing the concentration of Flashbead particles increases their relative velocity, with the maximum velocity increase of 113% significantly greater than Honite, at 48%. It should also be noted that this maximum was not achieved at the highest particle concentration, but at 16×10^{-4} .

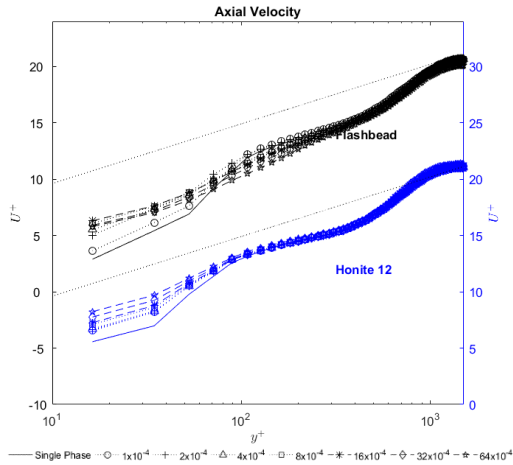


Figure 4.13 – Change in axial velocity with increasing concentration of Honite 12 and Flashbead particles plotted in wall units.

Even so at the highest particle concentration ($\phi = 64 \times 10^{-4}$) the percentage change of 97% due to Flashbead loading was still much greater than the Honite 12 measurements. Beyond this initial region between $y^+ = 50$ and 300 the presence of Flashbead particles begin to reduce the axial velocity below that of the single phase measurements. The maximum reduction

of 14% is seen around $y^+ = 100$, and within this region an increase in particle concentration translates to greater modulation of the velocity. This effect is not seen in the presence of Honite 12 particles where deviations from the single phase velocity measurements are less than 1%.

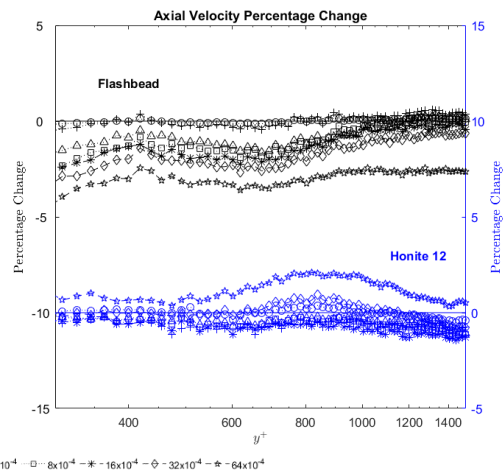
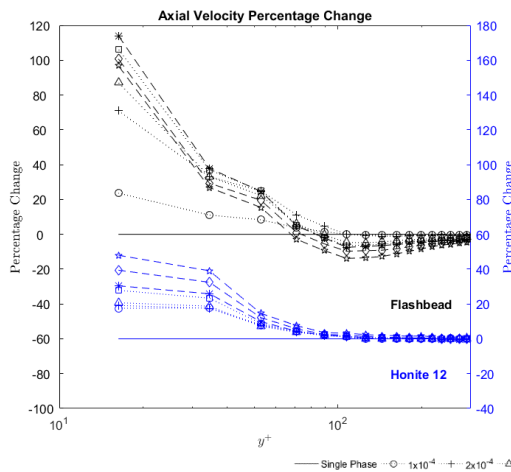


Figure 4.14 (left) – Percentage change in axial velocity with change in Honite 12 and Flashbead particle loading in the near wall region. Figure 4.15 (right) – Percentage change in axial velocity with change in Honite 12 and Flashbead particle loading in the bulk flow region.

4.3.2 Comparison of Changes in Axial Turbulence

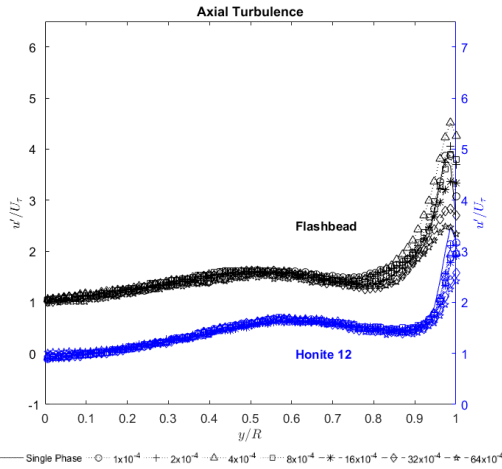


Figure 4.16 – Change in axial velocity fluctuations with increasing concentration of Honite 12 and Flashbead particles.

There is a significant difference in the particle velocity fluctuations between the two particle densities as seen in Figure 4.16. In the near wall region the denser Honite particles experience suppression of the velocity fluctuations, with the magnitude of this suppression increasing as the concentration of particles is increased. Such a simple behaviour is not

observed with the introduction of the neutrally buoyant Flashbead particles; where particle concentration and location determine whether turbulent fluctuations are enhanced or suppressed.

Figure 4.17 clearly illustrates this behaviour. In the first measurement location closest to the wall, particle volume fractions of Flashbead particles between 1×10^{-4} and 16×10^{-4} enhance velocity fluctuations, with a maximum enhancement of 56% seen at a volume fraction of 4×10^{-4} . As the concentration of Flashbead particles is further increased, the magnitude of enhancement is less than the 4×10^{-4} volume fraction for 8×10^{-4} and 16×10^{-4} particle volume fractions. Suppression of the velocity fluctuations is observed when compared with the single phase results as the particle volume fraction reaches 32×10^{-4} and the magnitude of suppression is greater as particle concentration is increased to 64×10^{-4} . Maximum suppression is seen around $y^+ = 50$, for Honite particles this occurs at the highest particle concentration and is equal to 34.9%, similar to the Flashbead at 36%. A secondary peak in turbulence enhancement of 26.7% is seen at $y^+ = 100$. Beyond this all particle concentrations experience a reduction in velocity fluctuations until $y^+ = 300$, at this point suppression is

observed. There is then a further change at $y^+ = 600$ where particles again experience enhancement of turbulent fluctuations. Figure 4.18 shows that as the pipe centreline is approached ($y^+ > 800$) all particle volume fractions except the highest at 64×10^{-4} result in turbulence enhancement, with the enhancement of a much greater magnitude compared with the Honite particles.

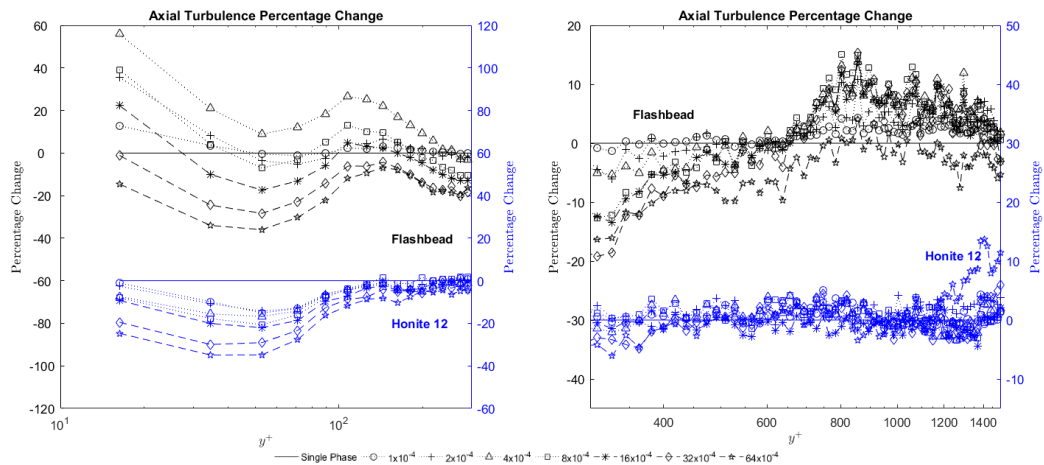


Figure 4.17 (left) – Percentage change in axial velocity fluctuations with change in Honite 12 and Flashbead particle loading in the near wall region. Figure 4.18 (right) – Percentage change in axial velocity fluctuations with change in Honite 12 and Flashbead particle loading in the bulk flow region.

4.3.3 Discussion of Changes in Particle Behaviour with Density

Significant differences in behaviour between neutrally buoyant Flashbead particles and denser glass particles have been observed. The neutrally buoyant particles which seem to have the greatest influence, especially as the particle concentration is increased. In the near wall region Flashbead particle velocities experience a significant velocity increase when compared with the single phase flow which then reverses and results in a velocity decrease in the turbulent core.

Channel flow experiments on similar neutrally buoyant particles by Rashidi et al., (1990) measured particle velocity profiles over a range of particle sizes. The authors found that the neutrally buoyant particles lagged behind the flow, with the difference between flow velocity and particle velocity increasing with particle size. They did not conduct measurements close

enough to the wall to compare the increase in velocity seen in the very near wall region. The authors found the relative difference between the particle velocity and fluid velocity arises due to the way particles are transported. Low speed streaks of particles form near the wall between pairs of counter rotating vortices, which then lift up the particles and eject them into the bulk flow.

This mechanism is shown in Figure 4.19. As there is a slight difference between the fluid and particle density, the particles eventually return to the wall region and the cycle repeats. Some of the particles

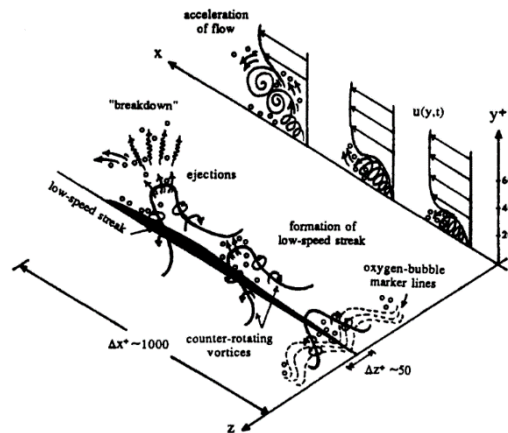


Figure 4.19 – Mechanism of particle resuspension. Rashidi et al., (1990)

will interact with ejections already in progress and get lifted up before reaching the wall. The fact that these particles are of lower velocity than the bulk flow results in particles lagging the fluid flow, and this is more significant for the larger particles as they have a greater response time with regards to the flow. As the size and density of the particles is increased the angle of lift up and maximum elevation of the particles decreases. Applying this theory to the current study would explain why the neutrally buoyant particles had a greater reduction in particle velocity. As the Flashbead particles are less dense a greater number of particles would be ejected from the pipe wall into the core region of the flow, these particles would then be recorded much more frequently as being of low velocity having just come from a low velocity flow region. The denser glass particles would be less likely to be ejected straight from the wall to the centre of the pipe and so the particles measured in that region would have migrated from neighbouring regions where the flow differential was much smaller.

This would also account for increased particle concentration resulting in a greater reduction in centreline velocity for both the Honite and Flashbead particles. Flashbead particles being of lower density would also be more likely to interact with other particles undergoing

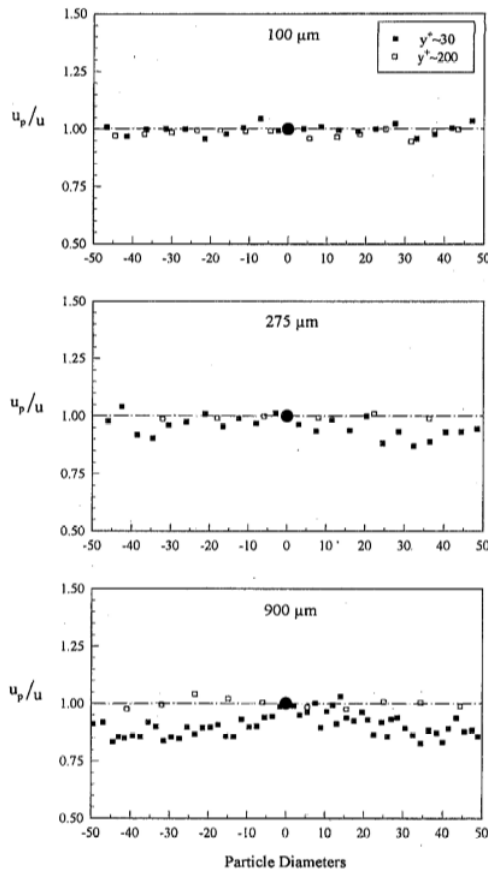


Figure 4.20 – Ratio of particle to fluid velocity immediately before and after the particle. Kaftori et al., (1995)

and fluid instantaneous velocities was very low in the immediate region around the particle, which can be seen in Figure 4.20. They suggest that this is due to the particles preferentially concentrating in low velocity regions of the flow. These low velocity regions of the flow are presumed to be funnel shaped vortices which are transported into the bulk flow via the entrainment of surrounding particles which are engulfed by this lower velocity flow. As the coherent flow structures break down the particles is rapidly accelerated to match the velocity of the surrounding fluid. The difference in behaviour between the Honite 12 and Flashbead particles as the greater inertia of the Honite 12 particles would prevent smaller

ejection and return to the pipe centreline whereas the denser glass particles have more inertia and are more likely to continue their trajectory towards the wall.

Kaftori et al., (1995) also found that polystyrene particles ($\rho=1050 \text{ kg/m}^3$) tended to lag behind the bulk flow. They found that there were significant concentration differences between the upper and lower halves of the flow which would agree with the proposal of Rashidi et al., (1990) that low velocity particles are ejected from lower velocity regions near the wall. However they found that the actual deficit between the local particle

scales of motion from causing the particles to concentrate in lower velocity regions in addition to having fewer ejections. DNS predictions by Kidanemariam et al., (2013), saw that at a volume fraction of 5×10^{-4} particles with a density 1.7x that of the fluid preferentially concentrated in low speed regions of the flow, creating streaks of particles which leads to the observed apparent lag of the particles behind the bulk flow.

Alajbegović et al., (1994) found that denser ceramic particles had velocity fluctuations smaller than that of the fluid phase turbulence, which accounts for the general behaviour seen in this study, where the particle velocity fluctuations are less than the single phase for the Honite measurements. Contrasting this with the polystyrene particles which were found to have much greater velocity fluctuations due to less inertia to damp their response to turbulent fluctuations. This can be seen in Figure 4.18 where the Flashbead particles display much larger fluctuations than the denser Honite.

This behaviour was also seen by Righetti and Romano, (2004) where when $\gamma^+ > 50$ particle velocity fluctuations were lower than the single phase fluid turbulence for both axial and radial velocity components. They propose that this is due to significant momentum transfer between the two phases in the buffer layer which leads to a reduction in the available turbulent energy which can be transferred to the outer region. The transition point in concentration from the particles enhancing turbulence to suppression is due to the mutual interaction between the particles and fluid phase. Zisselmar and Molerus, (1979) found that the presence of 50 μm glass particles caused an increase in turbulence in the near wall region until a critical value of 3% by volume, only once the point had been passed did the particles begin to dampen the turbulence. The reduction in turbulence is caused by interaction of particles hindering the flow, whereas the increase in turbulence is caused by the interaction of particles and eddies near the wall.

4.4 Effect of Particle Size on Fluid Flow

Table 4.5– Honite 8 particle properties.

Honite 8	
Particle Diameter (μm)	500
Particle Density (kg m^{-3})	2450
Particle Material	Silica Glass
Particle Settling Velocity (m s^{-1})	197.4×10^{-3}
Particle Response Time (ms)	34

This section examines how increasing particle size affects behaviour within the flow. Following the same procedure as before, particle velocities are measured with the concentration of particles gradually increased between runs. The particles examined in this section are 500 μm Honite 8, approximately twice the diameter of the Honite 12.

Particle properties are displayed in Table 4.5. In order to maintain continuity the particles are plotted against the Honite 12 measurements so comparisons can be easily observed. As the particles are of the same density the particle mass loading for both species (Honite 8 and 12) is the same and can be seen in Table 4.6.

Table 4.6– Mass of Honite particles for a given volume fraction.

Run #	Volume Fraction	Particle Mass (g)	Run #	Volume Fraction	Particle Mass (g)
1	0	0	5	8×10^{-4}	117.6
2	1×10^{-4}	14.7	6	16×10^{-4}	235.2
3	2×10^{-4}	29.4	7	32×10^{-4}	470.4
4	4×10^{-4}	58.8	8	64×10^{-4}	940.8

4.4.1 Comparison of Changes in Axial Velocity

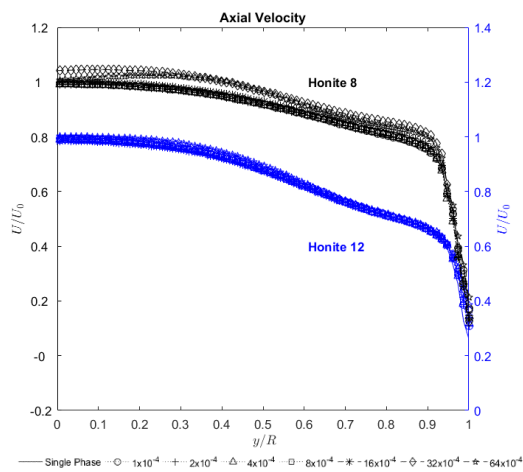


Figure 4.21 – Change in axial velocity with increasing concentration of Honite 8 and Honite 12 particles.

Immediately it can be seen in Figure 4.21 that there is a significant difference between the velocity profiles of the Honite 12 and the larger Honite 8 particles. The Honite 8 profile becomes flatter with increasing particle concentration up to a volume fraction of 16×10^{-4} . Beyond this particle concentration there is a deviation

from the standard profile as the concentration is increased, with the particles at a concentration of 32×10^{-4} travelling significantly faster than the measured fluid velocity. The shape of the profile at 32×10^{-4} and 64×10^{-4} volume fractions suggests there may be some form of flow disturbance at these concentrations, however this change in profile shape causes the profile to more closely approximate the profiles of the Honite 12 measurements. Such behaviour suggests that low particle concentration flows of the largest particles were not affected by the presence of the acoustic probe to the same extent as the flows with the smaller particles. Figure 4.22 shows that in the near wall region the particle velocity is reduced when compared with the single phase measurements at all but the highest volume fraction. We also see that the approximation of the log-law region holds up far better for the larger particles.

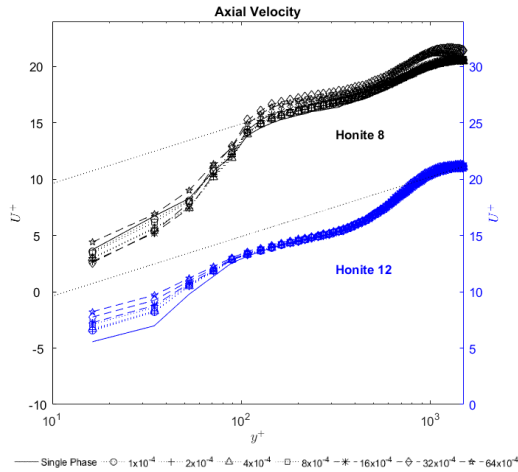


Figure 4.22 – Change in axial velocity with increasing concentration of Honite 8 and Honite 12 particles plotted in wall units.

In Figure 4.23 we can clearly see that below $y^+ = 100$ particle velocities for all but the two highest particle concentrations are lower than the single phase. As particle concentration increases the particle velocity decreases with a peak reduction of 32.4% seen at the measurement location closest to the wall and a volume fraction of 32×10^{-4} . However once $y^+ > 100$ this same

concentration is now traveling up to 8.8% faster than the single-phase flow.

Below a volume fraction of 16×10^{-4} the particles lag behind the flow in the turbulent core region, although the difference between the single phase measurement and the particle velocities is minimal remaining within 0.5% up to the pipe centreline. Such behaviour is also observed for the Honite 12 measurements.

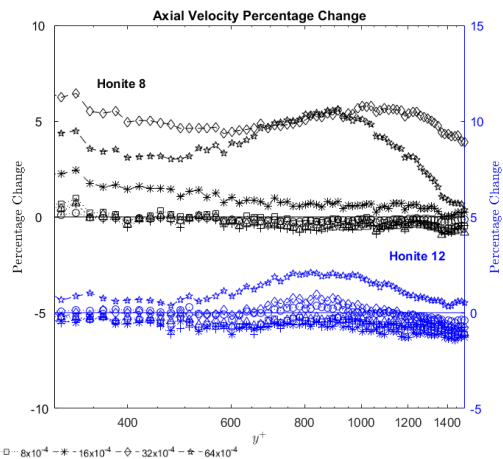
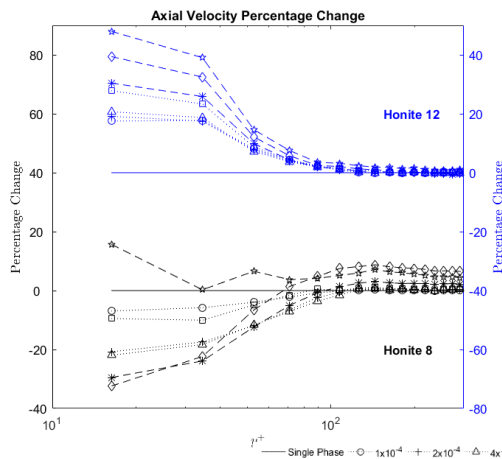


Figure 4.23 (left) – Percentage change in axial velocity with change in Honite 12 and Honite 8 particle loading in the near wall region. Figure 4.24 (right) – Percentage change in axial velocity with change in Honite 12 and Honite 8 particle loading in the bulk flow region.

4.4.2 Comparison of Changes in Axial Turbulence

There is a significant increase in axial particle velocity fluctuations at the two highest particle concentrations for the largest particles ($\varphi = 32 \times 10^{-4}$, 64×10^{-4}). A significant flattening of the central region of the turbulence profile at the highest volume fraction is observed, due to increasing magnitude of fluctuations in the central region of the pipe as can be seen in Figure 4.25. At lower particle concentrations the particle velocity fluctuations are similar to those of the smaller Honite 12 particles, showing a reduction in the magnitude of fluctuations compared with the fluid turbulence. Peak fluctuations occur in the same region for both particle species, however unlike the Honite 12 where greater dampening occurs with increased particle concentration, the larger Honite 8 particles undergo a transition from dampened to enhanced fluctuations as particle concentration increases.

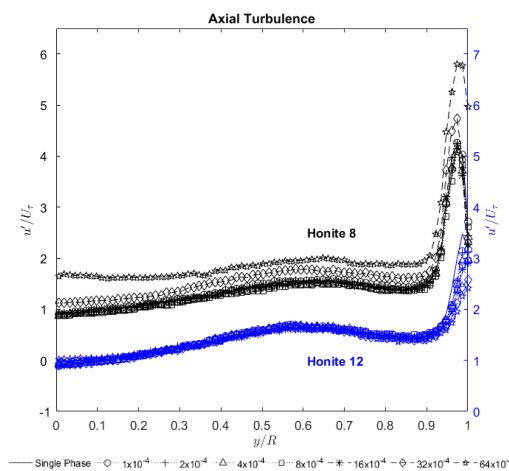


Figure 4.25 – Change in axial velocity fluctuations with increasing concentration of Honite 8 and Honite 12 particles.

As shown in Figure 4.25 in the immediate wall region, an increase in particle concentration of the Honite 8 particles leads to a reduction in velocity fluctuations, with a maximum reduction of 19.7% at 16×10^{-4} . The velocity fluctuations decrease slightly to 18.9% as the particle concentration increases to 32×10^{-4} , before drastically increasing to 75.9% as the

volume fraction reaches 64×10^{-4} .

The 16×10^{-4} volume fraction of Honite 8 particles shows very slight enhancement in the peak turbulence region ($y^+ \approx 60$) before fluctuations are either dampened or exhibit very weak enhancement across the pipe. The 32 and 64×10^{-4} volume fractions show a significant

increase in velocity fluctuations in both the peak turbulence region and approaching the pipe centreline, with the highest concentration showing velocity fluctuations 93.5% larger than the single phase measurements at the centreline.

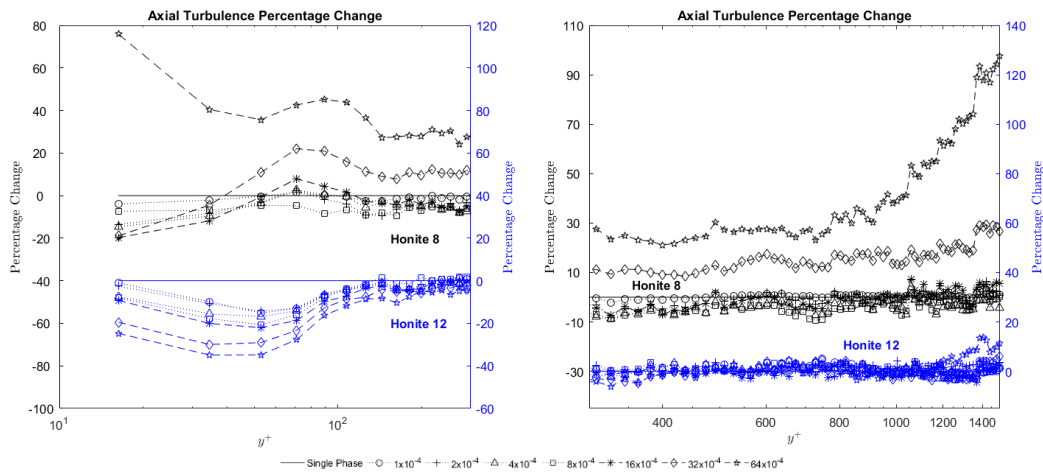


Figure 4.26 (left) – Percentage change in axial velocity fluctuations with change in Honite 12 and Honite 8 particle loading in the near wall region. Figure 4.27 (right) – Percentage change in axial velocity fluctuations with change in Honite 12 and Honite 8 particle loading in the bulk flow region.

4.4.3 Discussion

The larger Honite 8 particles behave very differently to the Honite 12 particles. In the near wall region the Honite 12 particles move faster than the single phase flow and the particle velocity increases with increasing particle concentration. The Honite 8 particles however appear to lag behind the flow and as particle concentration increases the lag increases, this was true for all particle concentrations tested except the highest particle volume fraction of 64×10^{-4} . One explanation for this would be that the increase in inertia of the particles prevented them from being ejected from the wall and instead rolled slowly along the edge. Rashidi et al., (1990) noticed in their channel flow experiment that their glass particles tended to settle along the bottom of the channel without interacting with the turbulence structures.

Kaftori et al., (1995) also noticed that as particle diameter was increased for their polystyrene particles the particles proceeded to lag the flow in the near wall region (around $y^+ = 30$) to a greater extent. They suggest that as particles are entrained by high speed sweeps which lift them from the wall, particle inertia means that initially the particles are moving slower than the bulk flow until sufficient time had elapsed for the particles to be accelerated, this would be especially prevalent in the wall regions of the pipe as this is where the particles have only just begun to be accelerated. A larger particle diameter means that more time is required to accelerate these particles.

Yung et al., (1989) found that the phenomena of particles being transported from the wall by coherent turbulent structures had a greater influence on larger particles however they also suggest that this influence is not enough to cause resuspension of the particle itself. Instead spalling occurs when the particle-wall holding force is exceeded by the fluid drag force, this leads to much longer residence times in the near wall region and would also contribute to lower particle velocities seen in the near wall region.

As we move further from the pipe wall the particles transition to moving faster than the surrounding fluid, in this region it is caused by particle migration towards the wall. As the particles have more inertia they resist deceleration in the slower regions of the flow, and in turn accelerate the surrounding fluid. Particles crossing streamlines enter the core flow region lagging behind the flow slightly due to the time required to accelerate the particle, this accounts for the slower velocities seen at the pipe centreline at concentrations between 1×10^{-4} and 8×10^{-4} .

Although particle velocities greater than the fluid have been observed by Kulick et al., (1994) and Alajbegović et al., (1994) these studies have been conducted in vertically oriented channels where gravitational forces act on the particles. The most likely explanation for the increase in particle velocity at the highest particle concentrations is measurement error. A

particle diameter of 500 μm is more than 1% of the pipe diameter and has a y^+ value of 25.7, meaning that individual particles are larger than the measurement channels of the acoustic probes. Supporting the idea that large concentrations of these particles lead to measurement uncertainties, it would also account for the very significant increase in velocity fluctuations present at the pipe centreline for the highest volume fractions.

In the near wall region at lower volume fractions we see that like the Honite 12 the Honite 8 velocity fluctuations are less than the fluid phase, and fluctuations continue to decrease as particle concentration increases. It may be expected that due to the increased inertia the levels of fluctuations would be reduced, however due to the size of the particle significant shear effects would be present. Therefore although fluctuations are less than the fluid phase they will be greater than the equivalent concentration of the smaller particles which have reduced velocity gradient acting upon them and so less interaction with the turbulence structures as seen by Rashidi et al., (1990).

4.5 Conclusions

This chapter has demonstrated the capability of Ultrasonic Doppler Velocimetry for both fluid and particle measurements. The technique works well for measurement of flows with high particle concentrations which is often a limiting factor for other measurement techniques. Some of the drawbacks of the technique are the fact that multiple probes would be required to obtain further data such as the radial velocity and velocity fluctuations. There is also an issue with minimum and maximum measurement ranges. Minimum measurement distances require the probe to be offset from the flow, whereas divergence and reflection mean that measurement of the opposite wall is difficult without either significant flow disturbance or some form of correction. These issues are highlighted in the single phase measurement section. The technique does however produce results in reasonable agreement with expected values and was able to measure a wide range of flow conditions clearly demonstrating changes in particle behaviour across a range of particle species.

It has been shown that changes in particle size, density and concentration drastically change the particle behaviour within the flow. As particle concentration increases there is a general trend for the particle behaviour to become more prominent. That is to say, if a particle velocity is greater than the fluid then an increase in particle concentration causes this difference to increase. However, this is not true in all cases, for example for the Flashbead particles a transition from enhancing the velocity fluctuations to then suppressing the velocity fluctuations was observed with increasing particle concentration.

The effect of particle size is mainly due to a combination of interaction with the turbulent structures within the flow and the inherent increase in inertia as particle size increases. This causes particles to resist influence by smaller scale turbulent eddies reducing particle velocity fluctuations, but increase turbulence within the system through the creation of wakes.

Reductions in particle density affect the rate at which particles transition from the pipe wall towards the centre, increasing the rate at which particles are ejected, thus resulting in an increase in turbulence and facilitating the transfer of momentum away from the pipe centreline resulting in a reduction of peak flow velocity.

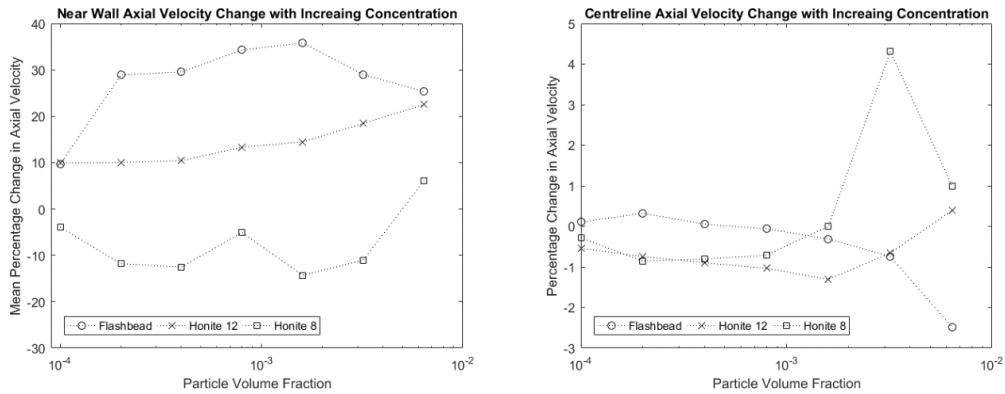


Figure 4.28 (left) – Near wall change in axial velocity with increased particle concentration. Figure 4.29 (right) – Centreline change in axial velocity with increased particle concentration.

Figures 4.28 and 4.29 show the changes in the near wall and centreline velocities with increased particle volume fraction. Due to the rapid changes in the near wall region the percentage change has been calculated as the mean change between $0 < y^+ < 100$, whereas the centreline value is the recorded change at the centreline since the flow in this region remains consistent. This also allows for the peak turbulence region to be captured when calculating the mean velocity fluctuations in this region as seen in Figure 4.25.

From Figures 4.28 and 4.29 we clearly see that in the near wall region the Flashbead particles have the highest velocity compared with the fluid, with a large initial increase as particle volume fraction increases. However, further increasing the number of particles has little effect on the particle velocity with the majority of the particle concentrations resulting in around a 30% increase in velocity in the near wall region. The Honite 12 behaves similarly although the magnitude is smaller with an initial 10% increase, which then slightly increases with particle concentration. The larger Honite 8 particles initially have a lower velocity than

the fluid which generally decreases with increased particle concentration until the highest volume fraction where the velocity becomes greater than the flow.

Centreline velocity changes are much smaller in magnitude. In this region the Flashbead particles seem to fully follow the flow at low particle concentrations, however as the particle concentration is increased the particles steadily begin to slow down. The Honite 12 particles follow the same trend as the Flashbead particles, however the particles lag the flow to a greater extent, until a transition point at 32×10^{-4} when the particle velocity becomes greater than the flow velocity. The Honite 8 particles show similar behaviour as the Honite 12 particles, however the transition condition is observed at a much lower volume fraction of 8×10^{-4} .

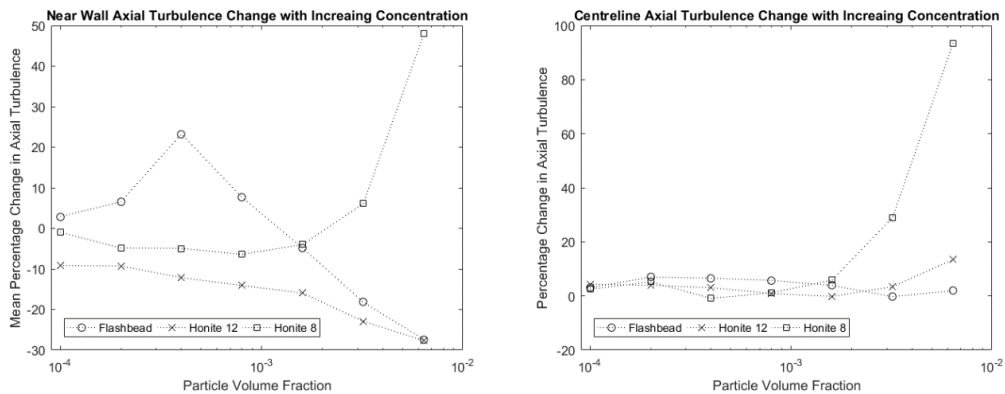


Figure 4.30 (left) – Near wall change in axial velocity fluctuations with increased particle concentration.
 Figure 4.31 (right) – Centreline change in axial velocity fluctuations with increased particle concentration.

Near wall particle fluctuations shown in Figure 4.30 decrease as the particle concentration increases for both the Honite species, until a volume fraction of 8×10^{-4} where the larger Honite 8 particles exhibit enhanced fluctuations beyond the single phase measurements. The Honite 12 particles continue to suppress turbulent fluctuations as particle concentration is increased. Initially, Flashbead particles enhance fluctuations with increased particle concentration however beyond a volume fraction of 4×10^{-4} this trend reverses and

suppression occurs once a volume fraction of 16×10^{-4} is attained. At the highest particle concentration ($\phi = 64 \times 10^{-4}$) the magnitude of suppression is very similar for the Honite 12 and Flashbead particles. Low particle concentration centreline turbulence measurements (Figure 4.31) show slight variations between the particle species although the magnitude of the effect is very similar. At higher particle concentrations the larger Honite 8 particles diverge from the other particle species and begin to cause significant enhancement in turbulent fluctuations.

The fact that some particles velocities in the near wall region experience an increase as the particle concentration increases has important implications in applications of multiphase fluid flows where particle settling and resuspension play an important role in the safety aspects of the system. Examples of such flows would be the transport of the highly active liquors and sludge found in nuclear storage and reprocessing sites. This research suggests that as the particle concentration decreases there is a reduction of velocity near the walls which can lead to difficulties when trying to 'flush out' a system as the minimum velocity for particle suspension may not be met. Alternatively, for the larger particles which appear to settle and travel very slowly at the walls, one possible remedy could be to introduce smaller or less dense particles to facilitate ejections and particle resuspension.

4.6 References

- Alajbegović, A., Assad, A., Bonetto, F. and Lahey, R.T. (1994). Phase distribution and turbulence structure for solid/fluid upflow in a pipe. *International Journal of Multiphase Flow*. **20**(3),pp.453–479.
- Elghobashi, S. (1994). On predicting particle-laden turbulent flows. *Applied Scientific Research*. **52**,pp.309–329.
- Kaftori, D., Hetsroni, G. and Banerjee, S. (1995). Particle behavior in the turbulent boundary layer. II. Velocity and distribution profiles. *Physics of Fluids*. **7**(5),pp.1107–1121.
- Kidanemariam, A.G., Chan-Braun, C., Doychev, T. and Uhlmann, M. (2013). Direct numerical simulation of horizontal open channel flow with finite-size, heavy particles at low solid volume fraction. *New Journal of Physics*. **15**(2),p.25031.
- Kulick, J., Fessler, J. and Eaton, K. (1994). Particle response and turbulence modification in fully developed channel flow. *Journal of Fluid Mechanics*. **277**,pp.109–134.
- Laufer, J. (1954). The structure of turbulence in fully developed pipe flow. *Naca Tr 1174*,pp.417–434.
- Marusic, I., Monty, J.P., Hultmark, M. and Smits, A.J. (2013). On the logarithmic region in wall turbulence. *Journal of Fluid Mechanics*. **716**.
- Rashidi, M., Hetsroni, G. and Banerjee, S. (1990). Particle-turbulence interaction in a boundary layer. *International Journal of Multiphase Flow*. **16**(6),pp.935–949.
- Righetti, M. and Romano, G.P. (2004). Particle-fluid interactions in a plane near-wall turbulent flow. *Journal of Fluid Mechanics*. (505),pp.93–121.
- Roberson, J.A. and Crowe, C.T. (1996). *Engineering Fluid Mechanics*. New York, John Wiley & Sons.
- Toonder, J. Den and Nieuwstadt, F. (1997). Reynolds number effects in a turbulent pipe flow for low to moderate Re. *Physics of Fluids*.
- Varaksin, A.Y., Polezhaev, Y. V and Polyakov, A.F. (2000). Effect of particle concentration on fluctuating velocity of the disperse phase for turbulent pipe flow. *International Journal of Heat and Fluid Flow*. **21**,pp.562–567.
- Wu, X. and Moin, P. (2008). A direct numerical simulation study on the mean velocity characteristics in turbulent pipe flow. *Journal of Fluid Mechanics*. **608**,pp.81–112.
- Yung, B.P.K., Merry, H. and Bott, T.R. (1989). The role of turbulent bursts in particle re-entrainment in aqueous systems. *Chemical Engineering Science*. **44**(4),pp.873–882.
- Zagarola, M. V. and Smits, A.J. (1998). Mean-flow scaling of turbulent pipe flow. *Journal of Fluid Mechanics*. **373**,pp.33–79.
- Zisselmar, R. and Molerus, O. (1979). Investigation of solid-liquid pipe flow with regard to turbulence modification. *The Chemical Engineering Journal*. **18**(3),pp.233–239.

5 Optical Measurements of Pipe Flows

This chapter will cover the use of PIV to measure fluid flows in pipes. Section 5.1 shows the single-phase measurements of the flow and comparisons with established data and the acoustic results. Section 5.2 explores the effect of particle concentration on the ability to make measurements and how this differs between the acoustic and optical (PIV) methods. Section 5.3 examines the effect of particle density on the fluid behaviour. Section 5.4 examines how particle size impacts the flow. Finally, Section 5.5 contains the chapter conclusions and summary. References are contained within Section 5.6.

5.1 Single Phase Measurements Using PIV

Like with the UDVP experiments a single-phase measurement needs to be made to compare with the multiphase data, ensure the equipment is working correctly and check that the results correlate with those found in the literature.

Throughout this chapter the effect of particles on the flow were tested at a Reynolds number of 50,000. The internal diameter of the pipe was 48 mm and the rig was operated with a mean fluid velocity of $1.045 \text{ m}\cdot\text{s}^{-1}$ giving a flow rate of $1.81 \text{ L}\cdot\text{s}^{-1}$. The PIV system was supplied by Dantec Dynamics and a combination of Dynamic Studio and MATLAB were used to analyse and process the experimental data. Full details of the experimental facility and data processing techniques can be found in Chapter 3.

5.1.1 Images and Flow Visualisations

One of the major benefits of the PIV system compared with acoustics is the fact that whole field measurements are made simultaneously, which allows for large regions of the flow to be visualised. To increase the resolution of the acquired images it was decided that only half of the pipe cross section would be captured. As the measurements are taken horizontally the assumption is made that the flow is symmetrical about the centreline. It was decided that the benefits of increased resolution outweighed the potential information losses from not measuring the entire pipe cross section. Alternatively, both sides of the pipe could have been measured in separate runs however this would possibly introduce inaccuracies due to realignment of the PIV camera.

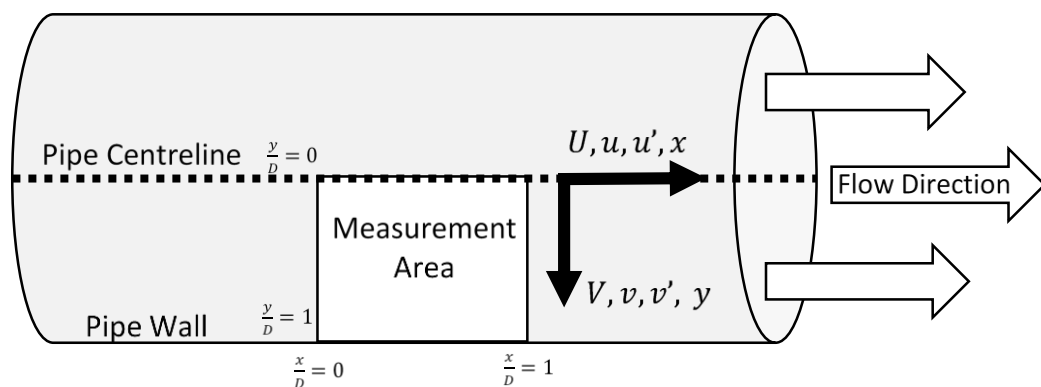


Figure 5.1 - Schematic of measurement area and coordinate system.

The following figures display contour plots of the flow, to aid understanding a schematic outlining the measurement area is shown in Figure 5.1.

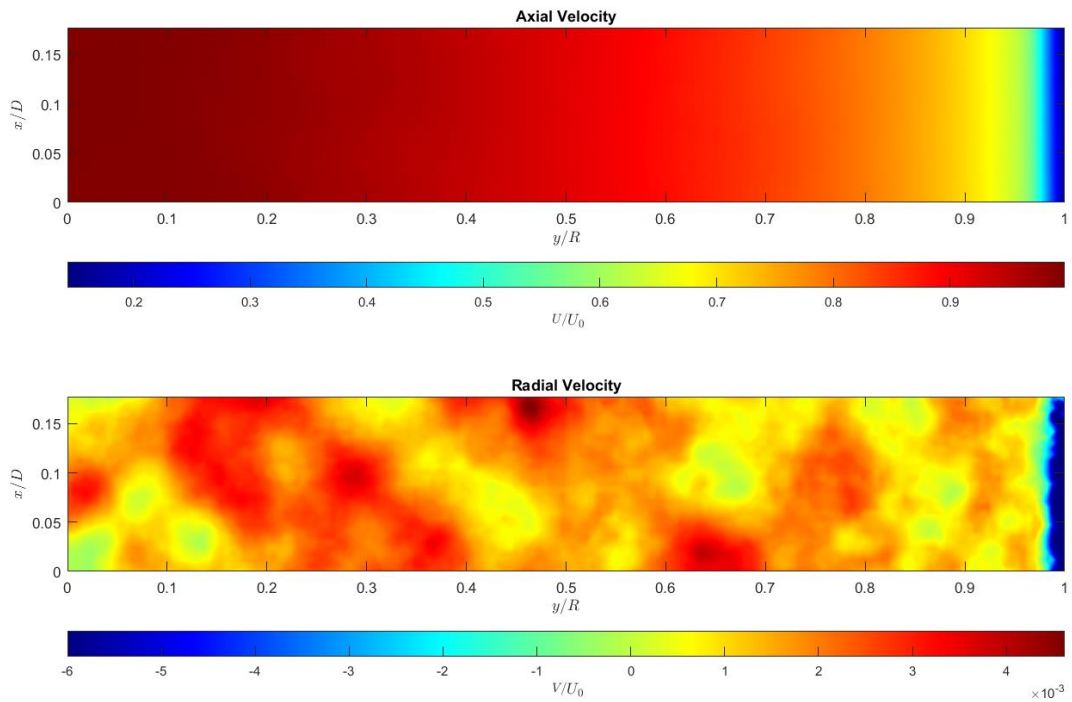


Figure 5.2 – Axial and radial velocity contour plots where the pipe wall is located at $y/R = 1$ and the centreline at $y/R=0$.

Figure 5.2 displays contour plots of the axial and radial velocities measured within the pipe. From the data, we can clearly observe that the axial flow decelerates rapidly beyond $y/D = 0.9$ as the wall is approached. There is a good degree of uniformity along the x-axis (the axial direction), this shows that the flow has fully developed and the entrance region has been surpassed as predicted when calculating the required pipe length in the development of the experimental rig. The radial contour plot shows a very slight bias towards positive values of radial velocity across the bulk of the pipe, meaning the tracer particles are slowly migrating towards the pipe wall, however this is effectively insignificant as the maximum value of this movement is less than 0.5% of the axial flow velocity.

The fact that the radial velocity is negligible compared with the axial velocity creates difficulty in obtaining accurate PIV measurements. As the relative shift in the radial direction is so much smaller than the axial, errors in calculating the particle displacement are more

likely to occur. However, this can be remedied in part by increasing the resolution of the images to reduce sub-pixel error as discussed in Chapter 3.

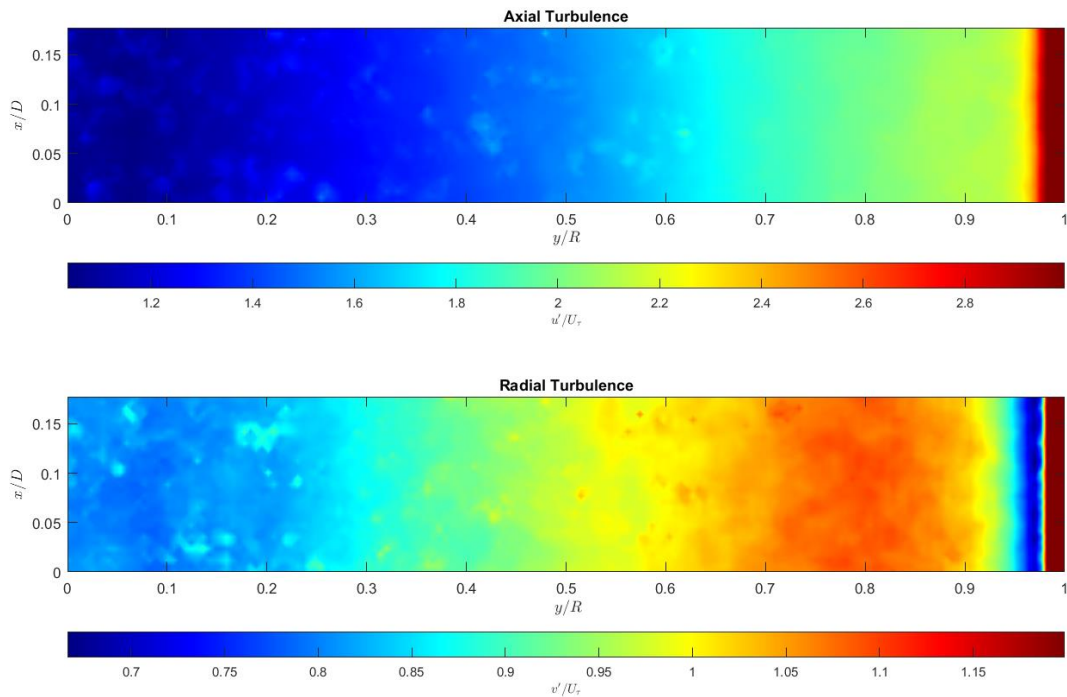


Figure 5.3 – Axial and radial turbulence contour plots where the pipe wall is located at $y/R = 1$, and the centreline at $y/R = 0$.

Figure 5.3 shows contour plots for the fluid turbulence in the region $y/D = 0-1$. The data highlights one of the major drawbacks of using optical techniques with a curved geometry. Measurements close to the wall become distorted, which results in some features of the turbulence field remaining unresolved. Axial turbulence gradually rises towards the wall and then in the near wall region ($y/D = 0.95$) increases significantly. However, due to the optical distortion the reduction in turbulence intensity to zero at the wall is not observed.

The same problem is observed in the radial turbulence measurements, where the turbulence peaks at $0.7 < y/D < 0.9$ and then reduces, however at $y/D > 0.98$ the turbulence appears to suddenly increase. An upper filter was applied to the data in this region with a cap of 1.2 enforced, this was done to prevent the contour plot scaling and obscuring smaller changes

in the flow. This behaviour is an artefact of the optical distortion, and thus data in this region ($y/D > 0.98$) is considered unreliable.

These distortions were minimised by the inclusion of a box section around the pipe and a reduction in thickness of the pipe wall. Further details on the steps taken to minimise optical distortion can be found in Chapter 3.

5.1.2 Velocity Profiles

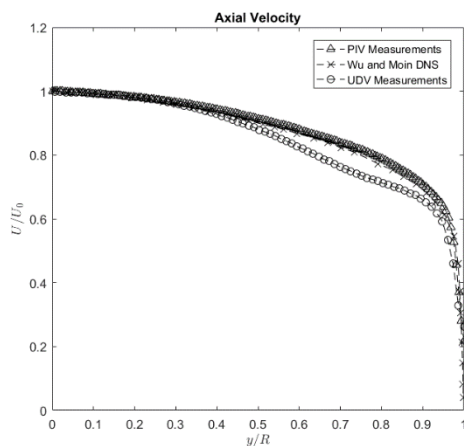


Figure 5.4 – Comparison of PIV axial velocity measurements, with UDV measurements and DNS predictions.

Although flow visualisations and contour plots provide useful information, the use of flow profiles allows more meaningful and accurate comparisons between data sets. As before we will first consider the axial velocity profile. Figure 5.4 shows the results of the PIV measurement compared with the predictions of Wu and Moin, (2008). As can be seen the PIV data are in

excellent agreement, with almost no difference between the DNS predictions and PIV measurement. Since PIV is a non-intrusive measurement technique, the interference seen in the profiles measured using UDV is not observed in the PIV data. Some of the difference between the acoustic measurement and DNS/PIV can be attributed to the flow being studied at the slightly higher Reynolds number of 50,000 using the PIV compared with 40,000 for the UVP. This results in the PIV flow being less parabolic, which is most obvious in the near wall region ($y/D > 0.9$).

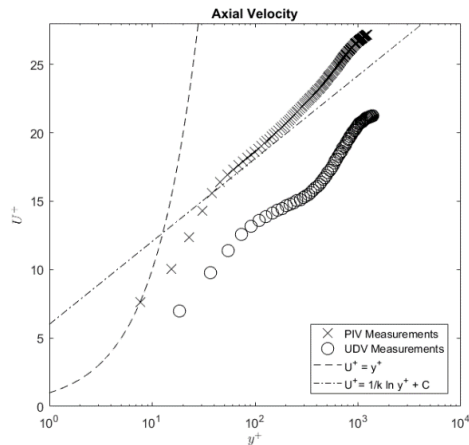


Figure 5.5 – Comparison of PIV and UDV measurements plotted in wall units.

Figure 5.5 shows the same data plotted in wall units, from which we can see that the PIV measurement shows a much better representation of the log-law region using constants within the limits found by Marusic et al., (2013). This is in part due to the increased resolution offered by the PIV

equipment and the fact there is no flow disturbance resulting from the ultrasonic probe causing a depression of the axial velocity.

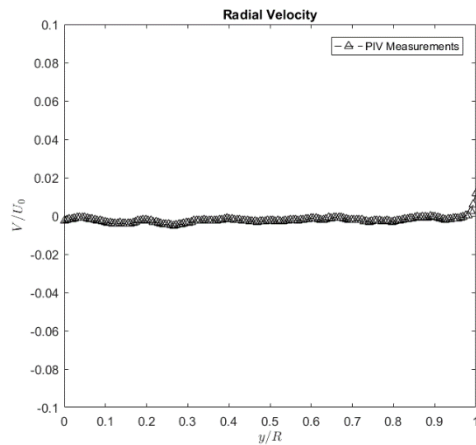


Figure 5.6 – PIV radial velocity measurements.

In addition to measurements of axial velocity PIV allows the simultaneous capture of radial movement. Figure 5.6 shows the radial velocity profile for the pipe. As can be seen the maximum radial velocity is less than 0.5% of the maximum axial velocity (V/U_0) and so this data is often neglected, both due to the

difficulties associated with acquiring reliable data, and its relative usefulness when describing pipe flow behaviour. It has however been included here for completeness. Once again this data clearly highlights one of the limitations of this implementation of the PIV technique, which is that the collection of data close to the pipe wall is limited by resolution.

5.1.3 Turbulence Statistics

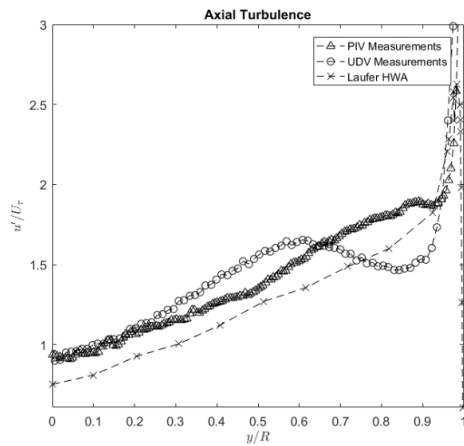


Figure 5.7 Comparison of axial PIV and UDV measurements against those of Laufer ,(1954).

Turbulence statistics were calculated using the method described in Chapter 3. Figure 5.7 shows the axial turbulence measured by PIV and compared with the published hot-wire anemometry data of Laufer, (1954), and the data collected using UDV. As shown in Figure 5.7 a reasonable agreement between the PIV and literature data is observed. Like the UDV data the PIV data report slightly higher levels of turbulence than those measured using hot-wire anemometry; however, this may be due to the method used to determine the value of the friction velocity which would result in scaling of the flow. The general shape of the profile (PIV) is in good agreement, apart from the measurements very close to the wall, as explained previously this is due to curvature at the pipe wall causing measurements to become distorted.

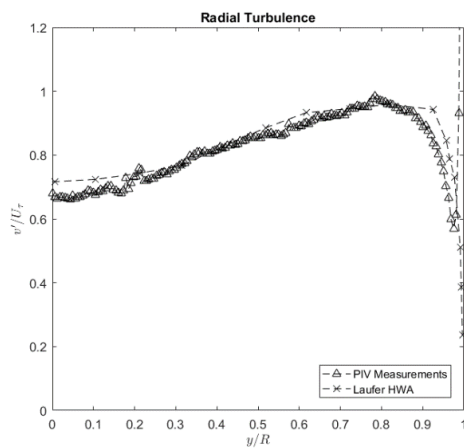


Figure 5.8 – Comparison of radial PIV measurements against those of Laufer, (1954).

Figure 5.8 displays the radial turbulence data. Again these data show excellent agreement with the results of Laufer, (1954), with both the radial turbulence profile and the turbulence levels in good agreement with literature values. As with the axial turbulence measurements there are slight discrepancies very close to the pipe wall, thus highlighting the issue of examining flows using PIV.

5.1.4 Discussion

The flow visualisations highlight one of the most powerful aspects of PIV. Whole field measurements allow for flows to be studied in more detail with transient behaviour more easily observed. Although this is not as important in pipe flow, especially in the region which is fully developed (i.e. the flow profile no longer changes along the pipes axis), but as will be seen in the following chapter the ability to observe how the flow changes in multiple dimensions allows for more robust analysis.

The whole field technique in this instance can be used to determine to what extent the flow has become fully developed and so further applications of this technique in pipes would be useful to study the flow disturbance caused by valves, fittings, pipe bends and other physical changes in the pipeline.

Velocity and turbulence profiles show that PIV can produce accurate results at high resolutions, with good agreements with other measurement techniques and computer predictions. Since the PIV measurement is external to the flow (camera + laser) there is no influence on the flow, and so artificial flow disturbances are not introduced unlike HWA and UDV techniques.

The pipe region where the reliability of the PIV data is poor is in the near wall region, where curvature of the pipe results in slight distortion of the image. Although steps have been taken to minimise distortion, the region closest to the wall is still difficult to analyse accurately. This region is arguably one of the most interesting and so modifications to obtain results in this region would be of benefit, unfortunately attempts to compensate for this were

unsuccessful as discussed in Chapter 3. The low flow velocities in this region are a compounding factor as even very slight distortions causing a shift in the interrogation areas intensity peak can lead to massive errors when calculating the velocity vector.

Further work to address this would include making extremely small scale PIV measurements at the pipe wall to determine the extent of the distortion which could then be accounted for mathematically. However, limitations of the project with regards to both time and facilities prevented this from being an option.

5.2 Effect of Concentration on Fluid-Phase Measurements

This section will explore the effects of changing particle concentration on the ability to make accurate measurements of the fluid phase. Unlike the UDV which tracked the behaviour of the particles in the flow, the PIV equipment has been set up to isolate changes in the fluid behaviour. This was done using fluorescent tracer particles and optical filters, which allowed for the solid phase to be filtered out, leaving only the tracers to be detected and analysed as discussed in Chapter 3. Issues arise due to the particles forming an optical barrier, hence flow measurements become more difficult. This contrasts with the UDV, or even PIV of particle flow where an increase in particles can lead to an increase in the quality of the results due to an increase in the number of sampling points.

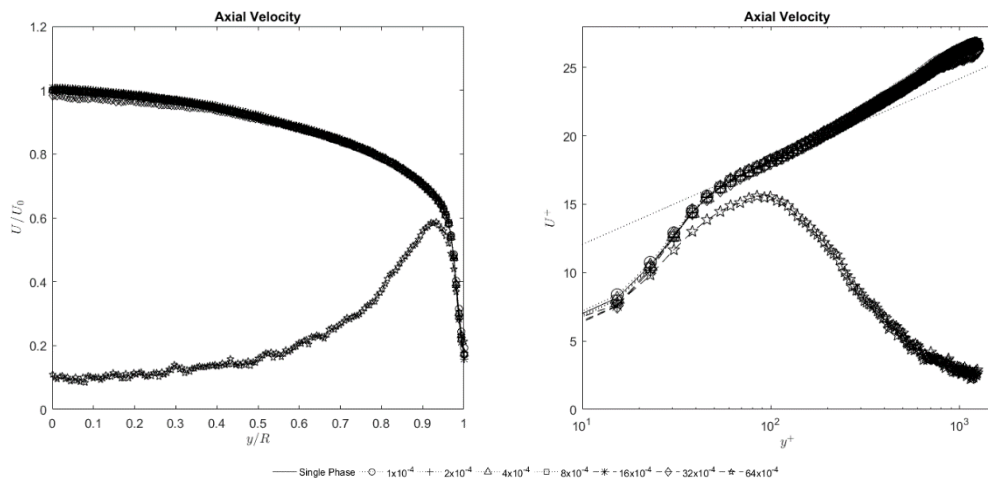


Figure 5.9 (left) – Change in axial velocity with distance and concentration.

Figure 5.10 (right) – Change in axial velocity with distance and concentration plotted in wall units.

Figure 5.9 shows the change in axial velocity with the change in particle concentration, and from the data the limitation of using an optical technique to measure a multiphase flow is clear. At low particle concentrations, the PIV technique works well, it can accurately track the movement of the tracer particles and the velocity profiles are well resolved. However, as can be seen the PIV technique is unable to accurately reproduce the characteristic pipe velocity profiles at particle volume fractions of 64×10^{-4} and greater. There is slight

uncertainty in the results at the pipe centreline when the particle volume fraction is increased to 32×10^{-4} with the data unusable across most the flow at a particle volume fraction of 64×10^{-4} .

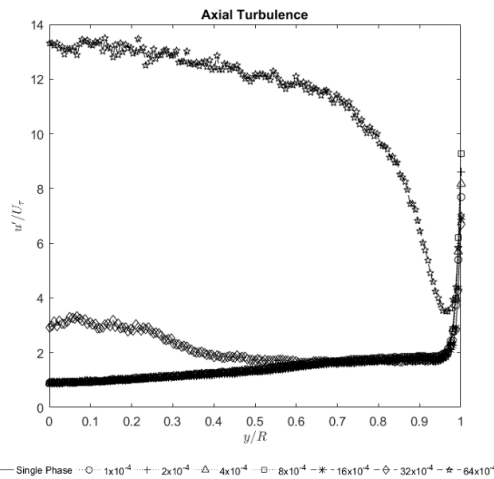


Figure 5.11 – Change in axial turbulence measurements with distance and concentration.

Figure 5.11 displays the axial turbulence measurements. As concentration is increased from a volume fraction of zero to 8×10^{-4} turbulence measurements are all in good agreement across most the pipe. Again, the wall region shows the expected issues due to distortion. Problems with the measurements at beyond a volume fraction of 8×10^{-4} are observed again,

especially at the centre of the pipe. This is due to the presence of particles creating an opaque suspension where individual particles could not be distinguished and full illumination by the laser was prevented. This is displayed in Figure 5.12 which shows the pipe becoming more opaque as the particle concentration is increased.

Due to the unreliability of the data at higher particle concentrations it was decided that the study will focus on lower particle concentrations to ensure validity of the data. For this reason, the comparisons between data sets will be performed up to a maximum particle volume fraction of 8×10^{-4} which appears to be the upper limit for high quality images, see Figure 5.12. The sudden change in light intensity is due to an increase in laser power output in an attempt to acquire particle images. For the data sets used in the results the power output of the laser remained fixed.



Figure 5.12 – Combined images of the same region as particle volume fraction is increased.

5.2.1 Discussion

Although PIV produces high quality results which more accurately represent the flow, the technique suffers from serious limitations when the particle concentration is too high. This is to be expected as optical techniques such as PIV and PTV rely on high quality images which degrade significantly as the particle concentration is increased. The greatest impact of low optical clarity is at the pipe centreline, with measurements closer to the wall being more accurate. The reason for this is simple, at the pipe centreline the light sheet and light emitted from the particles has a greater distance to travel through the fluid and so has more opportunity to be blocked and absorbed by other particles in the system.

What was surprising was the extent to which data could be extracted by the software when the fluid transparency was very low. Turbulence measurements were much more sensitive to the transparency of the fluid than velocity measurements. This is potentially due to the fact that turbulence is calculated as a deviation from the mean, however if there is uncertainty in the measurement due to poor quality images this would be seen as an increase in deviations about the mean and therefore an increase in turbulence. The same problem is not seen when calculating the mean, potentially because the error due to poor image quality is not biased in one direction, and so when the mean of the individual measurements is taken the error is eliminated. That is until the point where the fluid becomes opaque that the bulk movement of tracer particles cannot be resolved and so the recorded velocities tend towards zero.

Changing the intensity of the laser emissions can be beneficial in trying to penetrate the fluid, however as the light intensity is increased there is much more reflection from the solids in the system. This reflected light can then interact with the surrounding tracers which will fluoresce. These out of focus particles create significant light pollution further contributing to difficulties in obtaining reliable data.

The response of the fluid to the change in particle concentration will be discussed in more detail in the following sections where the results of the Honite 12 will be compared with other particle species.

5.3 Effect of Particle Density on Fluid Flow

Table 5.1 – Honite 12 particle properties.

Honite 12	
Particle Diameter (μm)	225
Particle Density (kg m^{-3})	2450
Particle Material	Silica Glass
Particle Settling Velocity (m s^{-1})	39.92×10^{-3}
Particle Response Time (ms)	6.9

Table 5.2 – Flashbead particle properties.

Flashbead	
Particle Diameter (μm)	225
Particle Density (kg m^{-3})	1050
Particle Material	Styrene Divinylbenzene Copolymer
Particle Settling Velocity (m s^{-1})	1.37×10^{-3}
Particle Response Time (ms)	2.9

This section will examine how particle density effects the behaviour of the fluid flow. Similarly to the acoustic measurements the neutrally buoyant Flashbead particles were used and of equivalent diameter to Honite 12, thus enabling the particle density effect to be elucidated. Honite 12 and Flashbead particle properties have been included in Table 5.1 and Table 5.2 respectively. The mass of particles added to the system with the relevant particle volume fractions are shown in Tables 5.3 and 5.4. Due to the previously mentioned reasons the fluid was only tested to a particle concentration of 8×10^{-4} .

Table 5.3 – Mass of Honite particles for a given volume fraction.

Honite Particle Loading					
Run #	Volume Fraction	Particle Mass (g)	Run #	Volume Fraction	Particle Mass (g)
1	0	0	4	4×10^{-4}	98.0
2	1×10^{-4}	24.5	5	8×10^{-4}	196.0
3	2×10^{-4}	49.0			

Table 5.4 – Mass of Flashbead particles for a given volume fraction.

Flashbead Particle Loading					
Run #	Volume Fraction	Particle Mass (g)	Run #	Volume Fraction	Particle Mass (g)
1	0	0	4	4×10^{-4}	42.0
2	1×10^{-4}	10.5	5	8×10^{-4}	84.0
3	2×10^{-4}	21.0			

5.3.1 Velocity Profiles

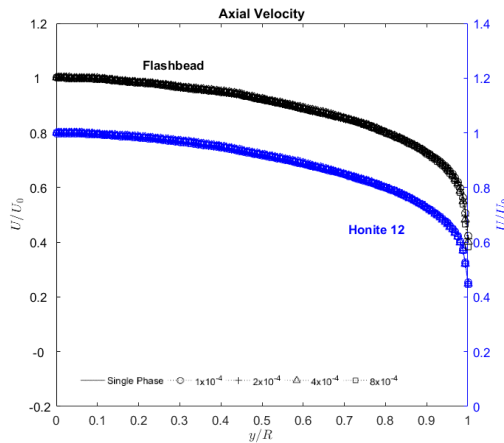


Figure 5.13 – Velocity profiles in the presence of increasing concentrations of Honite and Flashbead particles

Figure 5.13 displays the axial velocity profiles for both the Honite 12 and Flashbead particles for particle volume fractions up to 8×10^{-4} , to ensure clarity of the figures the data has been plotted on opposite axes, with the right-hand side y-axis offset slightly. As can be seen there is very little deviation from the single-phase data for either the Flashbead or the Honite

12. Figure 5.14 shows this data plotted in wall units. From the data, there is a very slight reduction in fluid velocity in the near wall region as the particle concentration is increased, however this change is almost non-existent for the denser Honite 12 particles.

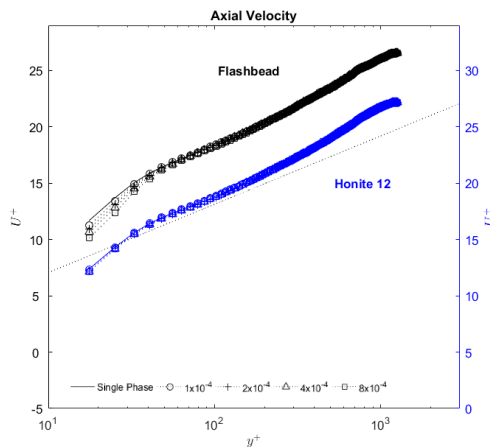


Figure 5.14 – Velocity profiles in the presence of increasing concentrations of Honite and Flashbead particles plotted in wall units

The mean percentage changes shown in Figures 5.15 and 5.16 confirm this effect. The maximum reduction in fluid velocity is 13.2% for the Flashbead particles, whereas the maximum reduction due to the presence of the Honite 12 particles is less than 2%. The introduction of particles also appears to cause a slight increase in fluid velocity in the bulk flow region for all the

tested concentrations of Flashbead and the higher 4 and 8×10^{-4} volume fractions of the Honite 12. The magnitude of this enhancement is however very small, generally less than 0.5% and so care must be taken when analysing this data. The lack of any trend with regards

to particle concentration, the magnitude and the fluctuations in the change may suggest that this is due to measurement uncertainty and not a real effect.

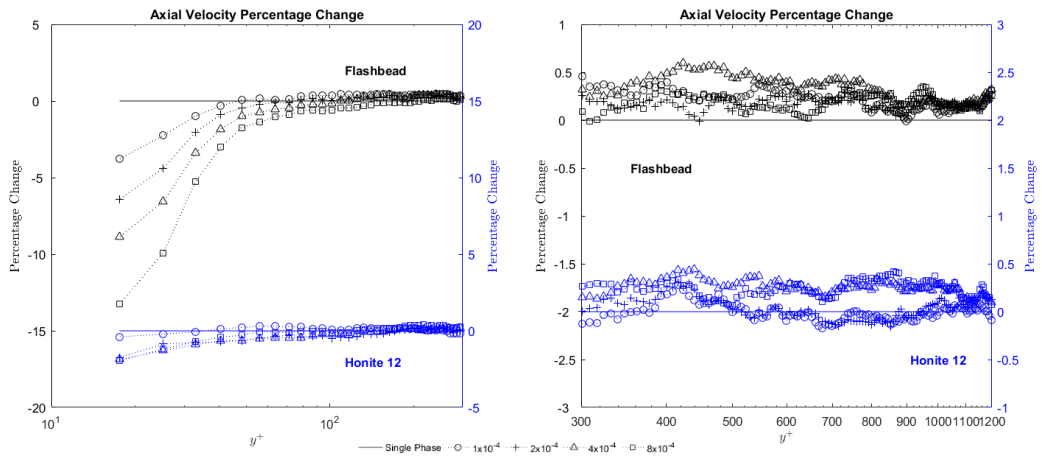


Figure 5.15 (left) – Percentage change in axial velocity with change in Honite 12 and Flashbead particle loading in the near wall region. Figure 5.16 (right) – Percentage change in axial velocity with change in Honite 12 and Flashbead particle loading in the bulk flow region

5.3.2 Turbulence Profiles

As previously discussed the turbulence profiles are in good agreement with those of Laufer, (1954) There is very little change in the fluid turbulence as the particle concentration is increased for either the Flashbead or the Honite 12 as can be seen in Figures 5.17 and 5.18.

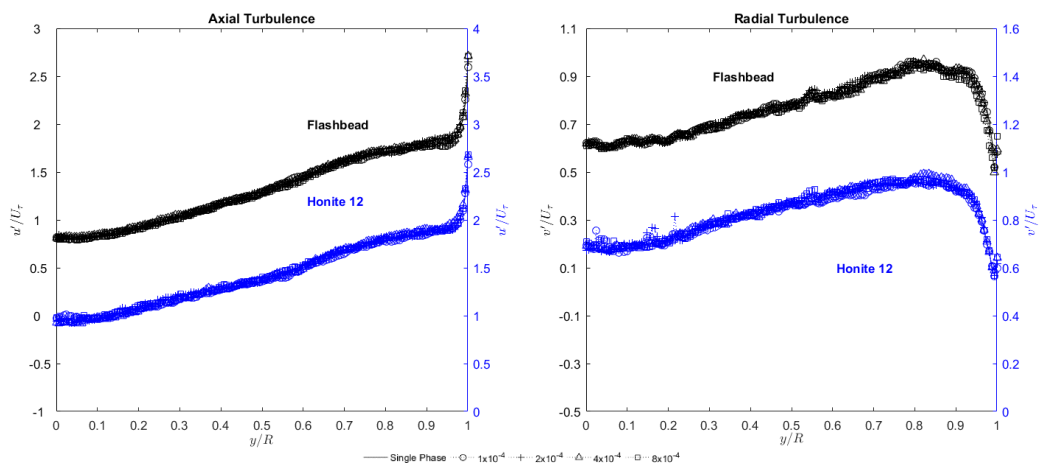


Figure 5.17 (left) – Axial turbulence profiles in the presence of increasing concentrations of Honite and Flashbead particles. Figure 5.18 (right) – Radial turbulence profiles in the presence of increasing concentrations of Honite and Flashbead particles.

The percentage change in axial turbulence is given in Figures 5.19 and 5.20. From the data, it is observed that at the measurement locations closest to the pipe wall ($20 < y^+ < 50$) there is a slight increase in turbulent fluctuations. This is more pronounced in the Flashbead measurements with a 7.3% increase in turbulence intensity for both the 4×10^{-4} and 8×10^{-4} particle volume fractions. These two higher fractions transition briefly into a turbulence damping region at $30 < y^+ < 200$ before the magnitude of the modulation becomes very small.

Throughout the pipe the axial turbulence is dampened in the presence of the Flashbead particles, with a slight increase in dampening as the particle concentration is increased. The Honite 12 particles have less of an effect in the near wall region, where the maximum enhancement is only 3.5% at the highest particle concentration, and only briefly demonstrate dampening in the region $y^+ \approx 150$. Beyond this the general trend for the Honite 12 particles is to cause enhancement of the fluid turbulence. This effect is amplified as the pipe centreline is approached with turbulence enhancement observed up to 10%.

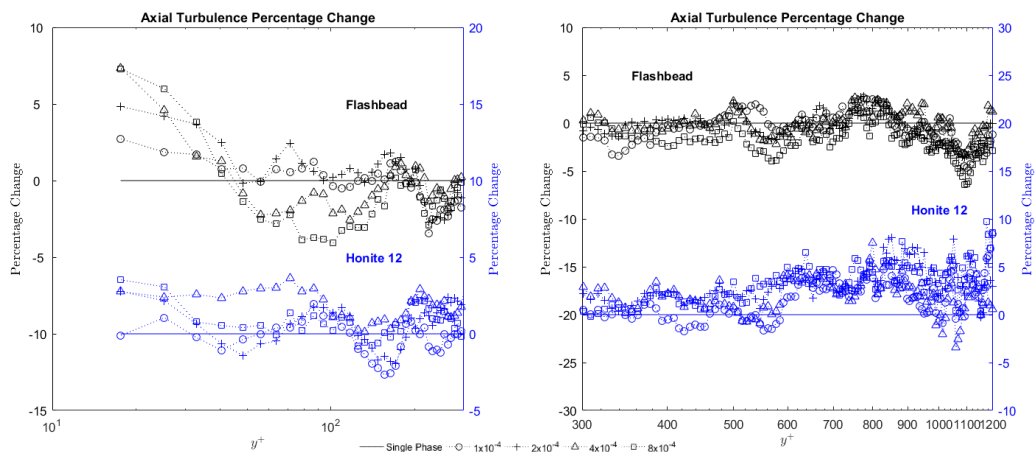


Figure 5.19 (left) – Percentage change in axial turbulence with change in Honite 12 and Flashbead particle loading in the near wall region. Figure 5.20 (right) – Percentage change in axial turbulence with change in Honite 12 and Flashbead particle loading in the bulk flow region.

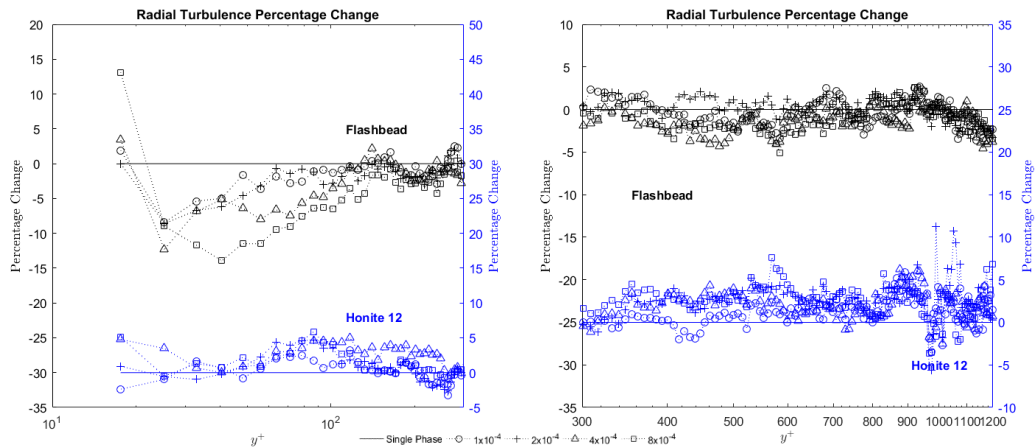


Figure 5.21 (left) – Percentage change in radial turbulence with change in Honite 12 and Flashbead particle loading in the near wall region. Figure 5.22 (right) – Percentage change in radial turbulence with change in Honite 12 and Flashbead particle loading in the bulk flow region.

For the radial turbulence measurements, it can be seen (Figures 5.21 and 5.22) that the neutrally buoyant Flashbead particles have a much greater influence in the near wall region. After an initial enhancement at the first measurement location of $y^+ = 18$ the presence of Flashbead particles dampens the velocity fluctuations. The magnitude of the dampening increases with increasing particle concentration but decreases with distance from the wall. The Honite 12 particles do not have the same dampening effect; instead the particles appear to slightly enhance radial fluid turbulence levels across the entire pipe section. The level of turbulence modulation is around the same level as for the axial modulations by the Honite 12 particles, whereas the Flashbead particles appear to have a greater effect in modulating radial turbulence than axial turbulence.

5.3.3 Discussion

Consistent with the results of Righetti and Romano, (2004) we observe that the fluid velocity near the pipe wall is decreased in the presence of particles; however the magnitude of change is much greater for the Flashbead particles. This coincides with an increase in fluid turbulence suggesting that energy is transferred from the mean flow to the creation of turbulent eddies, and energy is lost through the acceleration of particles in the surrounding region.

The limited velocity attenuation in the near wall region by the denser Honite 12 particles may be due to a localised reduction in the particle volume fraction in the near wall region as observed by Alajbegović et al., (1994). In agreement with Lee and Durst, (1982), in a solid-liquid vertical pipe flow, the authors found an almost particle free region existed in the near wall region $0.8 < y/D < 1$. They believe that the buoyancy and shape of the dispersed phase determines the lateral phase distribution and referenced literature showing the existence of both wall peaking and coring occurring in gas-liquid and solid-liquid systems. In a vertical pipe gravity acts axially, whereas in a horizontal pipe a component of gravity acts radially depending on the measurement location. The component of gravity which contributes to radial acceleration at the measurement location used in the present study is zero as the measurement plane is perpendicular to the gravitational force and so the particle behaviour in a vertical pipe should be applicable in this instance.

Horizontal channel flows of almost neutrally buoyant particles, like the Flashbead particles, performed by Kaftori et al., (1995) show that particles preferentially concentrated at the wall, however gravitational effects cannot be discounted which were not present in this study. An increase in local particle concentration would result in an apparent greater velocity and turbulence modulation by the Flashbead particles.

The lack of a linear correlation between the change in particle concentration and the effect on turbulence is also seen in the work of Tsuji and Morikawa, (1982), as well as by Wu et al., (2006). The authors found that when testing 60 μm particles in a horizontal channel the fluid axial turbulence initially decreased in the presence of particles, then as the particle loading increased the axial turbulence increased before finally decreasing again until it reached the same level as the single-phase flow. The same behaviour is observed for the Honite 12 particles, and can clearly be seen in the near wall region where the 4×10^{-4} particle loading shows a turbulence increase of around 4% whereas the 8×10^{-4} particle loading is almost the same as the single-phase flow.

The fact that the denser Honite 12 particles enhance radial turbulence whereas the neutrally buoyant Flashbead particles dissipate turbulence suggests that there is greater movement of the denser particles moving radially across the flow and crossing streamlines. This is supported by the observations of Sommerfeld and Huber, (1999). This would have the effect of generating turbulence whereas the Flashbead particles are more likely to follow the streamlines within the flow and dampen the small scale turbulent structures.

The increase in turbulence very close to the wall suggests that the neutrally buoyant particles are also more likely to be swept from the wall region and suspended in the flow. This would also account for the increase in axial velocity fluctuations seen as the Flashbead particles begin to accelerate axially before they are swept from the wall region gradually crossing streamlines while undergoing constant acceleration by the fluid.

The Honite 12 particles behave in a similar manner, however as seen with the results of Rashidi et al., (1990) there is a tendency for the glass particles to stick to the wall and roll along the pipe wall rather than be ejected back into the fluid, this coupled with a lower local particle concentration means the overall magnitude of modulation will be less.

5.4 Effect of Particle Size

This section will explore the effect of particle size and concentration on the fluid behaviour. Honite 22 (smaller) and Honite 8 (larger) particles were examined in addition to the more frequently studied Honite 12 particles at the same volume fractions as the previous section. Particle properties are given in Table 5.5. As the density of the three Honite particles remains constant the mass loading for each volume fraction is therefore the same and is given in Table 5.6.

Table 5.5 – Particle properties for various sizes of Honite particles.

	Honite 8	Honite 12	Honite 22
Particle Diameter (μm)	500	225	40
Particle Density (kg m^{-3})	2450	2450	2450
Particle Material	Silica Glass	Silica Glass	Silica Glass
Particle Settling Velocity (m s^{-1})	197.4×10^{-3}	39.92×10^{-3}	1.26×10^{-3}
Particle Response Time (ms)	34	6.9	0.2

Table 5.6 – Mass of Honite particles for a given volume fraction.

Honite Particle Loading					
Run #	Volume Fraction	Particle Mass (g)	Run #	Volume Fraction	Particle Mass (g)
1	0	0	4	4×10^{-4}	98.0
2	1×10^{-4}	24.5	5	8×10^{-4}	196.0
3	2×10^{-4}	49.0			

5.4.1 Velocity Profiles

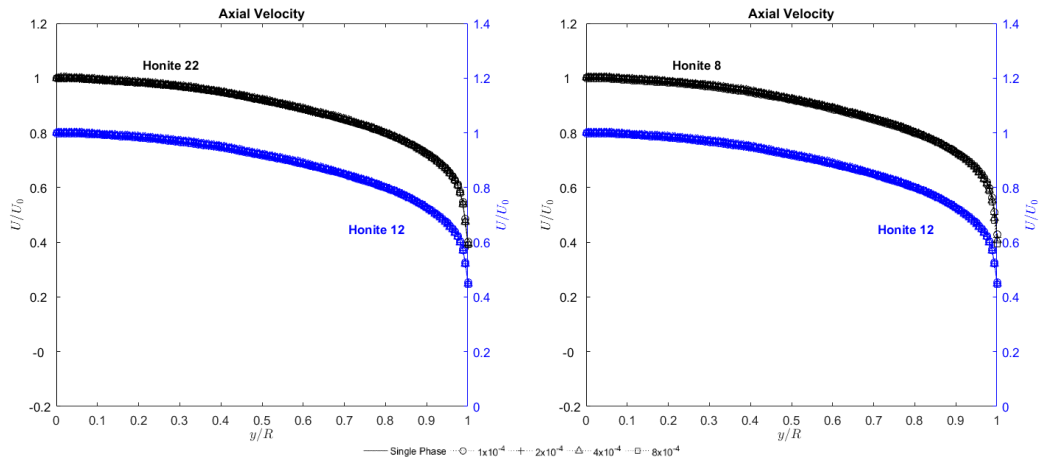


Figure 5.23 (left) – Comparison of the effect of Honite 12 and Honite 22 particles on the axial velocity profile. Figure 5.24 (right) – Comparison of the effect of Honite 12 and Honite 8 particles on the axial velocity profile.

Accounting for the y axis offset there is no discernible difference between the three particle sizes when the velocity profiles are examined shown in Figures 5.23 and 5.24. Examining the profiles in wall units (Figures 5.25 and 5.26) lets us highlight the very slight change in velocity at the wall for the larger Honite 8 particles, however even very close to the wall ($y^+ < 50$) the change in velocity is not especially significant for the Honite 12 and 22 particles.

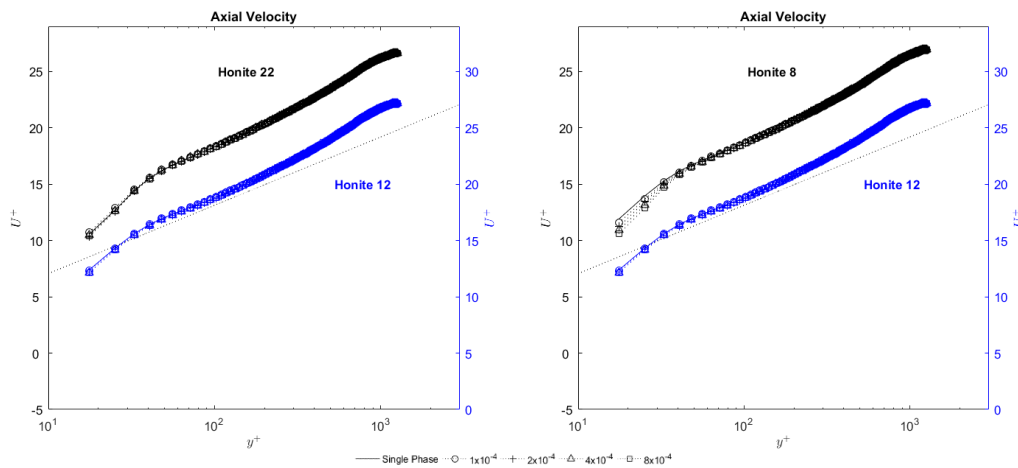


Figure 5.25 (left) – Comparison of the effect of Honite 12 and Honite 22 particles on the axial velocity profile plotted in wall units. Figure 5.26 (right) – Comparison of the effect of Honite 12 and Honite 8 particles on the axial velocity profile plotted in wall units.

Examining Figures 5.27 and 5.28 at the lowest particle concentration for the Honite 22 particles there was +2.8% change in fluid velocity compared with the single-phase flow, but as the particle concentration is increased this then reverses resulting in a decreased fluid velocity. At the particle volume fraction 8×10^{-4} the maximum change in fluid velocity of -4.4% is observed when compared to the single-phase flow. Beyond $y^+ = 100$ the maximum velocity change is less than 0.5% and on average is slightly less than the change for the the Honite 12 particles.

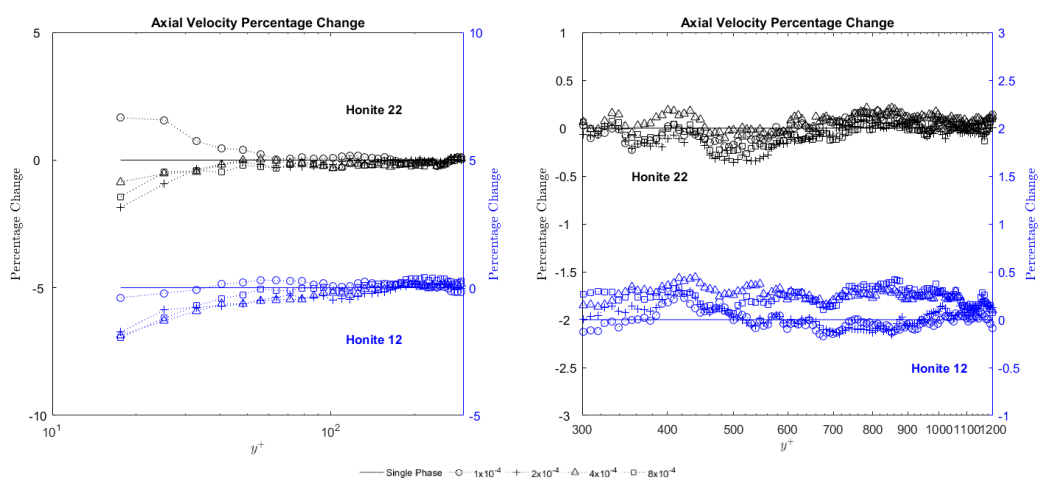


Figure 5.27 (left) – Percentage change in axial velocity with change in Honite 12 and Honite 22 particle loading in the near wall region. Figure 5.28 (right) – Percentage change in axial velocity with change in Honite 12 and Honite 22 particle loading in the bulk flow region.

Figures 5.29 and 5.30 show the percentage changes for the Honite 8 particles, where the velocity in the near wall region is more significantly reduced through the presence of the particles. At all particle concentrations, there is a reduction in fluid velocity, with the reduction increasing as the particle concentration increases. A maximum change of -11.2% is observed at the measurement location closest to the pipe wall ($y^+=18$). The magnitude of the velocity reduction then decreases as distance from the pipe wall increases. Across the bulk of the flow where the smaller Honite 22 particles tended to reduce the fluid velocity, the Honite 8 particles tend to cause a slight velocity increase, although again this change is less than 0.5%. Interestingly, the lowest concentration of Honite 8 particles tended to slightly

retard the velocity rather than increase the velocity. The Honite 12 loaded flow is closer to the Honite 22 loaded flow in the near wall region when $y^+ < 300$, but more accurately represents the Honite 8 loaded flow in the bulk flow region ($y^+ > 300$).

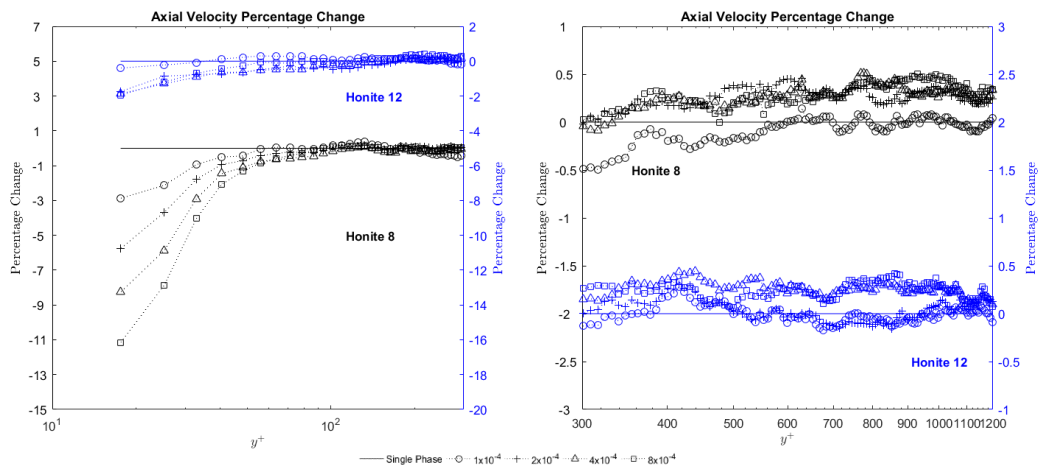


Figure 5.29 (left) – Percentage change in axial velocity with change in Honite 12 and Honite 8 particle loading in the near wall region. Figure 5.30 (right) – Percentage change in axial velocity with change in Honite 12 and Honite 8 particle loading in the bulk flow region.

5.4.2 Turbulence Profiles

Like the velocity profiles, the turbulence profiles in Figures 5.31 to 5.34 do not elucidate much information as the change in fluid turbulence between the different particle species is small. Such response shows that for the particle sizes considered in the current study there is minimal effect on the turbulence profiles of a flow, with both axial and radial turbulence remaining fairly constant and in good agreement with the results previously reported in the literature (Laufer, 1954). Comparisons between the Honite 8 (Figure 5.32) and Honite 22 (Figure 5.31) particles seem to suggest that the smaller particles (Honite 22) cause an increase in deviation from the single-phase flow, while the profiles for the larger Honite 8 particles overlap the single phase flow to a greater extent while the Honite 12 particles fall in-between the two (Figures 5.31 and 5.32).

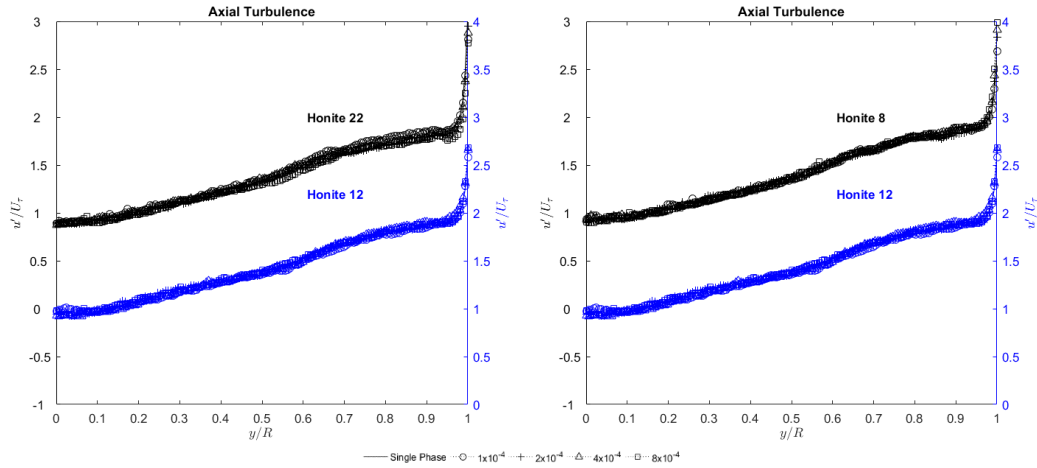


Figure 5.31 (left) – Comparison of the effect of Honite 12 and Honite 22 particles on the axial turbulence profile. Figure 5.32 (right) – Comparison of the effect of Honite 12 and Honite 8 particles on the axial turbulence profile.

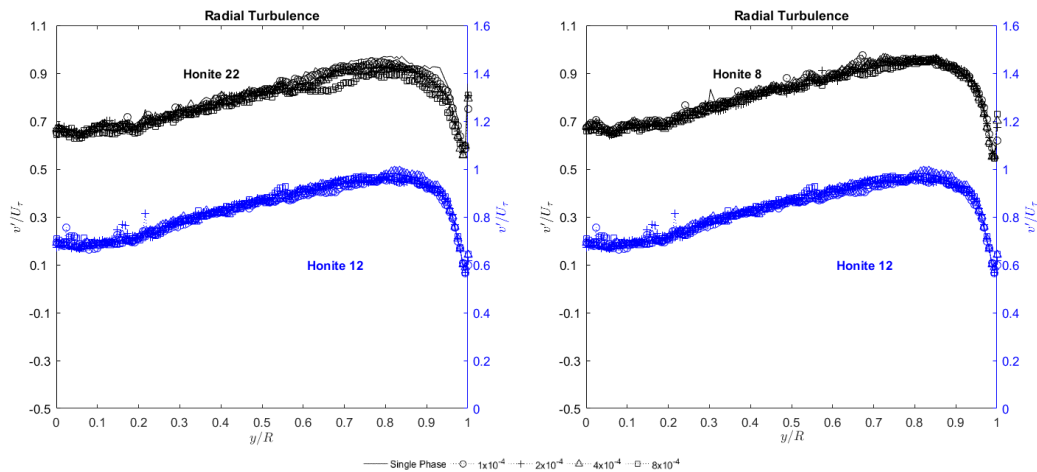


Figure 5.33 (left) – Comparison of the effect of Honite 12 and Honite 22 particles on the radial turbulence profile. Figure 5.34 (right) – Comparison of the effect of Honite 12 and Honite 8 particles on the radial turbulence profile.

Aside from the first measurement location at $y^+ = 18$, the trend for the Honite 22 particles is to suppress fluid axial turbulence in the near wall region with increased particle concentration enhancing this effect shown in Figure 5.35. This contrasts the Honite 12 and Honite 8 particles which can be seen to enhance turbulence in the near wall region. For the 8×10^{-4} particle volume fraction there is maximum modulation of the axial turbulence of around 10% which gradually declines to -5% at $y^+ = 100$. Beyond this the modulation fluctuates slightly however remains around -5% seen in Figure 5.36.

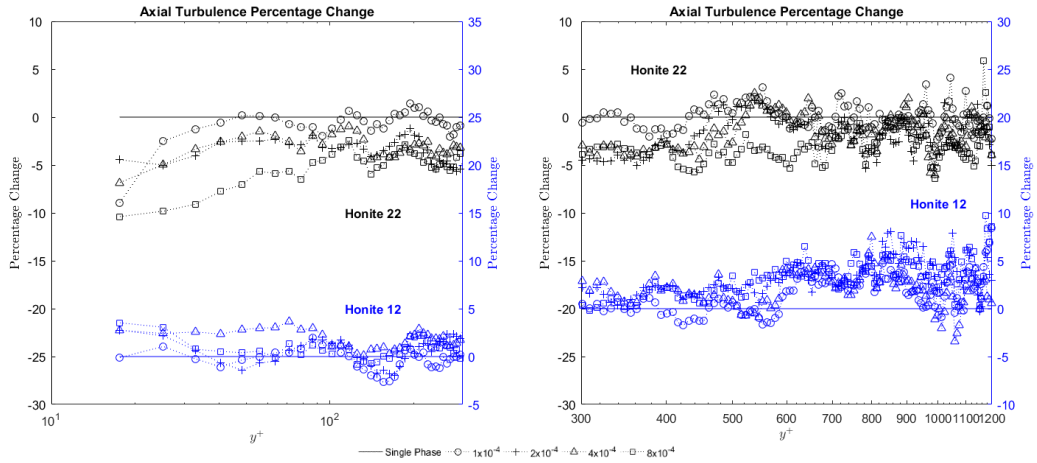


Figure 5.35 (left) – Percentage change in axial turbulence with change in Honite 12 and Honite 22 particle loading in the near wall region. Figure 5.36 (right) – Percentage change in axial turbulence with change in Honite 12 and Honite 22 particle loading in the bulk flow region.

Honite 8 particles can be seen to enhance axial turbulence increasing the effect as the particle concentration is increased as seen in Figure 5.37. At the highest particle volume fraction of 8×10^{-4} an increase of 14.9% is seen. This turbulence modulation does not extend as far from the wall as it does for the smaller Honite 22 particles, with the enhancement changing to suppression at $y^+ = 100$. This behaviour matches that of the Honite 12 particles which initially promote turbulent enhancement close to the wall, turbulence suppression around $y^+ = 100$, before reverting to turbulence enhancement beyond $y^+ = 200$ when compared with the single-phase flow.

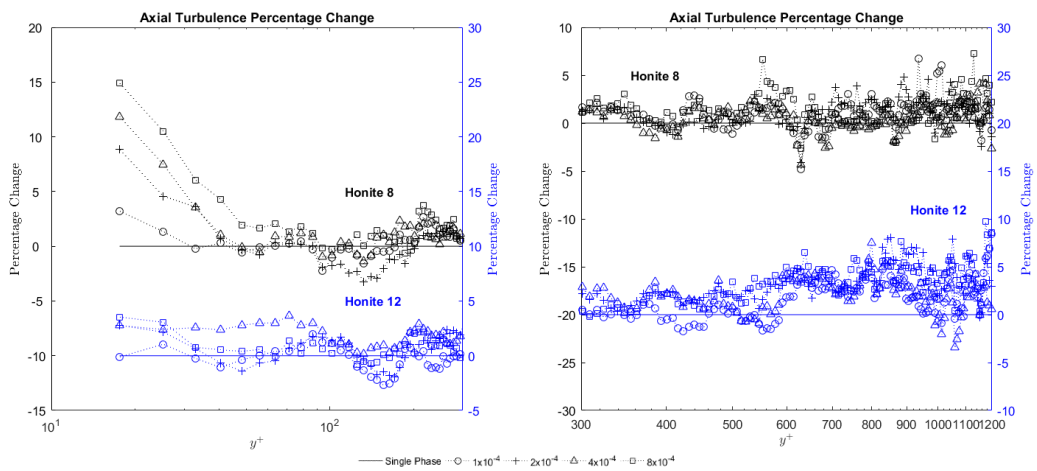


Figure 5.37 (left) – Percentage change in axial turbulence with change in Honite 12 and Honite 8 particle loading in the near wall region. Figure 5.38 (right) – Percentage change in axial turbulence with change in Honite 12 and Honite 8 particle loading in the bulk flow region.

Radial velocity fluctuations are modulated to a greater extent than axial velocity fluctuations, with the smaller Honite 22 particles having a much greater effect than both Honite 8 and Honite 12 particles. Interestingly, both the smallest (Honite 22) and largest (Honite 8) particles tended to suppress radial turbulence whereas the mid-sized Honite 12 particles showed a slight enhancement in radial turbulence as the particle concentration was increased. For the Honite 12 and 22 particles peak turbulence modulation occurs around the same point at $y^+ = 100$.

In the near wall region ($y^+ < 300$) at a particle volume fraction of 8×10^{-4} the Honite 22 particles caused suppression of radial turbulence of up to 15%. In the bulk flow region, this reduction decreases to around 10% until $y^+ = 500$, beyond this the magnitude of the reduction reduces to around 5%.

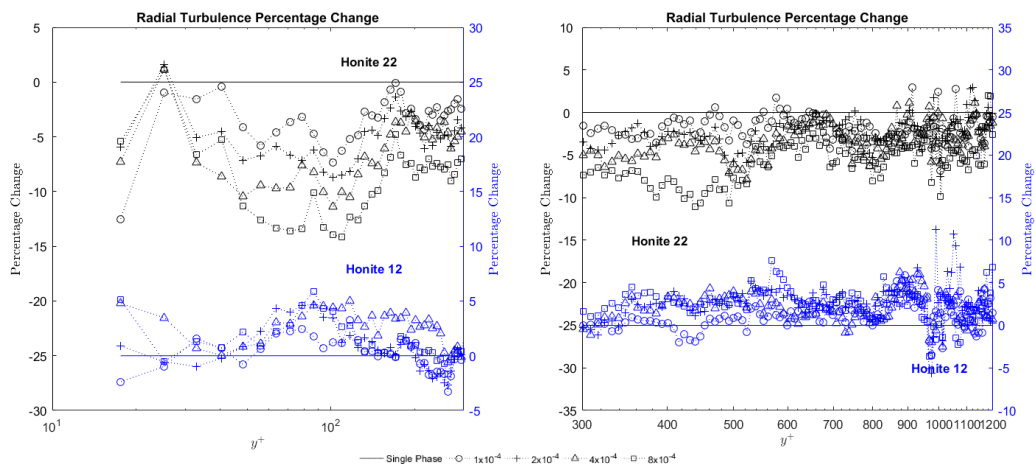


Figure 5.39 (left) – Percentage change in radial turbulence with change in Honite 12 and Honite 22 particle loading in the near wall region. Figure 5.40 (right) – Percentage change in radial turbulence with change in Honite 12 and Honite 22 particle loading in the bulk flow region.

The Honite 8 particles initially cause enhancement of up to 20% in the near wall region at $y^+ = 18$ followed by a peak in the magnitude of suppression around $y^+ = 30$. Average suppression at the highest particle concentration is approximately 5% between $y^+ = 50$ and 400. Beyond this distance the effect fluctuates with both enhancement and suppression occurring for all particle concentrations.

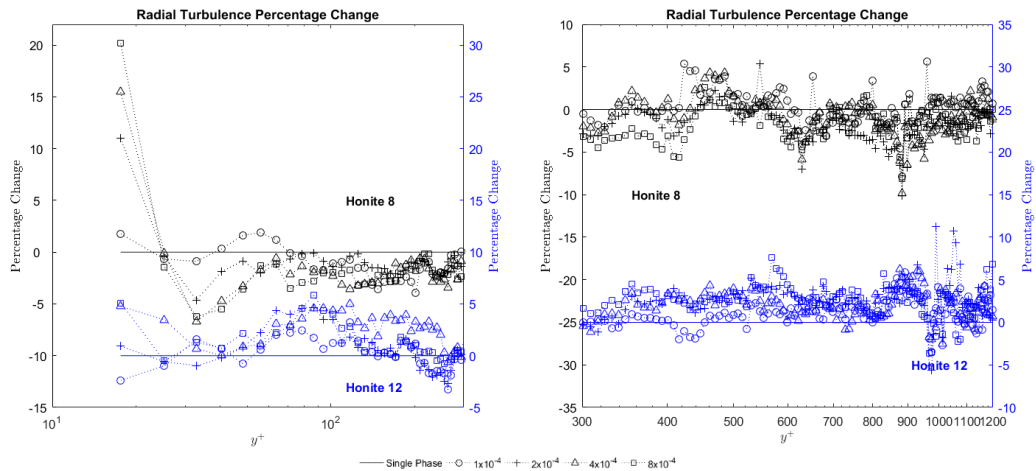


Figure 5.41 (left) – Percentage change in radial turbulence with change in Honite 12 and Honite 8 particle loading in the near wall region. Figure 5.42 (right) – Percentage change in radial turbulence with change in Honite 12 and Honite 8 particle loading in the bulk flow region.

5.4.3 Discussion

The fact that the presence of all sizes of Honite particles resulted in an increase in axial velocity in the bulk flow region $y^+ > 300$ is in contrast to the findings of Wu et al., (2006) who studied flows in air finding that both 60 μm and 110 μm particles resulted in a significant decrease in the fluid axial velocity, with increased particle concentration resulting in a greater reduction. However, the ratio of particle to fluid density is much greater in their work and so may explain the difference.

One possible explanation for the increase in axial velocity by the particles is the change in shape of the vertical velocity profiles. Gravity causes particles to drift towards the lower half of the pipe, resulting in an increase in the effective particle concentration in the lower region. Tsuji and Morikawa, (1982) examined the difference between 3.4 mm and 0.2 mm plastic particles ($\rho = 1000\text{kg/m}^3$) in a horizontal pipe with flowing air, finding that this segregation resulted in significant asymmetry in the velocity profiles, with the flow at the bottom of the pipe slowing in contrast to acceleration in the upper region, the net effect at the higher particle concentrations was an increase in velocity at the pipe centreline as can be seen in Figure 5.43.

The fact that the smaller Honite 22 particles had less of an effect on the mean axial velocity than either the Honite 8 or Honite 12 particles would corroborate this, as the lower settling velocity means that the particles remain dispersed within the pipe to a greater degree. As the mass loading was the same for all particle sizes it is unlikely that the increase is purely due to a momentum transfer from the particles to the fluid.

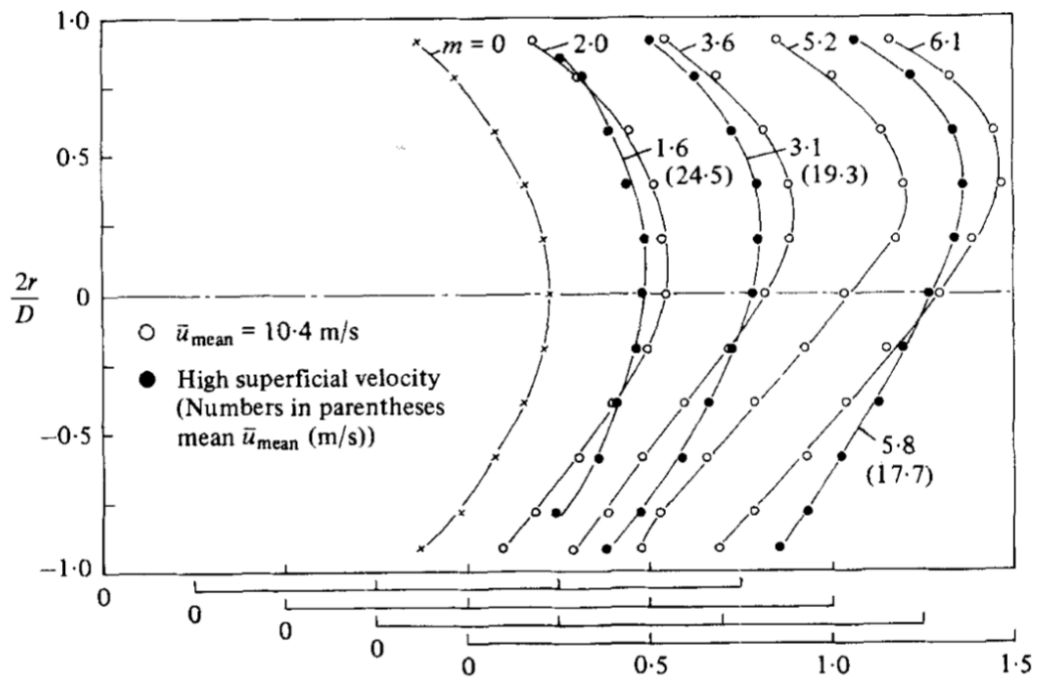


Figure 5.43 – Change in shape of velocity profiles as particle concentration is increased, Tsuji and Morikawa (1982).

Although further work would be required to confirm the presence of this asymmetry in this system if present it would manifest as an increase in the fluid velocity in the upper half including the measurement region of the pipe to compensate for the lower velocity in the lower regions.

The fact that the axial velocity is slightly reduced in the bulk flow region ($y^+ > 300$) when the particle volume fraction of Honite 8 particles at $\phi = 1 \times 10^{-4}$ is potentially due to the particle concentration not being sufficient to affect a significant change in the velocity profile; therefore, the pipe centreline velocity is not increased to the extent where the slowing effect

due to the particle inertia is overcome. Again, vertical velocity profiles would be needed to confirm this although it should be noted that a significant concentration gradient was observed while the measurements were being taken however the significance of this was not realised at the time and so recordings were not made.

The Honite 22 particles slightly increase the axial velocity beyond $y^+ = 600$ after going through a transition phase between $y^+ = 400$ to 600 where the velocity is reduced overall. This corresponds with the localised low velocity regions created by the smaller particles observed by Tsuji and Morikawa, (1982). The Honite 12 particles closely match the larger Honite 8 particles, as expected, due to the relative size of the three particles Honite 12 and 8 particles will migrate downwards to a much greater degree than the Honite 22.

The solid-liquid pipe flow examined by Hosokawa and Tomiyama, (2004) found that the inclusion of dense particles or bubbles into the system resulted in an increase in axial velocity. As the measurements were taken using a vertical pipe with the fluid travelling upwards it is logical that the buoyancy effects of the bubbles may be responsible for an increase in velocity, however no explanation is offered for why the denser particles would also cause an increase.

The fact that the smallest particles (Honite 22) result in a decrease in turbulence is again in accordance with the findings of Tsuji et al., (1984), who showed that the 0.2 mm particles suppressed turbulence intensity with increased particle loading. The effect of this change was most pronounced in the near wall region as was seen in the current study, see Figures 5.35 and 5.39. The authors also noted that the effect was more pronounced in the lower region of the pipe where a greater concentration of particles occurred, and believed there was a possibility that a maximum concentration existed. Beyond this increasing particle density no longer caused a reduction in turbulence intensity but instead caused the area of the

reduction to increase instead. This could not be tested here due to the orientation of the measurement system.

Zisselmar and Molerus, (1979) found that the presence of 50 μ m particles caused an increase in turbulence in the near wall region until a critical value of 3% by volume, only once the point had been passed did the particles begin to dampen the turbulence. This is a much greater concentration than the ones tested in this study and so it would not be possible to investigate this value however it correlates well with the findings of Wu et al., (2006) at much lower concentrations.

Zisselmar and Molerus, (1979) suggest that a reduction in turbulence is caused by mutual interaction of particles hindering the flow whereas the increase in turbulence they experienced is caused by the interaction of particles and eddies near the wall. They found the particle size was closely aligned with eddy size in the near wall region and suggest that this created a strong mutual influence which results in an increase in turbulence intensity. As the fluid velocity in this study is much greater it is possible that this mutual interaction does not occur and as such the particles only behave in such a manner as to dissipate turbulence.

Gore and Crowe, (1989) attempt to quantify whether a given particle will enhance or dissipate turbulence based on the ratio of particle diameter to length scale ratio with their results shown in Figure 5.44. The current data has been plotted using the same axes scaled to give a better view of the data and can be seen in Figure 5.45. They suggest a cut off for the ratio of particle diameter to characteristic eddy length of around 0.1, below this value particles will dissipate turbulence whereas above this value the presence of particles results in turbulence enhancement. From Figure 5.45 we can see that the current results are in reasonable agreement with this. Almost all of the tests which put the length scale ratio above 0.1 show enhancement of the turbulent fluctuations. Below this value the results are less

clear cut with some of the data showing enhancement and some showing suppression however the enhancement is generally very small and as the ratio continues to decrease the probability that a given test will show dissipation of turbulence increases.

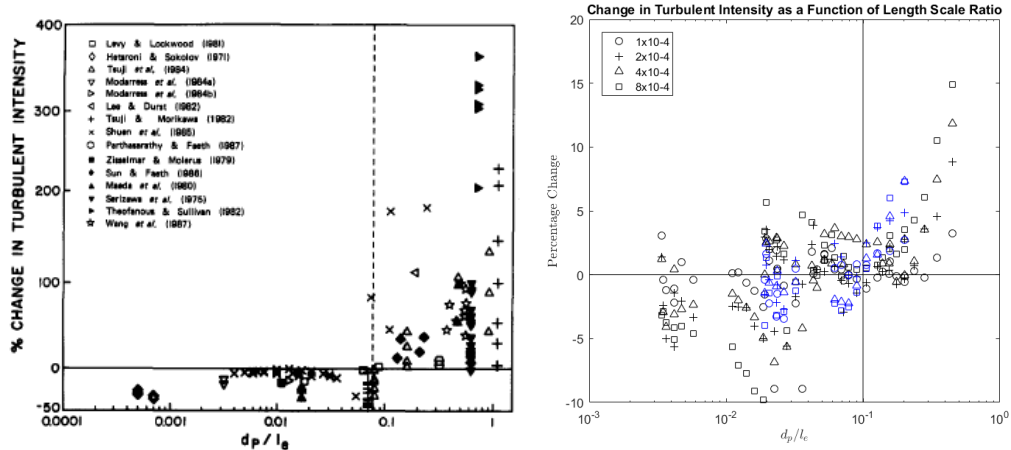


Figure 5.44 (left) – Change in turbulent intensity as a function of the ratio of particle diameter to characteristic eddy size Gore and Crowe (1989). Figure 5.45 (right) - Change in turbulent intensity as a function of the ratio of particle diameter to characteristic eddy size for PIV measurements.

Following this Hetsroni, (1989) proposed that particle Reynolds number can be used as an accurate indicator of the turbulence modulation effects. Stating that if the particle Reynolds number is above 400 turbulent enhancement occurs, due to vortex shedding by the particles. Below a particle Reynolds of 110 vortex shedding does not occur and so particles with smaller Reynolds numbers act to dissipate turbulence instead.

Figures 5.46 to 5.48 show approximate particle Reynolds numbers for Flashbead, Honite 8 and Honite 12 calculated using a combination of the UDV and PIV results. The relative change in fluid velocity with increased particle loading was calculated from the PIV results and used to calculate the fluid velocity in the acoustic system at particle volume fractions up to 8×10^{-4} using Equation 5.1.

$$Re_p = \frac{D_p(|U_p - U_f|)}{\nu}$$

Equation 5.1 – Calculation of particle Reynolds number (Re_p) where D_p = particle diameter, U_p =Particle Velocity, U_f = fluid velocity and ν = fluid kinematic viscosity

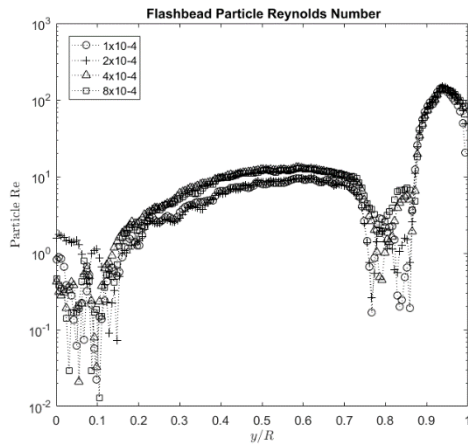


Figure 5.47 – Flashbead particle Reynolds number across the pipe.

From this we can see that for all the particle species the near wall region where $y > 0.9$ is where particle Reynolds number is greatest, however even in this region none of the particles have a Reynolds number greater than 350. In addition to this the three particle species display a transition zone, where particle and fluid velocities are closely aligned around $y = 0.9$. Approaching

the pipe centreline, the relative velocity of the Flashbead particles decays and particle Reynolds number decreases, this supports the theory that the Flashbead particles are more likely to follow the flow and cross streamlines gradually under constant acceleration by the flow. This contrasts with the Honite 8 which has a much more consistent particle Reynolds number of around 10 in the bulk flow region between the centreline and $y = 0.8$.

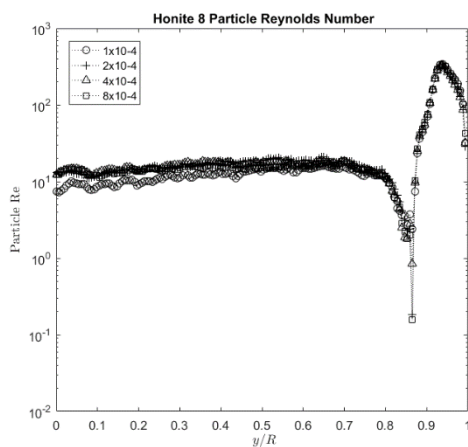


Figure 5.47(left) – Honite 8 particle Reynolds number across the pipe

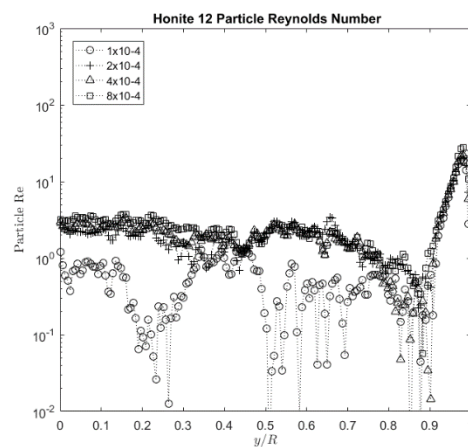


Figure 5.48 (right) – Honite 12 particle Reynolds number across the pipe

The particle Reynolds number of the Honite 12 is smaller than either the Honite 8 or Flashbead, in both the peak value of 28, (compared with 345 and 151 respectively) when $y > 0.9$ and in the bulk flow region ($0 < y < 0.8$) where the value fluctuates around a particle Reynolds number of 2. According to Hetsroni, (1989) this would mean that at no point could vortex shedding occur for the Honite 12 particles and as such fluid turbulence should be suppressed, however as seen in Figures 5.37 and 5.38 this is clearly not the case.

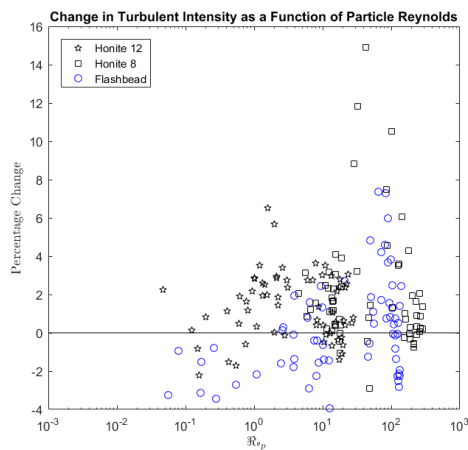


Figure 5.49 Percentage change in fluid turbulence with particle Reynolds number.

Figure 5.49 shows how particle Reynolds number effects fluid turbulence for the obtained data. It shows that particle Reynolds number is not a good indicator of whether a given particle will enhance or dissipate turbulence in the range of 1 to 400, below a particle Reynolds number of 1 particles tend to reduce fluid turbulence however more data would be required to

confirm this. The maximum magnitude of the turbulence modulation tends to increase as particle Reynolds increases for particles which enhance turbulence.

Elghobashi, (1994) suggested an alternative method for predicting turbulence modulation. Calculation of the ratio of particle response time to Kolmogorov length scale put the current flow regime in the region where Honite 22 and Honite 12 particles are predicted to dissipate turbulence at all tested concentrations and Honite 8 particles should enhance turbulence close to the wall ($y < 300$) and dissipate it elsewhere as can be seen in Figures 5.50 and 5.51. This is not the case with the current results and so although Elghobashi, (1994) attempts to introduce the effects of concentration, a critical component missing from the analysis of Gore and Crowe, (1989), the method is not robust enough to accurately predict the modulation effects of turbulence in this instance.

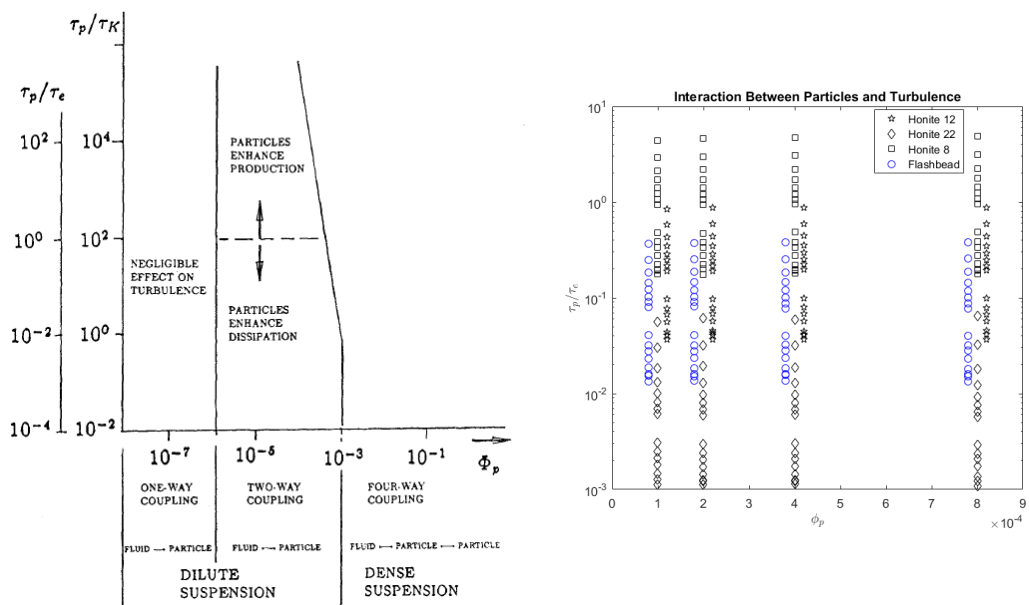


Figure 5.50 (left) - Map of regimes of interaction between particles and turbulence Elghobashi, (1994).
 Figure 5.51 (right) - Map showing locations of PIV results on a scaled version of Figure 5.50.

5.5 Conclusions

This chapter has demonstrated that PIV can be an effective tool for studying the behaviour of fluid flows, accurately capturing fluid velocity and turbulence statistics. It also however highlights one of the major difficulties in using optical measurement systems, in that the ability to make measurements is dependent on the clarity of the fluid being tested, and the geometry of the system. One of the major advantages of the whole field measurement technique could not be fully taken advantage of in this system as there were no significant differences in the measurements between the start and end of the measurement area. However, these will be realised in the following chapter where the fluid is divided into significantly different flow regions.

The effect of particle density and size on the fluid behaviour were explored, and both were shown to have an impact on the fluid, however the nature of a fully developed flow and the small particle concentration and relative density meant that these effects were small.

Importantly it was found that local particle concentration may be extremely significant in these studies and so in future studies it would be beneficial to attempt to quantify this to further explore the effect.

It was also found that varying the particle concentration can have a non-linear effect on velocity and turbulence modulation, with this likely due to differing particle-fluid and particle-particle interactions occurring as the concentration increases. Again, knowing the local particle concentration would be beneficial in exploring this further.

Work was performed comparing various methods for predicting the effects of particles on turbulence modulation. It was found that none of the methods tested could accurately predict the behaviour 100% of the time since none of the methods comprehensively account for all of the variables which effect how the particle impacts the flow. The method proposed by Gore and Crowe, (1989) appears to be reliable in predicting turbulent enhancement

however suffers when suppression is supposed to occur and fails to take into account particle concentration. The model suggested by Hetsroni, (1989) could not be fully tested as the calculated particle Reynolds numbers did not exceed 400 which was defined as the cut-off point above which enhancement occurs, however particle Reynolds numbers approaching 400 still showed suppression of the turbulence in some cases.

Elghobashi, (1994) created a map which considered concentration in addition to particle and flow properties, however this also struggled to accurately predict turbulent modulation. One of the reasons for this may be due to the tested particles falling into a boundary region between where turbulence should be dissipated or enhanced and so rather than a set value above which turbulence is either enhanced or dissipated it may be more realistic to define a transitional region where either or both can occur.

5.6 References

- Alajbegović, A., Assad, A., Bonetto, F. and Lahey, R.T. 1994. Phase distribution and turbulence structure for solid/fluid upflow in a pipe. *International Journal of Multiphase Flow*. **20**(3),pp.453–479.
- Elghobashi, S. 1994. On predicting particle-laden turbulent flows. *Applied Scientific Research*. **52**,pp.309–329.
- Gore, R. and Crowe, C. 1989. Effect of particle size on modulating turbulent intensity. *International Journal of Multiphase Flow*. **15**(2),pp.279–285.
- Hetsroni, G. 1989. Particles-turbulence interaction. *International Journal of Multiphase Flow*. **15**(5),pp.735–746.
- Hosokawa, S. and Tomiyama, A. 2004. Turbulence modification in gas – liquid and solid – liquid dispersed two-phase pipe flows. *International Journal of Heat and Fluid Flow*. **25**,pp.489–498.
- Kaftori, D., Hetsroni, G. and Banerjee, S. 1995. Particle behavior in the turbulent boundary layer. II. Velocity and distribution profiles. *Physics of Fluids*. **7**(5),pp.1107–1121.
- Laufer, J. 1954. The structure of turbulence in fully developed pipe flow. *Naca Tr 1174*,pp.417–434.
- Lee, S. and Durst, F. 1982. On the motion of particles in turbulent duct flow. *International Journal of Multiphase Flow*. **2**(8),pp.125–146.
- Marusic, I., Monty, J.P., Hultmark, M. and Smits, A.J. 2013. On the logarithmic region in wall turbulence. *Journal of Fluid Mechanics*. **716**.
- Rashidi, M., Hetsroni, G. and Banerjee, S. 1990. Particle-turbulence interaction in a boundary layer. *International Journal of Multiphase Flow*. **16**(6),pp.935–949.
- Righetti, M. and Romano, G.P. 2004. Particle-fluid interactions in a plane near-wall turbulent flow. *Journal of Fluid Mechanics*. (505),pp.93–121.
- Sommerfeld, M. and Huber, N. 1999. Experimental analysis and modelling of particle-wall collisions. *International journal of multiphase flow*. **25**(6–7),pp.1457–1489.
- Tsuji, Y. and Morikawa, Y. 1982. LDV measurements of an air-solid two-phase flow in a horizontal pipe. *Journal of Fluid Mechanics*. **120**(1982),pp.385–409.
- Tsuji, Y., Morikawa, Y. and Shiomi, H. 1985. LDV measurements of air- solid two-phase flow in a vertical pipe. *Journal of Fluid Mechanics*. **139**,pp.417–434.
- Wu, X. and Moin, P. 2008. A direct numerical simulation study on the mean velocity characteristics in turbulent pipe flow. *Journal of Fluid Mechanics*. **608**,pp.81–112.
- Wu, Y., Wang, H., Liu, Z., Li, J., Zhang, L. and Zheng, C. 2006. Experimental investigation on turbulence modification in a horizontal channel flow at relatively low mass loading. *Acta Mechanica Sinica/Lixue Xuebao*. **22**(2),pp.99–108.
- Zisselmar, R. and Molerus, O. 1979. Investigation of solid-liquid pipe flow with regard to turbulence modification. *The Chemical Engineering Journal*. **18**(3),pp.233–239.

6 Optical Measurements of Impinging Jets

This chapter will cover the use of particle image velocity and its use in studying the effect of particles on the flow behaviour of an impinging jet. Section 6.1 explores single phase measurements of impinging jets using PIV. Section 6.2 validates the single-phase results against other published results. Section 6.3 explores the effect of particle concentration and density on impinging jet flow. Section 6.4 then examines the influence of particle size on the fluid behaviour of an impinging jet. Section 6.5 contains preliminary velocity measurements of the solid phase of a multiphase impinging jet and compares particle behaviour with fluid behaviour. Section 6.6 provides a summary and conclusions for the chapter. Section 6.7 contains the references for Chapter 6.

6.1 Single Phase Measurements of Impinging Jets

Although a brief overview of the experimental set up is described here, the exact specifications of the impinging jet rig are detailed in Chapter 3. Single phase measurements were made with a water jet discharging from a 4 mm orifice perpendicularly onto the glass base of a square tank. The tank walls were located 200 mm from the jet centreline in all directions to minimise influence on the flow. The jet was positioned 24 mm above the base of the tank representing 6 diameters, henceforth represented as 6D. Fluid velocity was controlled using a needle valve with the flow rate set at 2.85 LPM, which gives a fluid velocity of 3.77 m/s and a Reynolds number at the jet orifice of 15,000. Like the pipe measurements the fluid was tracked using 1-20 μm polyamide tracer particles.

6.1.1 Flow Visualisations

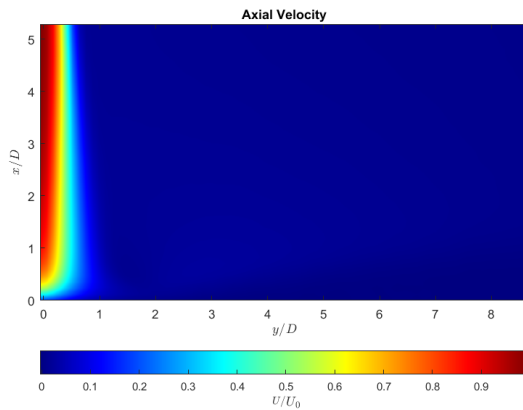


Figure 6.1 – Axial velocity contour plot from PIV measurements of the impinging jet.

A visualisation of the axial velocity is shown in Figure 6.1. From this we can see the expansion of the jet as the surrounding fluid is entrained and accelerated towards the base of the tank. The length of the jet potential core is in agreement with the findings of Bogusławski and Popiel (1979) who state that the core extends between 4

and 9D. This is the region where the jet retains most its velocity and extends to around $0.5x/D$. This is in agreement with the findings of Gutmark et al. (1978), who found the velocity of the jet was unaffected by the impingement surface for up to 75% of the jet length.

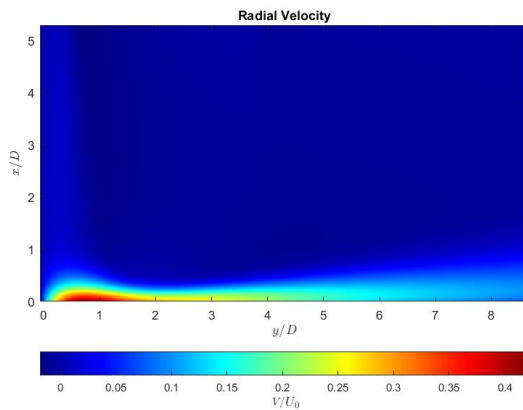


Figure 6.2 – Radial velocity contour plot from PIV measurements of the impinging jet.

Beyond $0.5x/D$ upstream influence from the base of the tank causes rapid deceleration of the flow. In this region, the flow is redirected radially as can be seen in Figure 6.2 which displays the radial velocity of the flow. We can see that the for the free jet region there is very little radial velocity

and it is only in the impingement region where radial movement of the fluid becomes relevant. Peak radial velocity occurs around $0.5y/D$ very close to the impingement surface, in excellent agreement with Tummers et al. (2011). Correlating with the findings of Cooper et al. (1993), and Fairweather and Hargrave (2002), we see that beyond $1.5y/D$ the fluid begins to decelerate as the radial wall jet expands vertically from the base of the tank.

Axial turbulence measurements are shown in Figure 6.3 and clearly show the turbulent mixing layer which surrounds the potential core. From this we can see that there is both an increase in turbulent intensity and thickness of this turbulent region as the jet develops.

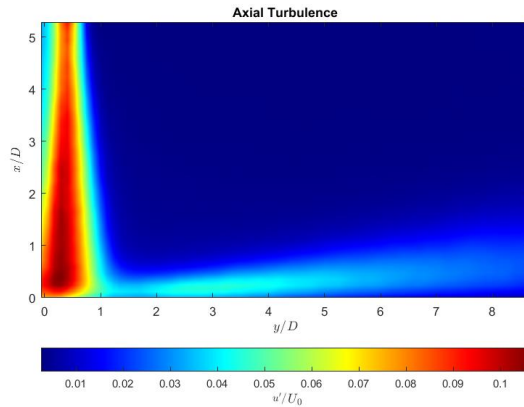


Figure 6.3 – Axial turbulence contour plot from PIV measurements of the impinging jet.

As expected from the results of Era and Saima (1976), due to the Reynolds number of the free jet, the resulting wall jet is also turbulent. We can also see there is a secondary peak in the axial turbulent intensity in the developing wall jet, this

increase coincides with the location of boundary layer separation identified by Landreth and Adrian (1990), where flow reversal would result in an increase in axial velocity fluctuations.

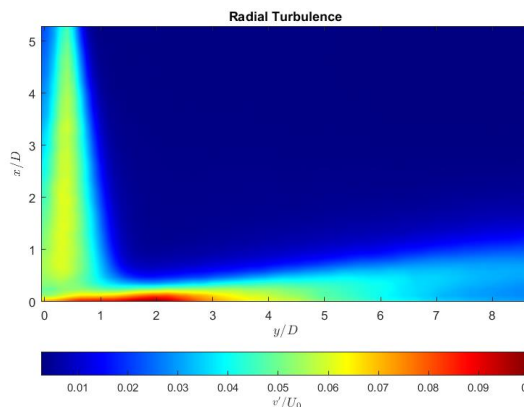


Figure 6.4 – Radial turbulence contour plot from PIV measurements of the impinging jet.

Like the axial turbulence measurements, the radial measurements in Figure 6.4 clearly show the turbulent mixing layer either side of the potential core, however as the jet develops the same increase in turbulent intensity is not seen.

That is until the impingement zone, where the redirection of the flow results in high levels of velocity fluctuations. This peak occurs around $2y/D$ beyond which the expansion of the wall jet leads to a gradual reduction in turbulent intensity.

6.1.2 Horizontal Velocity Flow Profiles

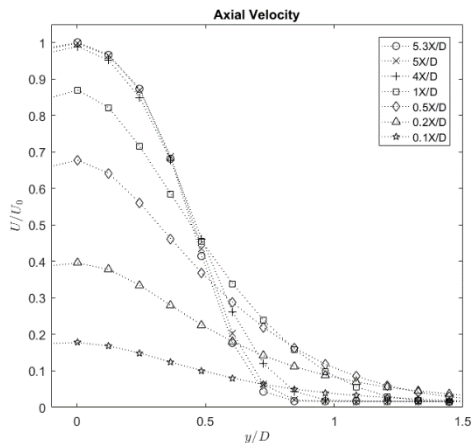


Figure 6.5 – Change in jet axial velocity as impingement plate is approached.

reduction of the jet centreline velocity at $1X/D$. As the jet continues to progress the upstream effects of the impingement surface begin to materialise and between $0.5X/D$ and $0.1X/D$ the velocity of the jet reduces from around 70% of the outlet velocity to around 20%. As the jet develops we also see axial acceleration of the surrounding flow, as fluid is entrained and the jet spreads radially.

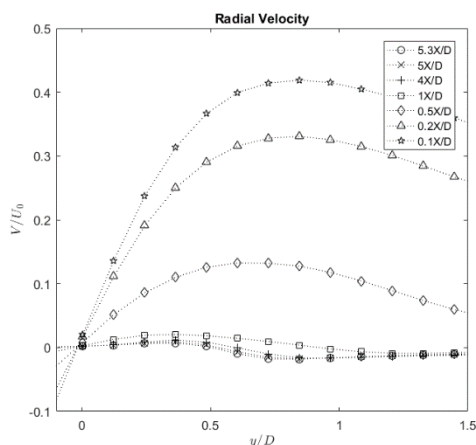


Figure 6.6 – Change in jet axial velocity as impingement plate is approached

upstream pressure becomes dominant and the flow is accelerated away from the jet

Axial velocity measurements are given for varying distances from the impingement plate in Figure 6.5. From this we can see there is very little change in jet velocity between the jet outlet and $4X/D$, with the profiles remaining very similar in magnitude and shape. As the flow continues to progress towards the plate we can see that there has been a 10%

This can also be seen in Figure 6.6 which shows the radial velocity measurements at the same locations. Slight negative velocities, the result of fluid entrainment, can be seen when $y/D > 0.5$ for the measurements outside of the influence of impingement i.e. $X/D \geq 1$. Beyond this, redirection of the jet radially due to

centreline. As the impingement surface is approached the maximum radial velocity increases significantly, in addition to moving outwards radially.

6.1.3 Horizontal Turbulence Flow Profiles

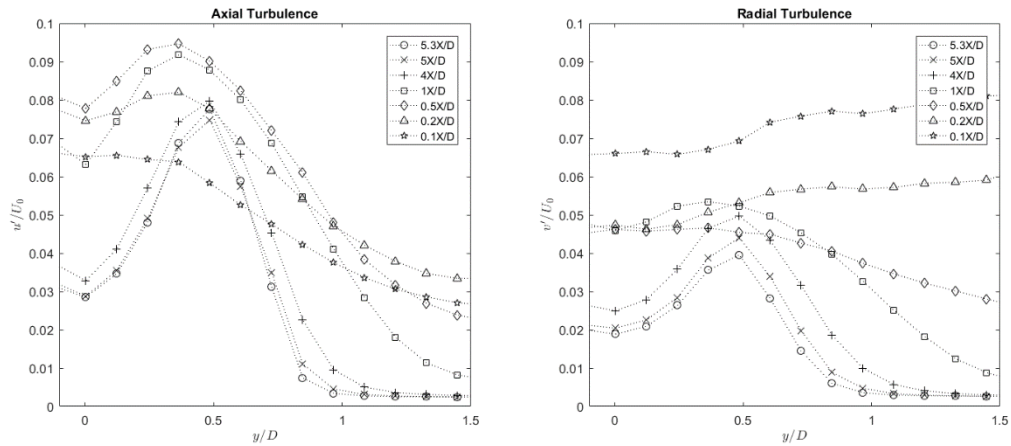


Figure 6.7 (left) - Change in axial turbulence as impingement plate is approached.

Figure 6.8 (right) - Change in radial turbulence as impingement plate is approached.

Axial turbulence measurements are shown in Figure 6.7. Here we can clearly see characteristic peak of the shear mixing layer in the free jet region ($X/D > 1$) this is a region of high turbulence which surrounds the potential core of the jet. In this region, peak turbulence measurements occur at $y/D = 0.5$. As the jet develops the magnitude of the axial turbulence initially increases, reaching a maximum of 0.095 at $X/D = 0.5$, before reducing as the jet reaches impingement. In this region we also see a flattening of the profile as expansion of the shear mixing layer occurs, this results in an increase in centreline turbulence measurements which is consistent with the findings of Fitzgerald and Garimella (1998) who found centreline turbulence measurements increased by over 60% as the jet approached the impingement region. The larger increase seen here can be attributed to the higher Reynolds number of the jet and increased jet height.

A similar behaviour can be observed for the radial turbulence profiles shown in Figure 6.8, with a flattening of turbulence profiles present. However, in this case there is no reduction

of turbulence near impingement, instead radial turbulent fluctuations continually increase as the impingement surface is approached. It can also be seen that in the free jet region maximum radial turbulence measurements are around half that of the axial, as seen by Hammad and Milanovic (2011).

6.1.4 Vertical Velocity Flow Profiles

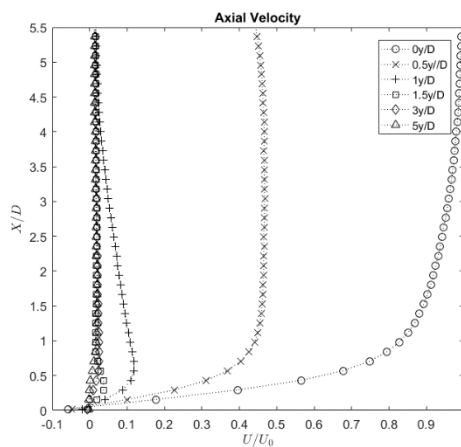


Figure 6.9 – Change in axial velocity as distance from the jet centreline is increased.

Figure 6.9 displays the change in axial velocity at different radial distances from the jet centreline. We can clearly see the reduction of the centreline velocity as the impingement surface is approached, with a gradual deceleration in the free jet region as fluid velocity is diminished from the potential core as the shear mixing layer grows. This occurs until around $1X/D$, at

this point the upstream effects of impingement become dominant and the deceleration becomes much more significant. The velocity in the shear mixing layer ($0.5y/D$) remains fairly constant at around 45% of the centreline velocity, until the impingement region is reached where again the flow is rapidly decelerated. At $y/D = 1$ the velocity increases as the jet develops, this is due to expansion of the jet and entrainment accelerating the fluid around the jet towards the base of the tank. Beyond $1D$ from the centreline the jet has almost no effect, except for the small region where the radial wall jet develops. We also see very slight negative velocities at the measurement location closest to the plate, which represents the expansion of the radial wall jet as it develops across the base of the tank.

Figure 6.10 displays the radial velocities at the same measurement locations; here we see the rapid acceleration of the jet radially in the impingement region. Like the experiments of

Loureiro and Freire (2012), and Fitzgerald and Garimella (1998) the maximum radial velocity occurred 1D from the jet centreline.

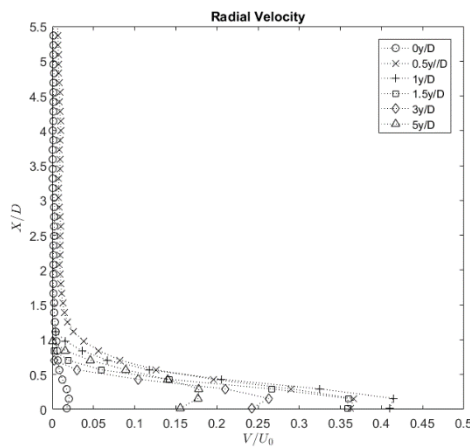


Figure 6.10 – Change in radial velocity as distance from the jet centreline is increased.

whereas Fitzgerald and Garimella (1998) were able to take measurements at $x/D = 0.02$, this value is not possible in the present study. The authors found the maximum velocity was 63% at $0.1X/D$ which would support the fact that the differences between the two experiments result from differences in measurement location.

The authors recorded a maximum velocity at this point of 89% of the jet centreline outlet whereas the current study found the maximum reached 41% of the outlet centreline velocity before deceleration due to expansion of the jet. This difference can be attributed to the difficulty in making

measurements very close to the plate,

6.1.5 Vertical Turbulence Flow Profiles

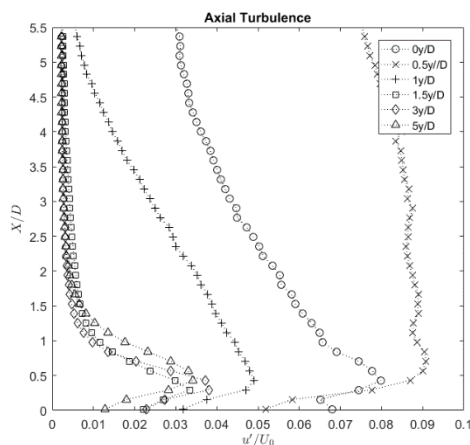


Figure 6.11 – Change in axial turbulence as distance from the jet centreline is increased

Axial turbulence profiles are shown in Figure 6.11; here it can be seen that maximum axial turbulence occurs within the turbulent mixing layer at $0.5y/D$ and remains around 9% of the centreline velocity as the jet develops; before undergoing a significant reduction in the stagnation region. We can also see the gradual increase in centreline turbulence

downstream of the jet orifice and the radial expansion of the shear mixing layer causing an

increase in turbulence 1D from the jet centreline. Further from the centreline, turbulence is minimal until close to the impingement surface where there is a growing turbulent boundary layer above the spreading radial wall jet.

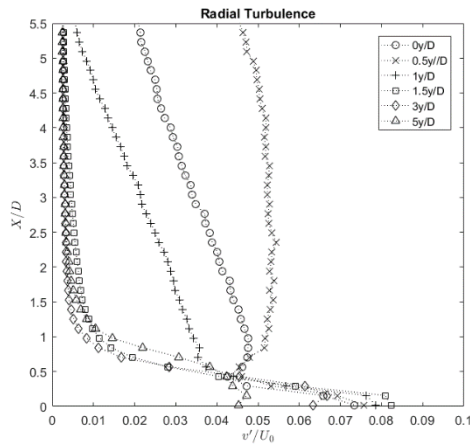


Figure 6.12 – Change in radial turbulence as distance from the jet centreline is increased.

For the radial turbulence measurements, the same growth and expansion can be seen of the turbulent mixing layer in the 0y/D and 1y/D profiles, with a steady increase in turbulence as the jet develops. For most the jet the maximum turbulence value is found in the shear mixing layer at $y/D=0.5$, this is until we reach the radial

wall jet, where maximum turbulence is found at 0.1X/D and 1.5y/D. This location is in agreement with the findings of Loureiro and Freire (2012) who also found peak radial turbulence occurred at 0.1X/D and y/D of 1.72 (the closest measurement point to 1.5 y/D).

6.2 Validation of Results

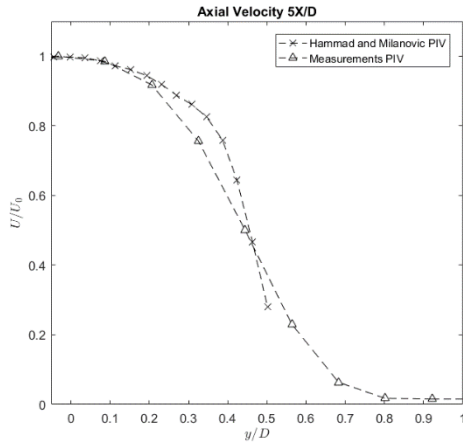


Figure 6.13 – Comparison of axial velocity horizontal flow profile with the PIV results of Hammad and Milanovic (2011).

see good agreement between the current PIV measurements and those of Hammad and Milanovic (2011), there is a slight change in the shape of the velocity profile due to the limitations of the measurement system. The measurements in the current study were at a

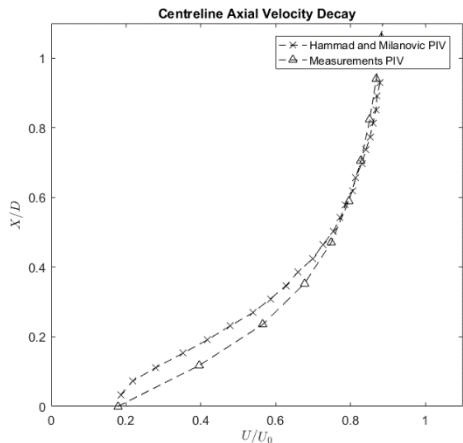


Figure 6.14 – Comparison of current PIV axial velocity decay with the PIV results of Hammad and Milanovic (2011).

decay within the impingement region, again the results are in a reasonable agreement with literature. Variation very close to the impingement plate $X/D < 0.4$ can again be attributed to averaging errors in the region of high velocity gradients.

Figure 6.13 shows the axial velocity recorded 1D from the jet outlet, compared with similar measurements made by Hammad and Milanovic (2011) who studied how jet-plate separation influenced the flow structure of impinging water jets. The data in Figure 6.13 is taken from a jet discharge height of $6D$ and a Reynolds number of $15,895$. Here we can

lower relative resolution so less data points could be captured within the bulk of the jet. Interrogation areas with high velocity gradients are prone to averaging errors, which is the case found in the shear mixing layer which surrounds the potential core of the jet.

Figure 6.14 shows the centreline velocity

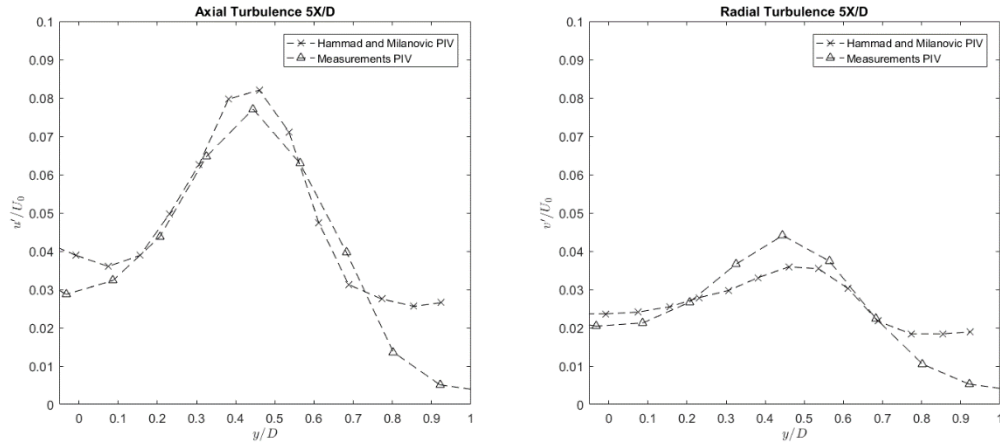


Figure 6.15 (left) – Comparison of current axial turbulence with the PIV results of Hammad and Milanovic (2011). Figure 6.16 (right) – Comparison of current radial turbulence with the PIV results of Hammad and Milanovic (2011).

Comparisons of the axial and radial RMS measurements 1D from the jet outlet are given in Figures 6.15 and 6.16. Again, we have good agreement between the two data sets with the profile shape and magnitude of the values aligning closely. Peak turbulence occurs around $0.5y/D$ for both axial and radial measurements with significant anisotropy present with the magnitude of the axial turbulence around double that of the radial turbulence.

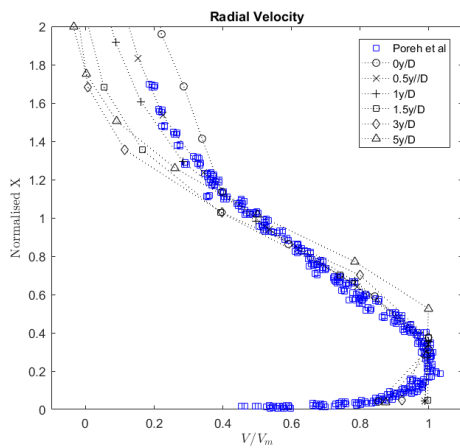


Figure 6.17 – Comparison of current PIV axial velocity with the results of Poreh et al., (1967)

divided by the distance between the plate and the location where the radial velocity (V) is half that of the maximum radial velocity (V_m). This is clarified in Equation 6.1.

Poreh et al. (1967) showed that the expanding radial wall jet can be collapsed to show self-similarity by dividing the radial velocity (V) by the maximum radial velocity at that radial distance from the centreline (V_m), and plotting the resultant value against a normalised X axis where the axial

distance from the impingement surface is

$$\text{Normalised } X = \frac{X}{x_{V_m=0.5}}$$

Equation 6.1 - X = axial distance from impingement surface, $x_{V_m=0.5}$ = axial distance from impingement where radial velocity is 0.5 its maximum.

By applying this normalisation to our results we can see that there is a good agreement between the results of Poreh et al., (1967) and the current study with the results collapsing to a reasonable degree. It is possible a better collapse would be possible if more measurement points were available to more accurately locate the point where $V_m = 0.5$.

Turbulence measurements with the same X normalisation have been plotted in Figures 6.18 and 6.19. Here we can see that there is a slight discrepancy between the axial measurements and the data of Poreh et al. (1967). Like before the most likely explanation is the measurement technique struggling in this region due to a combination of very low flow velocities and high velocity gradients. The radial turbulence measurements are however in good agreement, lending credibility to the idea that low velocities are in fact responsible for the slight discrepancies.

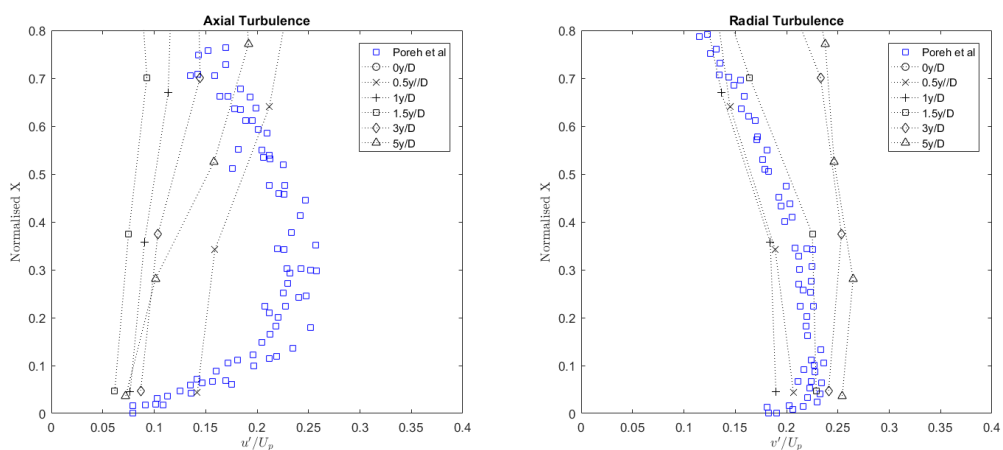


Figure 6.18 (left) – Comparison of current PIV axial turbulence with the results of Poreh et al., (1967).

Figure 6.19 (right) – Comparison of current PIV radial turbulence with the results of Poreh et al., (1967).

6.2.1 Discussion

As shown in this section PIV is more than capable of being used to measure the changing environment of the impinging jet. The technique works very well in capturing the behaviour of the free jet and although slight discrepancies between this jet and the published data exist in the impingement region, none of these are of the magnitude to prevent confidence in the results. The fact that PIV is a whole field measurement technique is one of the major advantages of using it to study changing flows such as an impinging jet, and the flow visualisations allow for a much clearer understanding of the jet behaviour.

The fact that all measurement locations are captured simultaneously reduces possible error due to outside influences such as pump behaviour or temperature changes which could affect the results if the measurements were taken sequentially.

Due to the rapidly changing nature of an impinging jet and the numerous variables which can affect the velocity and turbulence profiles, further comparisons with a like-for-like system proved difficult due to a lack of available data. However, validation was performed against a variety of published data sets. Good agreement of velocity and turbulence profiles at the jet outlet and the velocity decay in the impingement region coupled with the flow visualisations showing the expected flow features allows confidence in the results when making further analysis.

6.3 Effect of Particle Concentration and Density on Impinging Jet Flow

Table 6.1 – Honite 12 particle properties.

Honite 12	
Particle Diameter (μm)	225
Particle Density (kg m^{-3})	2450
Particle Material	Silica Glass
Particle Settling Velocity (m s^{-1})	39.92×10^{-3}
Particle Response Time (ms)	6.9

are added to the flow to create set volume fractions as done previously for the pipe flow experiments with the particle properties given in Tables 6.1 and 6.2, respectively.

Table 6.2 – Flashbead particle properties.

Flashbead	
Particle Diameter (μm)	225
Particle Density (kg m^{-3})	1050
Particle Material	Styrene Divinylbenzene Copolymer
Particle Settling Velocity (m s^{-1})	1.37×10^{-3}
Particle Response Time (ms)	2.9

profiles have been separated to show how the flow changes between measurement locations, unlike in the previous section where all measurement locations are combined on the same plot. For this reason, four horizontal and four radial profiles have been selected in various regions of the flow. The four horizontal profiles have been selected at 5, 1, 0.5 and 0.2X/D as this gives reasonable characterisation of the free jet and impingement region. 0, 0.5, 1, and 5y/D were selected as the radial profiles to give an overview of both the radial wall jet and the change in turbulence within the shear mixing layer. A visual representation of these locations can be seen in Figure 6.20.

This section will explore the response of the fluid phase of the jet to the introduction of particles at various concentrations. In addition, the change in response between two particle densities will be explored. Honite 12 glass particles and Flashbead polystyrene particles

To aid clarity when examining the data the flow profiles have been separated to show how the flow changes between measurement locations, unlike in the previous section where all measurement locations are combined on the same plot. For this reason, four horizontal and four radial profiles have been selected in various regions of the flow. The four horizontal

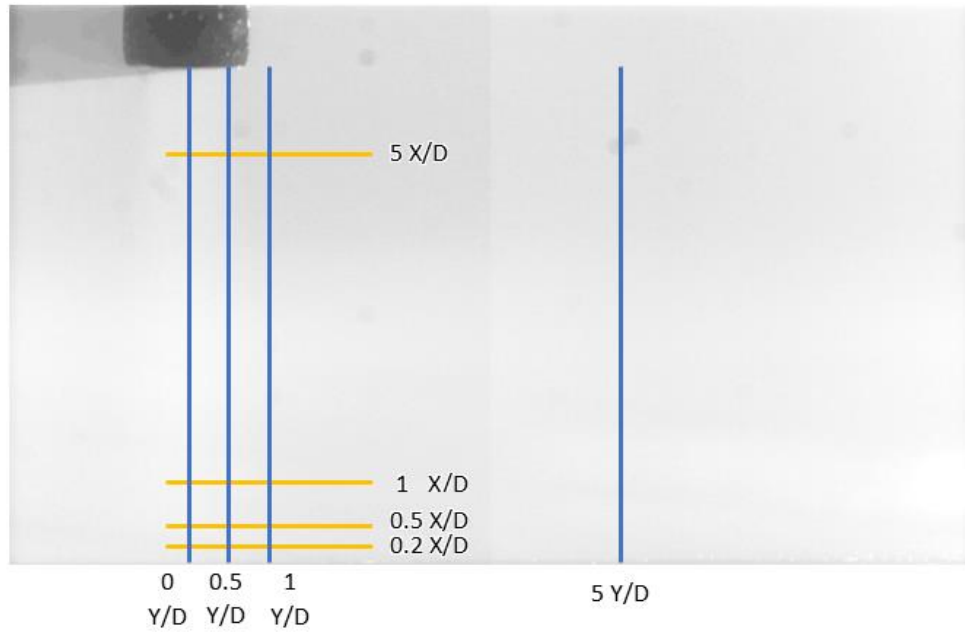


Figure 6.20 – Diagram of impinging jet measurement locations, yellow shows the location of the horizontal profiles whereas blue shows the location of the vertical profiles.

The volume fractions tested and the mass of particles added to the flow for each concentration are given in Tables 6.3 and 6.4. As seen with the pipe flow measurements, difficulty arises in obtaining measurements as the particle concentration increases, as the laser must travel through significantly more particle-laden fluid. Due to the geometry of the test tank the maximum particle concentration tested had to be reduced and so measurements were only made up to a volume fraction of 4×10^{-4} .

Table 6.3 – Mass of Honite particles for a given volume fraction.

Honite Particle Loading					
Run #	Volume Fraction	Particle Mass (g)	Run #	Volume Fraction	Particle Mass (g)
1	0	0	3	2×10^{-4}	58.8
2	1×10^{-4}	29.4	4	4×10^{-4}	117.6

Table 6.4 – Mass of Flashbead particles for a given volume fraction.

Flashbead Particle Loading					
Run #	Volume Fraction	Particle Mass (g)	Run #	Volume Fraction	Particle Mass (g)
1	0	0	3	2×10^{-4}	25.2
2	1×10^{-4}	12.6	4	4×10^{-4}	50.4

6.3.1 Horizontal Velocity Flow Profiles

Like in the pipe flow measurements, the Honite 12 particle measurements are plotted against the right-hand axis and the Flashbead particle measurements on the left-hand axis.

6.3.1.1 Axial Horizontal Velocity Profiles

Figures 6.21 and 6.22 display the axial velocity at 5 and 1 X/D for both the Flashbead and Honite 12 particles. From Figure 6.21 we can see that there is almost no change in the velocity at the outlet as particle concentration is increased, and this is true for both the Honite 12 and Flashbead Particles.

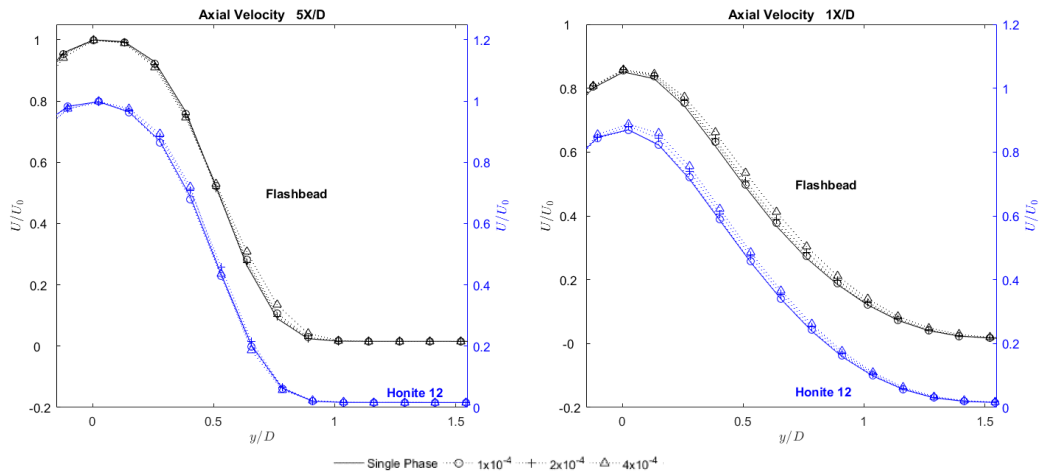


Figure 6.21 (left) – Change in axial velocity with increased Honite 12 and Flashbead particle concentration 5D from impingement. Figure 6.22 (right) – Change in axial velocity with increased Honite 12 and Flashbead particle concentration 1D from impingement.

However, as the jet develops we can see that the presence of particles causes a slight reduction in the deceleration of the jet. At 1X/D the 4×10^{-4} concentration of Honite 12

particles cause the centreline velocity to retain an additional 2.0% of its centreline velocity and the Flashbead particles retained 1.1%. This effect is much more pronounced in the impingement region as can be seen in Figures 6.23 and 6.24. The highest volume fraction of Honite 12 particles results in a 4.9% increase in centreline velocity at 0.5X/D and a 14.8% increase at 0.2X/D, when compared with the single-phase results. As the concentration of Honite 12 is increased the velocity retention increases, however the same behaviour is not seen with the less dense Flashbead particles. The centreline velocity retention initially increases as particles are added, however the retention is the same for both the 2×10^{-4} and 4×10^{-4} volume fractions suggesting that past a certain limit further increasing the particle concentration has no effect on the fluid velocity. At 0.5X/D centreline velocity is increased by 1.6% for both volume fractions of Flashbead particles, and at 0.2X/D the velocity increase is 5.0%.

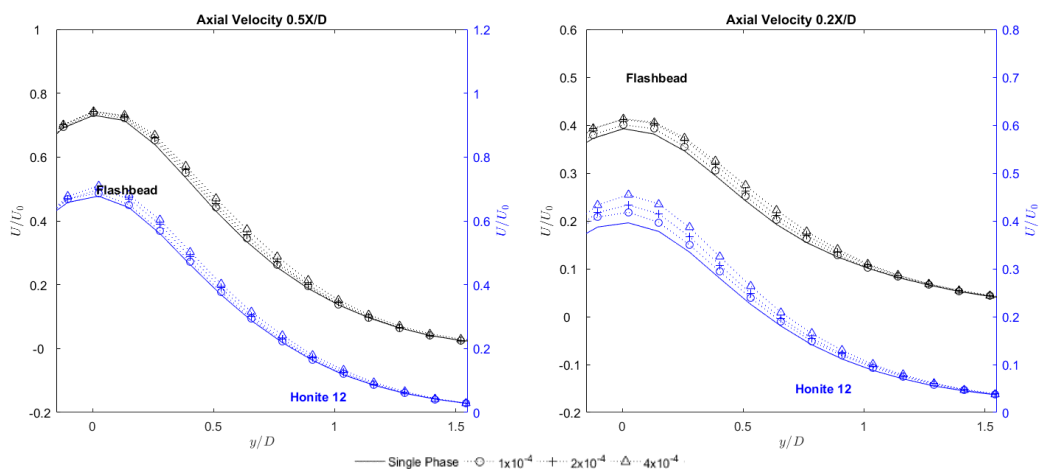


Figure 6.23 (left) – Change in axial velocity with increased Honite 12 and Flashbead particle concentration 0.5D from impingement. Figure 6.24 (right) – Change in axial velocity with increased Honite 12 and Flashbead particle concentration 0.2D from impingement.

6.3.1.2 Radial Horizontal Velocity Profiles

Radial velocity profiles are given in Figures 6.25 and 6.26, here we can see that both particle types have almost no influence on the radial velocity of the jet in the free jet region. The Honite 12 particles can be seen to cause a slight narrowing of the jet, shown in Figure 6.25,

confirmed by the earlier transition from expansion to entrainment as the radial velocity moves from positive in the expanding jet to negative in the surrounding fluid being drawn towards the jet.

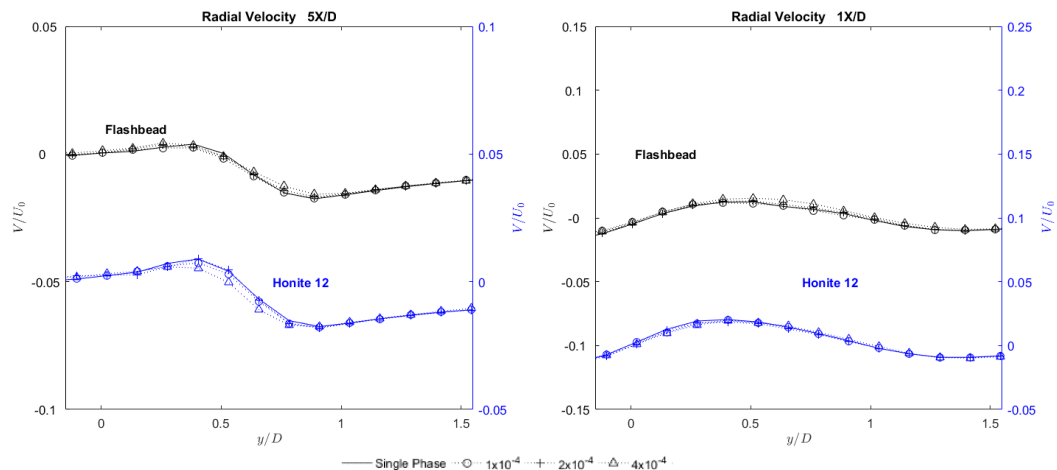


Figure 6.25 (left) – Change in radial velocity with increased Honite 12 and Flashbead particle concentration 5D from impingement. Figure 6.26 (right) – Change in radial velocity with increased Honite 12 and Flashbead particle concentration 1D from impingement.

Figures 6.27 and 6.28 show the radial velocity profiles in the impingement region. At 0.5X/D the Flashbead particles have almost no effect on the radial velocity, however we observe that the Honite 12 particles restrict the radial acceleration of the flow, with the maximum radial velocity at a volume fraction of 4×10^{-4} , 6.5% less than the single-phase flow. Progressing to 0.2X/D we see that in this region both the Honite and Flashbead particles restrict the radial acceleration of the flow. Interestingly, increasing the concentration of Honite 12 has little effect in this region and like the axial velocity measurements the effects remain the same for both the 2×10^{-4} and 4×10^{-4} volume fractions with a maximum velocity decrease of 5.8%.

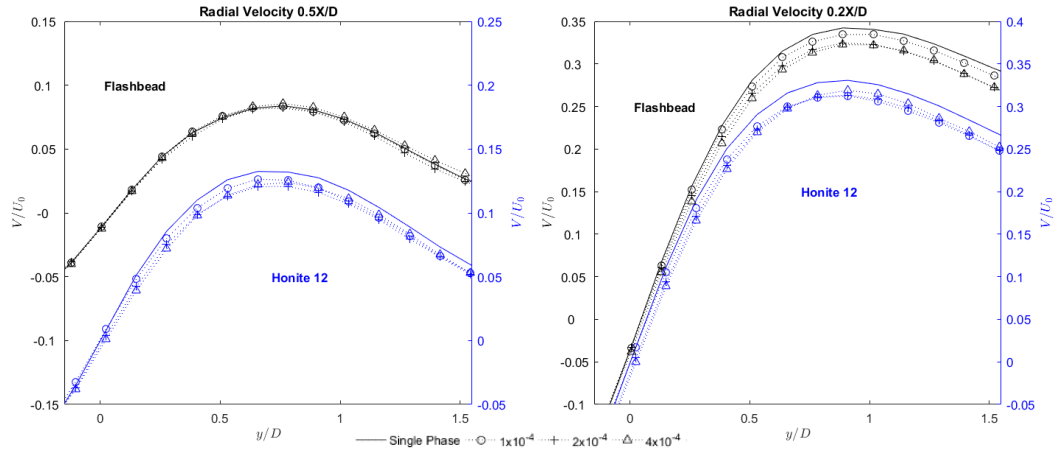


Figure 6.27 (left) – Change in radial velocity with increased Honite 12 and Flashbead particle concentration $0.5D$ from impingement. Figure 6.28 (right) – Change in radial velocity with increased Honite 12 and Flashbead particle concentration $0.2D$ from impingement.

6.3.1.3 Velocity Percentage Changes

Figures 6.29 and 6.30 show the percentage change in axial and radial velocity at $1X/D$. From the data, we can see the effect of particle loading towards the end of the free jet region. Also, it is clearly shown that Honite 12 particles are reducing spreading of the jet, causing axial centreline velocity to remain higher while the region outside of the potential core is accelerated more slowly. This is coupled with a reduction in the radial velocity in this region. We also observe that the lowest particle loading ($\varphi = 1 \times 10^{-4}$) has very little effect for both particle species. Flashbead particles have almost no effect in the potential core of the jet, and this is independent of particle concentration. Moving radially away from the jet centreline, axial velocity is enhanced in the presence of the Flashbead particles once the volume fraction has reached 4×10^{-4} . There is an inflection point in the radial velocity at $y/D = 1$ where a sudden transition from suppression of the flow to enhancement occurs, with this being present for both particle species, suggesting that the presence of particles suppresses velocity within the jet but enhances it outside the jet periphery. The magnitude of the percentage change is large due to very small velocities in this region and so any change is massively amplified.

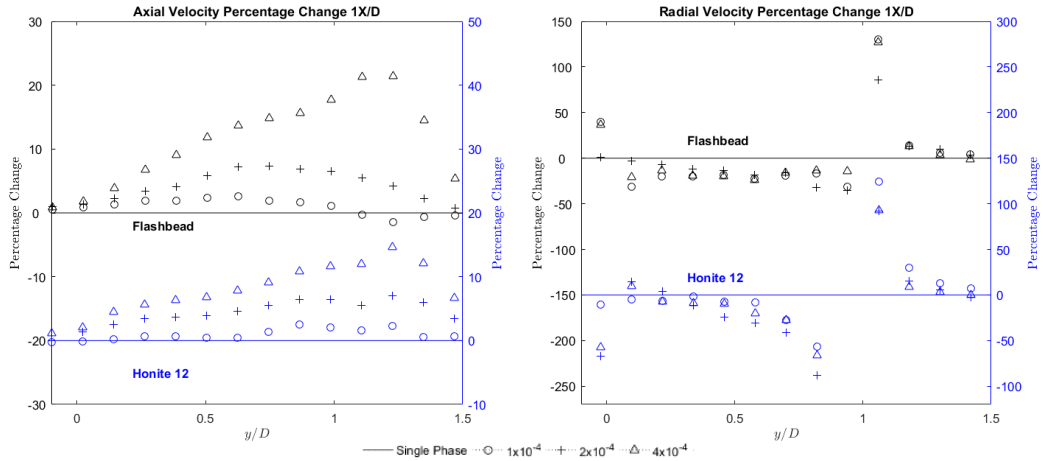


Figure 6.29 (left) – Percentage change in axial velocity with change in Honite 12 and Flashbead particle loading 1D from impingement. Figure 6.30 (right) – Percentage change in radial velocity with change in Honite 12 and Flashbead particle loading 1D from impingement.

The velocity percentage change at the various particle concentrations for the 0.2X/D profiles are displayed in Figures 6.31 and 6.32. When Flashbead particles are added, there is almost no change between the 2×10^{-4} and 4×10^{-4} volume fractions, for either the axial or radial velocity measurements, whereas for the radial measurements when $y/D > 0.5$ the velocity is independent of the Honite 12 particle volume fractions, but the axial velocity continues to increase as volume fraction increases.

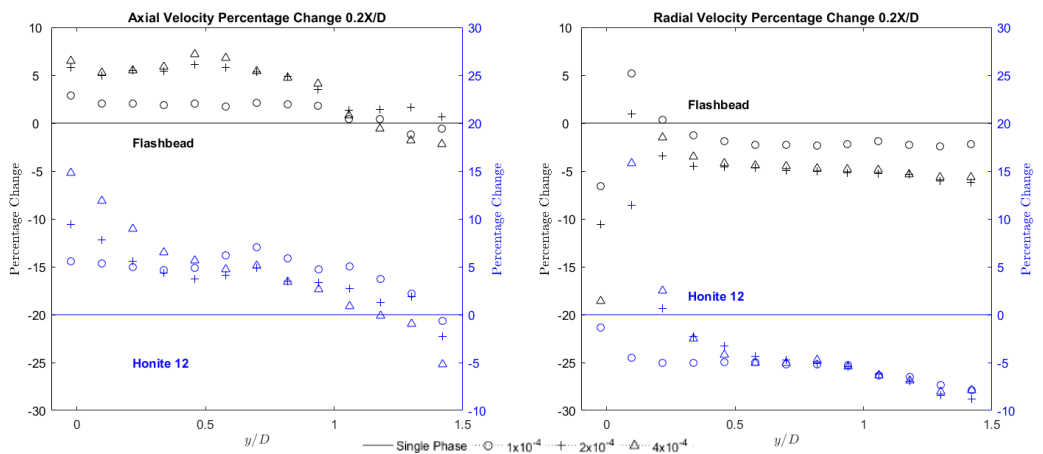


Figure 6.31 (left) – Percentage change in axial velocity with change in Honite 12 and Flashbead particle loading 0.2D from impingement. Figure 6.32 (right) – Percentage change in radial velocity with change in Honite 12 and Flashbead particle loading 0.2D from impingement.

6.3.2 Horizontal Turbulence Flow Profiles

6.3.2.1 Axial Horizontal Turbulence Profiles

At 5X/D axial turbulence is enhanced across the entire jet by both Honite and Flashbead particles shown in Figure 6.33. The Flashbead particles show a very slight enhancement either side of the maximum turbulence location at $y/D = 0.5$ at all particle concentrations, however only the highest volume fraction of 4×10^{-4} has any effect on the centreline velocity. The Honite 12 particles have almost no effect until $\varphi \geq 2 \times 10^{-4}$ at which point turbulence is enhanced significantly, with maximum axial turbulence measurements increasing 18.4% at $\varphi = 2 \times 10^{-4}$ and 82.2% at $\varphi = 4 \times 10^{-4}$.

As the jet develops the influence of particles on turbulence is lessened, this is caused by both an increase in the single-phase turbulence and a reduction in the maximum turbulence value recorded in the presence of particles as can be seen in Figure 6.34. From Figure 6.34 we observe a slight reduction in the axial turbulence in the presence of the Flashbead particles, which can be seen in more detail in the percentage changes shown in Figure 6.41.

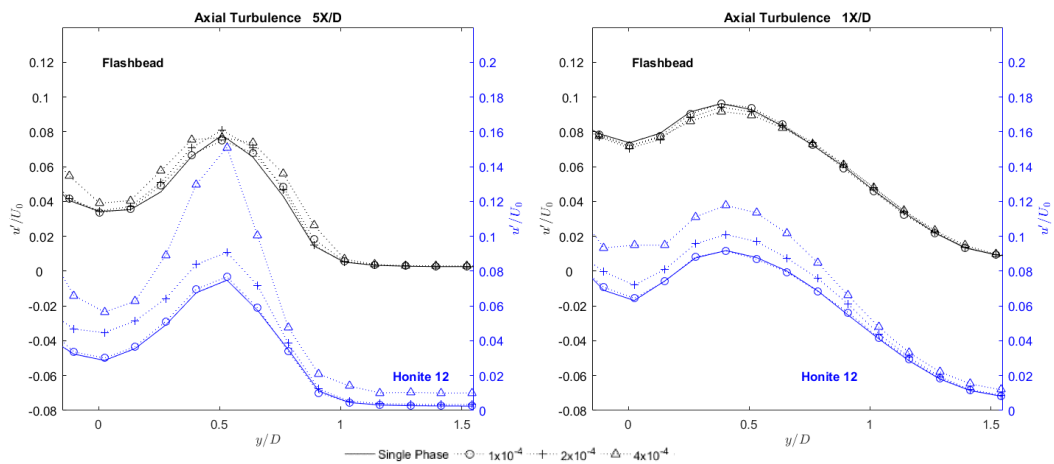


Figure 6.33 (left) – Change in axial turbulence with increased Honite 12 and Flashbead particle concentration 5D from impingement. Figure 6.34 (right) – Change in axial turbulence with increased Honite 12 and Flashbead particle concentration 1D from impingement.

Impingement region axial turbulence profiles are shown with measurements taken at 0.5D and 0.2D from impingement, see Figure 6.35 and Figure 6.36. At both 0.5X/D and 0.2X/D the Flashbead particles continue to cause a slight reduction in axial turbulence within the jet with a 4.9% reduction from the single phase seen at $y/D = 0.3$, and $X/D = 0.5$ seen in Figure 6.35. In keeping with the previous profile locations, the Honite 12 particles continue to enhance axial turbulence with the magnitude of enhancement increasing with increased solids concentration.

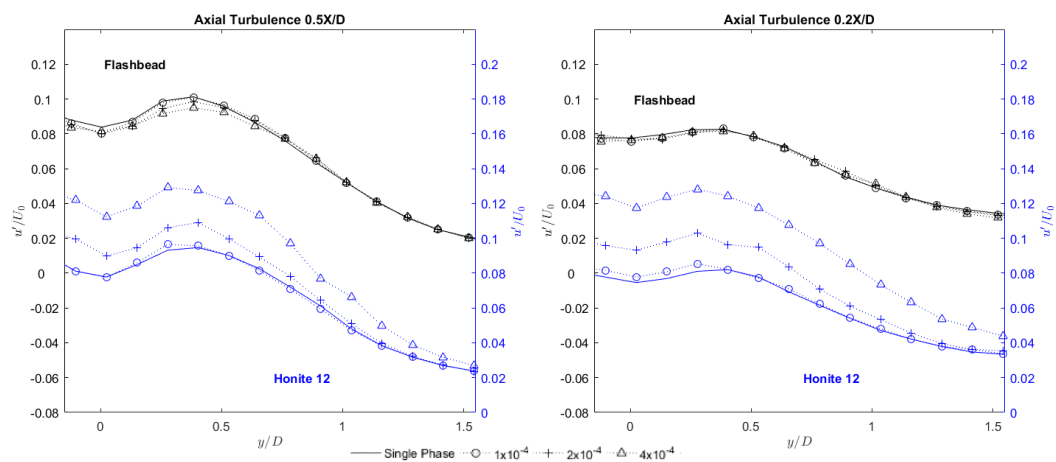


Figure 6.35 (left) – Change in axial turbulence with increased Honite 12 and Flashbead particle concentration 0.5D from impingement. Figure 6.36 (right) – Change in axial turbulence with increased Honite 12 and Flashbead particle concentration 0.2D from impingement.

6.3.2.2 Radial Horizontal Turbulence Profiles

Radial turbulence measurements are presented in Figures 6.37 to 6.41. From these we observe the evolution of radial turbulence as the jet develops. Whereas the Flashbead particles enhanced axial turbulence at 5X/D the radial turbulence is suppressed across the jet at this location. As the jet develops, suppression of the radial turbulence by the Flashbead particles is maintained at the jet centreline, with most the jet also exhibiting suppression.

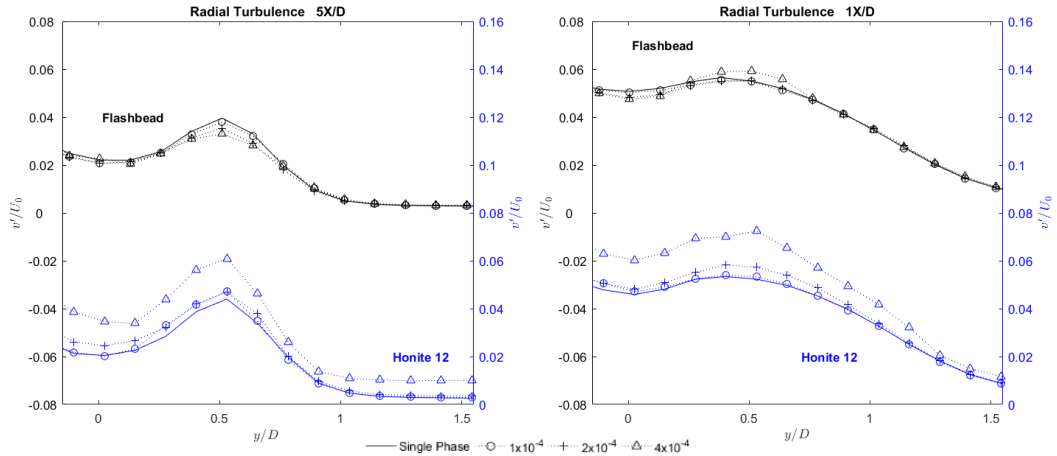


Figure 6.37 (left) – Change in radial turbulence with increased Honite 12 and Flashbead particle concentration 5D from impingement. Figure 6.38 (right) – Change in radial turbulence with increased Honite 12 and Flashbead particle concentration 1D from impingement.

There are some slight exceptions including a region of enhancement seen at the maximum radial turbulence value of $y/D = 0.5$ when the particle volume fraction increased to 4×10^{-4} , 1D from impingement. At $0.5X/D$ the Flashbead particles can be seen to minimally suppress turbulence at the centreline but have no significant effect beyond $y/D = 0.5$ and at the closest measurement location to impingement ($0.2 X/D$), the effect of Flashbead particles at any concentration is minimal with the suppression of turbulence at the centreline no longer seen.

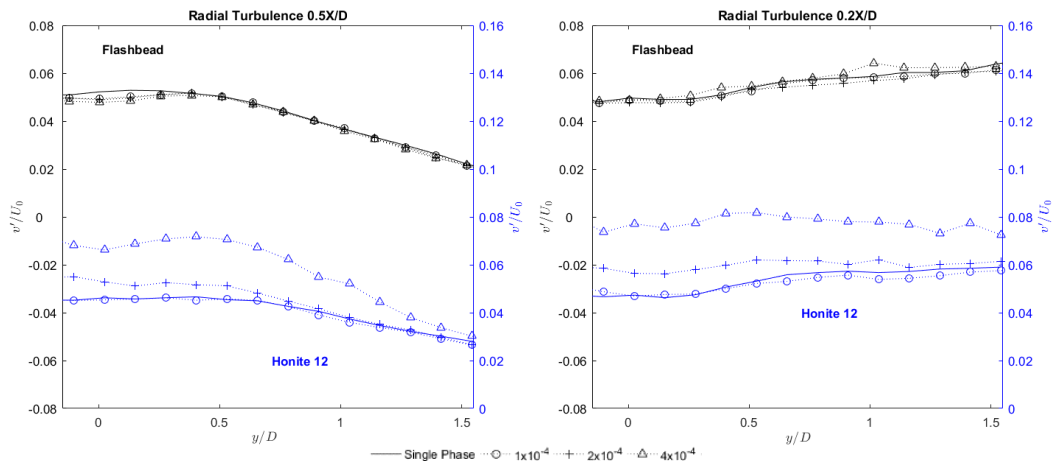


Figure 6.39 (left) – Change in radial turbulence with increased Honite 12 and Flashbead particle concentration 0.5D from impingement. Figure 6.40 (right) – Change in radial turbulence with increased Honite 12 and Flashbead particle concentration 0.2D from impingement.

As with the axial turbulence measurement the Honite 12 particles have a much greater influence than the Flashbead particles at volume fractions of 2×10^{-4} and 4×10^{-4} , the 1×10^{-4} volume fraction having minimal effect on the flow at all measurement locations. 5D from impingement the centreline radial turbulence is increased by 70% and the maximum radial turbulence value is increased from 0.044 to 0.068, an increase of 38% when $\varphi = 4 \times 10^{-4}$. Downstream of the outlet as the jet develops and the 1X/D measurement location is reached the magnitude of radial turbulence has increased in the presence of Honite 12 particles. Unlike the Flashbead particles which had a change in effect at this location the Honite 12 particles continue to enhance radial turbulence, with peak turbulence measurements again increased by around 38% when $\varphi = 4 \times 10^{-4}$. This continues as the impingement region is reached with the enhancement percentage increasing over 60%.

6.3.2.3 Turbulence Percentage Changes

The enhancement percentages can be seen more clearly in Figures 6.41 to 6.44 which show the axial and radial turbulence percentage changes at 1X/D and 0.2X/D. We observe the suppression of axial and radial turbulence in the region $0 > y/D > 1$, 1D from impingement. At the highest particle volume fraction the centreline axial turbulence is reduced by 2.9% and radial centreline turbulence is reduced by 8.5%.

Comparing Figures 6.41 and 6.42 we observe that in both axial and radial turbulence there is a dip in the magnitude of modulation by the Honite 12 particles around $y/D = 1$ when $X/D = 1$. At this point the Honite 12 particles suppress axial turbulence at all volume fractions, whereas radial turbulent enhancement is significantly reduced.

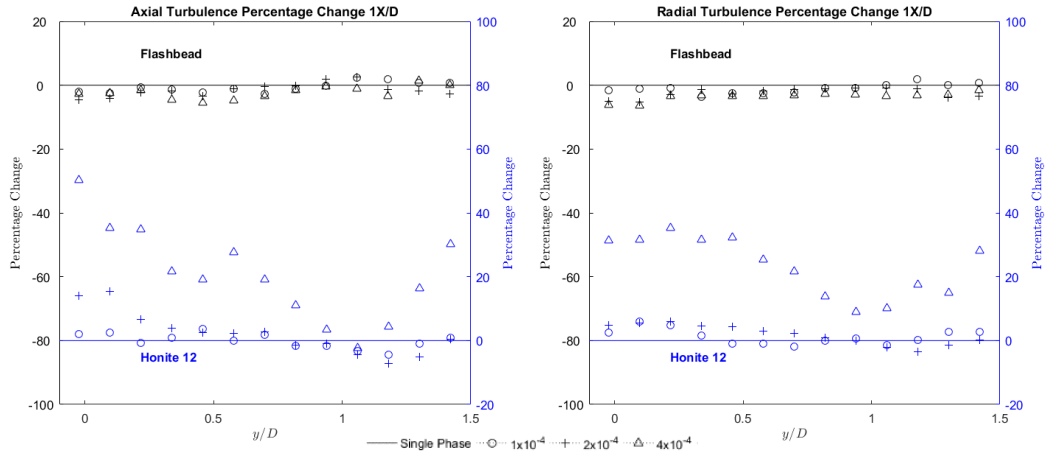


Figure 6.41 (left) – Percentage change in axial turbulence with change in Honite 12 and Flashbead particle loading 1D from impingement. Figure 6.42 (right) – Percentage change in radial turbulence with change in Honite 12 and Flashbead particle loading 1D from impingement.

The same dip is not seen at 0.2X/D, shown in Figures 6.43 and 6.44, instead the Honite 12 particles gradually reduce in effect as distance from the jet centreline is increased. Looking at the effect of the Flashbead particles in this region we see a transition from suppression of turbulence at the centreline to enhancement in the region $0.2 < y/D < 0.7$.

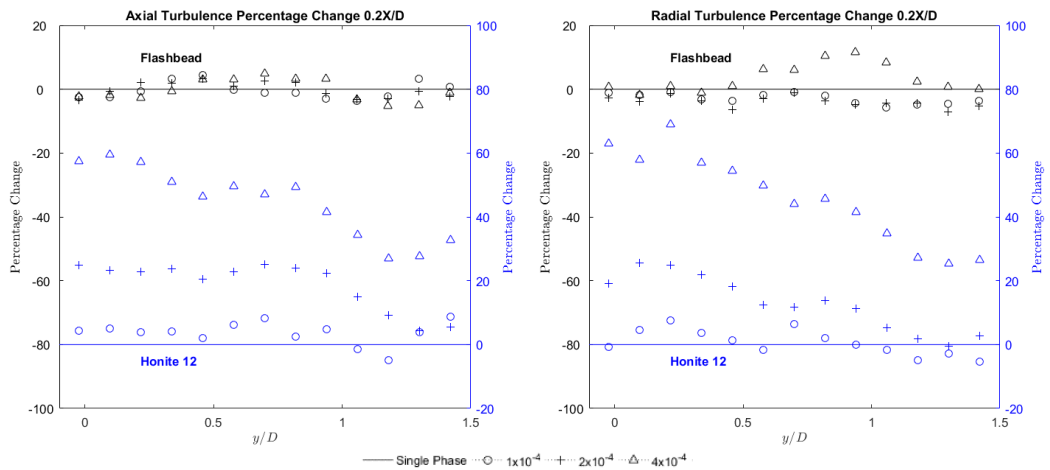


Figure 6.43 (left) – Percentage change in axial turbulence with change in Honite 12 and Flashbead particle loading 0.2D from impingement. Figure 6.44 (right) – Percentage change in radial turbulence with change in Honite 12 and Flashbead particle loading 0.2D from impingement.

6.3.3 Vertical Velocity Flow Profiles

The following sub-sections contain vertical flow profiles, to maintain consistency with the previous figures distance has been plotted on the x-axis and velocity on the y-axis, with the second set of figures plotted on a shifted y axis. Care should be taken to note that for these profiles the x-axis distance is measured in diameters from the impingement surface (X/D) whereas previously the x-axis represented distance from the jet centreline (y/D).

6.3.3.1 Axial Vertical Velocity Profiles

Figures 6.45 and 6.46 show the axial velocity along the jet centreline ($0 y/D$) and at the periphery of the jet outlet ($0.5 y/D$), respectively. Along the jet centreline we see that the presence of both Honite 12 and Flashbead particles results in a slight enhancement of the axial velocity as impingement is approached (right to left). However, this velocity enhancement becomes more pronounced as distance from the centreline is increased shown in Figure 6.45. For both the Honite 12 and Flashbead particles the magnitude of the effect in the developing jet region is very similar.

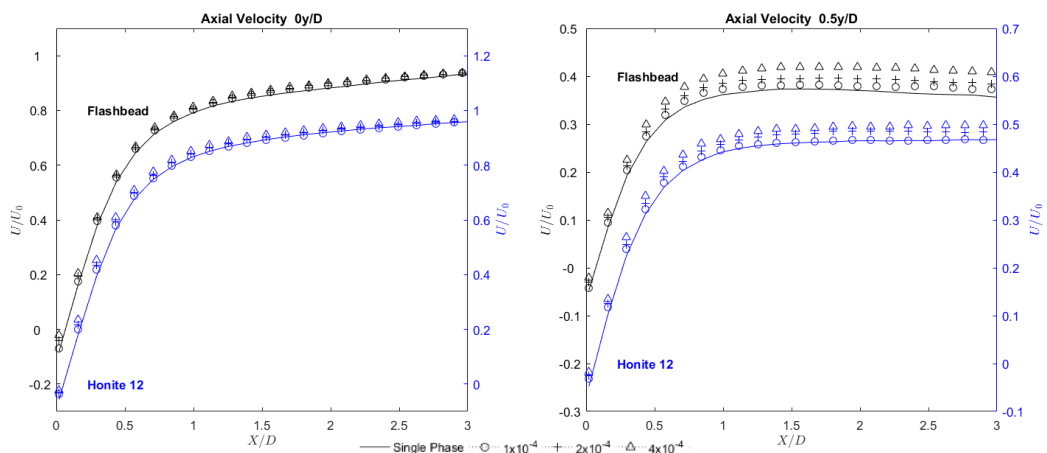


Figure 6.45 (left) – Change in axial velocity with change in Honite 12 and Flashbead particle loading along the jet centreline. Figure 6.46 (right) – Change in axial velocity with change in Honite 12 and Flashbead particle loading 0.5D from the jet centreline.

At 1D from the jet centreline we see that the axial velocity increases as the impingement surface is approached, until $0.5X/D$, at this minimum separation the flow begins to rapidly decelerate. This is due to fluid entrainment as the jet expands followed by redirection of the flow by the radial wall jet. In this region Figure 6.47 shows that both the Flashbead and Honite 12 particles enhance entrainment of the surrounding fluid below a separation distance of $3X/D$. At $5y/D$ the presence of either particle species no longer has any effect on the axial velocity, at any of the tested concentrations, as can be seen in Figure 6.48.

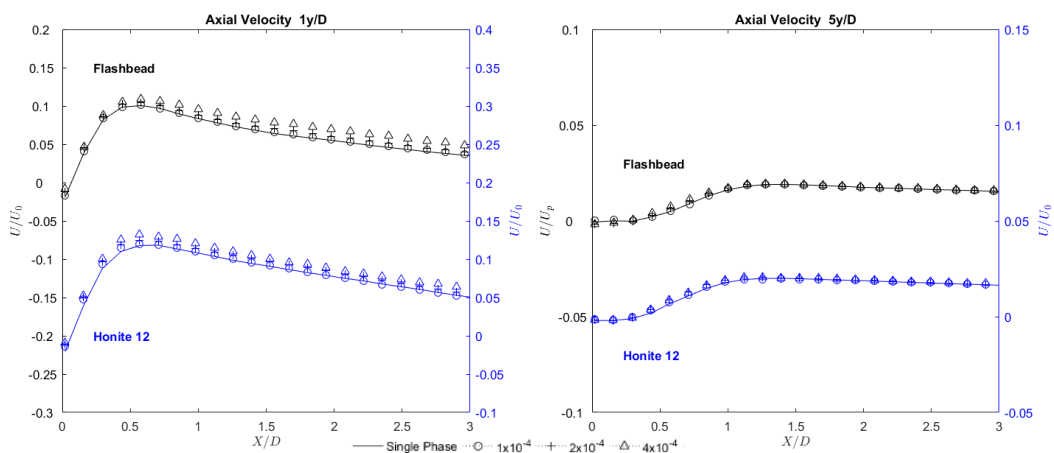


Figure 6.47 (left) – Change in axial velocity with change in Honite 12 and Flashbead particle loading 1D from the jet centreline. Figure 6.48 (right) – Change in axial velocity with change in Honite 12 and Flashbead particle loading 5D from the jet centreline.

6.3.3.2 Radial Vertical Velocity Profiles

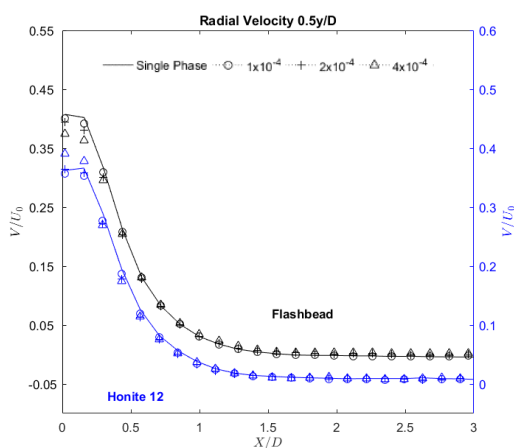


Figure 6.49 – Change in radial velocity with change in Honite 12 and Flashbead particle loading 0.5D from the jet centreline

Radial velocities at the same measurement points are given in Figures 6.49 to 6.51, excluding measurements along the jet centreline at $y/D = 0$ due to the fact there is no radial velocity at this point.

Figure 6.49 shows that 0.5D from the centreline Flashbead particles reduce the radial velocity in the impingement region

$0 < X/D < 0.5$ at all particle concentrations tested and as concentration is increased the fluid

velocity in this region is reduced further. The Honite 12 particles behave similarly until the particle volume fraction is increased to 4×10^{-4} , at this point below $X/D = 0.25$ enhancement of the radial velocity occurs. This enhancement of the radial velocity by the 4×10^{-4} volume fraction of Honite 12 is also present 1D and 5D from the jet centreline as seen in Figures 6.50 and 6.51 respectively. In contrast increasing the concentration of Flashbead particles causes the flow to be retarded to a greater extent close to the wall, seen at 1 y/D and 5 y/D.

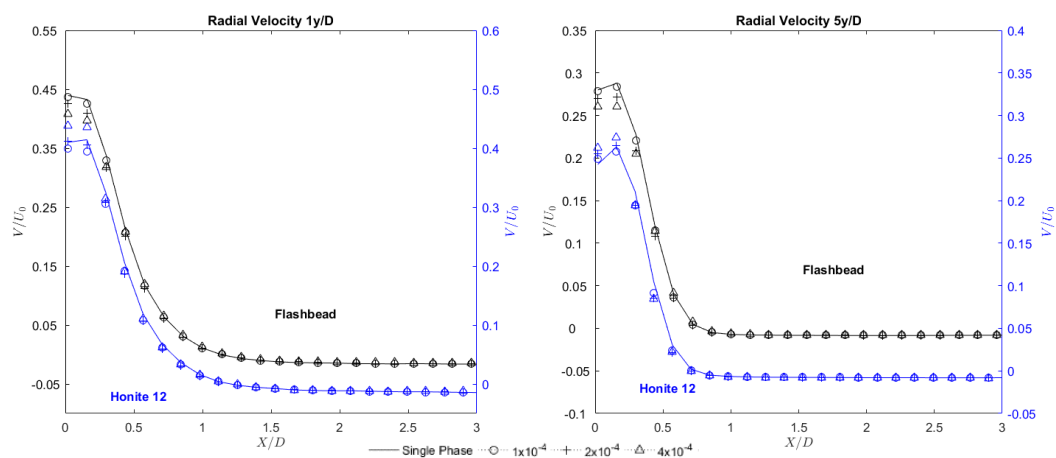


Figure 6.50 (left) – Change in radial velocity with change in Honite 12 and Flashbead particle loading 1D from the jet centreline. Figure 6.51 (right) – Change in radial velocity with change in Honite 12 and Flashbead particle loading 5D from the jet centreline.

6.3.4 Vertical Turbulence Flow Profiles

6.3.4.1 Axial Vertical Turbulence Profiles

Figures 6.52 through 6.55 show the evolution of axial turbulence as distance from the jet centreline is increased. As can be seen in Figure 6.52 Flashbead particles transition from turbulence enhancement at $3X/D$ to suppression in the region $0.5 < X/D < 2.5$ before enhancement occurs with the highest volume fraction ($\varphi = 4 \times 10^{-4}$) below $X/D = 0.5$. A similar pattern can be seen at 0.5D from impingement in Figure 6.53.

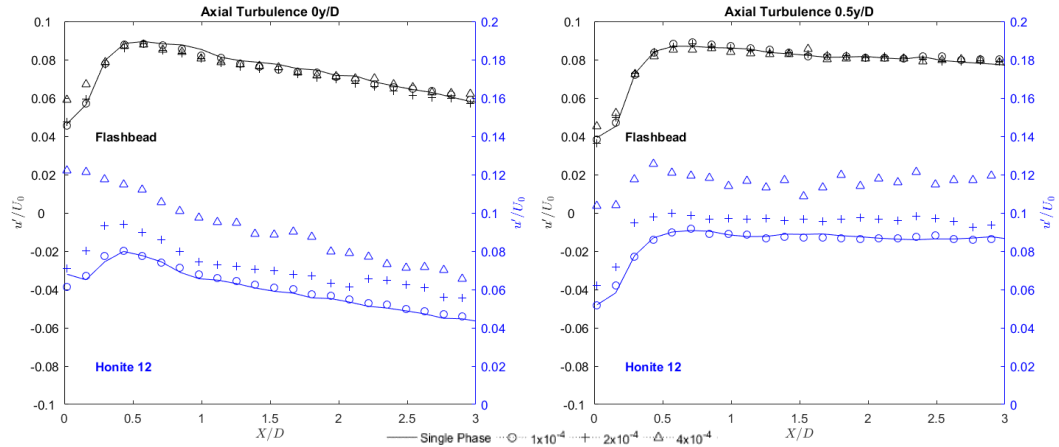


Figure 6.52 (left) – Change in axial turbulence with change in Honite 12 and Flashbead particle loading along the jet centreline. Figure 6.53 (right) – Change in axial turbulence with change in Honite 12 and Flashbead particle loading 0.5D from the jet centreline.

At 1D and beyond there is almost no effect of the Flashbead particles on the axial turbulence.

Honite 12 particles as seen previously has almost no effect at the lower volume fraction of 1×10^{-4} , however as the particle concentration is increased the effects become more significant. Along the jet centreline the presence of Honite 12 particles increases axial turbulence as seen in the horizontal profiles shown in Figures 6.33 to 6.36. This effect is also seen when $y/D = 0.5$, which in the horizontal profiles is the location of the peaks in turbulence. Further from the centreline in the developing wall jet ($0 < X/D < 1$, $1 < y/D < 5$) enhancement of the axial turbulence can also be seen with a 24% increase in the maximum turbulence value at $y/D = 5$ when the particle volume fraction is increased to 4×10^{-4} .

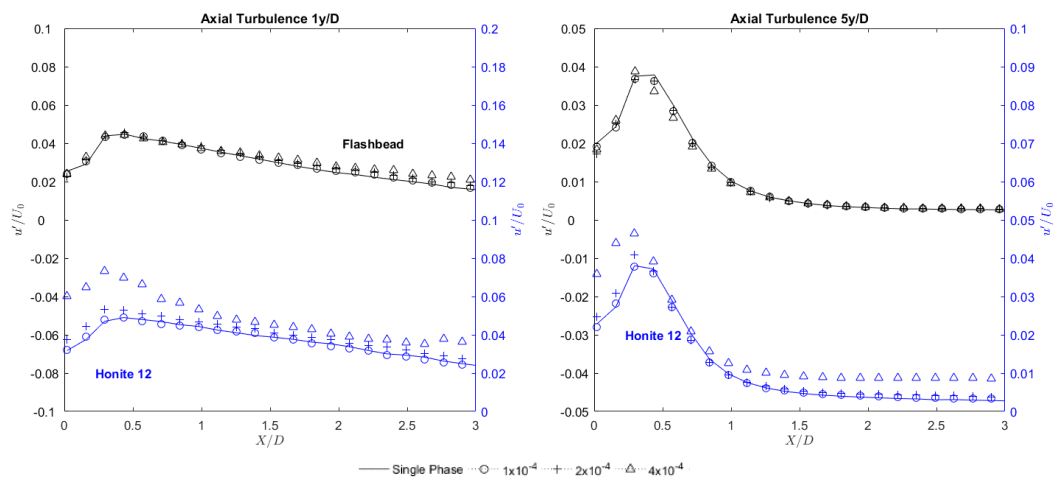


Figure 6.54 (left) – Change in axial turbulence with change in Honite 12 and Flashbead particle loading 1D from the jet centreline. Figure 6.55 (right) – Change in axial turbulence with change in Honite 12 and Flashbead particle loading 5D from the jet centreline.

6.3.4.2 Radial Vertical Turbulence Profiles

Like with the axial turbulence measurements the Flashbead particles have little to no effect on the radial turbulence shown in Figures 6.56 to 6.59. That is except for a slight suppression along the jet centreline which on average results in a -4% change compared with the single-phase flow which can be seen in Figure 6.56.

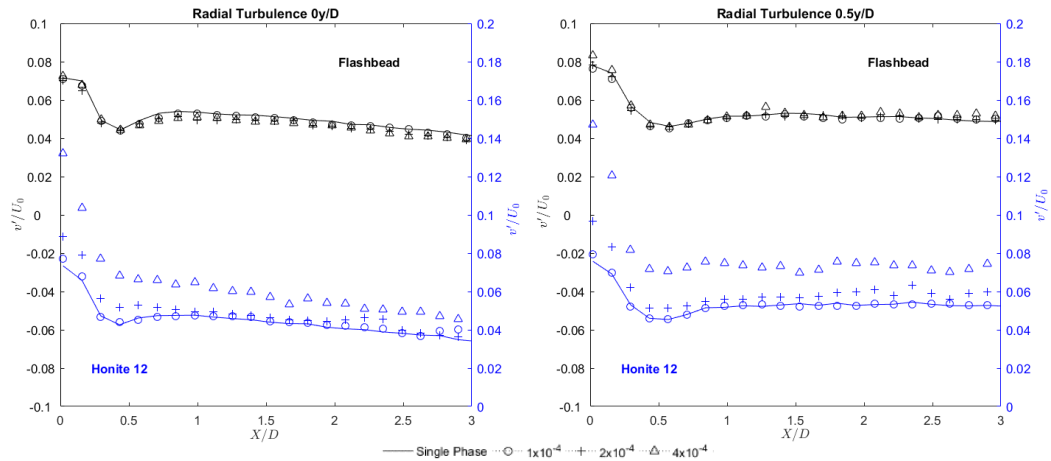


Figure 6.56 (left) – Change in radial turbulence with change in Honite 12 and Flashbead particle loading along the jet centreline. Figure 6.57 (right) – Change in radial turbulence with change in Honite 12 and Flashbead particle loading 0.5D from the jet centreline.

Honite 12 particles consistently enhance radial turbulence within the jet ($y/D < 0.5$) once a minimum volume fraction of 2×10^{-4} has been reached as seen in Figures 6.56 and 6.57 where the average enhancement in the region $0 < X/D < 3$ along the jet centreline ($y/D = 0$) is 9.4% when $\phi = 2 \times 10^{-4}$ and 38% when $\phi = 4 \times 10^{-4}$. For the same region of separation but further from the centreline at $y/D=0.5$ the enhancements are 12% and 45% for 2×10^{-4} and 4×10^{-4} volume fractions respectively.

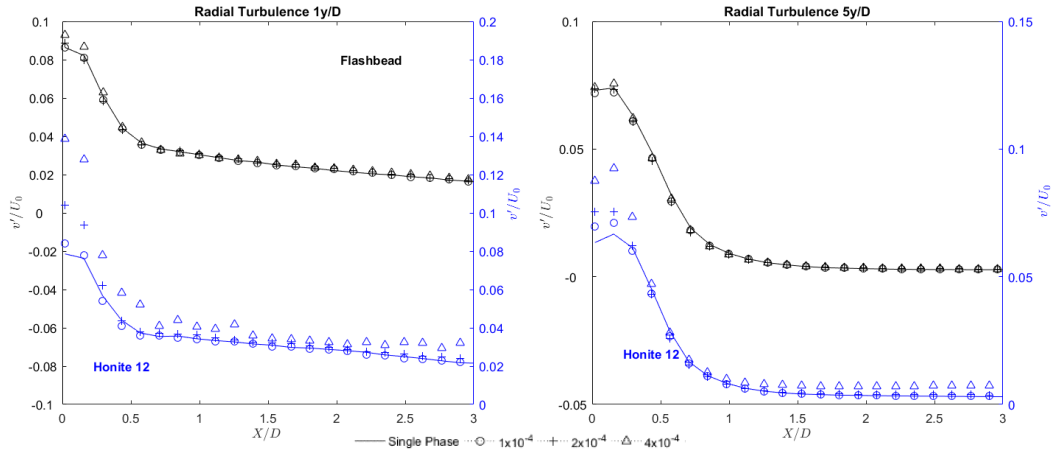


Figure 6.58 (left) – Change in radial turbulence with change in Honite 12 and Flashbead particle loading 1D from the jet centreline. Figure 6.59 (right) – Change in radial turbulence with change in Honite 12 and Flashbead particle loading 5D from the jet centreline.

In the developing wall jet ($0 < X/D < 1$, $1 < y/D < 5$) shown in Figures 6.58 and 6.59 we observe significant enhancement of radial turbulence. Maximum turbulence values at $y/D = 1$ are increased by 76% when $\varphi = 4 \times 10^{-4}$ compared with the single-phase flow. As the wall jet develops the magnitude of enhancement falls but is still significant resulting in radial turbulent fluctuations 24% greater than in the single-phase flow.

6.3.5 Discussion

When compared with the pipe flow results it becomes obvious that in the presence of particles the impinging jet flow field is influenced to a much greater degree. Immediately after the jet orifice the effect of particles is not readily apparent however as the jet develops the differences between the single phase and multiphase flows become prominent.

Both Flashbead and Honite 12 particles cause the jet to retain axial velocity as it develops. For the Honite 12 particles this is expected and can be seen in both the free jet work of Fleckhaus et al. (1987) and the impinging jet results of Yoshida et al. (1990), where the retention in velocity is attributed to momentum transfer from the particles to the fluid, this same momentum transfer is responsible for the reduction in radial velocity, of the Honite 12 particle-laden flow, in the impingement region as energy is lost accelerating the particles away from the jet centreline.

This explanation does not fully explain why the Flashbead particles would also result in axial velocity retention. The relative densities of the fluid and particles are such that although momentum transfer exists the magnitude would not be enough to explain the magnitude of velocity retention. As seen by Yoshida et al. (1990) an alternative mechanism contributes in that, the effect of Flashbead particles suppressing turbulence causes increased velocity retention, this turbulence suppression can be seen in Figures 6.33 to 6.40.

As the jet develops, energy is transferred to the surrounding fluid in the turbulent mixing layer, while further energy is lost through the energy cascade of small eddies, the suppression of both effects would lead to enhanced centreline velocity compared with the single-phase flow. In the impingement region, axial velocities are very similar for the 2×10^{-4} and 4×10^{-4} concentrations of Flashbead particles, which coincide with the fact that increased turbulence suppression does not occur as the volume fraction is increased from 2×10^{-4} to 4×10^{-4} .

A similar effect is seen in the radial velocity measurements where the flow at the 4×10^{-4} volume fraction does not lag the single-phase flow to a greater extent than the 2×10^{-4} volume fraction.

Although axial turbulence measurements at the jet outlet initially show enhancement in the presence of Flashbead particles, this quickly transitions to suppression as the jet continues to develop. According to Gore and Crowe (1989) turbulence enhancement or suppression is dependent upon the ratio of particle size to eddy length scale ratio, as a jet develops vortex stretching occurs Tsubokura et al. (2003), for a given particle size this would effectively reduce this ratio as the jet develops and so a transition from enhancement to suppression occurs.

This effect is not seen for the Honite 12 particles even though the particles are the same size as the increased density reduces the response time of the particle. This prevents the particle from being able to follow the flow and so slip velocities are created which in turn produce turbulence. This production of turbulence massively outweighs the reduction which would be caused by the mutual interaction of eddies and particles.

As the wall jet develops after impingement, the Flashbead particles can be shown to retard the flow more than the Honite 12 particles in the region very close to the impingement plate. This is likely due to low relative concentrations of Honite 12 particles in this region compared with the concentration of Flashbead particles. As observed by Anderson and Longmire (1995), particles with a larger Stokes number rebound from the impingement surface and back into the flow with a greater frequency and to a greater height than particles with a lower Stokes number. Radial acceleration of particles is dependent on the region of the flow where the particle resides the longest and so particles which rebound to a greater height are both accelerated to a smaller degree and have a lower concentration close to the impingement plate in the developing wall jet. This greater concentration of Flashbead particles very close to the impingement plate is responsible for the reduction in fluid velocity in this region.

Honite 12 particles which do enter the near base region, although fewer in number, have greater inertia and the particle rebound leads to drag on the particle which produces turbulence. Hence, the reason for the larger turbulent fluctuations when studying Honite 12 particle flows compared with the single phase or Flashbead particle flows.

Comparisons between methods for predicting the enhancement or dissipation of turbulence by Gore and Crowe (1989) and Elghobashi (1994) will be performed in the next section to avoid repetitiveness and allow particle size effects to be examined simultaneously.

6.4 Effect of Particle Size on Impinging Jet Flow

This section will explore how particle size influences the fluid behaviour in an impinging jet. Unfortunately, due to the size and construction of the impinging jet rig the larger Honite 8 particles could not be tested as they would clog the feed lines to the jet and so this section will focus on a comparison between Honite 12 and the smaller Honite 22 particles. As before the particle properties for the Honite 12 and Honite 22 are given in Table 6.5, mass loadings are the same for both species as the particles are of the same density, and are given in Table 6.6.

Table 6.5 – Particle properties for various sizes of Honite particles.

	Honite 12	Honite 22
Particle Diameter (μm)	225	40
Particle Density (kg m^{-3})	2450	2450
Particle Material	Silica Glass	Silica Glass
Particle Settling Velocity (m s^{-1})	39.92×10^{-3}	1.26×10^{-3}
Particle Response Time (ms)	6.9	0.2

Table 6.6 – Mass of Honite particles for a given volume fraction.

Honite Particle Loading					
Run #	Volume Fraction	Particle Mass (g)	Run #	Volume Fraction	Particle Mass (g)
1	0	0	3	2×10^{-4}	58.8
2	1×10^{-4}	29.4	4	4×10^{-4}	117.6

6.4.1 Horizontal Velocity Flow Profiles

As in previous sections the data is plotted with a shifted Y-axis to enable easier comparison of the results, in this case the Honite 22 is plotted in black on the left axis and the Honite 12 in blue on the right axis.

6.4.1.1 Axial Horizontal Velocity Profiles

Horizontal velocity profiles at 5X/D and 1X/D shown in Figures 6.60 and 6.61 show that the presence of the smaller Honite 22 particles results in a reduction of axial velocity compared with the single-phase flow with enhancement only seen in the two measurement locations closest to the jet centreline ($y/D = 0$). This is in contrast with the Honite 12 particles which show enhancement of the velocity up to $y/D = 1$.

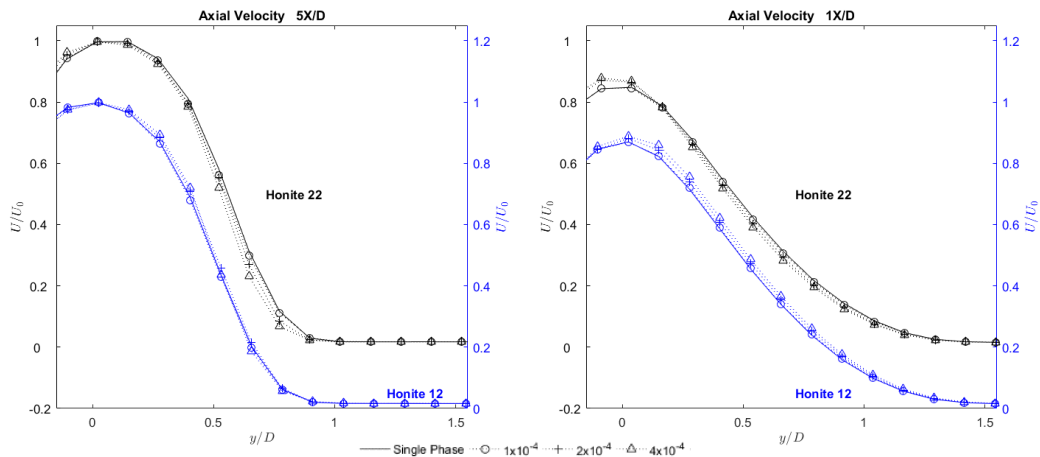


Figure 6.60 (left) – Change in axial velocity with change in Honite 12 and Honite 22 particle loading 5D from impingement. Figure 6.61 (right) – Change in axial velocity with change in Honite 12 and Honite 22 particle loading 1D from impingement.

Figure 6.62 shows that as the upstream influence of the impingement surface is detected at $X/D = 0.5$, the centreline velocity retention by the Honite 22 particles is greater than that of the Honite 12 particles, with centreline velocity increased by 8.7% compared with 4.9% for the maximum volume fraction of Honite 12. Away from the centreline when $y/D > 0.2$ the Honite 12 particles cause a greater retention of velocity, with the Honite 22 particles either having no effect in this region or causing the fluid to have a lower velocity than the single-

phase flow. Immediately before impingement ($X/D = 0.2$) this effect is even more pronounced with the maximum loading of Honite 22 particles causing a 24.6% increase in axial velocity compared with 14.8% increase for the same volume fraction of Honite 12 particles. Again, the enhancement is seen in a much tighter region ($0 < y/D < 0.5$) compared with the region of enhancement due to Honite 12 particles; which extends from the centreline to $y/D = 1$ as can be seen in Figure 6.63.

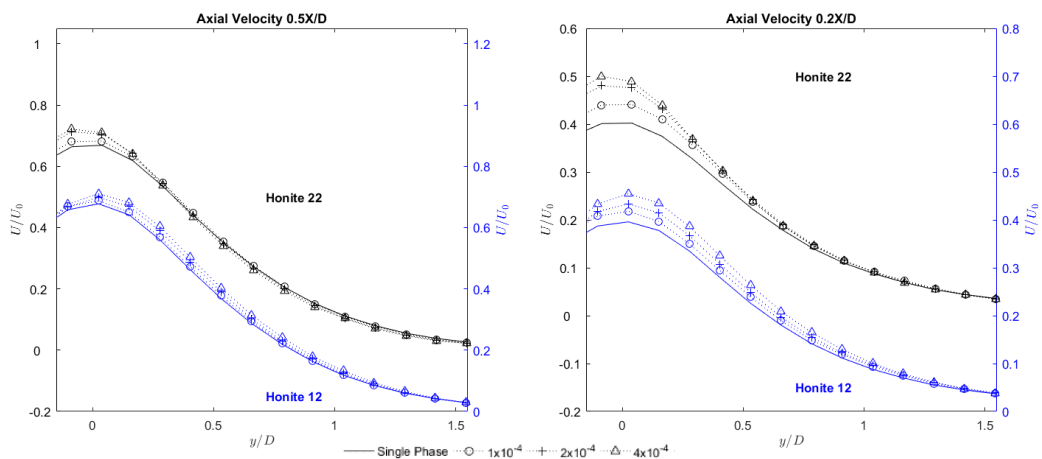


Figure 6.62 (left) – Change in axial velocity with change in Honite 12 and Honite 22 particle loading 0.5D from impingement. Figure 6.63 (right) – Change in axial velocity with change in Honite 12 and Honite 22 particle loading 0.2D from impingement.

6.4.1.2 Radial Horizontal Velocity Profiles

Radial velocity profiles in Figure 6.64 shows that like the Honite 12 particles the Honite 22 particles cause the jet to narrow, seen by the fact that entrainment of the flow is observed closer to the centreline. As the jet develops this effect becomes more pronounced, at $1X/D$ the Honite 22 profile shown in Figure 6.65 shifts towards the centreline as the particle concentration is increased. This is in contrast with the Honite 12 particles which cause a reduction in the maximum radial velocity as concentration increased.

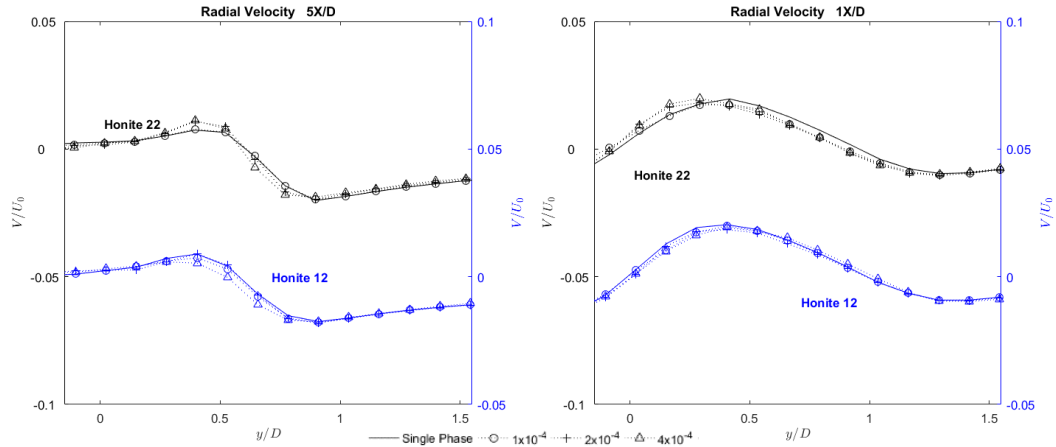


Figure 6.64 (left) – Change in radial velocity with change in Honite 12 and Honite 22 particle loading 5D from impingement. Figure 6.65 (right) – Change in radial velocity with change in Honite 12 and Honite 22 particle loading 1D from impingement.

As the upstream influence of the impingement surface is felt the jet is redirected radially causing the radial velocity to rapidly increase. The presence of both Honite 12 and Honite 22 particles hinders this radial acceleration, with increased concentration having a greater effect. The presence of Honite 22 particles at the lowest concentration has a much greater influence on the maximum radial velocity causing a reduction of 11.2% at 0.5X/D and 6.2% at 0.2X/D, compared with the Honite 12 particles which at the same concentration caused a reduction of 7.1% at 0.5X/D and 5.1% at 0.2X/D. In addition to causing a greater reduction, the Honite 22 particles also continued to reduce the radial velocity as particle concentration was increased, unlike the Honite 12 particles where continuing to increase the particle concentration had diminishing returns. This is especially true for the maximum radial velocity value at 0.2X/D where increasing the volume fraction of Honite 22 particles from 1×10^{-4} to 4×10^{-4} caused an additional 7.7% reduction in the radial velocity whereas the difference at this point for the Honite 12 particles is less than 0.5%.

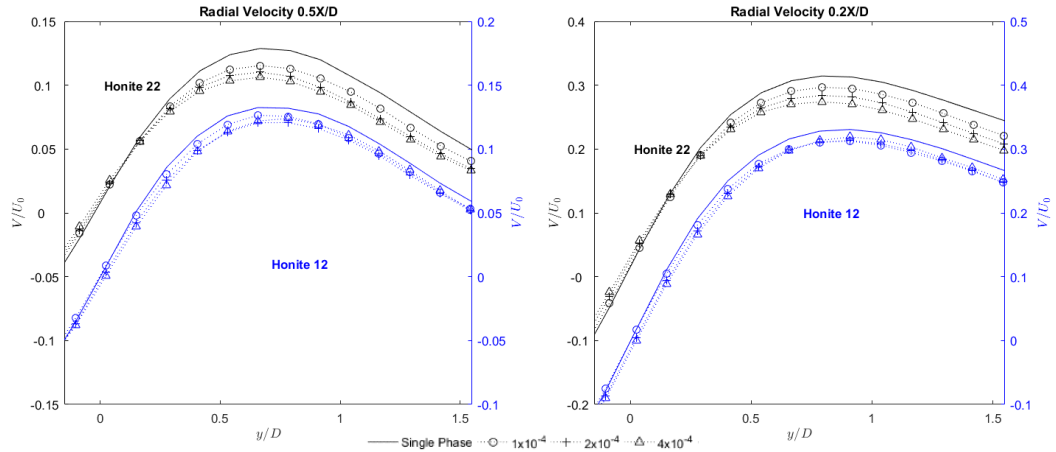


Figure 6.66 (left) – Change in radial velocity with change in Honite 12 and Honite 22 particle loading 0.5D from impingement. Figure 6.67 (right) – Change in radial velocity with change in Honite 12 and Honite 22 particle loading 0.2D from impingement.

6.4.1.3 Velocity Percentage Changes

These percentage changes are illustrated much more clearly in Figures 6.68 to 6.71. Here we observe the transition from enhancement of axial velocity to reduction by the Honite 22 particles contrasting with the continuous increase by the Honite 12 particles. In Figure 6.68 we can clearly see that the region of maximum enhancement for the Honite 12 particles coincides with the region of maximum reduction for the Honite 22 particles around $y/D = 1$.

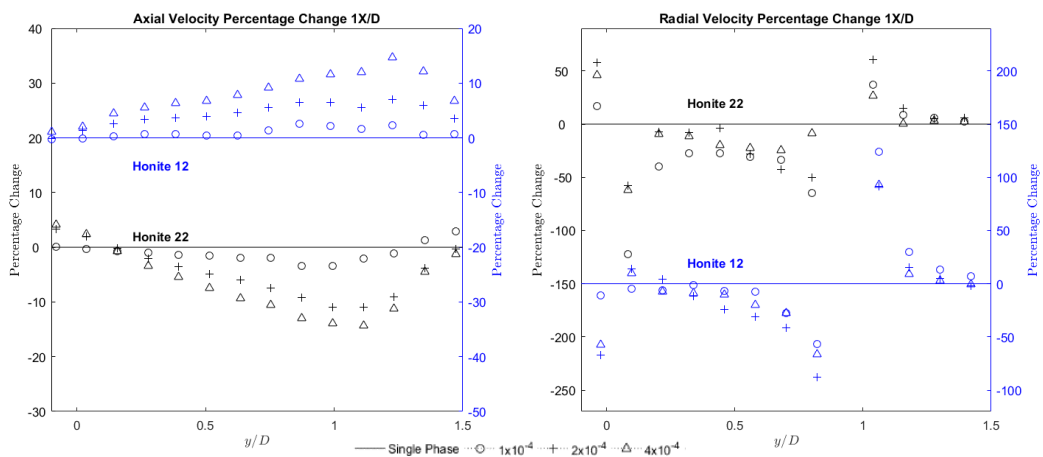


Figure 6.68 (left) – Percentage change in axial velocity with change in Honite 12 and Honite 22 particle loading 1D from impingement. Figure 6.69 (right) – Percentage change in radial velocity with change in Honite 12 and Honite 22 particle loading 1D from impingement.

In the impingement region ($0.2X/D$) we observe that the lowest volume fraction ($\varphi = 1 \times 10^{-4}$) of Honite 22 particles on average increases the axial velocity by approximately 7.3% in the region $0 < y/D < 1$ which is greater than the average enhancement caused by the highest loading of Honite 12 particles ($\varphi = 4 \times 10^{-4}$) of 6.4%. For the same region, the average enhancement by the 4×10^{-4} volume fraction of Honite 22 particles is 19.7%

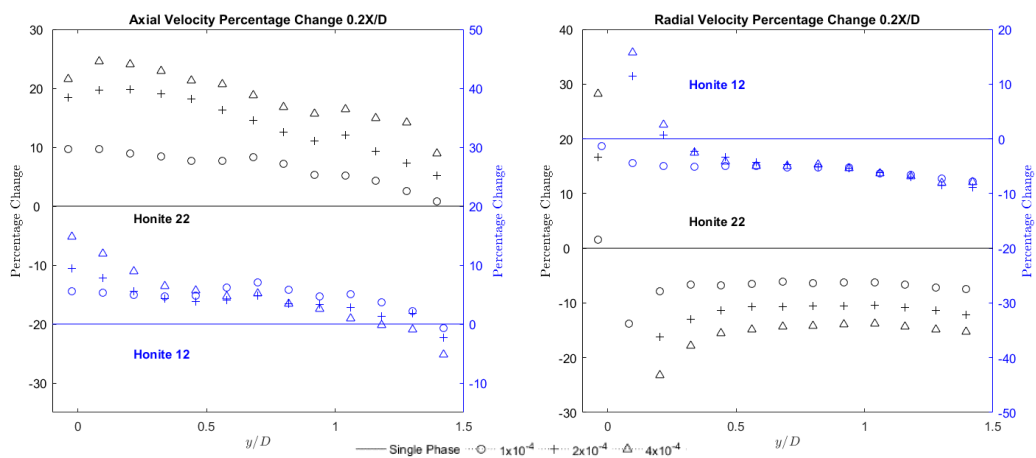


Figure 6.70 (left) – Percentage change in axial velocity with change in Honite 12 and Honite 22 particle loading 0.2D from impingement. Figure 6.71 (right) – Percentage change in radial velocity with change in Honite 12 and Honite 22 particle loading 0.2D from impingement.

6.4.2 Horizontal Turbulence Flow Profiles

6.4.2.1 Axial Horizontal Turbulence Profiles

Horizontal turbulence profiles in Figures 6.72 and 6.73 show that Honite 22 particles has less of an effect on axial turbulence than for the same mass loadings of Honite 12 particles, with both centreline and maximum turbulence values enhanced to a lesser extent. Again, the profiles for the Honite 22 particle loadings are shifted towards the centreline as concentration is increased with the maximum turbulence value occurring at $y/D = 0.3$ when the volume fraction is 4×10^{-4} as opposed to $y/D = 0.45$ for the single-phase flow.

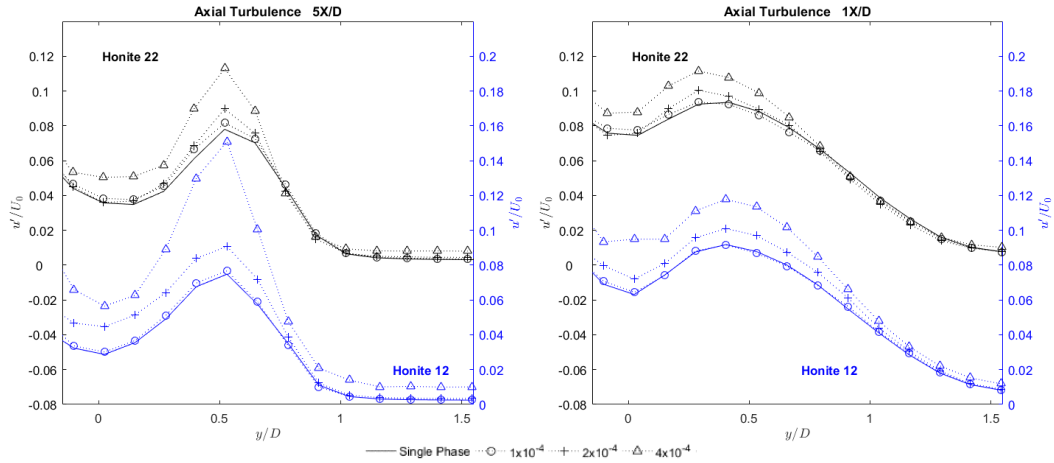


Figure 6.72 (left) – Change in axial turbulence with change in Honite 12 and Honite 22 particle loading 5D from impingement. Figure 6.73 (right) – Change in axial turbulence with change in Honite 12 and Honite 22 particle loading 1D from impingement.

Approaching the impingement region in Figures 6.74 and 6.75 the axial turbulence is enhanced in a much narrower region for the Honite 22 particles, as with the velocity enhancement seen in Figure 6.62. Again, the magnitude of the enhancement is much greater for the larger Honite 12 particles with peak turbulence 0.2D from impingement at the 4×10^{-4} volume fraction increasing by 49.4% compared with 16.1% for the Honite 22 particles.

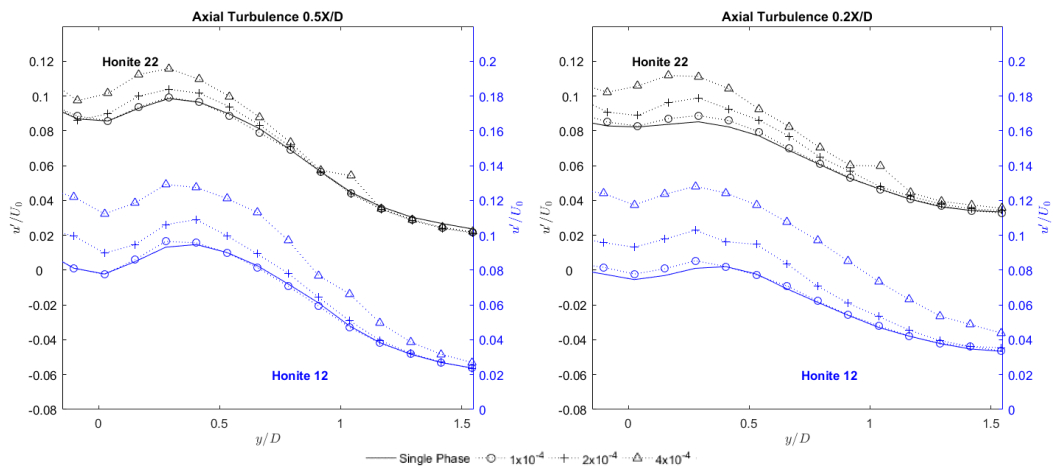


Figure 6.74 (left) – Change in axial turbulence with change in Honite 12 and Honite 22 particle loading 0.5D from impingement. Figure 6.75 (right) – Change in axial turbulence with change in Honite 12 and Honite 22 particle loading 0.2D from impingement.

6.4.2.2 Radial Horizontal Turbulence Profiles

Radial turbulence profiles are given in Figures 6.76 to 6.79. At 5D from impingement (Figure 6.76) radial turbulence is unaffected by the presence of Honite 22 particles at volume fractions of 1×10^{-4} and 2×10^{-4} , except in a small region within the shear mixing layer $0.3 < y/D < 0.6$. As the jet develops this region of effect expands and reaches the jet centreline 1D from impingement as seen in Figure 6.77.

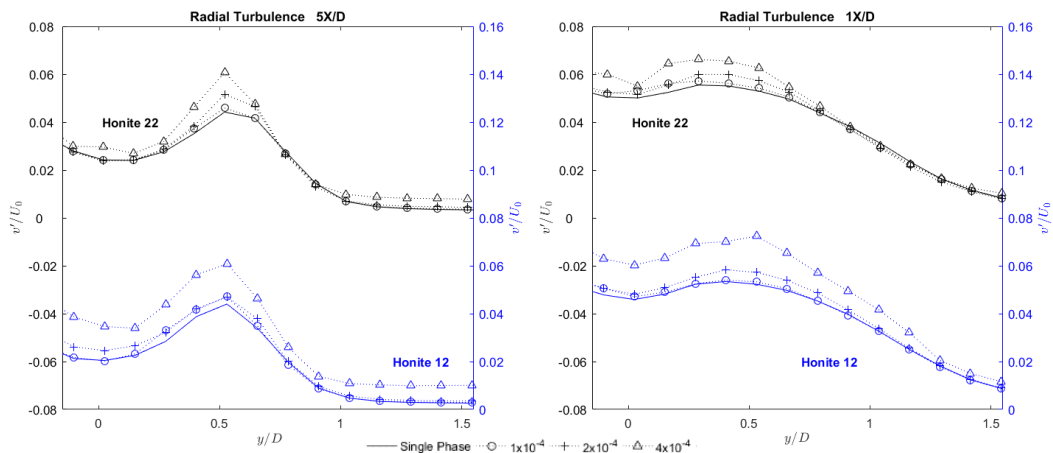


Figure 6.76 (left) – Change in radial turbulence with change in Honite 12 and Honite 22 particle loading 5D from impingement. Figure 6.77 (right) – Change in radial turbulence with change in Honite 12 and Honite 22 particle loading 1D from impingement.

As the upstream influence of the impingement surface is felt by the flow ($X/D = 0.5$) radial turbulence is enhanced in the presence of both Honite 12 and 22 particles, however immediately before impingement ($X/D = 0.2$) only the 4×10^{-4} volume fraction of Honite 22 particles cause enhancement with lower concentrations having either no effect or suppressing turbulent fluctuations. This same behaviour is exhibited at the 1×10^{-4} volume fraction of Honite 12 particles, with higher concentrations causing an increase in radial turbulence.

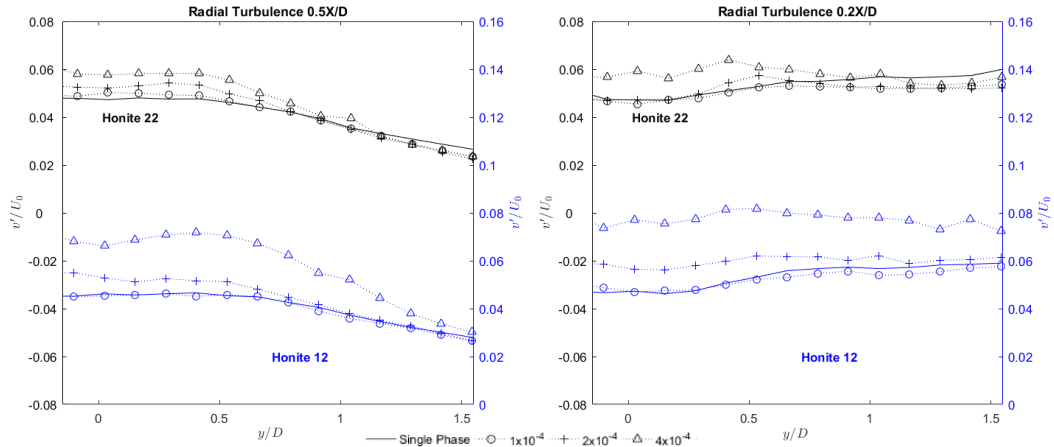


Figure 6.78 (left) – Change in radial turbulence with change in Honite 12 and Honite 22 particle loading 0.5D from impingement. Figure 6.79 (right) – Change in radial turbulence with change in Honite 12 and Honite 22 particle loading 0.2D from impingement.

6.4.2.3 Turbulence Percentage Changes

Percentage changes for the axial and radial turbulence measurements are given for 1D from impingement in Figures 6.80 and 6.81. Here we observe that between the jet centreline and $0.75y/D$ the effect of Honite 22 particles at the highest concentration causes axial velocity fluctuations to be enhanced by between 12.8% and 17.9%. In the same region ($0 < y/D < 0.75$), the same concentration of Honite 12 particles cause an enhancement of between 50.3% and 19.1%, showing that not only is the turbulence enhancement more significant there is also a much greater degree of variability across the jet. Radial turbulence patterns show a similar effect, however the degree of variability in the effect of the Honite 12 particles is reduced slightly, having a range between 35.3% and 21.6%. At lower concentrations ($\varphi = 1 \times 10^{-4}$, 2×10^{-4}) Honite 22 particles show very little enhancement of the turbulence and at some points even cause a slight suppression near the jet centreline. At $y/D > 1$ we see suppression of both axial and radial turbulence at these concentrations, which is also observed in the Honite 12 tests.

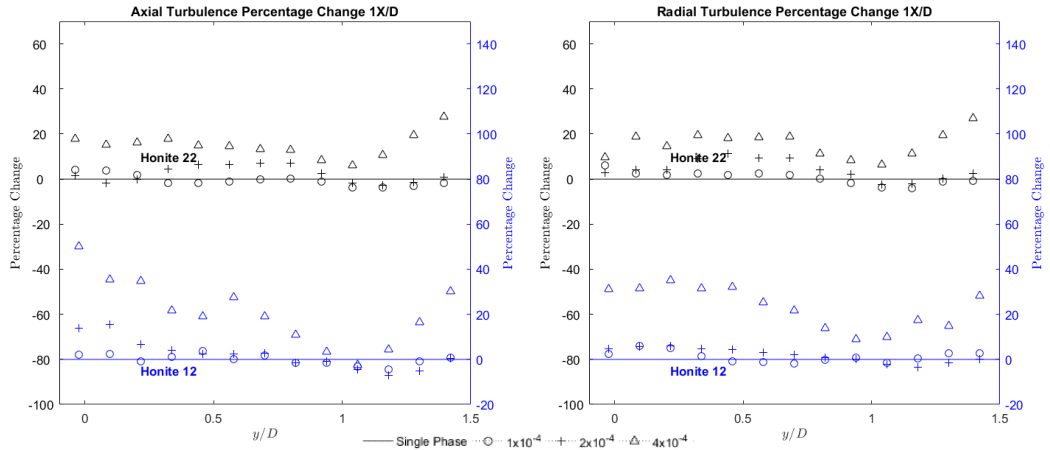


Figure 6.80 (left) – Percentage change in axial turbulence with change in Honite 12 and Honite 22 particle loading 1D from impingement. Figure 6.81 (right) – Percentage change in radial turbulence with change in Honite 12 and Honite 22 particle loading 1D from impingement.

Axial turbulence percentage changes are given for 0.2D from impingement in Figure 6.82.

Like the data at 1D from impingement (Figure 6.80) the Honite 22 particles cause a fairly consistent change in axial turbulence in the region $0 < y/D < 0.75$ at the highest particle concentration ($\varphi = 4 \times 10^{-4}$). The lowest concentration ($\varphi = 1 \times 10^{-4}$) of Honite 12 particles has a very similar effect as the Honite 22 particles at equivalent particle concentrations, however as the number of particles in the system increase their influence becomes much greater with enhancement up to 59.5% seen in contrast with the maximum enhancement by the Honite 22 particles of 28.5%.

Radial turbulence percentage changes 0.2D from impingement show that at lower concentrations ($\varphi = 1 \times 10^{-4}, 2 \times 10^{-4}$) Honite 22 particles cause suppression to occur as seen in Figure 6.83. At $y/D > 0.75$ the highest particle concentration ($\varphi = 4 \times 10^{-4}$) transitions from enhancement of the turbulence to suppression. This same transition from enhancement to suppression exists only for the lowest volume fraction of Honite 12 ($\varphi = 1 \times 10^{-4}$) higher particle volume fractions ($\varphi = 2 \times 10^{-4}, 4 \times 10^{-4}$) maintain enhancement across the entire measurement area. The magnitude of the enhancement radially is very similar in magnitude to the axial enhancement.

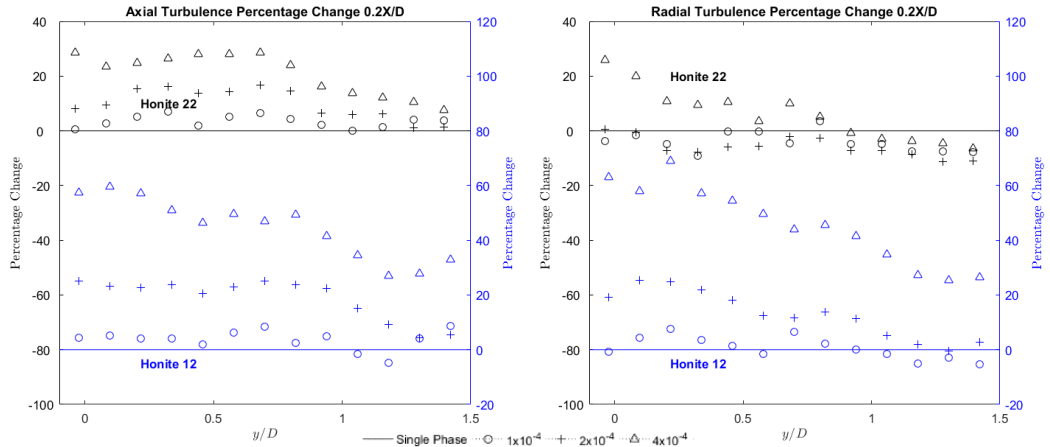


Figure 6.82 (left) – Percentage change in axial turbulence with change in Honite 12 and Honite 22 particle loading 0.2D from impingement. Figure 6.83 (right) – Percentage change in radial turbulence with change in Honite 12 and Honite 22 particle loading 0.2D from impingement.

6.4.3 Vertical Velocity Profiles

The following sub-section contains the velocity profiles taken along the direction of impingement, again they are plotted against a shifted y-axis to enable direct comparison between the two particle sizes.

6.4.3.1 Axial Vertical Velocity Profiles

In the region $1 < x/D < 3$ along the jet centreline, the lowest volume fraction of Honite 22 particles has almost no effect on the axial velocity, however as the concentration is increased ($\varphi = 2 \times 10^{-4}$, 4×10^{-4}) there is clear enhancement of the axial velocity as can be seen in Figure 6.84. The magnitude of the enhancement is very similar for both the 2×10^{-4} and 4×10^{-4} volume fractions suggesting that if a minimum concentration is reached then the effect will be present. This effect is not seen in the Honite 12 system, instead as particle concentration is increased the increase in axial velocity is enhanced. As the upstream influence of the plate is felt ($x/D < 1$) the additional Honite 22 particles at the 4×10^{-4} volume fraction cause axial velocity to be maintained to a greater degree than the 2×10^{-4} volume fraction.

As distance from the centreline is increased ($y/D = 0.5, 1$) the presence of Honite 12 and Honite 22 particles have the opposite effect away from the immediate impingement zone ($1 < x/D < 3$). Increasing the concentration of Honite 22 causes axial velocity to be lower than the single-phase flow whereas increasing the concentration of Honite 12 results in an increase in axial velocity compared with the single-phase flow, as can be seen in Figures 6.84 and 6.85. In the near wall region ($x/D < 1$) both particle species cause axial velocity to be enhanced.

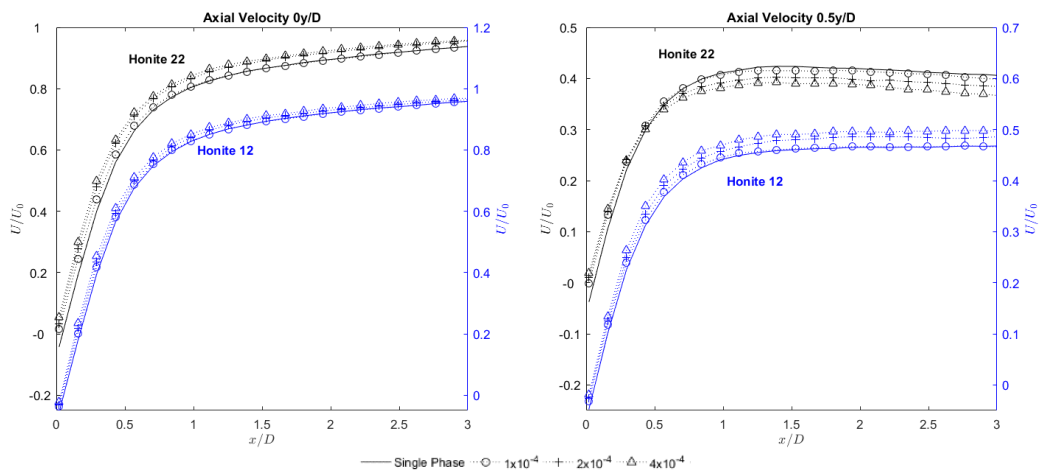


Figure 6.84 (left) – Change in axial velocity with change in Honite 12 and Honite 22 particle loading along the jet centreline. Figure 6.85 (right) – Change in axial velocity with change in Honite 12 and Honite 22 particle loading 0.5 D from the jet centreline.

Further from the jet centreline at $y/D = 5$ (Figure 6.87) the Honite 12 particles have almost no effect on the axial velocity and only the highest concentration of Honite 22 particles show deviation from the single-phase flow where slight enhancement in axial velocity is seen at less than 1D from impingement.

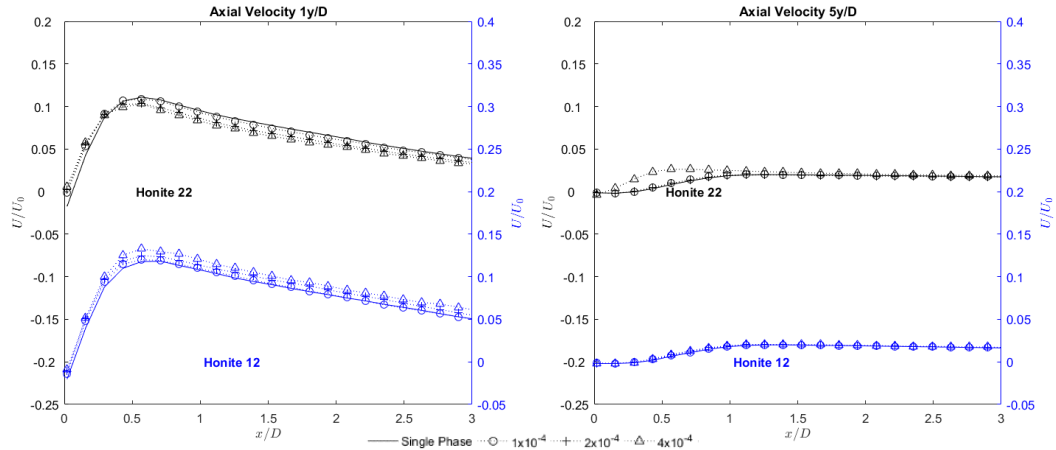


Figure 6.86 (left) – Change in axial velocity with change in Honite 12 and Honite 22 particle loading 1D from the jet centreline. Figure 6.87 (right) – Change in axial velocity with change in Honite 12 and Honite 22 particle loading 5 D from the jet centreline.

6.4.3.2 Radial Vertical Velocity Profiles

Figure 6.88 shows how increasing the particle concentration causes suppression of the radial velocity at $X/D > 0.25$ but enhancement below this, suggesting that the presence of particles causes a reduction in the spreading rate of the radial wall jet. The same behaviour is seen 1D from the jet centreline in Figure 6.89.

Only the 4×10^{-4} volume fraction of Honite 12 particles enhance the maximum radial velocity compared with all tested concentrations of the Honite 22 particles, which suggests it is not just a momentum transfer which is causing the velocity to increase.

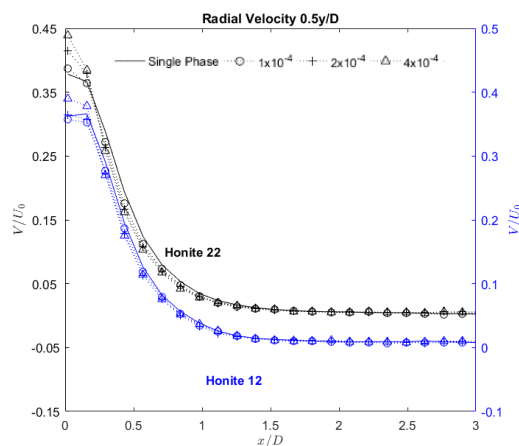


Figure 6.88 – Change in radial velocity with change in Honite 12 and Honite 22 particle loading 0.5 D from the jet centreline.

There is a significant change from the single-phase flow 5D from the centreline when the volume fraction of Honite 22 particles is increased to 4×10^{-4} . There is a significant increase in the maximum radial velocity at $y/D < 0.25$, and a significant reduction in the region $0.25 < y/D < 1$.

Figure 6.90 clearly shows this change in the

shape of the radial wall jet velocity profile. All other tested volume fractions for both particles species have very little effect on the radial velocity.

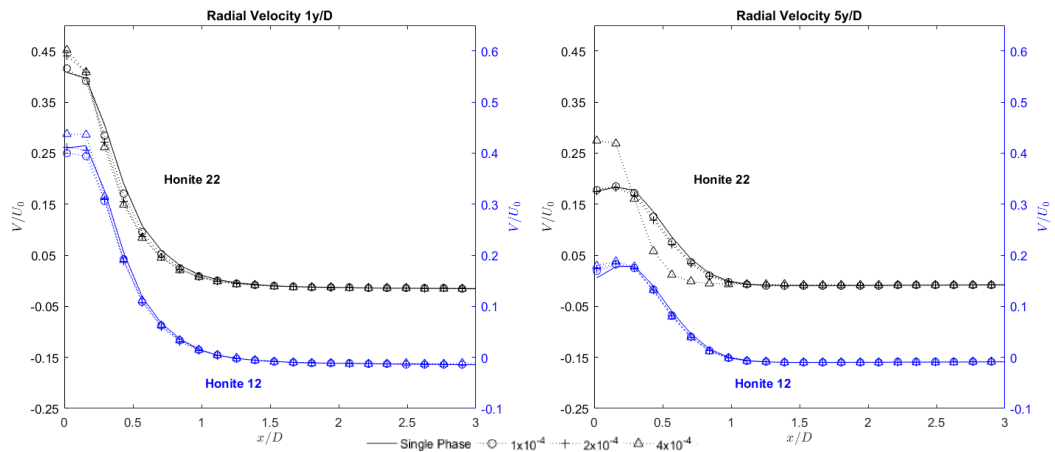


Figure 6.89 (left) – Change in radial velocity with change in Honite 12 and Honite 22 particle loading 1D from the jet centreline. Figure 6.90 (right) – Change in radial velocity with change in Honite 12 and Honite 22 particle loading 5 D from the jet centreline.

6.4.4 Vertical Turbulence Profiles

6.4.4.1 Axial Vertical Turbulence Profiles

Centreline axial turbulence is enhanced in the presence of both Honite 12 and Honite 22 particles, as expected the influence is more pronounced with the larger Honite 12 particles. The enhancement of the turbulence remains fairly constant as the jet continues to develop as can be seen in Figure 6.91. The 4×10^{-4} volume fraction of Honite 22 particles on average causes u'/U_p to increase by 0.013 whereas the same concentration of Honite 12 particles results in an average increase of 0.029. As radial distance from the centreline is increased the magnitude of the average increase is similar, at $0.5y/D$ the Honite 12 particle cause u'/U_p to increase by an average of 0.034 with the Honite 22 particles causing a 0.015 increase shown in Figure 6.92.

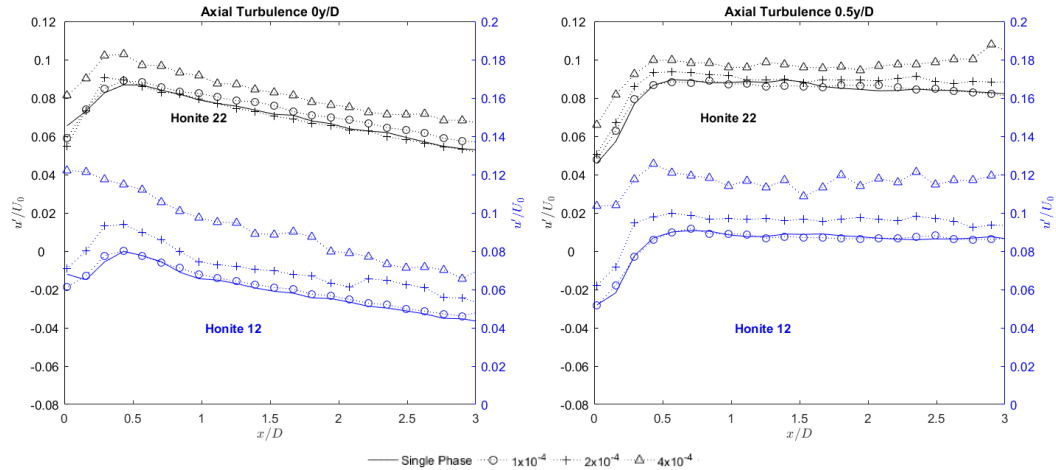


Figure 6.91 (left) – Change in axial turbulence with change in Honite 12 and Honite 22 particle loading along the jet centreline. Figure 6.92 (right) – Change in axial turbulence with change in Honite 12 and Honite 22 particle loading 0.5D from the jet centreline.

Figure 6.93 shows that 1D radially from the centreline the Honite 22 particle slightly suppress axial turbulence except for in the near wall region ($x/D < 1$) whereas the Honite 12 particles show slight enhancement at all concentrations. As the radial distance is increased further to 5 y/D there is very little effect of the lower volume fractions ($\phi = 1 \times 10^{-4}$, 2×10^{-4}) of either species of Honite particle. When $\phi = 4 \times 10^{-4}$ there is enhancement of the fluid turbulence at $x/D > 1.5$ for both species in addition to near the impingement surface at $x/D < 0.5$. In this region, we see a significant increase with the Honite 22 supporting the idea that modulation of the radial wall jet is occurring.

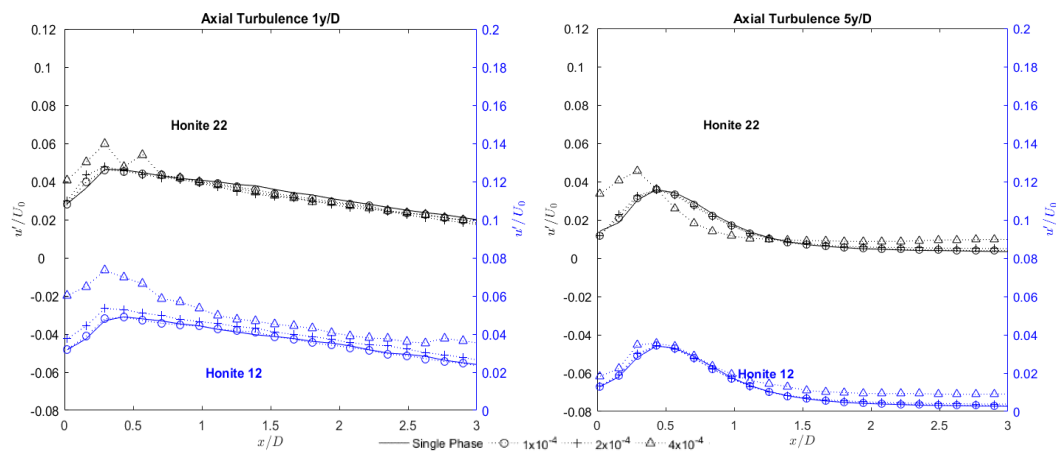


Figure 6.93 (left) – Change in axial turbulence with change in Honite 12 and Honite 22 particle loading 1D from the jet centreline. Figure 6.94 (right) – Change in axial turbulence with change in Honite 12 and Honite 22 particle loading 5D from the jet centreline.

6.4.4.2 Radial Vertical Turbulence Profiles

Figures 6.95 and 6.96 show radial turbulence along the jet centreline and 0.5D from the jet centreline, in both cases radial turbulence is enhanced in the presence of Honite particles. The largest effect is in the impingement region $x/D < 0.5$ where the 4×10^{-4} volume fractions of Honite 12 and 22 cause maximum centreline radial turbulence to increase by 86.6% and 24% respectively. At $y/D=0.5$ maximum radial turbulence is increased by 78.3% for the Honite 12 and 43.4% for the Honite 22.

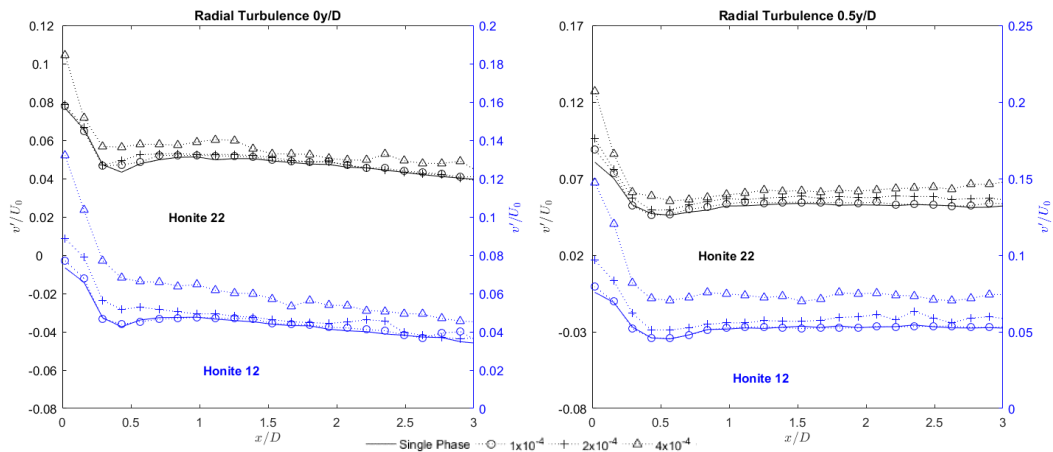


Figure 6.95 (left) – Change in radial turbulence with change in Honite 12 and Honite 22 particle loading along the jet centreline. Figure 6.96 (right) – Change in radial turbulence with change in Honite 12 and Honite 22 particle loading 0.5D from the jet centreline.

At $y/D = 1$ (Figure 6.97) radial turbulence like the axial turbulence measurements shown in Figure 6.93 are slightly suppressed in the presence of Honite 22 particles, except in the developing wall jet ($x/D < 0.5$) where significant enhancement occurs in line with the profiles shown at 0 y/D and 0.5 y/D (Figures 6.95 and 6.96). Honite 12 causes enhancement in the same region continuing as x/D increases but with a reduced impact. As y/D is increased to 5 the influence of particles is almost non-existent except in the case of the 4×10^{-4} volume fraction of Honite 22 particles. This has been the case for the axial turbulence measurements (Figure 6.94) as well as the axial and radial velocity measurements (Figures 6.87 and 6.90).

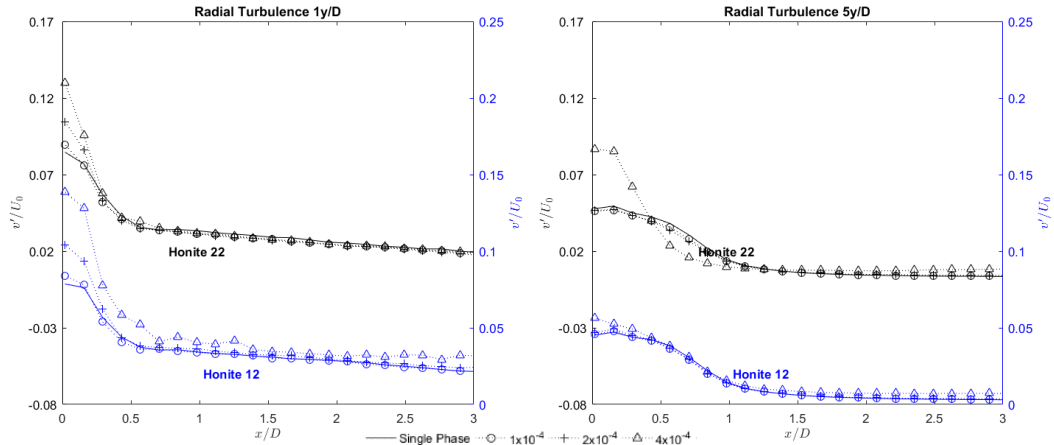


Figure 6.97 (left) – Change in radial turbulence with change in Honite 12 and Honite 22 particle loading 1D from the jet centreline. Figure 6.98 (right) – Change in radial turbulence with change in Honite 12 and Honite 22 particle loading 5D from the jet centreline.

6.4.5 Discussion

Honite 22 particles cause greater centreline velocity retention than the Honite 12 particles which can be seen at 5X/D and 1X/D, in both the axial and radial results. This was also seen by Tsuji et al. (1988) who found that for the same loading ratio smaller particles had a greater influence on the fluid velocity. This can be attributed to a much lower number density for the larger particles in addition to increased diffusion of the larger particles. This agrees with the current experimental results, wherein the impingement zone momentum transfer causes enhanced axial velocity along a narrow region of the jet for the Honite 22 particles. Suggesting that the Honite 22 particles remain within the jet whereas the Honite 12 particles disperse.

The concentration of particles along the jet centreline was seen by Longmire and Eaton (1992), where 55 μm glass particles were examined in an air jet at a Reynolds number of around 20,000. The authors observed that the particles were mainly concentrated within the inner two thirds of the jet and very few particles were present at the edge of the shear layer. However further downstream particles are drawn away from the potential core via larger vortices.

The greater inertia of the larger Honite 12 particles allows them to cross into the turbulent mixing layer, more easily than the smaller Honite 22 particles which will experience a greater proportion of drag due to their increased surface area. Tsuji et al. (1988) also suggests that irregular motion within the pipe leading to the jet orifice causes the larger particles to exit with a much greater radial velocity than the smaller particles. The ratio of jet diameter to particle diameter for the largest particles used by Tsuji et al. (1988) is 14.3 compared with the Honite 12 where the ratio is 17.8, so it would be expected that the same effects would be present in the current work.

Radial velocity is reduced more by the Honite 22 particles in the impingement zone, due to the particles having a greater residence time and so retard the flow to a greater extent. As discussed in the previous section, the Honite 12 particle rebound from the impingement surface, depending on the angle of incidence, can cause the particles to bounce out of the impingement region having no effect in this region. Figure 6.99 shows the measured particle trajectories of Anderson and Longmire (1995) for particles with a jet exit Stokes number of 2.4 (a) and 0.6 (b). These correspond well to the Honite 12 and 22 particles which have a calculated jet exit Stokes number of 8.63 and 0.25 using the same equation as Anderson and Longmire (1995) given in Equation 6.2. From this we can expect a much greater particle density in the impingement zone for the Honite 22 particles, contributing to the increased retardation of radial flow.

$$S_t = \frac{\tau_p U_0}{D}$$

Equation 6.2 - where S_t = Stokes number, τ_p = particle response time, D = jet orifice diameter and U_0 = Jet exit velocity.

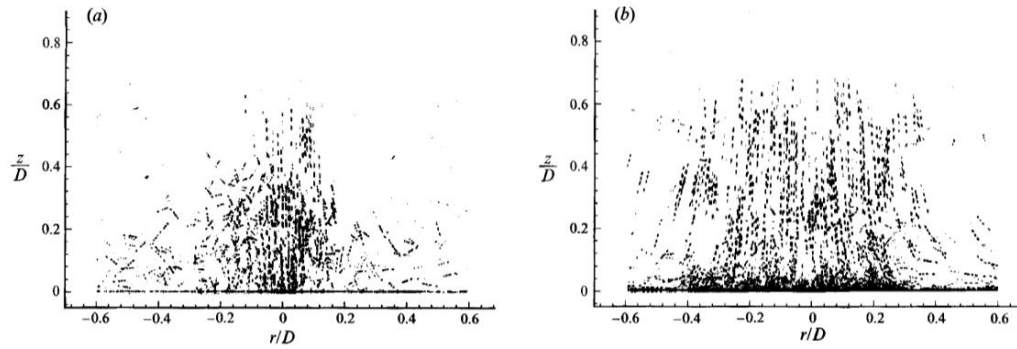


Figure 6.99– Particle trajectories in the stagnation zone. (a) $St, = 2.4$; (b) $St, = 0.6$. (Anderson and Longmire 1995)

Both Honite 12 and 22 particles enhance axial turbulence throughout the jet, consistent with the findings of Virdung and Rasmuson (2007), however the magnitude of the enhancement is reduced for the smaller Honite 22 particles. This is due to multiple effects, smaller Honite 22 particles are much more likely to be ejected from the free shear region as their Stokes number is low enough to be in the region where Hishida et al. (1992) predicts the particles to disperse more significantly than the fluid phase. This leads to much smaller relative concentrations in the shear layer leading to reduced effect. Due to the much lower response time of the smaller particles they rapidly match the fluid movements away from the jet shear mixing layer. At this point velocity gradients are much smaller and so drag induced turbulence is significantly reduced.

As the jet develops the characteristic peaks of turbulence in the shear mixing layer remain, suggesting an extension of the potential core for both the Honite 12 and 22 particles, while in the single phase flow the peaks of the shear mixing layer disappear as turbulence levels become constant across the jet. It is proposed that particles limit entrainment of the surrounding fluid, consistent with the observed narrowing of the jet by Hetsroni and Sokolov (1971) and the effects of limited entrainment by Geers et al. (2004).

As the radial wall jet develops both axial and radial turbulence is enhanced in the presence of Honite 12 and Honite 22 particles which is to be expected as the particles resist radial acceleration. This coincides with a reduction in radial velocity as momentum is lost to turbulence.

Further from the jet centreline at $y/D = 5$, the presence of both Honite 12 and 22 has almost no effect on the flow, except for the highest concentration of Honite 22 particles. One explanation for this effect is that as the tests would progress particles would begin to settle out of the flow and form a ring around the base of the tank. It is possible that flow disturbances from this observed ring of settled particles may have had an unintended influence on the flow, however due to the long processing times taken to obtain the PIV results it was too late to address this after the measurements had been taken.

6.4.6 Comparison with Turbulence Models

Similar to the pipe flow analysis, Figure 6.101 shows how the fluid properties compare with the predictions of Gore and Crowe (1989) (Figure 6.100), with the particle diameter to length scale ratio used to determine if turbulent enhancement or suppression will occur. The turbulent length scale for the jet was calculated using a combination of the methods of Hutchinson et al. (1971) and Wygnanski and Fiedler (1969), two methods used by Gore and Crowe (1989). It was decided to use the turbulent eddy size calculated inside the pipe leading to the jet as a minimum value, as it was considered that the equation used by Wygnanski and Fiedler (1969) (Equation 6.3) would give unrealistic values near the jet exit without setting a minimum size.

$$\frac{l_e}{x} = 0.039$$

Equation 6.3 – where l_e = characteristic eddy size and x = distance from jet orifice.

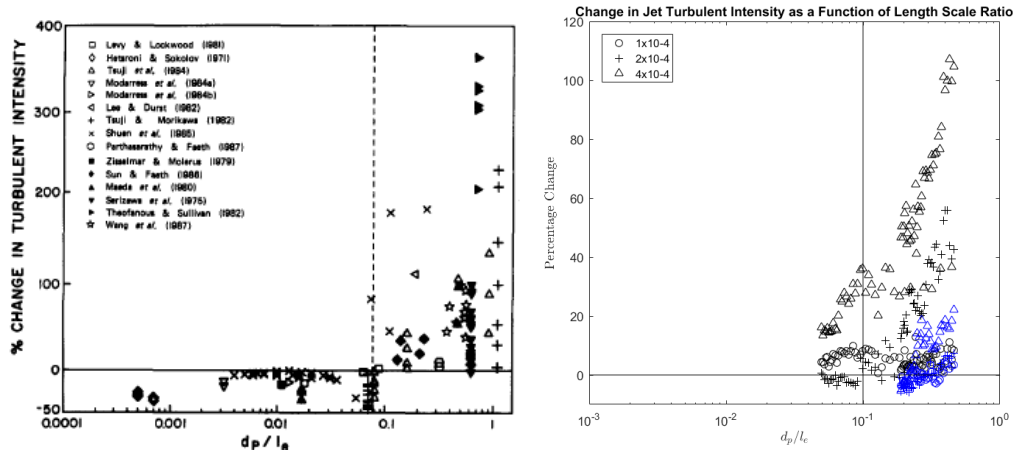


Figure 6.100 (left) – Change in turbulent intensity as a function of the ratio of particle diameter to characteristic eddy size Gore and Crowe (1989). Figure 6.101 (right) - Change in turbulent intensity as a function of the ratio of particle diameter to characteristic eddy size for impinging jet PIV measurements (Honite black, Flashbead Blue).

Results are shown for the effect of particles along the jet centreline. Figure 6.101 shows that turbulent enhancement tends to increase for the Honite particles as the length scale ratio increases. However, the Flashbead particles show turbulence suppression suggesting that density considerations must be made when determining the validity of this method. Turbulence suppression is seen when the length scale ratio is below 0.1 however this is only for the 2×10^{-4} concentration of Honite particles, with enhancement seen at volume fractions of 1×10^{-4} and 4×10^{-4} for the same length scale ratio.

Unfortunately, data was not available to test at much smaller length scale ratios to see if the lower limit for enhancement simply required shifting towards a lower value. It should also be noted that Gore and Crowe (1989) based their study on free jets and not impinging jets where significant redirection of the flow occurs and so particle behaviour and influence in this region is much more unpredictable.

Considerations with regards to particle density and concentration are made by Elghobashi (1994) (Figure 6.102), which uses both the ratio of the particle response time to the eddy turnover time in addition to particle volume fraction in order to predict whether enhancement or suppression of turbulence will occur. Figure 6.103 shows the impinging jet data plotted on a scaled version of the same axes. It should be noted that the concentration values have been shifted slightly for better clarity of information, however the tested volume fractions were consistent between the three particle species.

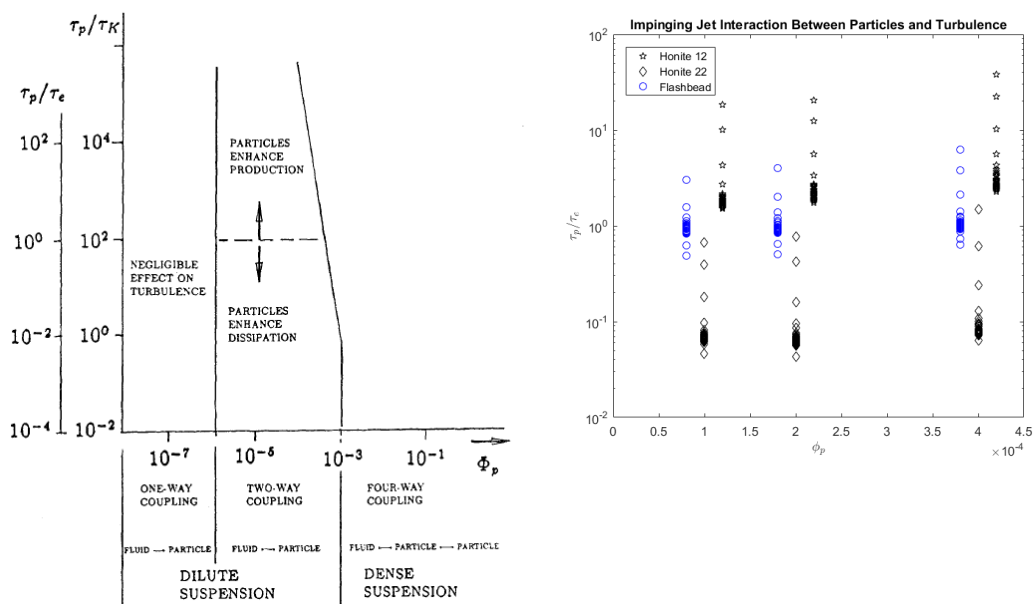


Figure 6.102 (left) - Map of regimes of interaction between particles and turbulence Elghobashi (1994). Figure 6.103 (right) - Map showing locations of impinging jet PIV results on a scaled version of Figure 6.102. Particles plotted at: Honite 22 ϕ , Honite 12 $\phi+0.2 \times 10^{-4}$ Flashbead $\phi-0.2 \times 10^{-4}$ to avoid overlap.

Comparing Figures 6.102 and 6.103 it can be seen that the map proposed by Elghobashi (1994) performs well in predicting the behaviour of the Honite 12 and Flashbead particles, with the Flashbead particles seen to go through a transition period between enhancement of the fluid turbulence and suppression.

Predictions for the smaller Honite 22 particles however suggest that the particles should dissipate turbulence whereas the current results show enhancement. This predicted dissipation was seen in the pipe flow measurements and so like with the method used by Gore and Crowe (1989), it appears that difficulties in applying either of these methods is due to the rapidly changing nature of the flow of an impinging jet.

One issue with both methods is the accurate calculation of the length of turbulent eddies, without direct measurement there exists the problem that the calculated eddy sizes maybe wrong. All of the results which are in the 'wrong' locations on the map produced by Elghobashi (1994) are within an order of magnitude of being in a region where the predictions would be correct, and so it is possible that using an alternative method for calculating the size of the characteristic eddies would result in better correlation between the results and the predictions.

6.5 Comparison of Particle and Fluid Measurements

This section compares measurements of the fluid in the presence of particles with PIV measurements of the particles themselves. Such measurement was only possible for the Honite 22 particles due to a minimum particle optical density required to obtain reliable PIV results with around 12 required as a minimum count per interrogation area (Chapter 3). As the particle size is increased the relative number of particles decreases drastically for the same volume fraction, around 180 times as many Honite 22 particles are in the system compared with Honite 12 at the same concentration and so to obtain results for larger particle sizes much greater concentrations would need to be tested.

The study was performed using the same experimental set up for the fluid measurements of the impinging jet, however the tracer particles were not introduced into the system and the optical filter was removed from the camera allowing the light reflected by the solids to reach the camera sensor.

6.5.1 Velocity Measurements

Figures 6.104 and 6.105 show the velocity measurements of both the fluid and the particles with increased particle loading 5D and 1D from impingement. Both figures show the Honite 22 particles are lagging the fluid away from the jet centreline and as the particle concentration is increased, the particles further away from the potential core of the jet move more slowly whereas particles at the jet centreline have an increased velocity. This pattern is matched by the fluid velocity, which increases at the jet centreline and decreases at the periphery of the jet.

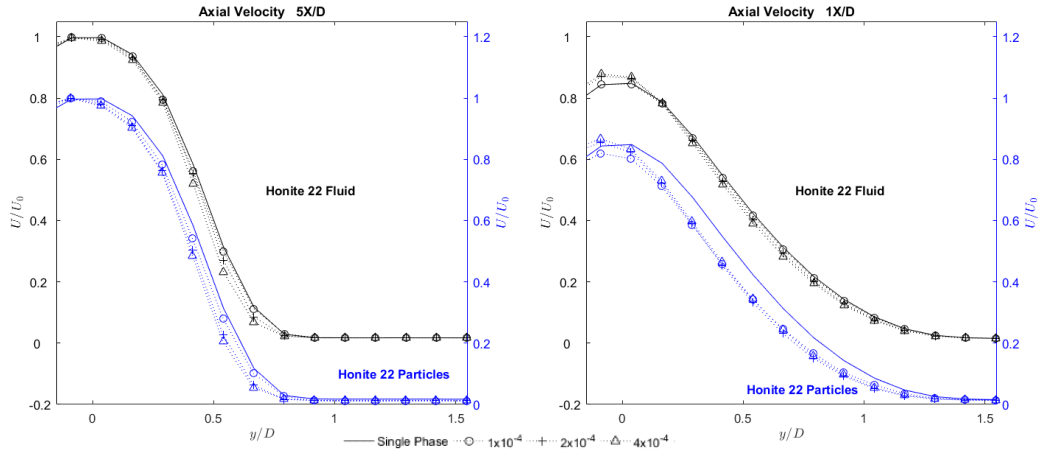


Figure 6.104 (left) – Change in axial fluid and particle velocities with change in Honite 22 particle loading 5D from impingement. Figure 6.105 (right) – Change in axial fluid and particle velocities with change in Honite 22 particle loading 1D from impingement.

As the jet progresses downstream, and the impingement zone is reached the particles along the jet centreline have a greater velocity than the fluid which can be seen at 0.5X/D and 0.2X/D (Figures 6.106 and 6.107), with an increase in particle volume fraction resulting in both increased particle and fluid velocities. An exception to this is seen in Figure 6.107 where the 1×10^{-4} volume fraction measurements show the particle velocity to be significantly lower than the measured fluid velocity for both the single-phase flow and the particle laden flow at the same concentration. It is believed that this is due to measurement error due to low particle numbers not meeting the required optical density for PIV measurements and will be discussed in more detail later.

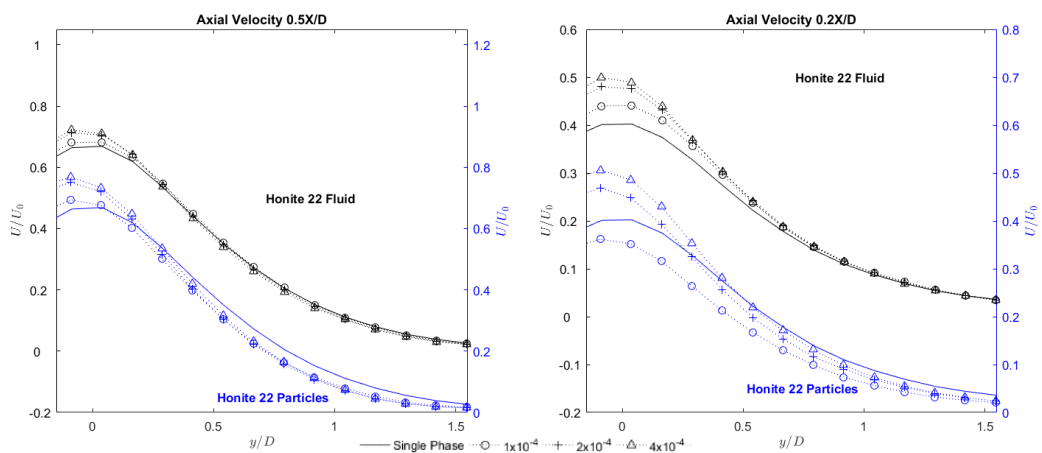


Figure 6.106 (left) – Change in axial fluid and particle velocities with change in Honite 22 particle loading 0.5D from impingement. Figure 6.107 (right) – Change in axial fluid and particle velocities with change in Honite 22 particle loading 0.2D from impingement.

Radial velocity measurements show that the particles exit the orifice with a slightly higher radial velocity component compared with the fluid with the maximum enhancement seen around $0.4y/D$ shown in Figure 6.108.

As the flow develops the particles begin to lag both the single phase and particle laden flows beyond $y/D = 0.5$ which can be seen in Figure 6.109. This in turn leads to a reduction in the fluid radial velocity.

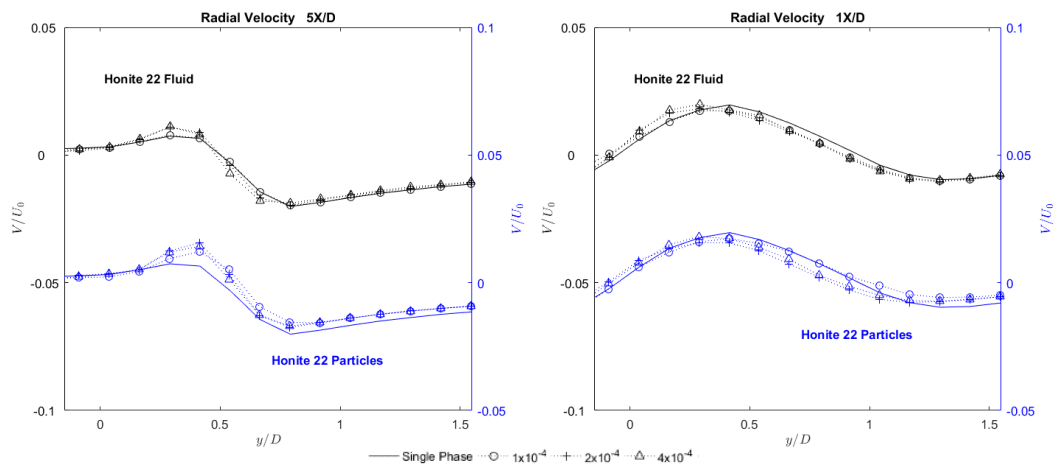


Figure 6.108 (left) – Change in radial fluid and particle velocities with change in Honite 22 particle loading 5D from impingement. Figure 6.109 (right) – Change in radial fluid and particle velocities with change in Honite 22 particle loading 1D from impingement.

At $0.5X/D$ (Figure 6.110) the upstream effects of the impingement plate begin to be felt by the fluid, however the particles are much more resistant to this effect and undergo less radial acceleration. At the 4×10^{-4} volume fraction the maximum radial component of velocity for the particles is 0.30 m.s^{-1} compared with the fluid velocity of 0.53 m.s^{-1} .

Figure 6.111 shows the radial velocities measured at the closest point to the impingement plate ($0.2X/D$). As particle concentration is increased the particles lag the flow to a greater extent which causes greater reductions in the radial velocity of the fluid. In this region,

maximum particle velocities are reduced by 19.3% compared with the single-phase flow, which causes a reduction in the fluid velocity of 13.5%.

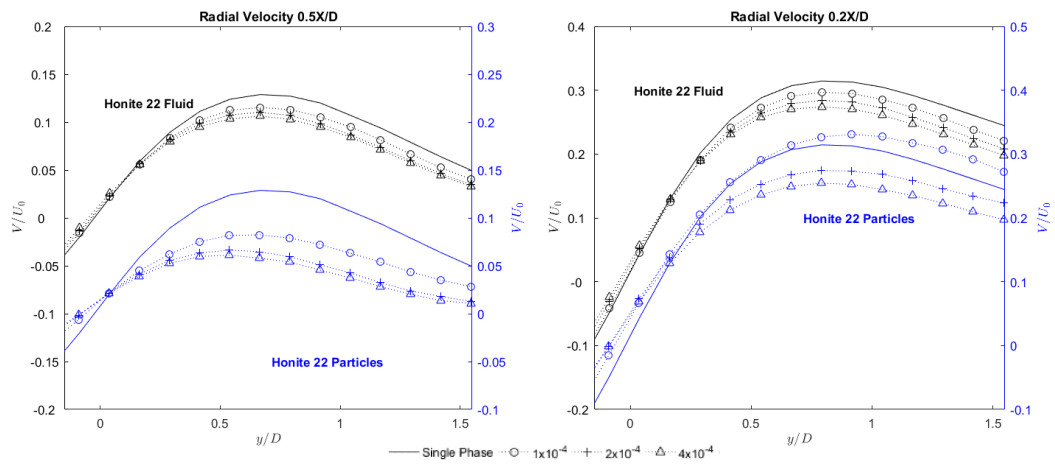


Figure 6.110 (left) – Change in radial fluid and particle velocities with change in Honite 22 particle loading 0.5D from impingement. Figure 6.111 (right) – Change in radial fluid and particle velocities with change in Honite 22 particle loading 0.2D from impingement.

6.5.2 Turbulence Measurements

The following figures compare particle velocity fluctuations with the measured fluid turbulence.

6.5.2.1 Axial Turbulence Measurements

At 5X/D shown in Figure 6.112 particle velocity fluctuations are significantly larger than the single-phase flow especially for the 1×10^{-4} particle volume fraction, whereas the fluid turbulence remains almost unaffected by the presence of particles at this concentration. This suggests, like velocity measurements at 0.2X/D, there is a slight problem with the results at this particle volume fraction. For this reason, analysis will mainly be focused on the 2×10^{-4} and 4×10^{-4} particle volume fractions.

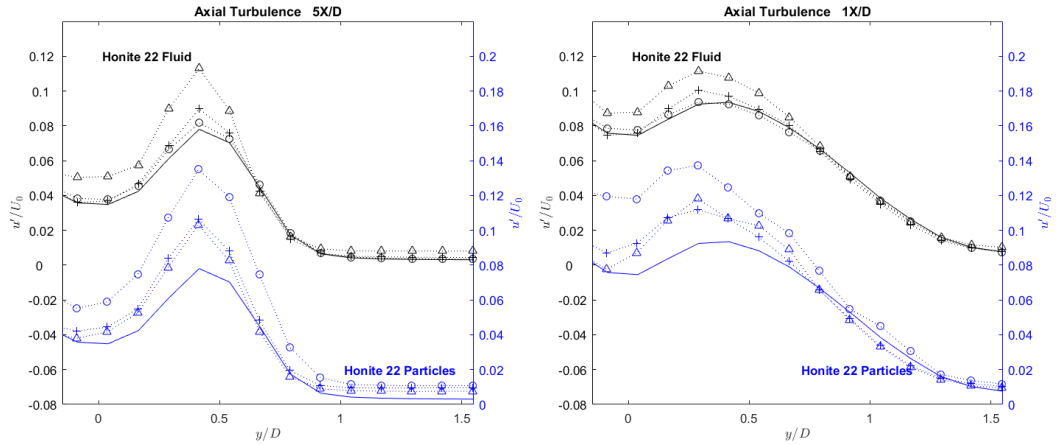


Figure 6.112 (left) – Change in axial fluid and particle velocity fluctuations with change in Honite 22 particle loading 5D from impingement. Figure 6.113 (right) – Change in axial fluid and particle velocity fluctuations with change in Honite 22 particle loading 1D from impingement.

As the particle volume fraction increases axial fluid turbulence is enhanced whereas the particle velocity fluctuations remain fairly constant with little difference between the fluctuations at volume fractions of 2×10^{-4} and 4×10^{-4} at all the measurement locations shown in Figures 6.112 to 6.115. In all cases the particle fluctuations are greater than the single-phase turbulence.

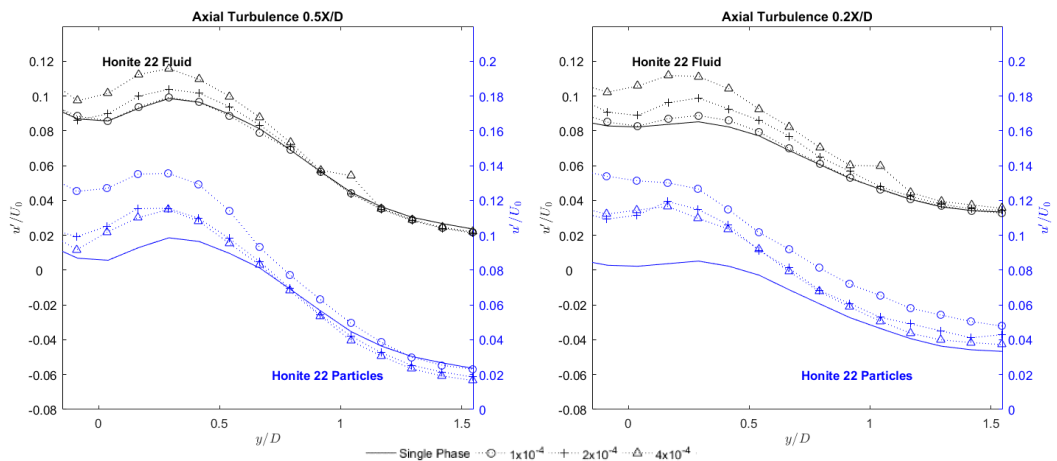


Figure 6.114 (left) – Change in axial fluid and particle velocity fluctuations with change in Honite 22 particle loading 0.5D from impingement. Figure 6.115 (right) – Change in axial fluid and particle velocity fluctuations with change in Honite 22 particle loading 0.2D from impingement.

6.5.2.2 Radial Turbulence Measurements

Radial turbulence measurements (Figures 6.116 to 6.119) show the same behaviour as the axial turbulence. At 5X/D (Figure 6.116) peak fluid turbulence at 0.45y/D coincides with peak particle velocity fluctuations. As distance from the jet centreline is increased particle velocity fluctuations match the single-phase fluid turbulence and no enhancement is seen in the particle laden fluid measurements. Figure 6.117 shows that as the jet progresses to 1X/D particle fluctuations beyond 0.5y/D are less than the single-phase fluid turbulence and slight suppression of the radial turbulence is seen in the particle laden fluid measurements.

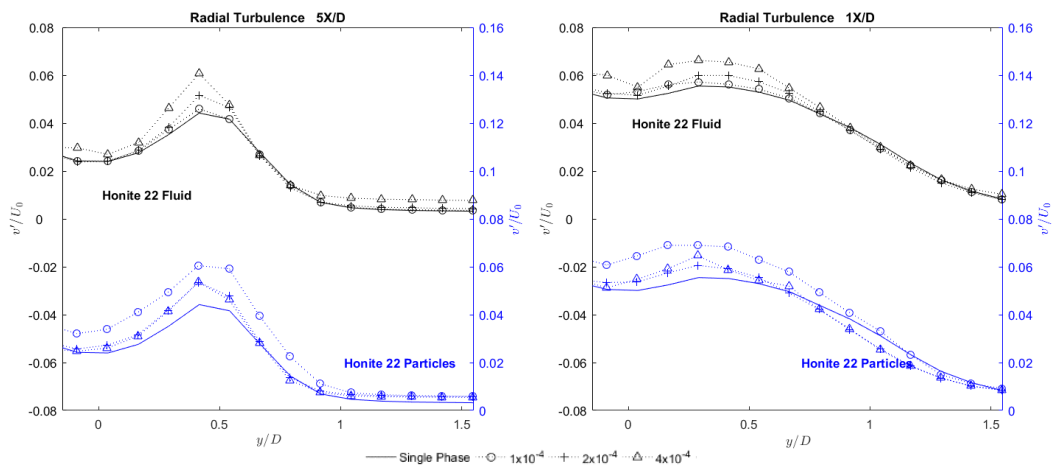


Figure 6.116 (left) – Change in radial fluid and particle velocity fluctuations with change in Honite 22 particle loading 5D from impingement. Figure 6.117 (right) – Change in radial fluid and particle velocity fluctuations with change in Honite 22 particle loading 1D from impingement.

In the impingement region ($X/D < 0.5$) shown in Figures 6.118 and 6.119 we observe enhancement in the fluid turbulence between the jet centreline and $0.75X/D$, whereas beyond this suppression occurs. At $0.5X/D$ particle velocity fluctuations are greater than fluid turbulence until $y/D = 1$ where the transition occurs. Particle velocity fluctuations at $0.2X/D$ are greater than single phase fluid turbulence measurements at all locations.

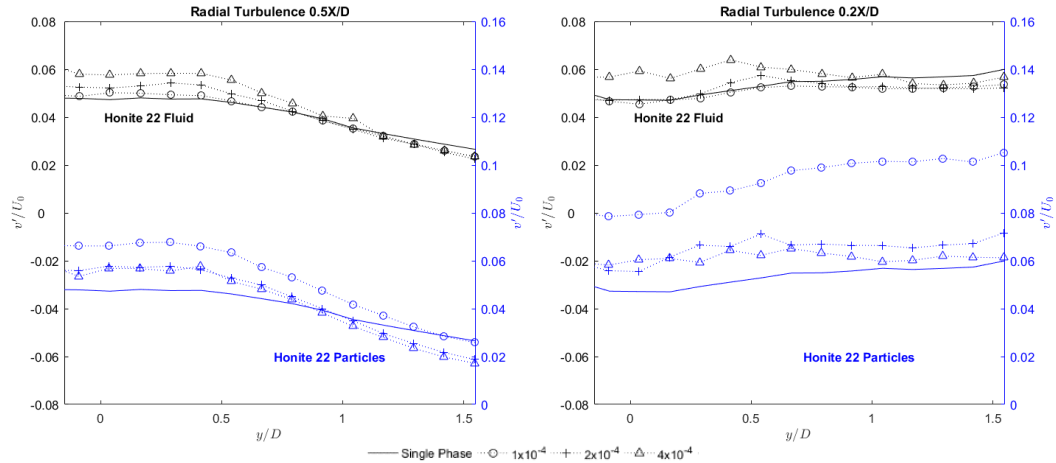


Figure 6.118 (left) –Change in radial fluid and particle velocity fluctuations with change in Honite 22 particle loading 0.5D from impingement. Figure 6.119 (right) – Change in radial fluid and particle velocity fluctuations with change in Honite 22 particle loading 0.2D from impingement.

6.5.3 Discussion

One of the biggest challenges in obtaining particle velocity and turbulence measurements using PIV is in obtaining a large enough number of particles per interrogation area for accurate calculation of the intensity peak displacement. In these measurements, it is believed that the 1×10^{-4} particle volume fraction measurements show increased turbulence enhancement compared with particles at higher concentrations ($\varphi = 2 \times 10^{-4}$, 4×10^{-4}) due to uncertainty in the measurement and not due to the particles causing an increase in the fluid velocity fluctuations.

Particles at the jet periphery appear to be lagging the flow close to the jet outlet. This is caused by the particle behaviour within the jet-line prior to exiting the orifice, which is essentially a pipe flow. Measured particle velocities in pipes (Chapter 4) are significantly lower than the bulk flow in the near wall region and so when these particles exit the jet there is a transition period as the particles are accelerated to match the fluid velocity.

During this transition period, significant differences between the particle and fluid velocities will lead to the production of turbulence. This is in addition to the particles having a larger component of radial velocity at the jet outlet, this supports the idea that particle collisions

along the wall of the jet-line allow the particles to enhance dispersion by providing additional radial velocity as seen by Tsuji et al. (1988).

In the impingement region the particles are travelling faster than the flow at the measurement location closest to the base of the tank, this will inevitably lead to the rebounding of particles seen by Anderson and Longmire (1995).

Acquisition of particle velocities in addition to the fluid velocities allows for the local particle Reynolds numbers to be calculated, Figures 6.120 and 6.122 show contour plots for the calculated difference between the particle and fluid velocities from which the particle Reynolds numbers can be calculated using Equation 6.4 producing the particle Reynolds contour plots shown in Figures 6.121 and 6.123.

$$Re_p = \frac{d_p(|U_p - U_f|)}{\nu}$$

Equation 6.4 – Calculation of particle Reynolds number (Re_p) where d_p = particle diameter, U_p =Particle Velocity, U_f = fluid velocity and ν = fluid kinematic viscosity

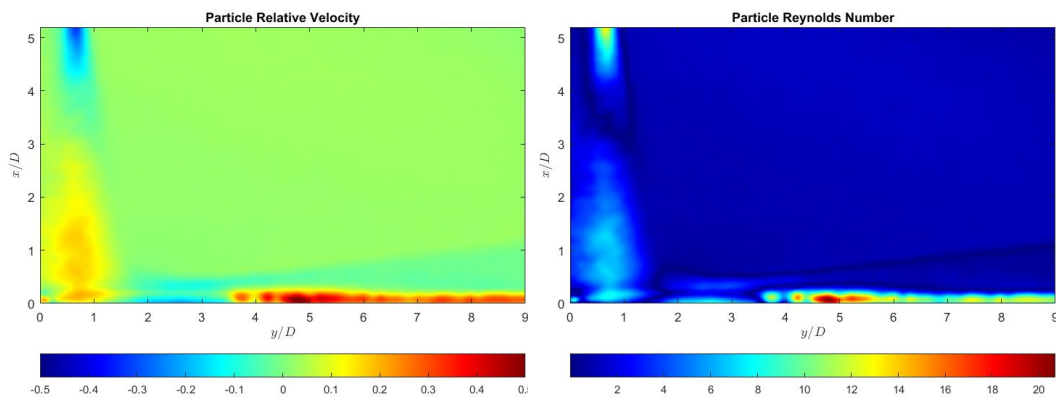


Figure 6.120 (left) –Contour plot of the relative velocity between the particles and the fluid for the impinging jet laden with Honite 22 particles at $\phi = 2 \times 10^{-4}$. Figure 6.121 (right) – Contour plot of the particle Reynolds number for the impinging jet laden with Honite 22 particles at $\phi = 2 \times 10^{-4}$.

From Figures 6.120 and 6.122 we observe four main regions where significant differences between fluid and particle velocities exist.

- Jet Outlet - this region extends from the outlet of the jet line to around $4X/D$ and exists between $0.5D$ and $1D$ from the jet centreline. Here particles are travelling more slowly than the surrounding fluid however no effect is seen on the fluid turbulence. This may be due to a lack of particles in this region as seen by Longmire and Eaton (1992).
- Impingement Zone - this region exists between $0.5X/D$ and the impingement plate and extends from the jet centreline to $1.5y/D$. Here the particles have a greater axial velocity than the fluid but a much lower radial velocity as the fluid is redirected along the base of the tank. This is caused by particle inertia and the associated lag time in the particles being accelerated to match the fluid speed. In this region the fluid turbulence is suppressed in the presence of particles as suggested by Hetsroni (1989) for particle Reynolds numbers less than 110.
- Inner Wall Jet Region - this region exists between the impingement surface and $0.5X/D$, and $4D$ to $6D$ from the centreline. In this region, the main component of particle velocity is now radial however the particles are still travelling more slowly than the fluid and are still being accelerated.
- Outer Wall Jet Region - the final region exists between the impingement surface and $0.5X/D$, and $4D$ to $6D$ from the centreline. In this region, the particles are travelling faster than the surrounding fluid. This occurs as the fluid is slowing in this region and gravity causes particles with greater velocity to drift towards the base of the tank where velocities are lower. Eventually particle velocities decay to more closely match the fluid velocity.

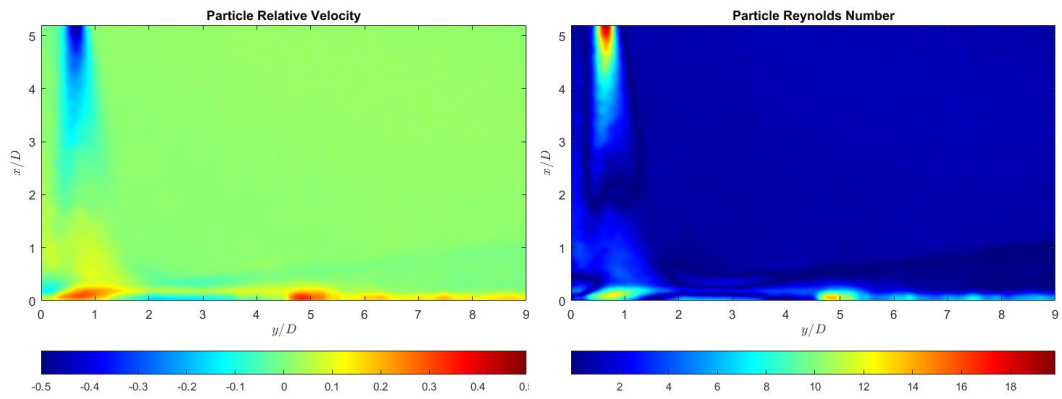


Figure 6.122 (left) –Contour plot of the relative velocity between the particles and the fluid for the impinging jet laden with Honite 22 particles at $\varphi = 4 \times 10^{-4}$. Figure 6.123 (right) – Contour plot of the particle Reynolds number for the impinging jet laden with Honite 22 particles at $\varphi = 4 \times 10^{-4}$.

Throughout the entire jet the particle Reynolds number does not exceed 20 for either the 2×10^{-4} or 4×10^{-4} particle volume fractions. Elsewhere in the jet fluid turbulence is seen to be suppressed in the presence of particles which is consistent with the results of Hetsroni (1989).

The magnitude of the axial and radial velocity fluctuations for the particles closely match that of the fluid turbulence levels which suggests that these particles undergo a strong mutual interaction with the fluid. The low particle Stokes numbers mean that the particles are receptive to the smaller scales of motion of the fluid, and so as the particles increase the fluid turbulence an increase in the particle velocity fluctuations also occurs.

6.6 Impinging Jet Summary and Conclusions

This chapter has shown that PIV is a powerful technique for capturing complex shear flows such as those seen in an impinging jet. The major advantage of PIV is a whole field approach which is relatively unobtrusive with regards to the influence of the measurement technique on the flow. The technique however suffers difficulties with optical clarity and the requirements of a minimum number of particles per interrogation area, this makes measurement of particle velocities at low concentrations difficult, and as particles numbers are increased optical clarity becomes an issue also making measurement difficult.

Single phase measurements of the jet were made and compared with other results in the literature which proved the technique was working well and accurately measuring fluid behaviour.

Selective measurements of tracer particles were then successfully made via the use of optical filters and fluorescent tracer particles. This allowed for the solid phase to be screened from the camera so that fluid velocities were obtained. The effect of Honite 12 and Flashbead particles on the fluid phase was examined and allowed for particle density effects to be studied in their effect on fluid velocity and turbulence. It was found that the particles can enhance centreline velocity through both momentum transfer in the case of the Honite 12 and the suppression of turbulence in the case of the Flashbead.

The effect of smaller Honite 22 particles was then examined allowing for particle size effects to be studied. This information was then used to compare how accurately the effect of particles on fluid turbulence could be predicted using the methods proposed by Gore and Crowe (1989) which works well for particles where the particle density is much larger than the fluid density, and the method proposed by Elghobashi (1994) which works well to account for particle density, however it was found to be inaccurate in predicting the effect

of small particles which enhanced turbulence where they would be predicted to dissipate turbulence.

Further work was then completed to track the movement of the Honite 22 particles within the flow. Larger particles could not be tracked due to the minimum number of particles required per interrogation area. From the tracking of Honite particles four main regions exist where there is a significant difference between the fluid and particle velocities. In these four regions suppression of the turbulence was seen where particle Reynolds numbers were less than 20, which shows good agreement with Hetsroni (1989) who suggests that particles with a Reynolds number less than 110 dissipate turbulence within the flow.

6.7 References

- Anderson, S.L. and Longmire, E.K. (1995). Particle motion in the stagnation zone of an impinging air jet. *Journal of Fluid Mechanics*. **299**,pp.333–366.
- Bogusławski, L. and Popiel, C.O. (1979). Flow structure of the free round turbulent jet in the initial region. *Journal of Fluid Mechanics*. **90**(3),pp.531–539.
- Cooper, D., Jackson, D.C., Launder, B.E. and Liao, G.X. (1993). Impinging jet studies for turbulence model assessment -- I. Flow-field experiments. *Int. J. Heat Mass Transfer*. **36**(10),pp.2675–2684.
- Elghobashi, S. (1994). On predicting particle-laden turbulent flows. *Applied Scientific Research*. **52**,pp.309–329.
- Era, Y. and Saima, A. (1976). An Investigation of Impinging Jet: Experiments by Air, Hot Air and Carbondioxide. *Bulletin of JSME*.
- Fairweather, M. and Hargrave, G. (2002). Experimental investigation of an axisymmetric impinging turbulent jet. 1. Velocity Field. *Experiments in Fluids*. **33**,pp.464–471.
- Fitzgerald, J. a. and Garimella, S. V. (1998). A study of the flow field of a confined and submerged impinging jet. *International Journal of Heat and Mass Transfer*. **41**(8–9),pp.1025–1034.
- Fleckhaus, D., Hishida, K. and Maeda, M. (1987). Effect of laden solid particles on the turbulent flow structure of a round free jet. *Expf*. **5**(323–333).
- Geers, L.F.G., Tummers, M.J. and Hanjalić, K. (2004). Experimental investigation of impinging jet arrays. *Experiments in Fluids*. **36**(6),pp.946–958.
- Gore, R. and Crowe, C. (1989). Effect of particle size on modulating turbulent intensity. *International Journal of Multiphase Flow*. **15**(2),pp.279–285.
- Gutmark, E., Wolfshtein, M. and Wygnanski, I. (1978). The plane turbulent impinging jet. *Journal of Fluid Mechanics*. **88**(4),pp.737–756.
- Hammad, K.J. and Milanovic, I. (2011). Flow Structure in the Near-Wall Region of a Submerged Impinging Jet. *Journal of Fluids Engineering*. **133**(9),p.91205.
- Hetsroni, G. (1989). Particles-turbulence interaction. *International Journal of Multiphase Flow*. **15**(5),pp.735–746.
- Hetsroni, G. and Sokolov, M. (1971). Distribution of mass, velocity, and intensity of turbulence in a two-phase turbulent jet. *Trans. ASME J. Appl. Mech.* **38**(2),pp.315–327.
- Hishida, K., Ando, A. and Maeda, M. (1992). Experiments on Particle Dispersion in a Turbulent Mixing Layer. *International Journal of Multiphase Flow*. **18**(2),pp.181–194.
- Hutchinson, P., Hewitt, G. and Dukler, A.E. (1971). Deposition of liquid or solid suspension from turbulent gas streams: a stochastic model. *Chemical Engineering Science*. **26**,pp.419–439.
- Landreth, C.C. and Adrian, R.J. (1990). Impingement of a Reynolds number turbulent circular jet onto a flat plate at normal incidence. *Experiments in Fluids*. **9**,pp.74–84.
- Longmire, E.K. and Eaton, J.K. (1992). Structure of a particle-laden round jet. *Journal of Fluid Mechanics*. **236**(217),pp.217–257.
- Loureiro, J.B.R. and Freire, A.P.S. (2012). Wall shear stress measurements and parametric analysis of impinging wall jets. *International Journal of Heat and Mass Transfer*. **55**(23–24),pp.6400–6409.

- Poreh, M., Tsuei, Y.G. and Cermak, J.E. (1967). Investigation of a Turbulent Radial Wall Jet. *Journal of Applied Mechanics*. **34**(2),p.457.
- Tsubokura, M., Kobayashi, T., Taniguchi, N. and Jones, W.P. (2003). A numerical study on the eddy structures of impinging jets excited at the inlet. *International Journal of Heat and Fluid Flow*. **24**(4),pp.500–511.
- Tsuji, Y., Morikawa, Y., Tanaka, T. and Karimine, K. (1988). Measurements of an axisymmetric jet laden with coarse particles. *Int. J. Multiphase Flow*. **14**,p.565.
- Tummers, M.J., Jacobse, J. and Voorbrood, S.G.J. (2011). Turbulent flow in the near field of a round impinging jet. *International Journal of Heat and Mass Transfer*. **54**(23),pp.4939–4948.
- Virdung, T. and Rasmuson, A. (2007). Hydrodynamic properties of a turbulent confined solid-liquid jet evaluated using PIV and CFD. *Chemical Engineering Science*. **62**(21),pp.5963–5978.
- Wynanski, I. and Fiedler, H. (1969). Some measurements in the self preserving jet. *Journal of Fluid Mechanics*. **38**(3),pp.577–612.
- Yoshida, H., Suenaga, K. and Echigo, R. (1990). Turbulence structure and heat transfer of a two-dimensional impinging jet with gas-solid suspensions. *International Journal of Heat and Mass Transfer*. **33**(5),pp.859–867.

7 Conclusions and Recommendations for Future Work

This final chapter contains a summary of the conclusions regarding the success of the project and its outcomes, this is followed by suggestions for relevant further work which would be of benefit to greater understanding in this field.

7.1 Effect of Introducing Dense Solid Particles

Introducing solid particles which are denser than the fluid (pipe flow system) had implications for both the fluid and particle behaviour. If the particles were suspended by the flow, mutual interaction between the two phases occurred. In the pipe flow system, this manifests as a slight velocity reduction at the pipe wall as the particles in this region remove energy from the flow and are gradually accelerated. This coincides with an increase in turbulence in this region as particles cross streamlines bringing high velocity fluid into low velocity regions and vice-versa.

Measurements in the bulk flow region, which comprises most of the pipe, show that although adding particles has an effect, the effect is dampened when compared with near wall measurements. Slight enhancement of the velocity in this region is seen which is attributed to a change in shape of the velocity profile, where the flow has a lower velocity towards the bottom of the pipe compared to the top due to stratification of the particles in the system.

In the impinging jet, the addition of particles caused the jet to retain velocity as the impingement surface was approached. This is due to the transfer of momentum from the particles which resist the deceleration of the jet. This results in an increase in turbulence in the impingement region as the particles and fluid interact. Such an effect is then followed by a reduction in the wall jet velocity as energy is sapped from the fluid to accelerate the particles away from the jet centreline.

7.2 Effect of Particle Concentration

In the general case, increasing the concentration of particles within the pipe flow system resulted in a magnification of the particles effect on the fluid in the near wall region. Increasing the volume fraction of almost neutrally buoyant Flashbead particles from 1×10^{-4} to 8×10^{-4} caused the fluid velocity at the wall to decrease by 10.2% which corresponded with an increase in the fluid axial turbulence of 4.8%. In the bulk flow region, no clear trends were observed as the concentration of particles was increased.

Particle behaviour in the pipe has a varied response to changing concentration than the fluid. This is because as the concentration continues to increase, particle-particle interactions begin to have a significant influence on the particle behaviour.

In the impinging jet, slight increases in Honite 12 particle concentration resulted in enhanced centreline velocity retention, and a significant increase in fluid turbulence. Where the glass particles had almost no influence on the axial or radial turbulence measurements at a volume fraction of 1×10^{-4} at 2×10^{-4} , peak axial turbulence was 18.4% higher than the single phase measurements and at 4×10^{-4} 82.2% higher 5D from impingement.

Increased concentration of Flashbead particles increased retention of centreline axial velocity when the volume was increased from 1×10^{-4} to 2×10^{-4} however, further increasing the volume fraction to 4×10^{-4} did not cause further increases in velocity retention. This same pattern of initial increase before plateauing (i.e. independent of solids concentration) was also observed in the reduction of axial turbulence where the presence of particles caused an initial reduction which did not increase with increased particle concentration.

7.3 Effect of Particle Size

As the particle size increased so did the particle response time, and the ratio of particle size to characteristic eddy length. In the pipe system at a volume fraction of 8×10^{-4} , increasing particle diameter from 225 μm to 500 μm caused a reduction in the particle velocity at the wall. These slower moving particles restrict the fluid flow in this region, causing fluid velocity to drop by up to 11.2%, coupled with an increase in axial turbulence of 14.9% compared with the single phase flow, as mutual interactions between turbulent eddies and particles enhanced energy transfer from the main flow. Reducing the particle diameter to 40 μm resulted in a smaller maximum reduction in fluid velocity (4.4%) however, unlike the larger particles this reduction in velocity did not coincide with an increase in axial turbulence, instead reductions in axial turbulence up to 10.0% were seen as the particles were able to follow the small scale turbulent motions and so sap turbulent energy in addition to energy from the main flow. In the bulk flow region, general trends showed suppression of the axial and radial turbulence by the 40 μm particles, while the 225 μm particles tend to enhance axial and radial turbulence, although the 500 μm particles enhanced axial turbulence but suppressed radial turbulence.

In the impinging jet, reducing the particle size from 225 μm to 40 μm resulted in an increase in velocity retention from 14.8% to 24.6% 0.2D from impingement at a particle volume fraction of 4×10^{-4} . This was due to increased dispersion of the larger particles causing the relative concentration of 40 μm particles to be greater. Axial turbulence was enhanced in the presence of both particles, with greater enhancement by the larger particles (49.4% compared with 16.1%) 0.2D from impingement. Immediately before impingement slight suppression of radial turbulence was seen in the presence of the 40 μm particles.

7.4 Effect of Particle Density

Particle density effects were investigated using Honite 12 glass particles ($\rho = 2450 \text{ kg m}^{-3}$) and almost neutrally buoyant Flashbead polystyrene particles ($\rho = 1050 \text{ kg m}^{-3}$). Reducing the particle density reduced the particle response time allowing for the tracking of smaller scale fluid motion.

In the pipe system, Flashbead particles had significantly more velocity than the Honite 12 particles in the region $y^+ < 50$. Further from the wall Flashbead particles have a slightly lower velocity than the single phase, due to particles concentrating in low velocity regions of the flow so their tracked velocities were lower. This transition location from enhanced to suppressed velocity coincides with the location of peak suppression of particle velocity fluctuations. The transition also coincides with a transition from enhancement of fluid axial turbulence near the wall to suppression of axial turbulence towards the pipe centreline. Radial turbulence was suppressed up to 14.8% in the presence of Flashbead particles but enhanced by up to 5.2% by Honite 12 particles.

Both particle species caused an increase in axial velocity retention of the impinging jet. For the dense glass particles this increase can be explained via momentum transfer, but an alternative mechanism was responsible for the polystyrene. As the densities of the particles and fluid become close, momentum transfer is minimal and so instead the increased velocity is due to a reduction of energy losses through turbulence. Where glass particles caused significant increases in axial and radial turbulence throughout the jet, polystyrene particles only caused increases immediately after the jet outlet. As the jet develops vortex stretching causes the ratio of particle size to eddy length to transition into a regime of turbulence suppression.

7.5 Summary

The main objective of the thesis was to obtain and analyse both particle and fluid behaviour in multiphase turbulent flows. The effectiveness of UDV for qualitative analysis of flows was proven for dilute flows, and quantitatively for particle volume fractions between 1×10^{-4} and 64×10^{-4} . UDV can be recommended in the study of much higher concentration flows than PIV and flows where optical clarity of the area of interest is not possible, whether due to geometry or fluid properties.

PIV was used to obtain precise, high accuracy measurements of multiphase flow within pipes, and allowed for small variations in fluid behaviour to be observed with changes in particle volume fraction. Although data capture was limited in the near wall region due to optical distortion, caused by pipe curvature, some near wall measurements could be made and showed that the influence of particles is greatest in this region.

PIV was also used to measure the influence of particles in an impinging jet system. The technique was shown to work well with the variable flow conditions and data was obtained for various particle concentrations. It was shown that even in dilute systems, the presence of particles can have significant effects on fluid turbulence which is important for a variety of systems which utilise this turbulent behaviour, such as mixing, cooling and mass transfer applications.

The data has been used to demonstrate some of the strengths and weaknesses of current models for predicting the influence of particles in turbulent flows. The PIV data for both the pipe and jet was suitable to act as validation for the development and refinement of turbulence models which will allow predictions of future systems to be more robust.

7.6 Future Work

To further strengthen the ability to make accurate predictions of flow behaviour, a good follow up to this study would be to continue to test a greater range of particle sizes and densities. This would allow for a comprehensive data set to be created mapping out regimes of particle behaviour. It would also allow for transition points to be identified where enhancement or suppression of velocity and velocity fluctuations occur, which would allow for the refinement of models that are used to predict particle behaviour.

Further development of the UDV experimental equipment to introduce multiple transducers which would allow for the measurement of radial and azimuthal velocities to provide a more comprehensive picture of particle behaviour. In addition, further work on the application of the measurement probes to reduce their influence on the flow. The capture of radial and axial measurements simultaneously is difficult due to the need for the probes to be mounted in the same location and at different angles, this means that although mean velocities can be captured, mapping instantaneous velocities to specific interrogation areas is difficult. Improved contact between the probes and the outside surface of the wall may help to solve the flow distortion issues however, problems arose with signal distortion and so it is recommended that work is performed to develop this due to its potential applications in high concentration multiphase flows.

Some aspects of this investigation were limited by the maximum resolution of the camera. It is proposed that experiments should be performed with a higher quality camera, this would allow for smaller particles to be used and a greater density of interrogation areas. This would

serve to reduce errors due to large velocity gradients and increase the resolution of the results. This creates a more functional data set for models to be compared against. Near wall measurements should also be performed for the pipe flow investigations, the use of higher magnification lenses and a high-quality camera would allow for the viscous sublayer of the flow to be measured. It should be noted that measurements in this region would require the trigger rate of the camera to be optimised for the lower relative velocity in this region. Chemical etching is a possible solution to the creation of the calibration plate which would allow for software to compensate for the optical distortion very close to the wall.

The presented results have shown that local concentration of particles may be responsible for some of the differences between particle species at the same volume fractions. Measurements of local particle concentration would provide greater accuracy when comparing these particle and concentration effects. Aside from direct measurement, if the local particle concentration was found to vary as expected with a concentration gradient from the bottom to the top of the pipe, then changing the orientation of the measurement equipment would allow for this effect to be examined in detail. However, this would also have the effect of negating gravitational effects so care should be taken when making comparisons between the current data set and those using different flow orientations.

As the impinging jet was used to represent the tanks used to store nuclear waste, it would be useful to examine a range of particle shapes to determine how shape influences the flow and if the equivalent hydraulic diameter can be used to predict particle behaviour and fluid response. Regarding the waste storage tanks, an array of impinging jets are used to suspend waste and so examination of the interaction between multiple impinging jets would also be of value as the interaction changes flow behaviour.

In addition to impinging jet arrays, the highly active storage tanks also contain cooling loops which would break-up the flow and create flow structures within the tank. It is suggested that PIV would be a suitable technique for studying the interaction of an impinging jet with these obstacles and may provide greater insight into the complicated flow behaviour within the storage tanks.

Measurement of particle velocities and velocity fluctuations would provide a more comprehensive picture of the flow and so it is recommended that future work is focused on the measurement of larger particles. Much of the turbulence modulation in the impingement region is due to differences in particle and fluid velocities, making further examination in this area of high importance. It is suggested that to avoid the issues with low particle numbers an alternative measurement technique is used, potentially particle tracking velocimetry (PTV), as it would require little to no modification of the current experimental equipment however, time restrictions prevented this work from being accomplished.